# The influences of spatially variable rainfall and localized infiltration on groundwater recharge in a water management context

by

Andrew James Wiebe

A thesis
presented to the University of Waterloo
in fulfillment of the
thesis requirement for the degree of
Doctor of Philosophy
in
Earth Sciences

Waterloo, Ontario, Canada, 2020

**Examining Committee Membership**

The following served on the Examining Committee for this thesis. The decision of the Examining Committee is by majority vote.

| | |
|---|---|
| External Examiner | Dr. Grant Ferguson<br>Associate Professor<br>Dept. of Civil, Geological and Environmental Engineering<br>University of Saskatchewan |
| Supervisor | Dr. David Rudolph<br>Professor and Chair<br>Dept. of Earth and Environmental Sciences |
| Internal Member | Dr. Philippe Van Cappellen<br>Professor<br>Dept. of Earth and Environmental Sciences |
| Internal-external Member | Dr. James Craig<br>Associate Professor<br>Dept. of Civil and Environmental Engineering |
| Other Member | Dr. Brewster Conant, Jr.<br>Adjunct Associate Professor<br>Dept. of Earth and Environmental Sciences |

# AUTHOR'S DECLARATION

This thesis consists of material all of which I authored or co-authored: see Statement of Contributions included in the thesis. This is a true copy of the thesis, including any required final revisions, as accepted by my examiners.

I understand that my thesis may be made electronically available to the public.

# Statement of Contributions

The main body of this thesis (Chapters 2 to 4) was written as a series of three manuscripts in preparation for submission of the individual chapters to journals. A paper based on Chapter 2 has already been published, and contributions by the co-authors are listed as follows. A.J. Wiebe is the first author and main contributor for this publication, and the author of the remainder of the thesis. P.G. Menkveld collaborated on instrument installations and monitoring associated with Chapter 3, as described below.

**Chapter 2**

A.J. Wiebe contributed to this manuscript during the phases of conceptualization, methodology, funding acquisition (NSERC IPS Scholarship application), field and numerical investigation, data curation, software analysis (modelling), formal analysis (statistical analyses, calculations), writing of the original draft, and editing. Contributions by co-author D.L. Rudolph included discussions regarding conceptualization and methodology, funding acquisition (NSERC Discovery Grant; assistance with NSERC IPS Scholarship), provision of resources including hydrological equipment and computers, supervision, and review of the manuscript.

**Chapter 3**

A.J. Wiebe and P.G. Menkveld collaborated on the initial equipment setup (wells, soil moisture instruments, temperature sensors) and monitoring for the first year of investigation at the site (Nov 2014 – Oct 2015). P.G. Menkveld oversaw data collection and installation of five observation wells between Jan and Apr 2014. After Oct 2015, A.J. Wiebe added further equipment installations and monitored the site for another 2.5 years.

# Abstract

Water management involves monitoring, predicting, and stewarding the quality and quantity of groundwater recharge at the watershed scale. Recharge sustains baseflow to streams and replenishes water extracted by pumping at wells; it is frequently estimated using numerical models that couple or fully integrate surface water and groundwater domains and use water budgets to partition water into various components of the hydrological cycle. However, uncertainty associated with the input data for large components such as precipitation and evapotranspiration may hinder model accuracy, and preferential flow dynamics such as depression focused recharge (DFR) may not be represented at typical modelling scales (≥10s of $km^2$) or with typical approaches. The present study addressed two themes related to groundwater sustainability and vulnerability: 1) the sensitivity of modelled recharge estimates to the spatial variability of rainfall, and 2) the vulnerability of public supply wells to DFR during large-magnitude rainfall or snowmelt events. The region investigated during this research was the Alder Creek watershed (78 $km^2$), a typical southern Ontario setting overlying glacial moraine sediments with mostly agricultural land use, some urban and aggregate resource development, and whose recharge supplies multiple municipal well fields for the cities of Kitchener and Waterloo.

Rainfall is often the largest component of the water budget and even a small uncertainty percentage may lead to challenges for accurately estimating groundwater recharge as a calculated residual within a water budget approach. However, rainfall monitoring networks typically have widely spaced gauges that are frequently outside the watershed of interest. Assessment of the influence of spatially variable rainfall on annual recharge rate estimates was performed by comparing transient simulations using input data from three different rain gauge networks within a coupled and fully-distributed numerical model. A local network of six weather stations with rain gauges was installed and operated in and around the study watershed for three years, and data from six regional stations (within 30 km of the watershed) and one national station (3 km from the watershed) were obtained from publicly available sources. Time series of distributed, daily rainfall were interpolated via the inverse distance squared method using data from each of the rain gauge networks for three calendar years. The temporal and spatial snowfall distribution was consistent among all scenarios, to maintain focus on differences caused by the rainfall input data. Results showed that annual average recharge rates could differ considerably between scenarios, with differences sometimes greater than the water-budget derived uncertainty for recharge. Differences in overall recharge between pairs of scenarios involving the local rain gauge network were largest, varying by up to 141 mm per year, or 44% of the steady state

recharge estimated in a previous study. Streamflow estimates for the local rainfall simulations were closer to observations than those using regional or national rainfall. Because the three scenarios used the same set of underlying soil parameters, the results suggest that the availability of local rainfall measurements has the potential to improve the calibration of transient watershed hydrogeological models.

The second theme of the present study was exemplified by the Walkerton tragedy in 2000, where pathogenic microbes were rapidly transported from ground surface to a public supply well during a heavy rainfall event. The vulnerability of such wells to surface-originating contaminants during major hydrological events remains poorly understood and is difficult to quantify. Such events may result in overland flow collecting in low topographic locations, leading to localized infiltration. If focused recharge occurs in the immediate vicinity of a public supply well, the threat to the water quality of that well may significantly increase temporarily. These conditions are frequently encountered within the glaciated landscape of southern Ontario. Conventional approaches for defining the threat of groundwater under the direct influence of surface water (GUDI) do not routinely account for this type of transient infiltration event and instead assume steady state flow fields without localized recharge. The present study combined the monitoring and modelling of a site in southern Ontario where DFR is routinely observed to occur within 50 m of a public supply well. Extensive site characterization and hydrologic monitoring were conducted at the site over a period of 3.5 years, specifically during large-magnitude hydrologic events including heavy rainfall and snowmelt. Integrated surface water – groundwater models employing HydroGeoSphere (HGS) were used to quantify the transport of potential contaminants infiltrating beneath a depression and a creek and the associated risk to the public supply well. Simulated relative concentrations at the well were below “detection” for typical median contaminant concentrations in surface water but > 1 cfu/100 mL with travel times between 118 and 142 days for creek and DFR solutes, respectively, based on maximum initial surface water concentrations. Results suggest that DFR and localized recharge could increase the threat to overburden wells under extreme conditions. Ponding reduced travel time by at least 58 days for the DFR solute.

In order to extend the analysis of recharge estimate sensitivity to spatial rainfall variability to the longer term, and to incorporate the influence of actual evapotranspiration (AET) uncertainty, a method was developed to employ stochastic rainfall time series and AET estimates in a Monte Carlo framework to quantify the resulting variability in recharge estimates and three groundwater

management metrics. Stochastic rainfall time series were generated via a parametric, mixed exponential method for three virtual stations within the Alder Creek watershed and constrained by field-derived spatial correlation coefficients. Observed snowfall data from one nearby national weather station were used to calculate total precipitation. Stochastic annual AET estimates were generated based on: 1) calculated annual potential evapotranspiration at the national weather station, 2) observed variation about the Budyko curve in 45 US MOPEX watersheds with $\overline{PET}/\bar{P}$ ratios within ±0.05 of the average ratio calculated for the national weather station near the watershed, and 3) a correction factor to remove AET from the saturated zone. Recharge rates for the Alder Creek watershed were calculated via a 46-year vadose zone water budget for each of 16,778 realizations. The surface water fraction of streamflow was estimated using hydrograph separation results for the watershed. It was hypothesized that spatially variable precipitation would exert more influence on recharge than AET because it is a larger component of the local water budget. Groundwater recharge results were applied to three different metrics related to water quality, well vulnerability, and water quantity. Results suggest that estimates of non-point source contaminant loadings to the water table could differ by up to ±14% from the average. Worst case changes in capture zone area estimates for a public supply well could be up to ±15% different from the average. The ratio of maximum to minimum cumulative recharge over all realizations was 1.31, though contributions from spatial rainfall variability alone led to a ratio of 1.15. This suggests that AET uncertainty and spatial rainfall variability each contribute nearly the same amount of variability to recharge estimates. This latter ratio is less than the result (~2) from a previous study of a much larger watershed in Spain. The results highlight the importance of AET estimates for recharge rate estimation, and their potential impacts on land use planning and groundwater management. This method could be used to project impacts of climate change on recharge variability at the watershed scale.

Overall, results suggest that the spatial variability of rainfall could impact recharge rate estimates in numerical models of small to medium sized watersheds (e.g., 78 $km^2$), especially during short simulations. Annual recharge estimates could vary over a range equivalent to 44% of a previously estimated steady state value, though long-term (46-yr) estimates could vary over a range equivalent to 12% of this value due to averaging over time. Non-point source loadings and capture zone areas could vary up to ±7.0% and ±7.4% from the average, respectively, over the long term due to spatial rainfall variability, though uncertainties associated with AET could increase this to ±14% or ±15%, respectively. The hydrological event characterization and well vulnerability modelling of the second research theme suggest that localized recharge could lead to increased microbial risks for wells

screened in overburden sediments during large hydrological events (≥ 40 mm rainfall over 4 days) through the phenomenon of temporary ponding. The method developed for the long-term stochastic recharge rate analysis could be applied in other settings as an alternative to, or to complement, large-scale, fully-distributed 3D numerical modelling.

# Acknowledgements

This research was supported by the Natural Sciences and Engineering Research Council of Canada (NSERC; IPS Grant #485430 to A.J. Wiebe, and Discovery Grant to supervisor D.L. Rudolph). Thanks to the Southern Ontario Water Consortium (SOWC; Ontario MEDI, Project #21616; FedDev Ontario, Project #801680) for the use of the large amount of hydrogeological equipment that made this study possible, and to Matrix Solutions for providing expertise and resources for the modelling in Chapter 2. Many thanks also to R. and W. Goettling, G. and L. Kaster, D. and P. Mighton, the Region of Waterloo, Colour Paradise Greenhouses, Herrle's Farm Market, Nith Valley Organics, Rebel Creek Golf Club, and the County of Oxford for allowing us to install equipment and collect hydrological data at many locations around Alder Creek watershed!

Thank-you to Philippe van Cappellen, James Craig, and Brewster Conant, Jr., for being committee members for me during this PhD process. I've valued your suggestions, and I think the research quality has increased because I knew that you would be reviewing it. Thanks also to Grant Ferguson for agreeing to review this work as the external examiner.

A big thank-you to the many SOWC Co-op students and fellow graduate students who assisted with the field work: Sage McKay, Jamie Dickhout, Kristen Blowes, Cailin Hillier, Jack Robertson, James Elliott, Emilie Mesec, Paul Menkveld, Nathanael Couperus, Niki Long, Jeffrey Stevens, Ian Mercer, Elliot Pai, Elton Huang, Sarah Indris, Joey Ju, Jeffrey Leon, and Andrew Wicke. Thanks especially to Paul and Andrew for good discussions about research. Emilie's photo of ponding in a field near a municipal well initiated the DFR study (Chapter 3). Thanks to the other students of the Rudolph Group for questions about the research and for camaraderie.

I'm grateful to Steve Murray and Paul Martin at Matrix Solutions for advice and assistance with the MIKE SHE modelling for Chapter 2 – thanks for sharing your expertise. Thanks to Gaelen Merritt for assistance with the van Genuchten parameters. Thanks to Christopher Neville, Brittney Glass, Maria Giovanna Tanda, Gonzalo Sapriza-Azuri, and two anonymous reviewers for reviewing previous versions of the Chapter 2 manuscript. Sylvain Gagné made some insightful comments on an early version of the Chapter 2 results at the GeoOttawa 2017 conference.

Thanks to Ning Luo and John Doherty for assistance with PEST, and to Alex Chik for comments on the critical relative concentration concept (Chapter 3). Thanks also to Paul Menkveld for collaborating on the initial site setup and monitoring of the Nov 2014 rainfall and snowmelt event.

I’m grateful to Nandita Basu for introducing my Ecohydrological Modelling class to the Budyko curve. Thanks to Young-Jin Park for assistance with the HGS models and philosophical conversations about modelling. Dr. Park suggested and assisted with the mathematical derivation of the drawdown cone extent in Appendix L.

No University of Waterloo Earth Sciences field study up to the present would be complete without the help of technicians Paul Johnson and Bob Ingleton. A big thank-you to Bob and Paul for assisting with the drilling of soil cores, equipment installations, construction of equipment in the lab, and even returning from retirement a few times to help! Thanks also to Terry Ridgway for equipment loans, and to Odum Idika for collaborating on the SOWC data collection.

Much credit and many thanks to my supervisor, Dr. Dave Rudolph. Thank-you, Dave, for being my teacher and fellow researcher for many years. I appreciate how you encourage and look for opportunities for all your students, and how you remind us to think about the big picture.

Thanks to my community outside the university. Thank-you to my wife Rachael for support and encouragement. Thank-you, Mom and Dad, for encouraging my pursuit of education and for asking me how my work was progressing. Thanks also to friends and neighbours for cups of tea and kebab barbeques during my studies.

Thanks to the Open Source software community, including the developers and maintainers of GNU Octave.

# Dedication

To all those good stewards of the land – and of the water, the atmosphere, and the depths – so that all may again become *tobe* [good].

# Table of Contents

# List of Figures

# List of Tables

# Chapter 1
# Introduction

## 1.1 Background

Two of the main considerations for groundwater management at the watershed scale are the quantity and quality of groundwater recharge, factors which influence the sustainability and vulnerability of well pumping rates and baseflow to streams. Groundwater recharge amounts are frequently estimated using numerical models. While these are powerful tools, the representation of complex, transient watersheds within models that link the surface and subsurface leads to questions regarding the impact of the scale of the input data: How much uncertainty is entrained in rainfall and evapotranspiration data? Are typical monitoring strategies and numerical modelling tools effective for understanding large-magnitude or extreme events? What role might localized recharge play for well water quality, especially in areas of heterogeneous and hummocky glacial moraine sediments?

Well vulnerability and sustainability are global and local issues. Extreme hydrological events, disease outbreaks, and groundwater wells have been linked in many countries including Canada (Hrudey et al., 2002; O'Connor, 2002), the United States (Curriero et al., 2001), the United Kingdom (Bridgman et al, 1995; Hunter, 2003), Turkey (Aksoy et al., 2007; Baldursson and Karanis, 2011), and Guatemala (Eisenhauer et al., 2016), among others. The Walkerton, ON, tragedy of May 2000 is an unfortunate example. Over 100 mm of rain fell in less than a week and pathogenic bacteria were rapidly transported to a shallow (5 to 8 m deep) well in fractured bedrock; improper chlorination, coupled with this contamination event, led to 2,300 cases of illness and seven deaths (O'Connor, 2002). Further, extreme rainfall is expected to become increasing frequent, globally, due to climate change (IPCC, 2013; Jiang et al., 2015). On the other extreme, drought occurrence is increasing in parts of the world (Dai et al., 2004; Trenberth, 2011). Warming could lead to fewer, more extreme rainfall events, increasing risks of both flooding and droughts (Trenberth, 2011). The spatial and temporal variability of rainfall, and therefore recharge rates and the vulnerability of wells, could undergo change as a result.

Numerical models are used to predict how wells will affect local or regional groundwater levels and the concentrations at which contaminants might arrive at wells. Many numerical simulations are conducted at steady state. This may be reasonable for long-term studies and non-point source contamination, if rainfall rates average out over the long term and if land use practices remain

relatively unchanged. If transient analyses are desired, for instance, for studying groundwater–surface water interaction, there may be few data available at time scales less than daily to guide or constrain modelling. Extreme rainfall events (100 - 200 mm) in southern Ontario can occur over small areas (e.g., 100 $km^2$) within hours (Paixao et al., 2015). These may be even more pronounced in other climates (e.g., rates > 200 mm/hr; Hamada et al., 2014). To complicate matters, runoff generation from large rainstorms is nonlinear (Paixao et al. 2015; Villarini et al., 2010), and stream rating curves may not include extreme event data due to safety issues and measurement challenges related to turbulent flow. One of the relevant questions for models concerns whether input data are available at an acceptable scale to capture dynamic watershed responses.

Previous work on spatially variable rainfall and recharge has been performed by Sapriza-Azuri et al. (2015) and by Mileham et al. (2008). Sapriza-Azuri et al. (2015) studied the 16,000 $km^2$ Upper Guadiana watershed in Spain. These authors were interested in how the spatial resolution of stochastic rainfall amounts applied to a fully-distributed model affected the recharge rates estimated. They found that recharge rates in simulations with the lowest and highest spatial grid resolution were different by a factor of around 2 over 40 years. Mileham et al. (2008) focused on a slightly different question. Rather, these authors looked at how the interpolation method chosen for rainfall data impacted recharge estimates in a semi-distributed soil moisture balance model of a 2,100 $km^2$ watershed in Uganda over 15 years. They compared results of rainfall interpolated via Thiessen polygons with results from inverse distance weighting applied to 25 km by 25 km areas. The present study complements these analyses in Chapter 2 by addressing how rain gauge network scale can influence simulated annual recharge rates when rainfall is interpolated by the same method onto the same grid (250 m by 250 m) in a smaller watershed (Alder Creek, 78 $km^2$). The long-term influence of spatially variable rainfall on recharge rates in this watershed was projected in Chapter 4 by using stochastic rainfall time series based on observed correlation characteristics.

Recharge rates and their distribution are also important for understanding microbial transport to public supply wells. Previous work on reactive transport modelling of microbes during a large-magnitude event in the context of well vulnerability has been conducted by Knappett et al. (2014). These authors simulated *E. coli* transport from a surface pond flooded with latrine effluent to shallow observation wells using Hydrus-2D under saturated conditions. The present study builds upon this work by investigating and simulating solute transport from ponding at the ground surface through the vadose and saturated zones to a well, as an analog to possible microbial contamination resulting from

a large hydrological event (Chapter 3). Other researchers have modelled microbial transport in the absence of hydrological event conditions, often via injections into wells and using analytical or simplified models (e.g., Bales et al., 1997; Mallén et al., 2005; Kvitsand et al., 2015; Schijven et al., 1999; Sinton et al., 1997). Well vulnerability is typically considered by generating capture zones for certain periods of travel time using numerical models that may assume 2D flow (e.g., 50 days, 1 year, 2 years, etc.; Frind et al., 2006). For instance, Worthington et al. (2012) calculated a 3-day capture zone based on particle tracks for a well involved in the Walkerton tragedy. Another example is the study by Eberts et al. (2012), who simulated breakthrough curves for conservative non-point source contaminants in the saturated zone over decades and compared particle tracking and lumped-parameter models. Sousa et al. (2013b) introduced a method to consider whether the vadose zone could reasonably be neglected or not when assessing contaminant migration toward a well. The vadose zone may be a crucial buffer preventing microbial contamination from reaching the saturated zone within a short enough time scale to be of concern in many cases.

The field site chosen for the present study was the 78 $km^2$ Alder Creek watershed, west of Kitchener-Waterloo, ON (population ~ 400,000). This watershed is located on the Waterloo Moraine and its overburden stratigraphy is a multi-aquifer-aquitard system (Martin and Frind, 1998), where groundwater recharge supplies water for up to seven well fields whose capture zones are located within or reach beneath it (Brouwers, 2007). This largely agricultural watershed has experienced some development in terms of urban areas and aggregate extraction (sand and gravel) pits; it represents a typical watershed in southern Ontario. Threats to water quality include non-point sources such as road salt and nitrate, and point-sources such as a landfill and surface water bodies. This watershed has been modelled multiple times (CH2MHILL and SSPA, 2003; Martin and Frind, 1998; Matrix and SSPA, 2014a, 2014b; Sousa et al., 2013a) due to its importance for municipal water supply.

The approach applied in the present study combined the collection of hydrological field data (rainfall, water levels, soil moisture, and parameters for reference evapotranspiration ($ET_o$) calculations) with numerical modelling to answer questions related to groundwater recharge and uncertainty. Characterization tools such as spatial correlation analysis (Chapters 2 and 4) and cataloguing and evaluating large-magnitude hydrological events (Chapter 3) are presented as methods that may be useful at other sites for similar studies. Within this framework, this research seeks to advance water management by addressing issues that have previously received little attention by

using characterization tools and numerical modelling strategies that then may be applied to other settings.

## 1.2 Objectives

The overall goal of this work was to address two themes related to groundwater management, and specifically groundwater recharge, that remain poorly understood. These two themes were: 1) the impact of the spatial variability of rainfall on recharge estimates, and 2) the impact of localized infiltration and recharge on well vulnerability. The research objectives of this thesis were: 1) to explore the impact of the spatial variability of rainfall on annual, watershed scale recharge estimation via a numerical model that couples surface and subsurface domains (Chapter 2); 2) to evaluate the potential threat of large-magnitude hydrological events to public supply wells from depression focused recharge and losing streams in glacial moraine landscapes (Chapter 3); and 3) to quantify the potential long-term variability of watershed scale groundwater recharge estimates due to the spatio-temporal variability of rainfall and the uncertainty of actual evapotranspiration, and the resulting variability of three metrics related to water quality, water quantity, and well vulnerability (Chapter 4).

## 1.3 Thesis Organization

The three topics noted above (Chapters 2 to 4) were written in manuscript format in preparation for submission as journal articles. A paper based on Chapter 2 has been published by a scientific journal as follows:

- Wiebe, A.J., Rudolph, D.L., 2020. On the sensitivity of modelled groundwater recharge estimates to rain gauge network scale. J. Hydrol. 585, 124741. https://doi.org/10.1016/j.jhydrol.2020.124741.

Chapter 5 contains conclusions and recommendations. The list of references that follows Chapter 5 includes references for all chapters and appendices. The acknowledgements section above is a compilation for all chapters. Seventeen appendices provide supplementary information at the end of

the document. One of the appendices is electronic (a pdf file) and contains the computer code used to perform the calculations for Chapter 4.

# Chapter 2
# On the sensitivity of modelled groundwater recharge estimates to rain gauge network scale

## 2.1 Introduction

The estimation of groundwater recharge is a challenging task at any scale of consideration. With the emergence of regional scale groundwater models, often applied at a watershed scale, the seasonality and spatial variability of recharge has become a hydrologic component of significant importance. This is particularly the case when considering its role as a forcing function in water budgets and contaminant transport processes. Recharge magnitude and distribution is frequently estimated by numerical models that employ a water balance approach, where the magnitude of the recharge is calculated as a residual of the other measured or estimated components of the overall water budget (Healy, 2010). The calculated recharge distributions are then used as boundary conditions in modelling exercises related to watershed-scale assessments of water resources, regional impacts of non-point source contaminants, and changing land-use impacts. The rainfall data that are required for the water budget estimations are often derived from local weather stations that vary in spatial proximity to the study area.

While the scales at which rainfall measurements are made are known to influence their spatial accuracy over regional scales (Hess et al., 2016; Villarini et al., 2008; Winter, 1981), the impact of measurement density on the spatial distribution of calculated groundwater recharge rates has received little attention (Sapriza-Azuri et al., 2015). In many environments, precipitation (P) tends to be the largest component of the water budget (Dingman, 2015). Thus, small percentage uncertainties associated with P will lead to large magnitudes of uncertainty for smaller components of the overall hydrologic flow system – such as groundwater recharge or discharge – that are often estimated as residuals of the total water budget (Thodal, 1997; Wiebe et al., 2015; Winter, 1981). For rainfall data collection, a rain gauge density of 3 gauges/100 $km^2$ has been recommended for the U.S. (Schaake et al., 2006), and densities between 1 gauge/900 $km^2$ and 1 gauge/600 $km^2$ have been recommended by the World Meteorological Organization (Dingman, 2015). The recommended measurement scale required for rainfall measurements to ensure a particular degree of confidence in the estimation of groundwater recharge for a particular area is largely unknown and dependent on local conditions.

Many studies focused on the spatial variation of rainfall and the uncertainty associated with a particular network density have been undertaken to illustrate the significance of precipitation measurement (e.g., Dingman, 2015; Hess et al., 2016; Huff, 1970; Huff and Schickedanz, 1972; Linsley and Kohler, 1951; Villarini et al., 2008; Winter, 1981). The impact of spatial rainfall variability on streamflow has also been addressed, and it is well known that the number of rain gauges and their locations impact the accuracy of modelled hydrographs (e.g., Andréassian et al., 2001; Bell and Moore, 2000; Faurès et al., 1995; Obled et al., 1994; Zhao et al., 2013). Villarini et al. (2008) found that spatial correlation among rain gauges tends to increase, and spatial sampling errors tend to decrease, for increasing data averaging times (e.g., 15 min, hourly, and daily). The authors do note, however, that the transferability of specific rainfall uncertainty results to other areas may not be directly applicable due to local site conditions.

Previous numerical studies addressing the influence of spatial rainfall variability on recharge have identified that interpolation techniques and the model's spatial grid size are important factors. Mileham et al. (2008) used a semi-distributed, soil-water budget model for a humid, tropical watershed in Uganda (2,098 $km^2$) over 15 years and found that cumulative recharge estimates differed by a factor of about 1.5 between a scenario interpolating precipitation via Thiessen polygons and one using inverse distance weighting with 20 rain gauges. Sapriza-Azuri et al. (2015) used a fully-distributed model with stochastic rainfall distributions generated from rain gauges at 151 weather stations and found that recharge estimates varied based on the scale of the interpolated rainfall data (2.5 km by 2.5 km, or 50 km by 50 km, or lumped over the entire 16,000 $km^2$ watershed). Applying rainfall at the smallest grid cell size over four decades resulted in 1.5 to 2 times the recharge estimated when rainfall was applied at the other two scales. Recommendations for both the spatial density of observation points and selection of grid sizes for model input are needed for other geographical contexts.

Precipitation is frequently measured by rain/snow gauge networks, and ground-based radar methods rely on these for calibration (e.g., Dingman, 2015). The density of Canada's rain gauge network (Metcalfe et al., 1997; OMNR, 2007) is less than 1 gauge per quaternary watershed (OMNRF, 2016) in southern Ontario, where quaternary watersheds are on average 312 $km^2$ in size. Extreme summer rainfall events in this area may occur over 100 $km^2$ (Paixao et al., 2015), and convective summer storms can be as small as 5 to 8 $km^2$ in size (Singh, 1992; Tsanis and Gad, 2001). Such events could easily evade detection by existing rain gauge networks, and these may become

increasingly important due to climate change (Collins et al., 2013; Cubasch et al., 2001; Jyrkama and Sykes, 2007). This is a potential concern for groundwater recharge estimation under both long-term and event-based conditions. The sustainable management of integrated water supplies depends on accurate quantitative estimates derived from precipitation measurements. Accurate precipitation estimates are also essential for assessing regional-scale water quality vulnerability related both to non-point contaminants and local, extreme hydrologic, event-based conditions near critical receptors such as public supply wells (e.g., Christie et al., 2009; the May 2000 Walkerton tragedy – O'Connor, 2002).

The objective of the present study was to assess the spatial correlation among point rainfall measurements, and to explore the sensitivity of modelled recharge estimates to spatial variations in rainfall in the vicinity of a typical watershed in southern Ontario. The watershed selected for this study represents watersheds where municipal water sources rely on glacial moraine aquifers, and agricultural activities and urban expansion present challenges related to water quality and quantity. It was hypothesized that recharge estimates in scenarios employing different rainfall networks' interpolated data would differ to a degree that could significantly impact regional water management decisions. The uncertainty associated with the recharge component of a near-surface water budget was employed as a metric of significance. Differences in recharge between scenarios were assessed based on: 1) visual analysis of the spatial distributions of total recharge, 2) the frequency of cell-by-cell differences in modelled total recharge, and 3) changes in water budget components such as cumulative streamflow. Three different spatial scales of rain gauge networks were used for the assessment: i) one national station located within 3 km of the watershed, ii) six regional stations within 30 km of the watershed, and iii) six local stations, five of which were within the watershed. The sensitivity was addressed by comparing the magnitude and spatial distribution of recharge results from three corresponding scenarios: (1) spatially uniform rainfall from the national network, and spatially variable rainfall interpolated from the (2) regional and (3) local networks. Spatially uniform reference evapotranspiration ($ET_o$) derived from the national network station was used for all scenarios, and spatial variations in snowfall were held constant in order to isolate rainfall as the variable of comparison.

For this investigation, field data collected from the local rain gauge network within the study region over a three-year period were utilized to illustrate natural precipitation variability. This relatively short temporal period was specifically addressed because this is the time scale at which fully-coupled

models may be used in practice by environmental consultants to study the impacts of dynamic hydrological events on city water supply systems (Meyer et al., 2017). There could be different results over a longer time scale.

## 2.2 Methods

### 2.2.1 Site Description

The Alder Creek watershed (78 km$^2$; Figure 2.1; GRCA, 1998) within the Grand River watershed (6,800 km$^2$; OMNRF, 2016) is located on the regional upland of the Waterloo Moraine. Located adjacent to the cities of Kitchener and Waterloo, ON, this watershed's glacial sands and gravels cover over half of its surficial area (CH2MHILL and SSPA, 2003; OGS, 2010) and facilitate recharge for about seven municipal well fields operated by the Regional Municipality of Waterloo (Brouwers, 2007). Due to its importance for water supply, the watershed and its surrounding area have been the subject of detailed hydrologic modelling in the past (e.g., CH2MHILL and SSPA, 2003; Martin and Frind, 1998; Matrix and SSPA, 2014a, 2014b; Sousa et al., 2013a). The availability of extensive subsurface geological data and hydrogeological interpretations derived from previous work in the area (e.g., Bajc et al., 2014; Blackport et al., 2014; CH2MHILL & SSPA, 2003; Martin and Frind, 1998) provides a valuable foundation for the current modelling exercises within the multi-aquifer system of the Waterloo Moraine.

Total annual precipitation is around 900 mm in this region, varying between 600 and 1100 mm at the nearby Environment Canada weather station at Roseville, ON, which is located less than 3 km outside the watershed (Government of Canada, 2019; OMNR, 2007). Actual ET (AET) for the region has been estimated at generally around 540 mm per year (Sanderson, 1998),[1] and streamflow is on average 140.5 mm per year at the gauging station within the watershed (Figure 2.1; based on daily data, 1973-2018; WSC, 2019). The average baseflow index (i.e., BFI, the fraction of total streamflow constituted by groundwater baseflow) for this station is 0.56, according to PART (Barlow et al., 2015) hydrograph separation results (based on daily data from WSC, 2019; 1973 to 2018).

National network daily precipitation and temperature data were obtained for the Roseville weather station (Government of Canada, 2019) noted above and shown in Figure 2.1; this is the closest national station to the Alder Creek watershed.[2] Rainfall data were recorded using a Canadian Type B

[1] See Appendix A for AET estimates based on the Budyko curve.
[2] Appendix B explains why only one national station was used.

rain gauge (113 mm diameter) at a height of 0.4 m and available on a daily timescale, while snow depths were manually measured each day and converted to snow water equivalent using a ratio of 0.1 (Government of Canada, 2013, 2019). No windshield was reported, so undercatch related to wind may be a factor for the Roseville rainfall dataset. Daily maximum and minimum temperatures (Government of Canada, 2019) were obtained from the Roseville station for $ET_o$ calculations.

Regional network rainfall data (GRCA, 2017a) were obtained from six stations operated by the Grand River Conservation Authority (GRCA) and shown on the inset map of Figure 2.1. Rainfall data were available at an hourly time scale from a network of tipping-bucket gauges installed for the purposes of flood forecasting (Shifflett, pers. comm., 2018). Windshields were not likely used at these stations, so related undercatch may also be an issue for this network.

Local network rainfall data were obtained from the Alder Creek field observatory of the Southern Ontario Water Consortium (SOWC; Wiebe et al., 2019).[3] This network of weather stations (Figure 2.1) employed tipping bucket rain gauges (200 mm diameter) that recorded data every 15 min. Each of the six gauges was installed at a height of 1 m above the ground surface and surrounded by an Alter-type wind shield. Data were available for January 2014 onward for all stations except WS5, where data records began in June 2014. Annual rainfall totals are shown in Table 2.1 for each of the three rain gauge networks. The local rain gauge network density was about twice the density recommended by others. Schaake et al. (2006) recommended two gauges per 10 $km^2$ and three gauges per 100 $km^2$ in order to accurately estimate precipitation in a watershed.

Snowfall constitutes 15% (Government of Canada, 2019; OMNR, 2007) of annual total precipitation in the Alder Creek watershed. Spatial variations in snowfall or snowpack thickness were not incorporated into the present study due to the focus on spatial rainfall variability and insufficient snowfall data, though spatially variable snowpack thickness could modify recharge distributions, especially during large snowmelt events. Available monthly rainfall and snowfall data are shown in Appendix D for all three networks. Additional information regarding the calculation of total precipitation from local or regional or national rainfall and national snowfall data may also be found in Appendix D.

[3] Appendix C provides an overview of the Alder Creek field observatory.

### 2.2.2 Spatial Correlation

Spatial correlation for rainfall was assessed using Spearman's rank correlation coefficient (Gibbons and Chakraborti, 1992; Villarini et al., 2010) for several accumulation times (following Villarini et al., 2008). Each coefficient was generated by comparing the data from a pair of stations. For each accumulation time (1 hr, 3 hr, and 24 hr), the sum of the data within each time interval of that size was compared. Each correlation coefficient measures the strength of the linear relationship between ranked data at a pair of stations. The Spearman rank correlation coefficient was used instead of the Pearson coefficient because the Pearson method assumes that the data are normally distributed, while the Spearman coefficient does not (Gibbons and Chakraborti, 1992). Rainfall data were assessed for the combined stations of the local and regional networks. The overall time period for this correlation analysis was three years, except for correlations involving station WS5, which employed 2.5 years of data. An exponential model (Villarini et al., 2008) relating the correlation coefficient, ρ, to the separation distance, h, was employed to fit the data and show general trends in correlation for the different accumulation times (Eqn. 2.1):

$$\rho(h) = c_1 exp\left[-\left(\frac{h}{c_2}\right)^{c_3}\right]. \tag{2.1}$$

The parameters $c_1$, $c_2$, and $c_3$ represent the nugget, correlation distance, and shape factor, respectively (Villarini et al., 2008). Following Villarini et al. (2010) and based on arguments by Krajewski et al. (2003) that a traditional network of rain gauges (one gauge per location) is insufficient to estimate $c_1$, a nugget value of $c_1 = 1.0$ was chosen in all cases. The correlation distance and shape factor for the field data were determined via the Levenberg-Marquardt algorithm (Gavin, 2009, 2019) in the scientific computation program GNU Octave (Eaton et al., 2011).

### 2.2.3 Water Budget and Uncertainty

Context for the recharge differences between scenarios was portrayed by calculating the uncertainty from an annual near-surface water budget (Eqn. 2.2),

$$R = P - AET_{VZ} - Q_{SW} - \Delta S_{VZ}, \quad (2.2)$$

where $R$ is recharge, $P$ is total precipitation, $AET_{VZ}$ is actual evapotranspiration from the vadose zone, $Q_{SW}$ is the surface water fraction of streamflow (i.e., 1 – baseflow index), and $\Delta S_{VZ}$ is net storage change in the vadose zone. Infiltration into the vadose zone has been replaced by $P - Q_{SW}$ in the above equation. This water budget assumes that recharge occurring from surface water bodies directly connected to the water table is negligible (i.e., all recharge migrates through the unsaturated zone). AET derived from the saturated zone is excluded from this water budget because the domain for this budget is the vadose zone; AET derived from the saturated zone has already become recharge ($R$) and thus should not be counted twice. Uncertainty on recharge ($\delta R$) was calculated under the assumption that the individual uncertainties are independent (e.g., Dingman, 2015) via (Eqn. 2.3),

$$\delta R = \sqrt{\delta P^2 + \delta AET^2 + \delta Q^2 + \delta \Delta S_{VZ}^2}, \quad (2.3)$$

where $\delta P$ is precipitation uncertainty (~10%, Dingman, 2015); $\delta AET$ is AET uncertainty (~10%, Kristensen and Jensen, 1975); $\delta Q$ is streamflow uncertainty (~5%, Herschy, 1973; Winter, 1981); and $\delta \Delta S_{VZ}$ is uncertainty related to vadose zone storage change (~5%, assumed similar to streamflow). Spatial interpolation errors for $P$ and $AET$ were not included. The uncertainty of the water budget components in Eqn. (2.3) was calculated using the input data and results for a scenario and year with a percentage uncertainty on $R$ that was similar to the average from all annual simulations, as an example of a typical case.

### 2.2.4 Numerical Model

The fully-distributed MIKE SHE software code (Abbott et al., 1986; Graham and Butts, 2005; Refsgaard and Storm, 1995) was used to conceptually explore the sensitivity of recharge estimates to spatial variations in rainfall. This code internally couples the saturated zone (3D), unsaturated zone (1D), overland flow (semi-distributed), and streamflow (1D) processes, with surface boundary inputs and outputs such as P and $ET_o$. Advantages of MIKE SHE include its ability to simulate all major aspects of the hydrological cycle and internally couple them, which is particularly advantageous for

groundwater-surface water interaction and overland flow-drainage-recharge flow paths. The model includes a Richards equation option for the unsaturated zone, which is comparable to many models (Barthel and Banzhaf, 2016) such as FEFLOW (Zhou et al., 2011), FEFLOW coupled with HELP (Guay et al., 2013), CATHY (Camporese et al., 2010), and MODHMS (Werner et al., 2006). Disadvantages of MIKE SHE include its inability to simulate lateral flow in the unsaturated zone, which excludes the representation of possible perched groundwater and any associated interflow component of streamflow.

The ground surface topography and seven geological layers for the model were imported from an existing three-dimensional groundwater flow model (Region of Waterloo Tier Three water budget and risk assessment; Matrix and SSPA, 2014a) and interpolated onto a grid with 50 m by 50 m cells that composed the domain for the present study. This included hydraulic conductivity values that had been calibrated for steady state conditions in the existing model, which used the finite element-based model FEFLOW (DHI-WASY, 2011). Hydraulic head values from the existing model were applied at the boundaries of the Alder Creek watershed and specified as the initial conditions within the domain. The boundary of the domain (Figure 2.1) was designed to coincide with the New Dundee dam at the outflow of Alder Lake, about 8 km upstream from the actual outflow of Alder Creek into the Nith River. This allowed for a well-defined hydraulic head boundary in the surface water portion of the model. The resulting model domain area was 68 $km^2$, and the revised boundaries adjacent to the dam followed local topographic ridges (GRCA, 1998) to the watershed divide.

Precipitation inputs to the model were developed from daily national data, hourly regional data, and 15 min local rainfall data. Rainfall data for the regional and local scenarios were aggregated to the daily time scale and interpolated onto a 250 m by 250 m grid using the inverse distance squared technique. The inverse distance squared technique is the recommended technique for sparse spatial data among those included with the model software (DHI, 2017a) and has the advantages of being simple (Stisen and Tumbo, 2015) and applicable for data that are not normally distributed, unlike Ordinary Kriging (Chen and Liu, 2012). Disadvantages include a strong dependence on gauge locations, which appear as peaks in the interpolated distribution, and the fact that locations far from observation points assume an average rainfall value (Stisen and Tumbo, 2015). Rainfall data for the national scenario were applied at the daily time scale in a spatially uniform manner because there was only one station with a sufficiently complete dataset. All scenarios employed daily snowfall data from the Roseville station. The model used the average daily air temperature at the Roseville station

(Government of Canada, 2019) to calculate the accumulation and melting of snow, based on a modified degree day method (DHI, 2017a). Possible undercatch at the rain gauges of the three networks was not evaluated in the present study.

Drainage of water in the unsaturated zone was represented by the 1D Richards' Equation option (DHI, 2017a). Soil columns for each grid cell were composed of one single soil type corresponding to the surficial soil because the model framework did not allow automated incorporation of the detailed geological layering into the unsaturated zone. Each column was discretized with 0.1 m cells down to 10 m, then 0.2 m cells to 30 m, and then 1 m cells to 55 or 80 m depth. The spatial distribution of nine surficial soil types (Figure 2.2) was based on OGS (2010). Saturated hydraulic conductivity, porosity, and residual moisture content parameters for the van Genuchten curves were based on literature values (D. Graham, pers. comm., 2017; Schaap et al., 1999; Sousa et al., 2013b), and the n, alpha, and Green and Ampt suction at the wetting front parameters were selected in order to vary in a conceptually reasonable manner in comparison with the UNSODA soil types (D. Graham, pers. comm., 2017; Leij et al., 1996; Table 2.2). No macropore flow was simulated. The default pressure head values for field capacity and wilting point (-1 m H2O, and -100 m H2O, respectively), and the default shape factor for unsaturated hydraulic conductivity (0.5) were selected based on DHI (2017b) recommendations.

Daily $ET_o$ inputs to the model were calculated based on the Penman-Monteith method for reference ET, using the UNFAO56 ETo Calculator (Allen et al., 1998; Raes, 2009). The maximum and minimum daily temperatures at the Roseville station were used to calculate $ET_o$ for all three scenarios. The "light to moderate winds" option (2 m/s at a height of 2 m above ground surface) was selected to fill in missing wind speed data in the $ET_o$ calculations.

The upper three geological layers that were imported from the existing model were merged into one computational layer for the saturated zone simulation. This ensured that the water table would be present in the uppermost saturated zone cell, improving the stability of the model. The minimum geological layer thickness was set to match the input layers from the existing model (0.1 m). The finite difference option (DHI 2017a) was used to represent flow in the saturated zone. Public supply wells within the watershed were incorporated into the model and their average 2008 pumping rates (total extraction: 23,000 $m^3/d$; Matrix and SSPA, 2014b) were employed.

Land use and vegetation data (Figure 2.3) were compiled from ROW (2010) and from the Ontario Ministry of Natural Resources (OMNR, 2008). The sparse paved areas were not treated specially

beyond maintaining an assigned background rooting depth, as required by the model, though the urban areas were assigned a leaf area index (LAI) value representing grass. Maximum LAI and root depths were obtained from the literature (Canadell et al., 1996; Scurlock et al., 2001). The LAI values for agricultural areas were assigned a linear increase from zero up to the respective literature value for each cell during the month of May; rooting depths linearly increased during the growing season (May to mid-September). LAI was specified to linearly increase for forest areas during May, be held constant during the growing season, and then linearly decrease during the last two weeks of September. See Appendix E for a summary of LAI values. No irrigation was included in the model.

Overland flow was represented using a semi-distributed approach via the finite difference method (DHI, 2017a). A Manning's n value of 0.3 $m^{-1/3}s$ was applied throughout the domain to represent the majority agricultural land use with a value for light brush, and detention storage was specified based on literature values (Chin, 2006) for five of the land cover types, excluding wetlands and open water.

Stream channels were generated based on the pre-processed (interpolated) model topography to obtain more reasonable agreement between the streamflow and overland flow processes, and cross-sections were generated every 200 m. Manning's n values for the channel were based on GRCA (2017b): 0.035 $m^{-1/3}s$ for the channel thalweg, and 0.05 $m^{-1/3}s$ otherwise.

The model employs independent, automatically adjusted time steps for its overland flow, unsaturated zone, and saturated zone processes (DHI, 2017c; Graham and Butts, 2005). Groundwater recharge is calculated iteratively as an internal flux from the unsaturated zone to the saturated zone during simulations (Graham and Butts, 2005); the accumulated amount for a single cell or the entire watershed was obtained via post-processing. Additional model settings may be found in Appendix E.

### 2.2.5 Comparison of Model Simulations

The scenarios were simulated one year at a time for the years 2014 to 2016. The 2014 simulations followed a three-year model spin-up period that employed spatially uniform daily rainfall and snowfall data from the Roseville station. Scenarios 2 and 3 were started from the same initial conditions as Scenario 1 in all three years. The method of comparing simulations with different rainfall inputs that start from identical initial conditions has been used in other studies (e.g., Schuurmans and Bierkens, 2007; Sapriza-Azuri et al., 2015). The present study differs from Schuurmans and Bierkens (2007) by focusing on groundwater recharge rather than hydraulic heads

and discharge, and from Sapriza-Azuri et al. (2015) by addressing a much smaller watershed (~70 $km^2$ vs. 16,000 $km^2$) using rainfall interpolated from observations within different networks rather than stochastic values derived from the overall network. Results from the numerical model were saved on a weekly basis, so each year was represented by 52 weeks during analysis of the simulations. The results were compared based on maps of the spatial distribution of total recharge, the frequency of cell-by-cell differences in total recharge, the visual match between observed and modelled cumulative streamflow, and differences in overall water budget components.

None of the three simulations were calibrated. This study compared the impacts of the different rainfall input data on the precision of the estimated recharge distributions. Each set of input data would result in a different calibrated model, but modifications to the parameters of the model (e.g., hydraulic conductivity values) would obscure the effects of the input data on recharge rates. Using the same starting point for each 52-week simulation allows the differences in recharge rates to be compared for a model domain structure that is identical in all cases (i.e., the same set of hydraulic conductivity values for the geological layers). The comparison of modelled streamflow for each scenario to observed streamflow provides a sense of the degree of calibration that still would be required to match existing conditions.

Observed and simulated rainfall amounts were compared as follows. The spatial correlation of the numerical model's interpolated rainfall datasets was assessed by selecting 36 uniformly spaced cells from the grid, extracting their precipitation time series, and calculating Spearman correlation coefficients for days with no Roseville snowfall. Days with snowfall were omitted because the observed and simulated daily snowfall amounts differed slightly due to the model's partitioning of rain and snow based on temperature. Rainfall frequency distributions for these 36 cells were also compared with the observed distributions.

## 2.3 Results

The spatial correlation of rainfall was found to vary substantially at both the regional and local scales. Figure 2.4 suggests a continuum in the spatial correlation relationships as distance increases from the local to the regional scale. Daily Spearman correlation coefficients ranged between approximately 0.4

and 0.8 (Figure 2.4).[4] Correlation distances and shape factors for the combined stations of the local and regional networks are shown in Table 2.3 for different time scales. Correlation distances associated with the fitted curves on Figure 2.4 ranged from 88.4 to 113.3 km. Correlation coefficients in the local network were substantially lower than those reported for a dense monitoring network (50 gauges in 135 $km^2$, 6 years of data) in the Brue Watershed, SW England (Villarini et al., 2008). Daily (Pearson) coefficients were ≥ 0.85 in that study, while these varied between roughly 0.6 and 0.9 for the local network in the present study. The spatial correlation analysis indicates that: 1) rainfall may not be sufficiently uniform temporally and spatially in the region around Alder Creek to justify either reliance upon a single rain gauge to represent the watershed or the neglect of rainfall variation within the watershed itself, and 2) the local network is providing additional rainfall information not captured by the regional network.

The inverse distance squared interpolation technique was found to increase the spatial correlation of the interpolated daily precipitation distributions for the regional and local rainfall scenarios. All Spearman coefficients among 36 uniformly spaced sample points for both Scenarios 2 and 3 were between 0.7 and 1.0, a higher range than observed. Appendix F includes examples of the rainfall interpolation for four representative days with a range of rainfall rates. The interpolated daily rainfall frequency distributions at these 36 points for Scenarios 2 and 3 were similar to those observed within the local and regional networks (Appendix F).

A simple, annual water budget for the vadose zone provided a metric for the differences in recharge between scenarios. Figure 2.5 shows that typical instrument and method uncertainty values on these components lead to a substantial accumulated percentage uncertainty on recharge (±27%), prior to accounting for spatial interpolation uncertainties for P or ET. The uncertainty on recharge (δR) could be at least ±100 mm per year (using Scenario 3 data for 2015; Table 2.4), with precipitation measurement uncertainty as the largest contributor. Analysis of error for small groundwater components is often disregarded when conducting calibration and water budget uncertainty estimations (Wiebe et al., 2015).

The water budget results from the three scenarios are listed in Table 2.4, along with other relevant values for the watershed: the observed streamflow totals from the WSC gauge (WSC, 2019), and a regional, steady state model's estimate of average recharge (M.H. Brouwers, pers. comm., 2017;

[4] In contrast, $ET_o$ was highly correlated at the regional scale and had much less influence on recharge estimates than spatially variable rainfall (Appendix A).

Matrix and SSPA, 2014a). The average total precipitation driving the water budget in the numerical model was different in each of the three rainfall scenarios, and the direction of change from year to year sometimes differed. Table 2.4 shows that average total precipitation increased from 2015 to 2016 in both Scenarios 1 and 2, while it decreased for Scenario 3. Precipitation differences between scenarios for a given year were up to about ±20% of the long-term average from Roseville. Differences in average recharge varied up to 141 mm per year, or 44% of average steady state recharge (321 mm; M.H. Brouwers, pers. comm., 2017; Matrix and SSPA, 2014a), although Scenarios 1 and 3 showed nearly equivalent average recharge for 2016. Differences in average recharge with respect to Scenario 3 were greater than the magnitude of the water budget δR for both comparisons in 2014, and for the comparison with Scenario 2 in 2015. Vadose zone AET rates were similar (within ±11 mm of Scenario 3) in 2014 and 2015; AET for Scenarios 1 and 2 differed from Scenario 3 by +106 mm or +44 mm in 2016, respectively, despite having identical $ET_o$ input values. This shows a "cascade" effect of the variation of rainfall on other water budget parameters calculated by the numerical model: Differing rainfall inputs can influence AET rates which in turn influence recharge rates. Figure 2.6 shows the spatial distribution of recharge rates for the three rainfall scenarios. Net groundwater discharge conditions are generally present along the Alder Creek channel and tributaries. The 2014 maps (a, d, and g) show similar recharge distributions for Scenarios 1 and 2, and higher recharge rates everywhere except near the stream channels for Scenario 3. The 2015 maps (b, e, and h) particularly show differences in recharge rates between different scenarios in the sand and gravel soil types. The 2016 maps (c, f, and i) show similar spatial recharge patterns for Scenario 1 and Scenario 3 and lower recharge for Scenario 2, reflecting the lower precipitation in Scenario 2 (Table 2.4). While general spatial differences in recharge rates may be observed in the Figure 2.6 information, Figure 2.7 presents the frequency of cell by cell differences between scenarios. Despite the similar overall average recharge in the local and national rainfall scenarios in 2016 (Table 2.4), the frequency plot (Figure 2.7c) shows that this is the result of a balancing of increases and decreases in recharge across the domain. Comparisons involving the local rainfall scenario produced a broader distribution of cell by cell differences in recharge, while the differences between the regional and national scenarios resulted in a more general shift that affected more cells similarly. That is, a greater number of cells changed by differing amounts of recharge when the local rainfall scenario was compared with either of the other two rainfall scenarios.

Figure 2.8 shows that the cumulative streamflow results for the scenario employing local rainfall were closer to the observed streamflow in all three years simulated. Scenario 3 streamflow was about

3% lower than the observed cumulative flow at the WSC gauge at the end of 2014, about 10% lower at the end of 2015, and about 20% lower at the end of 2016. Cumulative streamflow results from Scenario 1 were between 25 and 31% lower during the three years, whereas Scenario 2 results were between 27 and 43% lower. Because Scenario 3 provided closer agreement with recorded values in all three years, the local rainfall scenario could be interpreted as requiring less extensive calibration than the other two. However, the baseflow indices at the node representing the WSC gauge were between 0.21 and 0.31 for all scenarios. Scenario 3 had the lowest baseflow values. The model predicted a larger overland flow component of streamflow and much lower baseflow than observed. BFI values ranged from 0.60 to 0.64 for 2014 to 2016, based on PART (Barlow et al., 2015) hydrograph separation analysis of data from WSC (2019).

Overall, the poor spatial correlation in rainfall near the study area resulted in differences in recharge rate estimates for 2014 to 2016 that were largest when the local rainfall scenario was compared with either the regional or national network scenarios. Local rainfall interpolations generally led to recharge and streamflow results that were markedly different than those associated with rainfall from the regional or national networks, suggesting a high degree of sensitivity of recharge rates to the scale of rainfall input data.

## 2.4 Discussion

The results suggest that annual recharge distributions estimated through numerical modeling can be quite sensitive to the spatial variability of rainfall, as characterized by the spatial correlation analysis. Longer term monitoring followed by modelling would provide a more complete evaluation of the issue. However, this study suggests that the significant investment required for a longer study would likely produce non-trivial differences in modelled recharge rates for watersheds similar to Alder Creek for some years. Annual recharge rates could differ by a considerable percentage of the average long-term recharge (e.g., 44%). Local rainfall measurements are frequently unavailable at the scale of watersheds used for public water supply, yet models are frequently used for water management at this scale and in similar settings. The implications of the results are discussed below, following discussion of several aspects of the study itself.

The four main factors that could have influenced the recharge results of this study are: 1) the uncertainty associated with measured rainfall amounts, 2) the frequency of applied rainfall intensities

in the model, 3) the increased correlation of rainfall caused by the interpolation method, and 4) the rainfall regimes sampled by the short-term monitoring of the local rainfall network (3 years). First, the accuracy of the readings at the individual rain gauges could influence the interpolated rainfall distribution applied to the model, and therefore recharge. All rainfall measurements are susceptible to human and instrument errors. The local network rain gauges were observed to have instrument errors up to ±10% on average when tested. Though the local network data were assessed for anomalous readings associated with snow accumulation and melt, the installation of cameras at the weather stations would have improved this analysis. The wind screens around the local network's gauges reduce the degree to which wind effects are expected to bias the data, while the regional network likely has a higher level of uncertainty due to infrequent calibration and a typical lack of wind screens. The daily volumetric capture of the Roseville rain gauge was likely to be measured quite accurately, though the wind effects would be different because the gauge type differs from the other two networks. The potential for undercatch, especially for the regional and national rain gauges, was not quantitatively determined in the present study, but the uncertainty assigned to precipitation in the water budget calculations (±10%) was greater than common literature values for undercatch.

Second, Mileham et al. (2008) found that the frequencies of interpolated daily rainfall amounts impacted recharge rate estimates. In contrast to the Mileham et al. (2008) study, interpolated daily frequencies of rainfall amounts for the regional and local rainfall scenarios in the present study were similar to each other and to the frequencies observed at the local rain gauges (Appendix F). The lack of noteworthy frequency differences between the interpolated and measured amounts suggests that variations in the rainfall frequency distribution are not a major factor.

Third, recharge rates could have been influenced by the increased spatial correlation of rainfall caused by the inverse distance squared interpolation technique. Interpolation shifted the entire range of Spearman correlation coefficients upward by about 0.2, from about 0.4 to 0.8 for the observed rainfall to about 0.7 to 1.0 for the simulated. Two related issues are: 1) software packages used for fully-distributed watershed modelling typically restrict the user to the choice of a small number of interpolation methods, and 2) a more advanced method such as kriging may require a larger number of observation points than are frequently available.

Fourth, the short-term nature of data collected by the local rain gauge network may have biased the recharge results by limiting the period of analysis to three years. Thus, the concern is that the limited analysis may not be representative of the actual long-term data. However, the dataset does include

two of the types of years that would be desirable in a more extensive study: the rainfall at Roseville in 2016 was essentially equal to the long-term average rainfall over 1973 to 2018, and the rainfall in 2014 and 2015 was lower than average (by about 12 and 9%, respectively). Though the recharge modelling is missing a comparative, higher than average rainfall amount for Roseville, the results do suggest that drier years (at the national station) may be more interesting in terms of greater variability in rainfall and recharge (Table 2.4). While modelling longer-term impacts of the choice of rain gauge measurement network on recharge variability would be preferable, the purpose of present study was to conduct an initial assessment and suggest whether investments in local rainfall monitoring might improve confidence in groundwater recharge estimates.

The results of this study have implications for the calibration of hydrogeological models, and therefore implications for the delineation of wellhead protection areas (capture zones), the estimation of groundwater contribution areas for stream reaches, the quantification of the groundwater volume available for long-term extraction, and the assessment of contaminant loadings and transport. The results also provide advice on hydrological monitoring investments. While boundary conditions such as spatial variation in rainfall rates could be estimated during the calibration process (e.g., Anderson and Woessner, 1992), it is common in practice to apply whatever precipitation data are available to fully-distributed models and focus calibration efforts on modifying hydraulic conductivity values in order to match observed hydraulic heads and streamflow (Kampf and Burges, 2010). This is a potential concern. In either transient or steady state calibration, a lack of precision in the rainfall distribution will be compensated for by adjustments of the hydraulic conductivity and other soil parameters, potentially mis-representing the actual geology and biasing infiltration and drainage rates. For example, He et al. (2013) commented that calibration compensated for temporal and spatial differences in rainfall inputs. Steady state models would be unable to incorporate repeating rainfall patterns that may exist at small scales without being captured by existing national networks. Such patterns could be caused by trends in wind direction and rainfall distributions associated with evaporation from large lakes (Dingman, 2015) or a heat-island effect near cities (Renard, 2017). The sustainable management of groundwater resources could be impaired by water budget errors related to the precision of rainfall data. For instance, a recharge uncertainty of ±100 mm (Figure 2.5) over the 68 $km^2$ model domain in the present study is roughly equivalent to ±50% of the adjacent City of Kitchener's (population ~ 230,000) annual groundwater extraction (Matrix and SSPA, 2014b).

The magnitude and spatial distribution of recharge is a significant uncertainty for steady state capture zone delineation (Sousa et al., 2013a). This would be further pronounced for transient capture zones (e.g., Graham and Butts, 2005). Precise rainfall measurements could also affect the recharge rates used to delineate areas of groundwater contribution for stream reaches, which could be an important aspect of land use planning and low impact development strategies aimed at maintaining baseflow to streams (e.g., Chow et al., 2016).

Contaminant loadings and transport depend on accurate recharge rates. Recharge distributions also affect the flowpaths of contaminants to receptors such as wells and wetlands and their associated reaction potential (e.g., Loschko et al., 2016). In addition to the potential amount of dilution experienced by contaminants based on recharge rate variation due to the rainfall input data employed, the estimation of dispersion coefficients could also be affected (Yin et al., 2015). Factors such as rainfall amounts, timing, and intensity that could influence recharge rates have been found to influence pesticide leaching rates in the vadose zone (Isensee and Sadeghi, 1995; Sadeghi and Isensee, 1994).

Spatial correlation information for rainfall could be used to enhance groundwater modelling. Correlation statistics could guide the design of rainfall monitoring networks used to collect model input data. Comparison of the spatial correlation coefficients for rainfall in the Brue watershed (Villarini et al., 2008) and the Alder Creek watershed suggests that Alder Creek requires relatively more rainfall observation points to capture the spatial variability over small distances (< 15 km). Correlation could also be used to interpret how well sparse rainfall observation stations represent an area, or discrepancies between sparse rainfall data and water table responses.

In addition to the use of spatial correlation information, radar-based rainfall estimates can be used to interpolate rainfall distributions for groundwater models. He et al. (2013) state that radar estimates can fill in missing spatial rainfall information not captured by a rain gauge network but caution that the mean bias between rainfall interpolated from radar and from the set of all rain gauges may increase when the number of gauges employed is reduced. This suggests that the spatial density of rain gauges could impact recharge rates even when radar-based rainfall estimates are used. More work on how radar-based estimates translate their uncertainty to recharge estimates is needed. One of the few studies relating radar rainfall data and recharge variability, He et al. (2011), used short-term (1 year) simulations of radar rainfall estimates within MIKE SHE to estimate the uncertainty of recharge in a watershed in Denmark. These authors used a simple, two-layer water balance method

for partitioning ET and recharge in the unsaturated zone and found that the coefficient of variation (standard deviation / mean) of recharge was similar to that of precipitation. Longer-term studies and more complex representations of the unsaturated and saturated zones could clarify the advantages and limitations of using radar products to represent spatial variations in rainfall and to estimate recharge.

If it is the case that considerable uncertainty exists for modelled recharge estimates based on rain gauge network scale, how might this uncertainty be reduced in a cost-effective manner? Increased data collection from the watershed of interest can be costly. Strategies might include drilling more wells or installing more weather stations. A comparison of the results discussed above with Appendix A suggests that rainfall monitoring scale is of greater value for recharge estimate variability than monitoring parameters related to Penman-Monteith $ET_o$ estimates. The related AET component's uncertainty was not addressed in the present study but is worthy of further evaluation in future studies. Rainfall/precipitation data provide information on the input of water to the model water budget. Precipitation station components could cost ~$10,000 or less per station and conceptually represent a certain area of the watershed based on spatial precipitation correlation and gauge density. On the other hand, drilling wells provides different information. Soil cores enhance interpretation of stratigraphic layers but may represent a smaller lateral area because of subsurface heterogeneity. Except for the water table fluctuation method (Healy and Cook, 2002), direct recharge estimates with wells are not possible. Modelling must generally be conducted with both precipitation data and well data to estimate recharge. A single well is also likely to cost several times more than a precipitation station, without accounting for the ongoing maintenance and data collection/analysis costs necessary in both cases. If the goal is to reduce uncertainty in modelled recharge estimates, installing rain gauges within the watershed of interest may be the most cost-effective method.

Watershed studies at shorter time-scales (transient as opposed to steady state) in certain regions are likely to benefit from more spatially precise rainfall data. The results of the present study suggest that the scale of available data could bias hydraulic conductivity values as calibration compensates for a lack of precise rainfall observations, thus mis-representing recharge and discharge in the near-surface environment. Increasing the density of rain gauges may also be the most cost-effective way to reduce uncertainty associated with recharge estimates, when compared with the cost of collection of subsurface information at the point scale, such as drilling more wells.

## 2.5 Conclusions

The results of this study indicate that rain gauge network scale can have a significant impact on recharge rate estimates at the watershed scale during short (annual) time scales. Daily Spearman spatial correlation coefficients between gauges of the local and regional networks were typically < 0.8. These correlations show that rainfall is not uniform in the vicinity of the Alder Creek watershed. Simulation of the three rainfall networks resulted in differences in overall average recharge of up to 141 mm, or 44% of previously estimated steady state recharge (M.H. Brouwers, pers. comm., 2017; Matrix and SSPA, 2014a). Differences in recharge rates between the scenario employing local rainfall and each of the other two rainfall scenarios were more variable than comparisons between the national and regional scenarios, and cumulative streamflow for the local rainfall scenario visually appeared to provide a closer match with observed streamflow. The overall conclusion is that in a setting such as the one described by the observed ranges of local and regional spatial rainfall correlation coefficients, fully-distributed, transient models may frequently be compensating for actual rainfall inputs via adjustment of hydraulic conductivity values during calibration. This is a concern for land use planning with the goal of maintaining baseflow to streams, for long-term water resources projections, for representing transient hydrological events, and for contaminant transport models that rely on accurate recharge rate estimates.

Future work should address the incorporation of radar rainfall data to better characterize the extent to which spatial precipitation variability leads to variability in recharge estimates, and also an improved assessment of the contribution of snowfall distribution and snow melt to recharge estimate variability at the watershed scale. The spatial variability of snowpack thickness could be especially important during large melt events.

## 2.6 Tables

Table 2.1. Annual rainfall[*] (mm) recorded at stations of the local, regional, and national networks.

| | Rainfall | | |
|---|---|---|---|
| Weather Station | 2014 | 2015 | 2016 |
| WS2 | 987 | 839 | 371 |
| WS3 | 794 | 784 | 797 |
| WS4 | 892 | 853 | 665 |
| WS5 | N/A[†] | 725 | 746 |
| WS6[‡] | 800 | 927 | 414 |
| WS7 | 560 | 673 | 789 |
| Wellesley[§] | 849 | 690 | 888 |
| Baden[§] | 731 | 626 | 537 |
| Laurel Creek[§] | 701 | 612 | 605 |
| Cambridge[§] | 677 | 464 | 747 |
| Paris[§] | 597 | 759 | 892 |
| Burford[§] | 432 | 641 | 329 |
| Roseville[**] (755) | 665 | 689 | 746 |

[*] Snowfall data are not included. Roseville snowfall amounts were 183 mm, 111 mm, and 153 mm for 2014, 2015, and 2016, respectively (Government of Canada, 2019).

[†] N/A – not available. WS5 data collection started in June 2014. Jun to Dec 2014: 600 mm.

[‡] The rainfall time series at WS6 is a composite from two gauges at this station.

[§] Grand River Conservation Authority weather station (GRCA, 2017a).

[**] Environment Canada Weather station (Government of Canada, 2019). The amount in brackets is the average rainfall from 1973 to 2018.

Table 2.2. Unsaturated soil properties (D. Graham, pers. comm., 2017; Leij et al., 1996; Schaap et al., 1999; Sousa et al., 2013b).

| Soil Unit | $K_{sat}$ [*] (m/s) | $\theta_{sat}$ [†] (-) | $\theta_{res}$ [‡] (-) | n [§] (-) | α [¶] ($cm^{-1}$) |
|---|---|---|---|---|---|
| Outwash gravel | $5x10^{-4}$ | 0.28 | 0.04 | 4.0 | 0.040 |
| Ice-contact gravel | $3x10^{-4}$ | 0.33 | 0.04 | 3.3 | 0.040 |
| Outwash sand | $6.5x10^{-5}$ | 0.43 | 0.05 | 3.2 | 0.035 |
| Ice-contact sand | $7x10^{-5}$ | 0.35 | 0.05 | 3.3 | 0.035 |
| Bog/swamp deposits | $1x10^{-5}$ | 0.60 | 0.20 | 3.0 | 0.030 |
| Stream alluvium | $1x10^{-6}$ | 0.41 | 0.07 | 1.5 | 0.010 |
| Port Stanley Till | $5x10^{-6}$ | 0.40 | 0.06 | 1.5 | 0.020 |
| Maryhill Till | $1x10^{-6}$ | 0.45 | 0.06 | 1.2 | 0.021 |
| Lacustrine deposits | $1x10^{-6}$ | 0.45 | 0.09 | 1.3 | 0.020 |

[*] $K_{sat}$ = saturated hydraulic conductivity

[†] $\theta_{sat}$ = saturated moisture content

[‡] $\theta_{res}$ = residual moisture content

[§] n = van Genuchten fitting parameter

[¶] α = inverse air entry pressure for van Genuchten curve

Table 2.3. Fitting parameters for the spatial correlation best-fit curves.

| Network | Method | Time scale | Nugget ($c_1$; -) | Correlation Distance ($c_2$; km) | Shape Factor ($c_3$; -) |
|---|---|---|---|---|---|
| Local with Regional | Spearman | 1 hr | 1.0 | 88.4 | 0.21 |
| | | 3 hr | 1.0 | 113.3 | 0.24 |
| | | 24 hr | 1.0 | 91.2 | 0.39 |

Table 2.4. Numerical model water budget results and comparisons (results in mm per yr).

| Year | Component | Scenario | | |
|---|---|---|---|---|
| | | 1 | 2 | 3 |
| 2014 | Precipitation | 849 | 895 | 1048 |
| | Evapotranspiration* | 392 | 376 | 381 |
| | Overland Runoff† | 91 | 96 | 124 |
| | Storage change‡ | -53 | -33 | -20 |
| | Recharge§ | 421 | 456 | 562 |
| | Streamflow at node representing WSC gauge** | 107 | 112 | 148 |
| | Total Streamflow†† | 121 | 127 | 157 |
| 2015 | Precipitation | 789 | 714 | 897 |
| | Evapotranspiration* | 425 | 421 | 428 |
| | Overland Runoff† | 68 | 61 | 85 |
| | Storage change‡ | 7 | -9 | 20 |
| | Recharge§ | 288 | 241 | 364 |
| | Streamflow at node representing WSC gauge** | 84 | 75 | 101 |
| | Total Streamflow†† | 97 | 88 | 116 |
| 2016 | Precipitation | 879 | 756 | 771 |
| | Evapotranspiration* | 444 | 382 | 338 |
| | Overland Runoff† | 78 | 64 | 93 |
| | Storage change‡ | 13 | 25 | -10 |
| | Recharge§ | 344 | 285 | 349 |
| | Streamflow at node representing WSC gauge** | 96 | 79 | 112 |
| | Total Streamflow†† | 107 | 91 | 122 |
| Recharge Estimate from Previous Study (Tier Three‡‡) | | | 321 | |
| Streamflow estimates from WSC gauge§§ | 2014 | | 153 | |
| | 2015 | | 112 | |
| | 2016 | | 135 | |

* AET excluding AET from the saturated zone. Total AET values were: 493, 476, and 496 mm for Scenarios 1 to 3 for 2014; 521, 505, and 533 mm, respectively, for 2015; and 540, 466, and 439 mm, respectively, for 2016.

† Overland flow into stream.

‡ Includes storage change (unsaturated, snow, and overland flow zones), and boundary flows out of the unsaturated zone (~5 mm/yr/scenario). Boundary flows into the unsaturated zone: 0 mm.

§ Recharge can be calculated via Eqn. (2.2).[5]

** Area above gauge = 47.4 $km^2$ (WSC, 2019).

†† Area of model domain = 68.2 $km^2$ (GRCA, 1998).

‡‡ Annual results from calibrated, steady state, saturated zone FEFLOW simulation for Regional Municipality of Waterloo Tier Three Assessment (M.H. Brouwers, pers. comm., 2017; Matrix and SSPA, 2014a).

§§ WSC (2019). The sums here are based on the 52-week periods of the simulations. There were twelve days with missing data at the start of 2016.

[5] Eqn. (2.3) was erroneously referenced in Wiebe and Rudolph (2020); the correct reference is Eqn. (2.2).

## 2.7 Figures

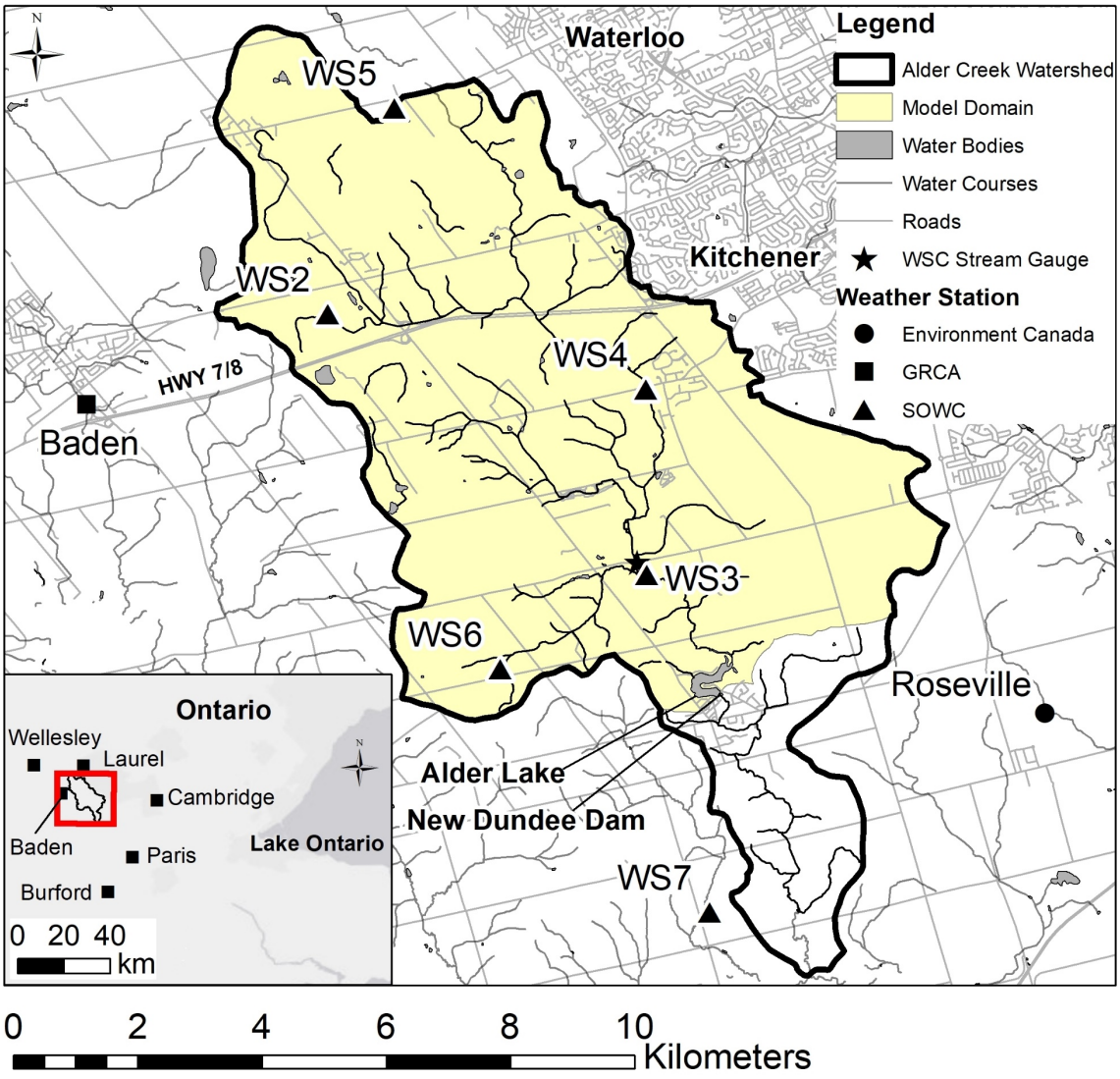


Figure 2.1: The Alder Creek watershed, with Environment Canada, GRCA, and SOWC weather station locations (DMTI, 2011; Esri et al., 2019a; Government of Canada, 2019; GRCA, 1998, 2017a; WSC, 2019). The Water Survey of Canada (WSC) stream gauging station location is also shown near WS3.

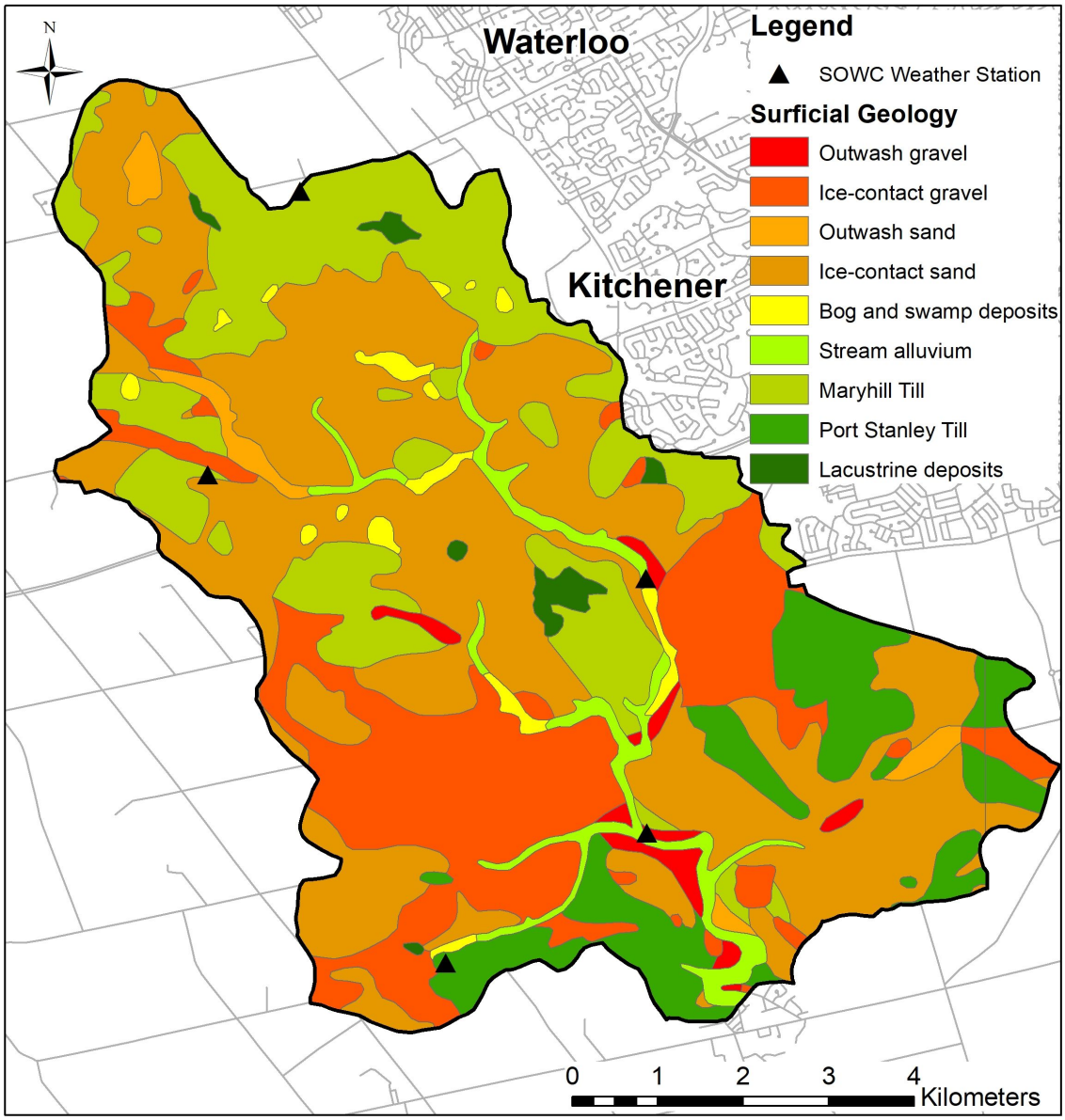


Figure 2.2: Surficial soils in the model domain (DMTI, 2011; GRCA, 1998; OGS, 2010).

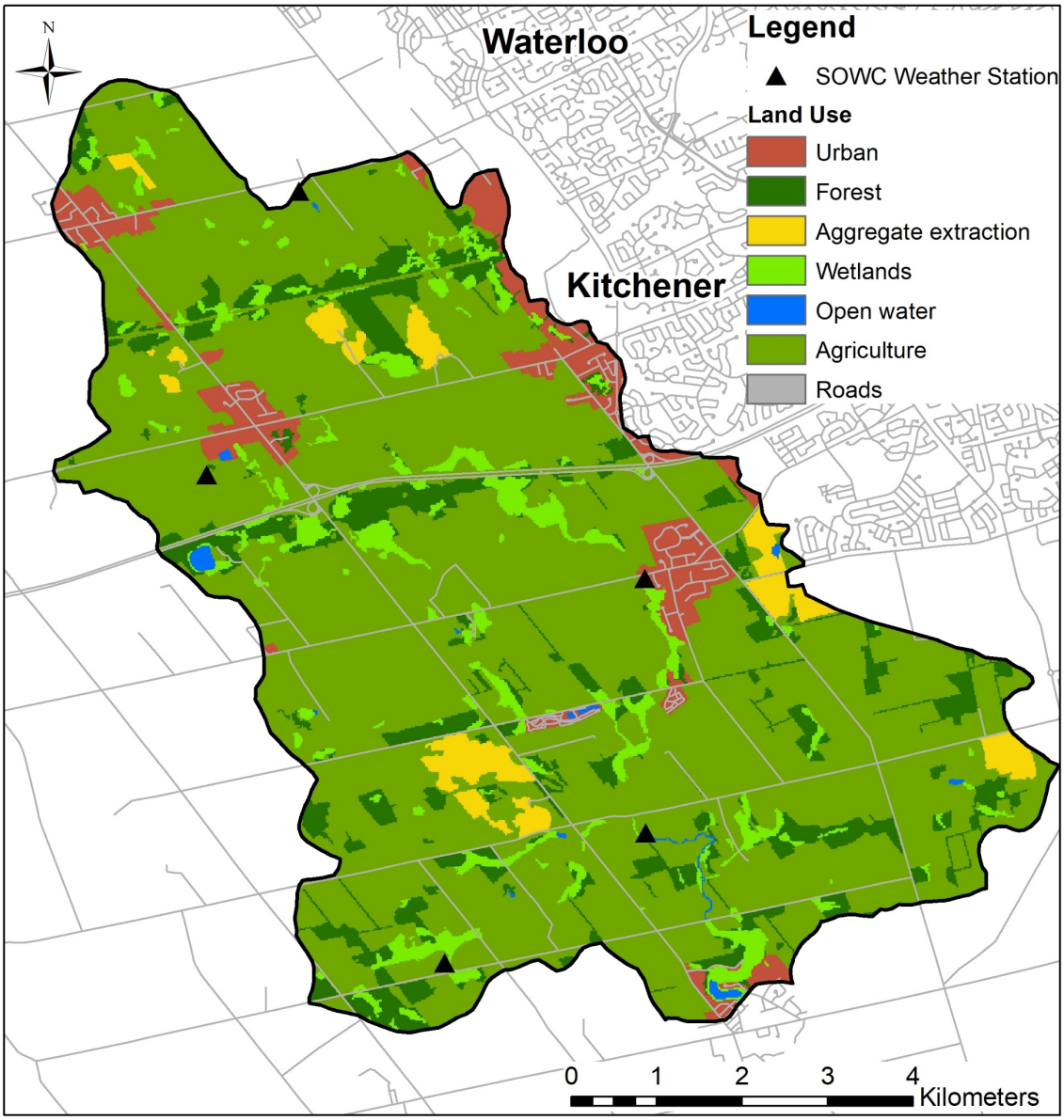


Figure 2.3: Land use in the model domain (DMTI, 2011; GRCA, 1998; OMNR, 2008; ROW, 2010). The "Agriculture" category includes minor areas of recreation and open land.

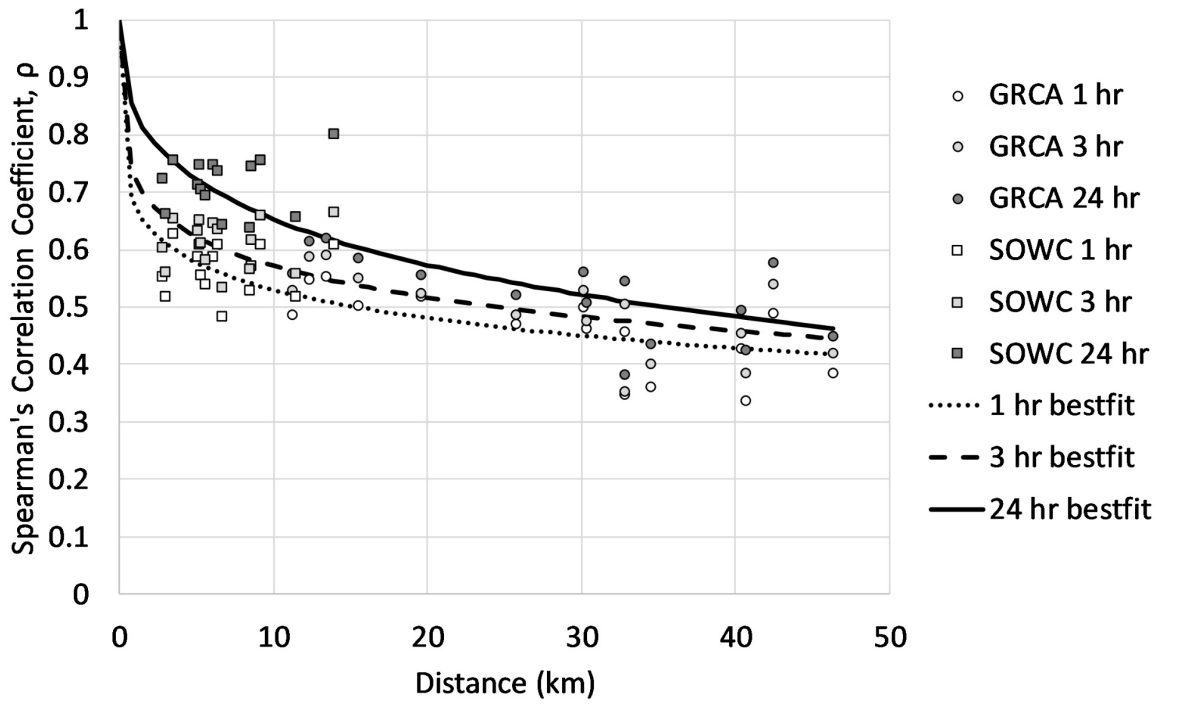


Figure 2.4: Spatial correlation between rainfall measurements for the combined stations of the local and regional networks (GRCA, 2017a; Wiebe et al., 2019).

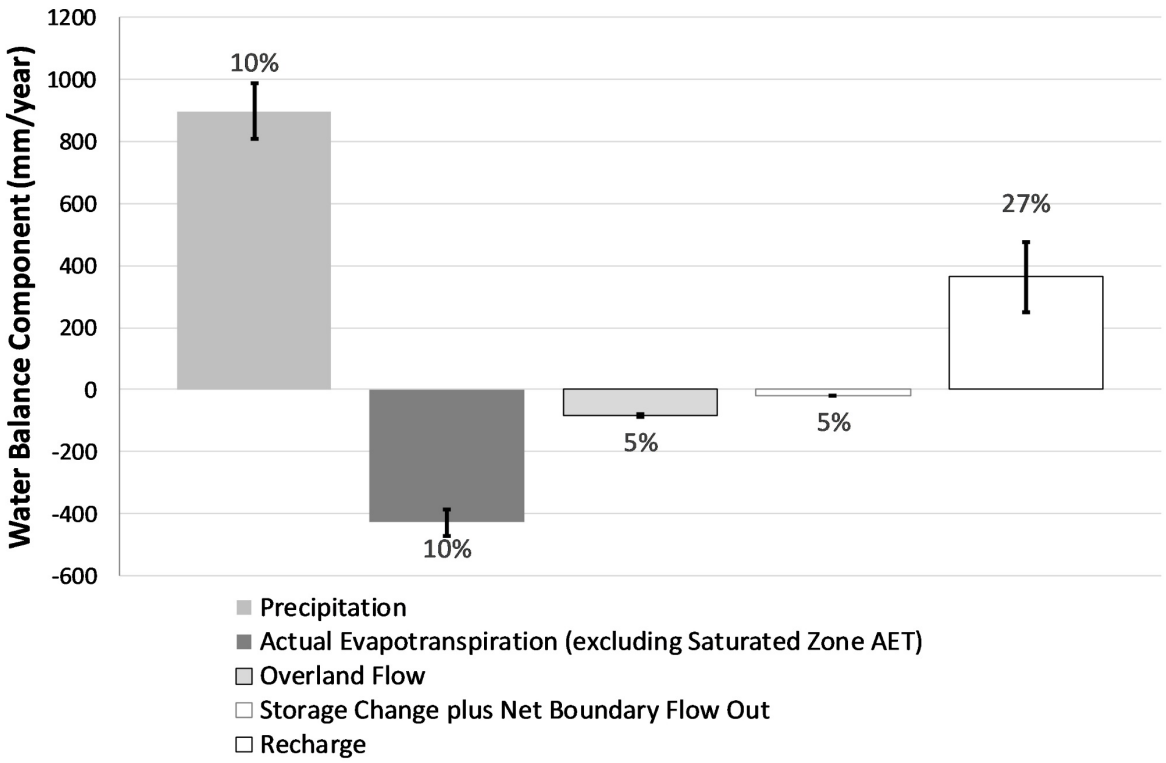


Figure 2.5: Instrument and method uncertainty for the Scenario 3 (2015) near-surface water budget.

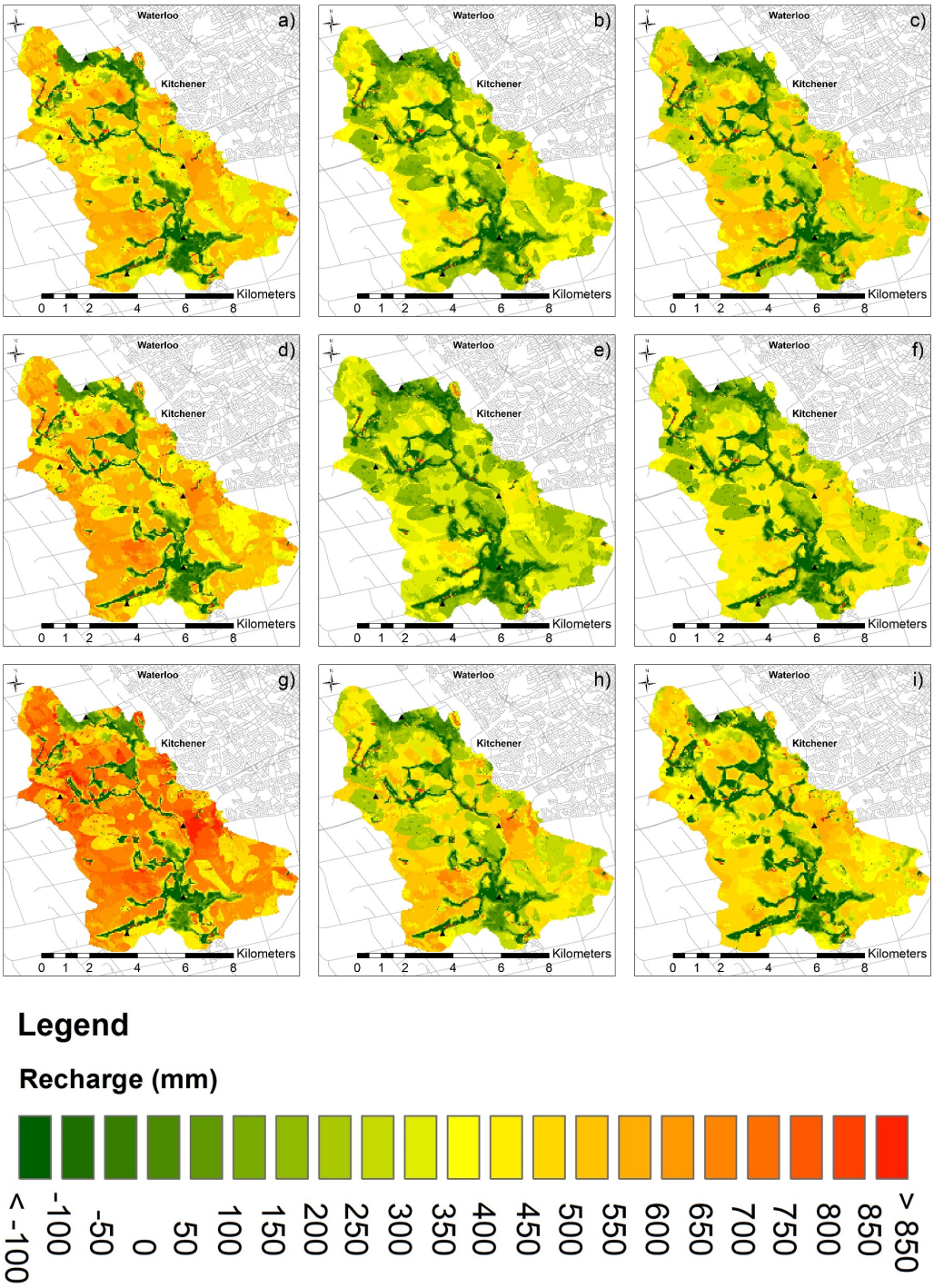


Figure 2.6: Recharge estimates for the three rainfall scenarios (GRCA, 1998; DMTI, 2011). Maps show results as follows: Scenario 1 (national), (a) 2014, (b) 2015, and (c) 2016; Scenario 2 (regional), (d) 2014, (e) 2015, and (f) 2016; and Scenario 3 (local), (g) 2014, (h) 2015, and (i) 2016. The local weather stations are shown as black triangles.

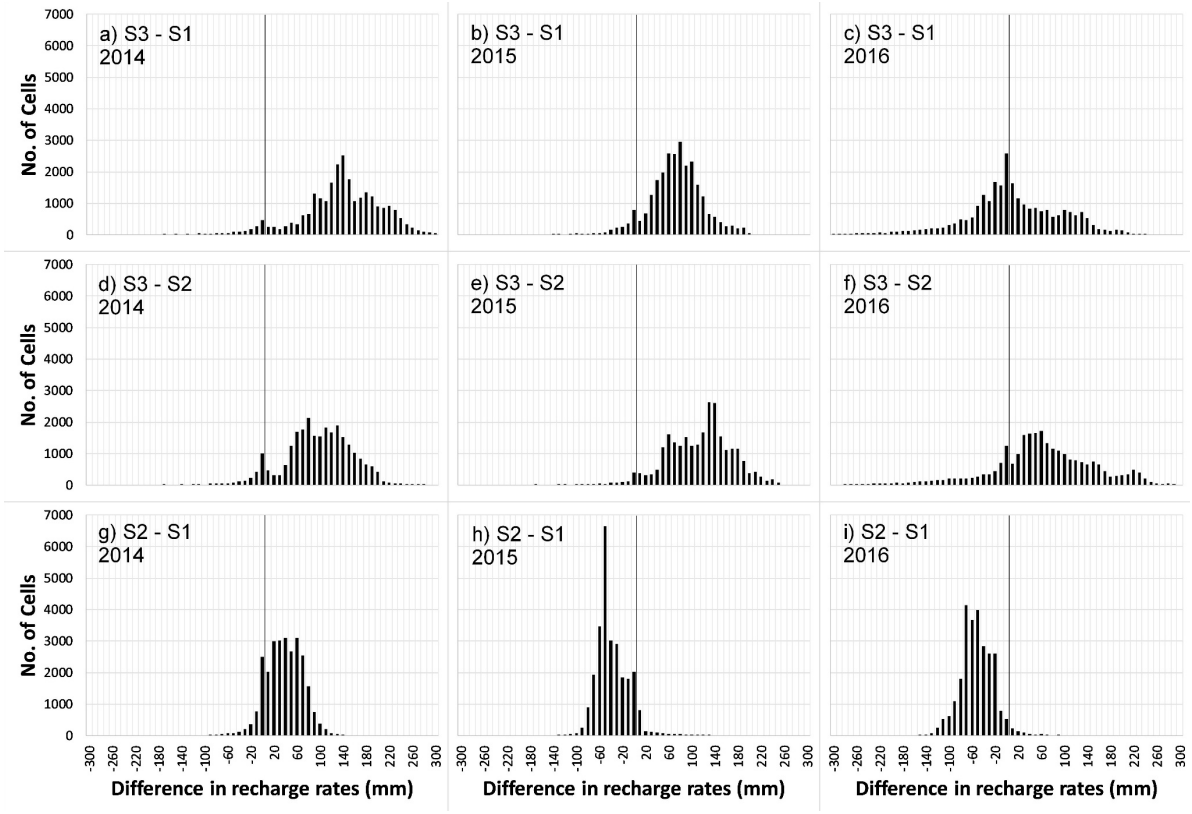


Figure 2.7: Frequency of differences in recharge rates between the three rainfall scenarios. “S3 - S1” implies a cell-by-cell subtraction of Scenario 1 from Scenario 3, etc. The emphasized grey vertical line in each subplot indicates a difference of 0 mm.

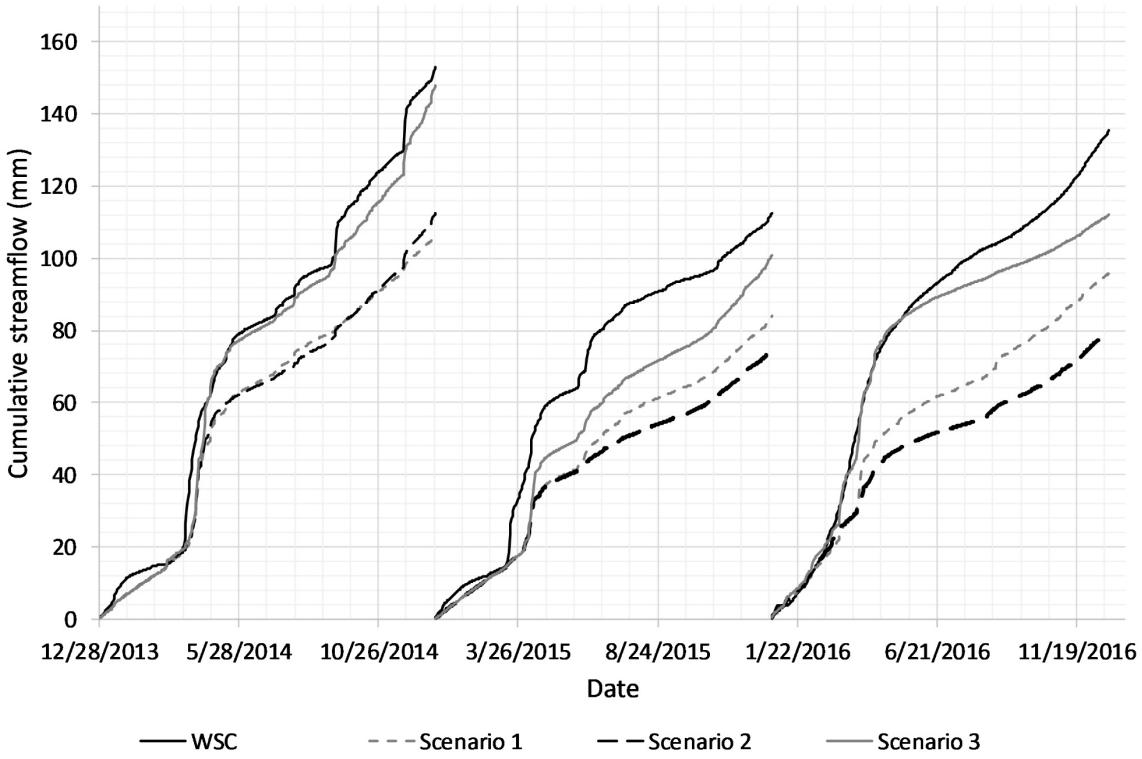


Figure 2.8: Comparison of cumulative streamflow results for the three simulations with recorded flows at the Water Survey of Canada (WSC) gauge (WSC, 2019). The WSC gauge was missing 12 days of data at the start of 2016.

# Chapter 3

# Assessing public supply well vulnerability to depression focused recharge during hydrological events

## 3.1 Introduction and Background

Hydrological events such as heavy rainfall, rapid snowmelt, and rain-on-snow events may lead to an increased risk of contamination for wells (Hrudey et al., 2003). Such events are dynamic, and the magnitudes of overland flow and recharge within a watershed vary based on factors such as: topography, permeability of soils, vegetation, and land use (Blackport et al., 2009; Freeze and Cherry, 1979; Healy, 2010); the presence or absence of soil frost (Greenwood and Buttle, 2018); the magnitude and timing of rainfall (Freeze and Cherry, 1979) and snowmelt events (Blackport et al., 2009; Wu and Xu, 2005); the aerial extent of impermeable surfaces (Matrix and SSPA, 2014b); and the degree of soil saturation (e.g., Freeze and Cherry, 1979). Recharge rates in glacial overburden sediments are mediated, in part, by the distribution and thicknesses of soil units with varying degrees of permeability. Glacial moraines are commonly relied upon as drinking water sources, and as a result of their characteristic hummocky topography, depression focused recharge (DFR) tends to be a significant process (Blackport et al., 2009; Greenwood and Buttle, 2018). DFR and localized recharge processes have the potential to channel overland flow and associated contaminants into the subsurface during large-magnitude hydrological events. If these depressions are situated in the vicinity of a public supply well, the travel time from ground surface to the well may temporarily decrease, thus increasing the threat to the well (Sousa et al., 2013b).

Regulations regarding the vulnerability of wells to surface-originating pathogens (e.g., Clean Water Act; Province of Ontario, 2006) were drafted in multiple Canadian provinces following the Walkerton tragedy of 2000. Heavy rainfall near Walkerton, ON, in early May 2000, led to the formation of temporary surface water features near several public water supply wells. The resulting focused groundwater recharge phenomena carried pathogenic bacteria from agricultural fields through thin overburden soils and highly permeable fractured bedrock to the supply wells. As a result of insufficient water treatment infrastructure, more than two thousand cases of illness and seven deaths resulted (Hrudey et al., 2003; O'Connor, 2002). The response to this tragedy revolutionized the management of public groundwater supplies in Canada, leading to the adoption of so-called GUDI (Groundwater Under the Direct Influence of surface water) risk analysis and improved wellhead and

source water protection strategies. However, although the Walkerton tragedy was associated with a heavy rainfall event, the Ontario regulations for existing wells (Province of Ontario, 2018) mainly discuss such events in the context of permanent surface water features that may contribute source water to public supply wells. The guidelines for new water well permits briefly mention well vulnerability in terms of storm events. Pathogenic microbes are typically found in greater numbers in surface water during these types of events, when overland runoff may transport pathogens from manure fertilizer, depositional manure (from livestock pastures), or failed private septic systems into streams (Bradshaw et al., 2016). A well can be certified as having effective in-situ filtration based on a hydrogeologist's report regarding microbial particle counts during events and seasonal changes; this reporting must address potential threats to water supply infrastructure due to large-magnitude events (OMECP, 2019). While the potential threat of permanent surface water bodies (lakes and streams) to well water quality is acknowledged in the Ontario regulations, the degree to which seasonal hydrological events may increase risks is less well understood. Large-magnitude events may increase recharge rates by increasing soil saturation and may modify the spatial distribution of recharge through temporary flow and ponding at the ground surface, potentially influencing the transient capture zone of a well.

It is challenging to characterize event-based risks. Such risks: i) may rarely or never be observed by water managers and field technicians; ii) may evade or incapacitate typical monitoring strategies; and iii) may not easily be incorporated into existing regional hydrogeological models. Large-magnitude hydrological events that occur with a frequency of once or twice per year are less likely to be observed than general conditions, especially if there is a bias toward fair-weather field work. Typical observation wells have screens installed at depth and do not routinely focus on capturing "event" water arriving at the water table. In addition, conventional groundwater flow models designed to estimate well capture zones rely on steady state simulations and are unable to address transient event risks.

Research in glacial moraine environments in southwestern Ontario has identified hydrological event responses that may be of concern to public supply well water quality. These phenomena are not specifically considered within current source water protection risk assessments for existing wells. Temporary surface water features that form during snowmelt periods and persist for several days have been observed on agricultural fields within the wellhead protection areas of public supply wells near Woodstock, ON (Brook, 2012; Christie et al., 2009; Pasha, 2018), and Mannheim, ON (Menkveld,

2019; Menkveld et al., 2015). Christie et al. (2009) found that indicator species for microbial pathogens were present in both the surface water and in shallow groundwater wells during these events. Menkveld (2019) monitored two snowmelt events involving overland runoff and temporary ponding in the base of a topographic depression within 50 m of a public supply well in Mannheim, ON. There was some evidence of pathogen indicator species in the topographic depression and the nearby creek, though less rigorous procedures than those recommended by Myers et al. (2014) were used. The Mannheim site is the subject of the present study and will be discussed further below. Runoff collecting in the depression in this case was influenced by surrounding agricultural land management practices and overflow from a stormwater management pond collecting water from the impermeable surfaces of a greenhouse roof.

Recharge pathways to wells are important for estimating travel times, understanding biogeochemical reactions, and quantifying potential threats to drinking water supplies. Three types of recharge pathways from the surface to the water table are (de Vries and Simmers, 2002; Lerner et al., 1990): 1) Direct recharge, a diffuse distribution occurring over broad areas from precipitation that infiltrates vertically; 2) depression focused recharge (DFR) or localized recharge that occurs following overland flow and infiltration, and 3) indirect recharge, which occurs beneath water courses such as losing streams. Focused recharge has been found to be a significant process in the Prairie Pothole Region of western Canada, where researchers have estimated that about 40% of the recharge occurs through about 5% of the land surface area, within depressions in the landscape (Zebarth et al., 1989). The numerous topographic depressions collect overland runoff from larger areas and facilitate net infiltration (infiltration > evapotranspiration); these cumulatively constitute a regionally significant source of recharge (Hayashi et al., 2016). Playas have been identified as an important source of focused recharge in the High Plains Aquifer, USA (Crosbie et al., 2013; Gurdak and Roe, 2010; Scanlon and Goldsmith, 1997; Wood and Sanford, 1995). DFR has also been studied on the Oak Ridges Moraine (ORM), north of Toronto, ON. Greenwood and Buttle (2018) studied topographic depressions in agricultural and forested settings on the ORM and found that the development of soil frost caused overland flow on agricultural fields, leading to ponding; recharge rates in depressions on two fields were factors of 1.5 and 11.3 times larger than the rate at the crest of the respective topographic basin. Large topographic depressions have been identified and modelled as suspected “hot spots” for recharge on the Waterloo Moraine in Ontario (CH2MHILL and SSPA, 2003), though the overall impact of smaller depressions on water quantity and quality in this setting remains unknown. While depression size may not necessarily influence the consistency of infiltration

activity (Berthold et al., 2004), underlying soil hydraulic conductivity and the amount of overland flow into a depression are important factors influencing the amount of DFR (Blackport et al., 2009; Delin et al., 2000; Tosomeen, 1991). Further detailed studies are needed to assess indirect and focused recharge in the field with respect to potential implications for water quality in drinking water wells.

Quantifying threats to drinking water wells is often done by simulating contaminant breakthrough curves. Previous studies have used such curves to assess specific well vulnerability (Frind et al., 2006), where accounting is made for characteristics of the porous medium and the contaminant. Frind et al. (2006) suggested that solute transport simulations could be used to estimate the peak concentration, peak arrival time, and total exposure time experienced by a public supply well via contaminant breakthrough curves. Knappett et al. (2014) modelled *E. coli* attachment and transport from a latrine effluent pond to observation wells within 10 m of the pond under saturated conditions, generating breakthrough curves with their 2D model. Eberts et al. (2012) modelled breakthrough curves for conservative tracer migration to public supply wells under pumping conditions using particle tracking and lumped-parameter models, representing the migration of non-point source contaminants applied at the land surface for more than two decades.

The present study seeks to assess potential event-specific microbial threats to a public supply well based on the projected breakthrough curve of a conservative tracer originating in a nearby topographic depression. First, soil stratigraphy and hydrological conditions were characterized and evaluated at a site where DFR was suspected to occur. Distinct hydrological events were catalogued and compared over 3.5 years. Next, numerical models were constructed to represent the vadose zone and the flow field from the DFR location to the well. Relative concentration breakthrough curves for a simulated contaminant were calculated for two large-magnitude hydrological events that were monitored in the field, and also for background conditions with no ponding in the topographic depression. It was hypothesized that event conditions (ponding in the topographic depression) would lead to travel times (time to "detection") that were sufficiently short to be of concern for pathogenic contamination (i.e., < 50 days; CH2MHILL, 2002; Enzenhoefer et al., 2012; Frind et al., 2002; Nalarajan et al., 2019; OMECP, 2019). Breakthrough curves for a second hypothetical solute released in a creek near the well were also simulated for comparison.

## 3.2 Methods

### 3.2.1 Field Site

The field site for the present study (Figure 3.1; "Mannheim" site) is located within the Alder Creek watershed on the Waterloo Moraine. This watershed is immediately adjacent to the twin cities of Kitchener and Waterloo (combined population ~400,000), and up to seven municipal well fields capture water recharged within its topographic boundaries (Brouwers, 2007). The site contains the base of a topographic depression (~160 $m^2$) in a field adjacent to Alder Creek (Menkveld, 2019; Menkveld et al., 2015); its catchment area is likely ~10,000 $m^2$ (based on aerial imagery; First Base Solutions, 2006). A cross-section through the site consists of the creek, an 8 m riparian zone, the base of the depression, and a gradual upland slope (Figures 3.2 and 3.3). A stormwater management pond for a greenhouse operation, located 65 m upslope of the depression base, occasionally overflows during large rainfall events (e.g., > 10 mm/day) and causes overland flow that reaches the base of the depression. The ditch beside the road north of the site also channels overland flow toward the depression base. Across the creek and within 50 m of the depression base is a public supply well that has recently been inactive for several years due to rehabilitation challenges related to iron and manganese precipitates (Stantec, 2013). This well is screened in overburden sediments.

Ponding events occur frequently in response to heavy rainfall and snowmelt. The silty topsoil in the field is conducive to allowing overland flow to occur during large-magnitude rainfall events. Dynamics of water flow and infiltration, observed in the absence of pumping at the public supply well, are governed by factors such as: 1) the magnitudes of snowmelt volume and rainfall rate, 2) whether the soil is frozen or not, and 3) the stage of the creek. The amount of transmission losses during overland flow across the field is unknown.

The reach of Alder Creek that flows through the site has been observed to be hydraulically disconnected from, i.e., perched with unsaturated soil above, the water table during at least certain times of the year (CH2MHILL, 2002; Wiebe et al., 2019), though the vadose zone region under the stream and above the average water table position may become fully saturated during significant infiltration events. The base of the stream channel consists of low permeability materials. Regional groundwater flow in the vicinity of the field site is generally toward the southeast (CH2MHILL and SSPA, 2003).

Surficial geology mapping (Figure 3.2) suggests a narrow floodplain of stream alluvium between ice-contact sand in the west and outwash gravel to the east of the creek, while the underlying, generally unconfined sand and gravel aquifer in which the public supply well is screened is quite permeable (hydraulic conductivity ~ 1 x $10^{-3}$ m/s; CH2MHILL and SSPA, 2003). Figure 3.3 shows the shallow soils in cross-section A-A' through the site. A compact, stony unit composed of gravelly sand was commonly encountered during drilling at approximately 1 m depth at locations on the west side of the creek. This gravel layer was typically observed to be underlain by a silty sand layer that contained the water table at a depth of 2 to 4 m below ground surface, and then by a medium to coarse sand layer, in shallow soil cores (Menkveld, 2019). Coarse sands and gravels were observed in deeper boreholes on both sides of the creek (Hillier, 2014; OMECP, 2018). Hillier (2014) reported a silt unit between 0.5 and 2 m thick, encountered around 6 m below ground surface. This unit is shown with dotted lines in Figure 3.3.

DFR within closed topographic basins is known to occur naturally in this type of glacial moraine setting (Blackport et al., 2009; CH2MHILL and SSPA, 2003; Greenwood and Buttle, 2018; Stantec, 2012). The site is typical of the setting of many public supply wells in southern Ontario and is an excellent example to explore the issue of the potential impact of large-magnitude events on well water quality through numerical simulations based on field characterization. Three general types of recharge are present at the site: diffuse recharge across the field, DFR beneath the base of the topographic depression, and indirect recharge beneath the stream and possibly beneath overland flow channels.

### 3.2.2 Field Data and Analysis

Field data collection occurred from November 2014 to April 2018 at the monitors shown on Figures 3.1 and 3.4. Soil cores were collected with a direct-push Geoprobe drilling rig to characterize shallow stratigraphy. Cores were logged, and the sediment types were classified and then assigned to one of the four major units shown on Figure 3.3 (Appendix G; Menkveld, 2019). Data were collected to monitor event responses in terms of overland ponding depths, soil moisture, and groundwater and surface water levels. Infiltration and water table responses were monitored at three locations: 1) beneath the base of the topographic depression, 2) beneath the creek, and 3) beneath the middle of the field, where background conditions were hypothesized to exist. Eighteen observation wells (Wiebe et al., 2019; Menkveld, 2019) were installed on the west side of the creek, augmenting existing wells (Hillier, 2014). Water levels in several of the wells located outside of the base of the topographic

depression were assessed for background water level dynamics. A neutron probe (CPN, 2013) was calibrated using gravimetric water content analyses on soil cores in order to periodically monitor soil moisture at initially three (Menkveld, 2019) and later five locations along the transect (Appendix H). Three drive-point piezometers were installed beneath the stream (Menkveld, 2019) in order to measure water levels when saturated conditions were present and to calculate the vertical flow direction. Water levels along transect B-B' (Figure 3.4) from the creek to CPP6 were obtained using pressure transducers, corrected for barometric pressure as necessary, and adjusted to match manual measurements. Extensive data analysis was performed on hydrological events that resulted in > 9 cm of water level rise at CPP3 under the base of the topographic depression. A list of the magnitudes of water level rise, and the time intervals between background and peak water levels was compiled (Appendix I). The combined datasets were used to judge the likelihood of whether the creek or the base of the topographic depression was the main source of recharge during events. Two contrasting events (Nov 2014 and Jul 2017) were selected to be represented via model simulations.

Precipitation data were collected and estimated as follows. A weather station (WS4; Figure 3.1) installed at the site measured rainfall with a tipping bucket rain gauge. Rainfall data (Wiebe et al., 2019) were checked for anomalous values corresponding to days of snowmelt. Snowmelt was estimated based on reductions in the thickness of measured snowpack (Government of Canada, 2019) at the Roseville Environment Canada weather station 8 km from the site. A time series for estimated effective precipitation (rainfall + snowmelt – actual evapotranspiration; Appendix J) was developed from: 1) daily rainfall values (Wiebe et al., 2019) from the weather station on site, 2) daily estimates of snowmelt based on the nearby Roseville station (Government of Canada, 2019), and 3) an estimate of daily actual evapotranspiration.

### 3.2.3 Numerical Modelling

The investigation outlined below focused on assessing event-related microbial threats to a public supply well via solute transport modelling using a quasi-3D, wedge-shaped domain. Parameters for this simulation experiment were derived during two calibration steps. The first step was designed to derive estimated values of the horizontal ($K_x = K_y$) and vertical ($K_z$) hydraulic conductivity for the vadose zone and shallow soil layers through the calibration of a numerical model to a highly monitored infiltration event. Matching of transient hydraulic head data collected from several of the monitoring wells beneath the depression was conducted during this calibration. A separate 1D

infiltration model was used to inform the streambed hydraulic conductivity for the first step. Calibration was performed on an event with a non-negligible (10s of cm) water table rise beneath the base of the topographic depression but very little response (< 10 cm rise) in the creek (26-30 Mar 2017). This event was chosen to minimize the suspected impacts of superposition (Menkveld, 2019) of the influences of ponding in the depression and the losing reach of the creek on water levels beneath the base of the depression. Hydraulic conductivity (K) values for the main aquifer were estimated in the second step, where a 34-day pumping test was simulated and observed water levels were used for calibration. Solute breakthrough curves were calculated during the simulation experiment after spinning up the background conditions for the two events of interest.

The physically-based, fully-integrated groundwater and surface water model HydroGeoSphere (HGS) was chosen to represent the Mannheim site. This model solves the 2-D diffusion wave equation for surface water flow, and a 3-D version of the Richards equation for the vadose and saturated zones (Aquanty, 2015a, 2015b). It also has the capability to simulate solute transport. The seamless integration of surface water, the vadose zone, and the saturated zone seemed advantageous for application to a question of contaminant migration from the ground surface to a pumping well. The goal of the numerical modelling was to assess the event-related threats to the public supply well at the site by simulating breakthrough curves at the well for dispersive, conservative solutes originating in the base of the topographic depression and in the creek during two selected hydrological events (Nov 2014 and Jul 2017).

#### 3.2.3.1 Vadose Zone Model

The model design used for the first step of calibration consisted of a triangular mesh that was generated via Grid Builder (McLaren, 2012). The domain region was 100 m by 100 m in plan view with a depth varying between 23 and 26 m, depending on ground surface topography interpolated from GPS elevation surveys (Figures 3.4a and 3.5a; CH2MHILL, 2002; Hillier, 2014; OMECP, 2018; OMNR, 2010; Wiebe et al., 2019). The elevation of the bottom boundary of the domain was assigned to coincide with the approximate elevation of the upper surface of the first major regional aquitard (Lower Maryhill Till, ATB3; Bajc et al., 2014), approximately 312 m above sea level (asl) based on local borehole data (CH2MHILL, 2002; OGS, 2017; OMECP, 2018). The lateral extent was developed by estimating the region of influence of infiltration beneath the base of the topographic depression on the water table, based on observed water level responses at wells during the largest

DFR event on record (Nov 2014). The base of the topographic depression was located at the centre of the model domain. Forty-nine grid layers were used to discretize the interpreted major stratigraphic units of the subsurface beneath the depression (Figure 3.5). This model is hereafter referred to as the "Vadose Zone Model".

Soil properties in the Vadose Zone Model were developed as follows. Soil layers were derived from soil cores from several locations on the west side of the creek, with specific focus on the stratigraphy observed beneath the topographic depression (CP6 soil core, Appendix G). Porosity values could have been estimated from neutron probe and TDR measurements (Appendix H), but values derived from the TDR sensors were unrealistically high and there was much scatter about the best-fit calibration line for the neutron probe, so appropriate literature values were used (e.g., Domenico and Schwartz, 1998). The hydraulic parameters required to represent partially saturated flow conditions (van Genuchten parameters) were derived from the UNSODA database (Leij et al., 1996; D. Graham, pers. comm., 2017), according to the different sediment types identified in the soil cores. Initial estimates for the saturated hydraulic conductivity of the soil layers were specified along with reasonable ranges and adjusted through an automated calibration procedure using PEST (Doherty, 2015). Specific storage values were obtained from the literature (Batu, 1998; Domenico and Mifflin, 1965; Duffield, 2019). The hydraulic conductivity values for the deeper sediments associated with the main Sand and Gravel aquifer were chosen based on preliminary estimates (literature values for lower permeability units; Theis analysis by CH2MHILL and SSPA, 2003 for sand and gravel unit), and the final values were verified to yield a similar match between simulated and observed water levels.

A steady state spin-up was used to obtain initial conditions for one event simulation (Mar 2017). These conditions were developed to mimic pre-event water levels beneath the topographic depression by specifying typical background recharge rates across the domain and larger rates within the topographic depression, and by fixing the hydraulic head values at the outer east and west boundaries during a steady-state spin-up period. No-flow boundaries were located along the north and south sides and bottom of the domain. The lateral boundaries were specified in this way as a simplification of the general southeast flow direction suggested by CH2MHILL and SSPA (2003). Assuming equivalent fixed head values at the east and west boundaries was unlikely to influence the event simulation because of its short duration (4 days) and the predominantly vertical infiltration beneath the base of the topographic depression. The steady state recharge rates and outer fixed head boundary conditions

were calibrated via PEST. Rainfall data collected on site were specified as a variable flux to the top of the model during the transient event calibration.

Hydraulic properties for the streambed were developed based on HGS simulations using a one-dimensional column ("Streambed Model") whose upper boundary was the streambed and whose lower boundary was the depth of the CPP13 observation well screen (Figure 3.4). Creek water levels from a pressure transducer in the stream were specified as the upper, transient hydraulic head boundary condition, while the lower transient head boundary was defined by the transducer water levels for CPP13. Isotropic hydraulic conductivity values for the Streambed unit were varied manually in an attempt to match simulation results with manual water levels from three piezometers located at intermediate depths between the streambed and the screen of CPP13. Specific storage values were again chosen based on literature values (Batu, 1998; Domenico and Mifflin, 1965; Duffield, 2019). The column consisted of Streambed material underlain by Silty Sand, based on hydraulic testing at wells beneath and beside the creek (Appendix K). All monitoring wells used in this analysis were located within close proximity of each other laterally. As such, variations in hydraulic head with depth were assumed to be a reasonable approximation of the vertical hydraulic gradient.

#### 3.2.3.2 Pumping Test Calibration (Wedge 1) Model

The second calibration step involved the estimation of hydraulic properties for the main Sand and Gravel aquifer and related stratigraphic units. Initial K values for the main aquifer units were selected based on estimates from CH2MHILL and SSPA (2003), and these were subsequently revised through calibration (via PEST) to the pumping test data. A radial flow model domain ("Wedge1") that included the public supply well and the topographic depression was used for this step (Figure 3.5b). The grid for this model was constructed in Grid Builder (McLaren, 2012) and consisted of a wedge with two nodes per arc and an arc angle of 18.64°. The ground surface boundary for this calibration of K values for the deeper stratigraphic units was specified to have a uniform elevation equal to the overflow point of the base of the topographic depression, i.e., 335.9 m asl, while the bottom boundary of the domain was the same as for the Vadose Zone Model. Stratigraphy was represented by 70 layers categorized into the major units interpreted beneath the topographic depression, with one clay lens specified near the well based on borehole data (Figure 3.5b; CH2MHILL, 2002; Hillier, 2014; OGS, 2017; OMECP, 2018). The soil properties from the Vadose Zone Model were included for the near

surface layers within the region representing the floodplain and for the Silt3 layer. The Silty Topsoil unit was extended across the entire wedge domain, and the main Sand and Gravel aquifer was specified to underlie either the floodplain soil layers or the Topsoil. The radial extent of the model used for calibration was 2400 m, more than twice the estimated radial drawdown cone extent (Appendix L). Recharge flux through the top boundary was given a calibration range of 290 to 330 mm/yr that included a previously estimated average steady state recharge value for the watershed (321 mm/yr; M.H. Brouwers, pers. comm., 2017; Matrix and SSPA, 2014a). The effective pumping rate at the public supply well was specified as the rate reported for the pumping test (42 L/s) for both the steady state spin-up and transient 34-day simulations. Because the wedge was only a fraction of a full circle, the effective pumping rate was the same fraction of the reported rate. Details of the spin-up process and PEST calibration settings are listed in Appendix M. A feedback process was employed to incorporate hydraulic conductivity values resulting from the calibration of the Vadose Zone Model into the Wedge1 Model and vice versa.

#### 3.2.3.3 Solute Transport (Wedge2) Model

A truncated version of the Wedge1 Model ("Wedge2 Model") was used for event simulations of solute transport for potential dissolved contaminants originating in both the base of the topographic depression and in the creek during the solute transport simulation experiments (Figure 3.5c). Truncating the Wedge1 Model was a telescoping approach that assumed steady state flow in order to facilitate reducing the actual volumetric area modelled and therefore grid refinement. This model domain was 183.6 m long, with two nodes along each arc and 320 nodes along each of the two axes; it was again constructed in Grid Builder (McLaren, 2012). Nodes were spaced at minimum intervals of 0.3 m in the transport region between the well and the base of the topographic depression based on calculations related to the Peclet criterion ($Pe \leq 2.0$; Daus et al., 1985). Specifically, radial nodes were spaced at intervals of 0.3 m from 1 to 60.1 m, at intervals of 0.6 m between 60.1 and 80.5 m, at intervals of 0.9 m between 80.5 m and 90.4 m, and at intervals of 1.2 m between 90.4 m and 183.6 m along each axis. The mass balance for each solute was verified to have a residual of < 0.1% of the input mass over the entire simulation, as a check of numerical dispersion. The arc angle of this wedge domain was the same as for Wedge1, an angle whose width encompassed the typical extent of ponding in the base of the topographic depression. Nodal locations for the contaminant source features (i.e., the creek and the base of the topographic depression) were chosen to ensure that their

lateral distances from the pumping well were similar to observations in the field, and that the area of the base of the topographic depression was also similar to observations. Nodal spacing in the vertical direction was ≤ 0.3 m for all 71 layers; the layer containing the Clay Lens from the Wedge1 Model was split into two layers to facilitate this. The vertical profile of head values for nodes at radii of 183.6 m in the Wedge1 Model after a simulation length of 60 years was used as the outer, fixed head boundary condition, approximating steady state conditions. Ground surface topography was again specified as a uniform elevation corresponding to the outflow of the base of the topographic depression, except in the region near the base of the topographic depression and the creek, where elevations of nodes were estimated based on field observations. Solute transport was performed using a longitudinal dispersivity ($\alpha_L$) of 5.0 m for the Sand and Gravel aquifer based on a rule of thumb of 10% of the transport scale (50 m). A transverse lateral dispersivity of 0.5 m and a vertical dispersivity of 0.05 m were also applied to this aquifer based on general order-of-magnitude recommendations by Gelhar et al. (1992). For reference, a literature-based estimate of $\alpha_L$=3.0 m would be recommended based on a summary of dispersivity and field scale (Fetter, 2001; Equation 14b in Xu and Eckstein, 1995). A value of $\alpha_L$=5.0 m is thus more conservative and would be expected to facilitate earlier contaminant arrivals at the well. Longitudinal and transverse dispersivity values (Appendix M) for the vadose zone layers, Silt3 layer, and Clay Lens were specified based on Rockhold et al. (2016). The rate at which the extended pumping test was conducted, Q = 42 L/s (CH2MHILL and SSPA, 2003), was used for all simulations. This was considered a likely maximum production rate for this specific well.

A conservative but dispersing tracer was used as an analog for colloid transport during event simulations. Colloid transport in the soil matrix is not specifically supported in the modelling code employed (E. Sudicky, pers. comm., 2019). Well vulnerability has often been evaluated based on advective flow (backward particle tracking; Frind et al., 2006). Pure advective transport ignores colloid specific processes (Cey et al., 2009; Ginn et al., 2002; Harvey et al., 1989; Ryan and Elimelech, 1996; Schijven and Hassanizadeh, 2000; Unc and Goss, 2003) such as filtration and die-off that attenuate colloid concentrations and processes such as pore size exclusion that could enhance the tracer velocity. The addition of dispersion allows for an analog to some of the processes that could lead to non-uniform velocities. Ultimately, the present study sought to examine whether hydrological events have the potential to increase pathogen threats to a well from infiltration at a nearby topographic depression, rather than to represent the precise details of colloid transport in the subsurface.

The daily effective precipitation rates calculated as described in Section 3.2.2 and Appendix J were applied as a flux to the upper surface of the porous media. The influence of the exact timing of the snowmelt occurring weeks or months after the events was expected to be negligible compared with the influence of ponding in the topographic depression during the events.

Transport simulations were conducted as follows. Conservative tracers were introduced via fixed concentration boundary conditions into the topographic depression and the creek simultaneously over the time period of observed ponding in the base of the depression during each of the November (Simulation N1) and July (Simulation J1) events. Table 3.1 lists details for the two calibration steps (shaded) and the background and event simulations. Initial concentrations were arbitrarily set to 100 kg/m$^3$ because the analysis considered only the relative concentrations. Pressure transducer data were used to provide a temporally averaged, observed ponding depth that was imposed as a specified head in the base of the depression during this time period. Transducer data were also used to provide observed, fluctuating creek water levels that were imposed as a transient, specified head boundary condition throughout the simulation. In order to compare with a background case with no ponding in the base of the topographic depression, two additional simulations introduced the topographic depression solute over the same time periods as in the above cases for the November and July events, but with no ponding specified (Simulation N1NP and Simulation J1NP, respectively, where "NP" indicates "no ponding"). The free-solution diffusion coefficient of each solute was specified as a value for a non-reactive chemical species in water (Freeze and Cherry, 1979).

Breakthrough curves were plotted from the relative overall concentrations of the two solutes at the well over time. Each flow-weighted concentration in the well was calculated via (Eqn. 3.1):

$$C_t = \left[\frac{dM/dt}{Q}\right]_t, \tag{3.1}$$

where $dM/dt$ is the rate of change of mass obtained from the model output files, $Q$ is the total pumping rate at the well, and $C_t$ is the concentration leaving the domain during the time step ending at time $t$. The relative concentration was then obtained by dividing the flow-weighted concentration by the initial concentration applied in the base of the topographic depression or creek. The critical

relative concentration corresponding to the "detection" of a fecal indicator species such as *E. coli* in the raw water at the well was estimated via (Eqn. 3.2):

$$C_{crit,rel} = \frac{C}{C_{sw}}, \tag{3.2}$$

where $C$ is the typical minimum quantifiable concentration of 1 cfu/100 mL, and $C_{sw}$ is a typical *E. coli* concentration estimate based on either the median or maximum observation at a nearby creek (Canagagigue Creek, about 20 km away; 220 cfu/100 mL or 31,000 cfu/100 mL, respectively; Van Dyke et al., 2010). The median concentration was similar to observations at the Mannheim site (Menkveld, 2019) and about twice the maximum concentrations found in snowmelt runoff near the Thornton well field in Woodstock, ON (Christie et al., 2009). The time ($t_{crit}$) at which each breakthrough curve first reached $\frac{C_{tracer}}{C_{sw}} = C_{crit,rel}$ was recorded.

The actual breakthrough of the creek solute would be underestimated by the above process because the Wedge2 Model does not represent the continuity of the creek as a line source extending outside of the boundaries of the wedge. Representing only a small section of the creek at its minimum distance from the well is appropriate for determining first arrival times, but microbial contaminants could infiltrate at greater distances from the public supply well and thus could contribute additional contaminants to the well at later times. This is a limitation of the simplified geometry chosen for the solute transport modelling. The assumption that the contamination event in the creek corresponds to the timing of the presence of ponding in the base of the topographic depression is a further simplification. Contamination in the creek could persist over a longer time period and lead to higher concentrations at the well.

## 3.3 Results

Field monitoring of several ponding events during the study suggested that the enhanced recharge flux occurring beneath the topographic depression significantly influences the local groundwater flow system under conditions of no pumping at the nearby public supply well (Figure 3.6; Appendix I; Menkveld, 2019). Figure 3.6a illustrates water level responses to the Nov 2014, Mar 2017, and Jul 2017 events, Figure 3.6b shows the overall range of soil moisture profiles observed for the soil

beneath the base of the depression, and Figure 3.6c shows the relationship between groundwater levels and rainfall intensity at four monitoring wells along transect B-B' (Figure 3.4). Hydraulic head values under the base of the topographic depression (CPP3) were usually larger than those measured beside the stream (CPP1) and always larger than those in the middle of the field (CPP8, CPP6) during events. This suggests that DFR has a larger impact on local water levels than the localized recharge occurring beneath the creek. The amplitude (peak water level – pre-event background water level) of the water table fluctuation beneath the base of the topographic depression was always larger than event responses at other wells during large rainfall events (> 10 mm; Figure 3.6c). Large-magnitude hydrological events at the site (water level rise > 1 m under the base of the topographic depression) were found to occur about 4 times per year, when sufficient rainfall and sometimes snowmelt led to ponding in the topographic depression (Appendix I). Over half of these large events were associated with rainfall > 10 mm. Soil moisture content values in vertical profiles near CPP1, CPP3, and CPP6 were observed to increase by up to around 5% during events, compared with pre-event conditions (Figure 3.6b; Appendix H). General water level fluctuations in deeper wells located > 20 m away from the base of the topographic depression (e.g., CPP6, CPP18, and MWB; Wiebe et al., 2019) showed seasonal water table fluctuations within a range of 1.2 m on an annual basis, and the water table was located between 2 and 4 m below ground surface. For comparison, water levels under the base of the topographic depression (CPP3) varied from 2.4 to 0 m below ground surface.

The Vadose Zone Model was used to derive saturated hydraulic conductivity values for the near surface soils under the base of the topographic depression by matching simulated to observed water levels during calibration. Table 3.2 shows the final derived parameters. Seven soil layers were interpreted beneath the base of the topographic depression, including silt layers above and below the Gravelly Sand unit (Silt1 and Silt2), a Silty Sand unit that combined observed silty sand and medium to coarse sand units (Figure 3.3), and the Silt3 unit (Table 3.2; Figure 3.5, "SILT" layer). The horizontal and vertical hydraulic conductivity values for the Silty Topsoil were estimated to be 3.0 m/d and 8.5 m/d, respectively, based on the calibration; these were one order of magnitude larger than a value estimated by Guelph Permeameter measurements in the field (Menkveld, 2019; Missori, 2015). Estimated hydraulic conductivity values for the Gravelly Sand unit under the floodplain were consistent with reasonable values (Freeze and Cherry, 1979) for a clean sand, and values for the Silty Sand were reasonable for the type of material. The hydraulic conductivity values for the Silty Sand were within ±50% of the estimate from hydraulic testing at CPP3 (Appendix K). Hydraulic conductivity for the Streambed was in the range for silt (Freeze and Cherry, 1979) and agreed well

with slug test results (Appendix K); this value allowed unsaturated conditions to develop beneath the creek during certain times of year, as observed (Wiebe et al., 2019).

Recharge rates for the base of the topographic depression and for other areas of the domain in the Vadose Zone Model were estimated to be 370 mm and 330 mm per year, respectively, during the steady state spin-up period of calibration. Figure 3.7a shows that a reasonable match with observed event (Mar 2017) water levels was obtained for the rising limb of the groundwater level response at CPP5 and CPP1, though rising limb observations at CPP2 were matched less well. The delayed simulated response at CPP2 could be related either to the initial conditions or uncertainty regarding soil layering. The simulated initial conditions were generated via a steady-state spin up, while water levels at the field site were receding after a previous infiltration event. The presence of possible underlying lower permeability soil layers not included in the Vadose Zone Model could have had an effect on the observed rate of response at CPP2. The inclusion of thin silt layers interpreted from borehole data was critical for matching the observed CPP5 event response. The falling limb of the CPP5 groundwater hydrograph was matched to a lesser degree by the simulations, though this was matched more precisely at CPP2. The Vadose Zone Model calibration generally captures the dynamics of the observed Mar 2017 event.

Figure 3.7b shows the results of matching a 2002 pumping test with the Wedge1 Model. The calibrated $K_x$ value (86 m/d) for the main Sand and Gravel aquifer is within the range of previous estimates for the site (50 to 112 m/d for a saturated thickness of 16 m; CH2MHILL and SSPA, 2003; Hillier, 2014). $K_z$ for the main aquifer was estimated to be 25 m/d, with a resulting anisotropy ratio of 0.3, similar to the estimate of 0.35 by Hillier (2014) for the site. Recharge to the top of the domain was calibrated to be 292 mm per year during the steady state spin-up that preceded the pumping test. Appendix M contains a list of the final boundary conditions and additional information for the models.

Results of the solute transport simulations are shown in Figure 3.8 and Table 3.3. Figure 3.8 shows selected breakthrough curves, including the DFR solute for the two events and one background simulation, and two creek solute curves. The sharp increase in breakthrough in Simulation N1 around 110 days for the creek solute and around 120 days for the DFR solute is likely related to: 1) increased creek water levels around 110 days (Appendix M, Figure M.5), and 2) increased effective precipitation around 120 days (Appendix M, Figure M.5). The $C_{crit,rel}$ value corresponding to "detection" of *E. coli* in the raw water of the well (at a concentration of 1 cfu/100 mL) was estimated

to be $5 \times 10^{-3}$ for the median $C_{sw}$ and $3 \times 10^{-5}$ for the maximum $C_{sw}$. This latter value is indicated on Figure 3.8. Table 3.3 shows that peak relative concentrations for all events were at least one order of magnitude below $C_{crit,rel}$ for the median $C_{sw}$ case, suggesting that it would be unlikely for non-zero concentrations to be detected by sampling at the well for average contaminant conditions, in the absence of preferential flow paths. Under extreme conditions, when $C_{sw}$ was two orders of magnitude larger than the median value, relative concentrations exceeded $C_{crit,rel}$ for both solutes during Simulation N1. Simulation N1NP resulted in peak relative concentrations for the DFR solute of up to half of $C_{crit,rel}$ for the maximum $C_{sw}$ (Figure 3.8). Maximum relative concentrations for the creek solute were comparable and of the same order of magnitude as those for the DFR solute during Simulation N1, and five orders of magnitude lower during Simulation J1. Critical travel times, $t_{crit}$, were > 50 days for both solutes in all cases. In Simulation N1, $t_{crit}$ was 142 days for the DFR solute and 118 days for the creek solute. For comparison, the site of the May 2000 Walkerton tragedy had thin overburden soils and fractured bedrock that allowed bacteria to migrate from the surface into shallow wells within about two days (Worthington and Smart, 2017).

Overall, field observations indicated that infiltration beneath the topographic depression during events had a larger influence than the creek on local groundwater levels. Several models were used to match the observed dynamics related to the streambed, vadose zone, and saturated zone by modifying hydraulic conductivity values, and to simulate solute transport from the base of the topographic depression and the creek to the well. Critical concentrations corresponding to a typical (median) initial surface water concentration were not reached at the well for either of the events simulated. Critical travel times for a potential maximum initial concentration were > 50 days for both DFR and creek solutes. For a large initial surface water microbial concentration, the DFR solute attained concentrations of concern at the well after 142 days when ponding and DFR occurred in the base of the topographic depression, but did not reach concentrations of concern within 200 days when no ponding occurred. Despite $t_{crit}$ > 50 days, Simulation N1 results suggest that ponding and associated DFR can lead to increased risk to an overburden public supply well by reducing the arrival time by at least 58 days, compared to Simulation N1NP. The creek solute reached critical concentrations at the well after 118 days in Simulation N1, but relative concentrations were six orders of magnitude below $C_{crit,rel}$ in Simulation J1.

## 3.4 Discussion

Threats to public supply wells due to transient hydrological events are not commonly assessed. The present study combined the results of detailed field site characterization and event monitoring with numerical modelling to assess the potential risk to an overburden well by contamination from rapid, short-duration, focused infiltration of potential contaminant species during large-magnitude hydrological events. Consideration of the threat of DFR to microbial water quality at public supply wells may be most important when considering the location of new water supply wells, or existing wells that could be exposed to a higher degree of risk following hydrological events. The following text: 1) discusses contaminant breakthrough at the well and highlights the large difference in $t_{crit}$ for the DFR solute between the N1 and N1NP simulations, 2) outlines several challenges related to quantifying microbial travel times of concern using breakthrough curves, and 3) discusses focused recharge more broadly.

Despite $t_{crit}$ values being much larger than (more than two times) the 50-day threshold in the present study, factors such as preferential flow paths, well depth, and colloid-specific processes that enhance microbial transport could generally lead to earlier and larger relative concentration breakthrough at a well. The commonly used 50-day threshold is based on the assumption that pathogens will be inactivated to the extent that they pose an acceptable risk after this period of travel time in groundwater (Ferguson et al., 2003). This threshold is not necessarily a robust indicator of pathogen threat (Schijven et al., 2010). Some viruses can survive more than 200 days in groundwater (Murphy et al., 2017; Espinosa et al., 2008). Additional analysis such as microbial sampling results should always be considered in addition to numerical modelling results (A. Chik, pers. comm., 2020).

The phenomenon of ponding in the base of the topographic depression appears to be one factor differentiating the N1 simulation, where the relative DFR solute concentration exceeded $C_{crit,rel}$, from the N1NP simulation, where relative concentrations were below the threshold. The results suggest that there could be large differences in $t_{crit}$ between scenarios that consider or ignore event ponding and DFR. The $t_{crit}$ value for the DFR solute was 142 days in Simulation N1 and was not identified $\left(\frac{Ctracer}{C_0} < C_{crit,rel}\right)$ within 200 days in Simulation N1NP. The duration of ponding also seemed to be a major factor for whether relative breakthrough concentrations approached $C_{crit,rel}$. Figure 3.8 shows increasing relative concentration breakthrough as scenarios progressed from no ponding (Simulation N1NP, DFR solute) to 24 hours of ponding (Simulation N1, DFR Solute) to

continuous ponding (Simulation N1, creek solute). The reason for the DFR solute results for Simulation J1 not fitting this pattern (peak concentrations were lower than N1NP peak concentrations at 200 days) is possibly related to lower creek water levels during the J1 simulation. Creek water levels during Simulation J1 were 0.71 m lower at the start of the event and were 0.11 m lower on average (Appendix M). Proximity of the contaminant source zone also influences breakthrough. The difference between the breakthrough of the creek solute and the DFR solute in Simulation N1 relates to the distances between their source areas and the well, where the creek solute (26.7 m from the well) reaches $C_{crit,rel}$ prior to the DFR solute (41.2 m from the well). The relative magnitudes of the creek solute and the DFR solute are reversed in the Simulation J1 results. Infiltration of the creek solute may have been more inhibited by the lower permeability of the streambed in Simulation J1 because of the lower water levels. Peak concentrations resulting from the creek may also be low because the model does not include contamination from reaches of the stream outside the model domain that would also normally be captured by the well.

One of the challenges of the approach of using breakthrough curves in association with microbial contaminants is the inability to quantify the concentration or time of "first arrival" of the contaminant at a well. The point in time at which a sample is collected that is found to contain more than one fecal coliform is not truly the first arrival because of noncontinuous sampling and laboratory analytical method detection limits. The measurement of a concentration of 1 cfu /100 mL implies that the well would already be capturing millions of these indicator species per day if pumping at the flow rate noted above (42 L/s). The arrival (at concentrations of concern) of a contaminant species with a more clearly defined drinking water threshold or maximum allowable concentration would be easier to quantify with a breakthrough curve approach (e.g., Frind et al., 2006). Microbial contaminants are considered on more of a presence/absence basis related to sampling (Ahmed et al., 2019). Single grab samples are the norm due to costs and laborious analysis procedures, and it has generally not been possible to obtain continuous microbial concentration measurements (Besmer et al., 2016). The probability of detecting relatively small numbers of pathogen indicator species from a well pumping at reasonably high flow rate (e.g., 42 L/s) with a single sample is low. The use of a detection-based concentration (such as 1 cfu/100 mL) as a threshold of concern during simulations is intuitive and analogous to sampling for pathogen indicator species. However, threats to public health related to microbes could exist before this threshold is reached for the raw well water.

A second challenge is parameter uncertainty. For instance, the $\alpha_L$ characteristics of the porous media (vadose zone and saturated zone) could affect travel times by weeks. Dispersivity is generally

understood to vary with the scale of transport (e.g., Xu and Eckstein, 1995). Though values may be selected based on the literature or an expert opinion based on the site scale, accurate local values may be difficult to obtain without conducting a tracer test at the site. Further uncertainties relate to the concentration of pathogen indicator species in surface water during an event.

Another challenge is the potential discrepancy between the advective-dispersive transport of a conservative solute and the more complex dynamics of colloid transport. Processes that enhance or attenuate microbial transport were not specifically incorporated into the present study. The present study illustrates the difference between advective-dispersive transport with and without consideration of surficial ponding, and between simulations with different ponding duration.

The presence of unsaturated soil above the water table (hydraulic disconnection) can be seen as a source water protection mechanism. Hydraulic disconnection may significantly slow the migration of contaminants from ground surface to the water table. The magnitude of the hydraulic conductivity in unsaturated soils may be one or two orders of magnitude smaller than the saturated value because it is a function of the soil water content. Soil under the base of the topographic depression became saturated essentially from the initial water table position up to the surface during some observed events, while the well was not pumping. When the well was simulated to be pumping, the soil did not become saturated up to ground surface because of the lower initial water level beneath the topographic depression. Other researchers have noted that the proximity of the water table to the ground surface could be a concern for sand and gravel extraction or other development operations that remove overburden sediments, because decreasing vadose zone thickness could potentially reduce this buffer against contaminant transport (Peckenham et al., 2009; Sousa et al., 2014).

Monitored events showed a threshold response and repeated patterns in terms of overland runoff and ponding (McDonnell et al., 2007). Ponding, infiltration, and DFR typically occurred following a large magnitude of combined rainfall/snowmelt (> 10 mm), and large water table responses (> 1 m amplitude) beneath the topographic depression occurred about four times per year, most often over the winter months from Nov to Apr (Appendix I). DFR could be an aspect of landscape-scale enhanced recharge and preferential flow, analogous to Prairie Potholes in western Canada or playas in the High Plains Aquifer, USA (Crosbie et al, 2013; McDonnell et al., 2007; Zebarth et al., 1989). Researchers in these areas have found that focused recharge locations within the landscape are an important management consideration for source water protection and for the maintenance of recharge functionality during land use change (e.g., Gurdak and Roe, 2010; van der Kamp and Hayashi, 2009).

Permanent water courses such as the reach of Alder Creek at the Mannheim field site are more obvious microbial contaminant threats than intermittent ponding in topographic depressions. The creek in this case was a losing stream, but field data suggested that DFR had a larger influence on the local water table than localized recharge beneath the creek. The simulations suggested that relative creek tracer concentrations at the well could be similar to those corresponding to the DFR solute in certain scenarios such as the large November event. Despite some results (Simulation J1) pointing to a minor role for the creek in transmitting microbial contaminants into the subsurface, the creek was located closer to the well than the base of the topographic depression and was observed to overflow its banks during snowmelt events. The simulations did not specifically address this type of scenario, and the creek could generally be a larger threat than indicated by the Simulation J1 results. The creek would also be a larger threat if the streambed deposits did not have a hydraulic conductivity (Table 3.2) that limited flow and was orders of magnitude less than the banks and surrounding deposits.

Monitoring of hydrological events can be a labour intensive task. Collecting manual measurements during event water level peaks is difficult in terms of timing. Yet any manual measurements collected during events are valuable as verification of sensor data. The minimum required equipment to monitor events would be a pressure transducer installed at the ground surface in locations of potential ponding. Shallow observation wells allowed arrival of draining event water at the water table to be verified via water level responses. Event monitoring in the present study could have been improved with the use of cameras to record event responses when no field staff were on site. Cameras could be useful for verifying the presence of ponded water. This could be especially important during times of freeze-thaw cycles (e.g., Menkveld, 2019) when a surface water transducer's data might be unreliable due to freezing of the sensor diaphragm.

Detailed analysis of both hydrological events and site stratigraphy, in association with solute transport modelling, has the potential to aid assessment of well vulnerability to large-magnitude events. Provincial public supply well management policies in Ontario provide a limited focus on hydrological events, despite the fact that the May 2000 Walkerton tragedy involved a heavy rainfall event. Guidance is also lacking in terms of how to proactively characterize the vulnerability of proposed public supply wells to events. The present study suggests that increased risk may exist not only for public supply wells screened in fractured bedrock but also for those screened in overburden sediments during the sudden challenges (Rizak and Hrudey, 2007) posed by large-magnitude

hydrological events. Inclusion of ponding and its duration, and the proximity of infiltration to the well are likely two of the most important factors related to projecting arrival time and peak concentration.

## 3.5 Conclusions

The present study illustrates how topography-induced overland runoff leading to DFR has the potential to increase microbial risk to overburden public supply wells during large-magnitude rainfall and/or snowmelt events. Simulations suggested that under extreme conditions, arrival times for tracers representing microbial contaminants originating at the ground surface within 50 m of a well could decrease by at least 58 days if ponding and DFR occurred. The DFR solute was simulated to reach a public supply well at concentrations analogous to detection within a travel time of 142 days during a large November rainfall and snowmelt event. For a background case with no event ponding, the peak relative concentrations were three times lower, below the estimated detection threshold, and considered unlikely to be a threat. These results suggest that the limited focus on hydrological events within public supply well management could be ignoring potential problems related to temporary, event-induced ponding during extreme events for some sites. The results also suggest consideration of event-related risks for a broader range of wells than merely those screened in fractured bedrock, such as those implicated in the Walkerton 2000 disease outbreak.

The conditions related to microbial concerns $\left(\frac{C_{tracer}}{C_{sw}} \geq C_{crit,rel}\right)$ at the study site were found to be associated with the most extreme hydrological event within the field data record. The largest event on record in the 3.5-year period was a late autumn heavy rainfall event that followed the melting of a 20 cm snowpack (November 2014). This was the only event simulated to exceed a threshold for relative concentrations analogous to detection of pathogen indicator species at the well for a solute originating in ponding in the base of a topographic depression. A summer (July 2017) rainfall event with half of the effective precipitation and half of the duration of ponding resulted in relative concentrations below the threshold of concern. Threshold relative concentrations were only exceeded in the largest event for a high surface water pathogen indicator species concentration (31,000 cfu/100 mL). Calculations using a typical median surface water pathogen indicator species concentrations for another creek in the area (220 cfu/100mL; Van Dyke et al., 2010) seemed unlikely to estimate concentrations of concern in raw well water.

Breakthrough of a tracer originating in a creek located between the topographic depression and the well differed depending on the event, likely as a result of creek water levels and overbank flooding. In the November event, the estimated critical travel time for the creek solute was 118 days and the peak relative concentrations were of the same order of magnitude as the DFR solute. Peak relative concentrations for the creek were six orders of magnitude below the threshold related to the higher initial surface water pathogen indicator species concentration during the July event, when creek water levels were initially 0.71 m lower, and on average 0.11 m lower, than in the November event simulation.

For many public supply wells, the major acute threat could be the possibility that the transport of event water could deliver large concentrations of pathogenic microbes to a well. This is typically mitigated by attenuation within the subsurface and by sufficient water treatment. DFR may in extreme cases be a threat to the raw water at nearby overburden public supply wells.

Cameras, pressure transducers installed at ground surface, and shallow wells instrumented with pressure transducers could be used to ascertain whether event-induced ponding and DFR occurs in topographic depressions when no field staff are on site. Such monitoring could provide water purveyors with early warning of future potential impacts on the water quality in their supply wells.

## 3.6 Tables

Table 3.1. List of events simulated.

| Event | Model | Total precip.* (mm) | Ponding duration for base of topographic depression (hr) | Description† |
|---|---|---|---|---|
| 26 – 30 Mar 2017 (Calibration) | Vadose zone | 19 | 6.5 | Calibrate properties for upper three soil layers ($K_x$‡ = $K_y$, $K_z$). Minimal stream influence (stream rise ≤ 10 cm). Average ponding depth = 2 cm. |
| 2002 Pumping Test (Calibration) | Wedge1 | N/A | 0 | Calibrate main aquifer properties ($K_x$‡ = $K_y$, $K_z$). Q = 42 L/s§. Pump shut off for 4.2 days, then restarted. |
| Background conditions (Simulation N1NP) | Wedge2 | Based on observat-ions¶ | 0 | Spin-up. Q = 42 L/s§. |
| Nov 2014 (Simulation N1) | Wedge2 | 87 | 24 | Largest event on record. Heavy rainfall (67 mm) followed snowpack melting (20 mm SWE**). Unfrozen soil. Average ponding depth = 10 cm. Q = 42 L/s§. |
| Jul 2017 (Simulation J1) | Wedge2 | 43 | 11.5 | Summer event. Unfrozen soils. Rapid response: shortest rising limb of any observed groundwater hydrograph. Average ponding depth = 5 cm. Q = 42 L/s§. |

* Total precipitation over the previous 4 days and up to the time of the peak water level.

† Event observations (for Nov 2014, Mar 2017, and Jul 2017) from Appendix I and Wiebe et al. (2019).

‡ K = saturated hydraulic conductivity. The direction is specified as "x", "y", or "z".

§ Q = effective 3D pumping rate (CH2MHILL and SSPA, 2003; the wedge model applied a fraction equivalent to the total pumping rate multiplied by the ratio of the angle of the wedge to 360°).

¶ Effective precipitation was calculated based on rainfall and snowmelt observations as described in Appendix J.

** SWE = snow water equivalent; assuming a 10:1 ratio of snow thickness to liquid water height.

Table 3.2. Model parameters.

| Soil Unit | $K_x = K_y$* (m/d) | $K_z$ (m/d) | Specific Storage† ($m^{-1}$) | van Genuchten parameters‡ | | | |
|---|---|---|---|---|---|---|---|
| | | | | α ($m^{-1}$) | n | θs§ | θr |
| 20 Apr 2016 to 19 Apr 2017 – Streambed Model (Transient Calibration) | | | | | | | |
| Streambed | 6.0E-3 | 6.0E-3 | 3.0E-3 | 2.0 | 1.2 | 0.5 | 0.1 |
| Silty Sand | See below | | | | | | |
| 26-30 Mar 2017 – Vadose Zone Model (Transient Calibration) | | | | | | | |
| Silty Topsoil | 3.0 | 8.5 | 1.0E-4 | 1.2 | 1.39 | 0.4 | 0.1 |
| Silt1 | 6.7E-2 | 0.26 | 1.0E-4 | 1.2 | 1.39 | 0.4 | 0.1 |
| Gravelly Sand | 17 | 5 | 5.0E-5 | 1.5 | 3.8 | 0.3 | 0.05 |
| Silt2 | 6.6E-2 | 3.2E-2 | 1E-4 | 1.2 | 1.39 | 0.4 | 0.1 |
| Silty Sand | 0.20 | 0.11 | 5.0E-4 | 2.5 | 2.3 | 0.37 | 0.08 |
| Sand and Gravel | See below | | | | | | |
| Silt3 | 1.9E-3 | 1.1E-3 | 1.0E-4 | 1.2 | 1.39 | 0.4 | 0.1 |
| Streambed | See above | | | | | | |
| 2002 Pumping test at public supply well – Wedge1 Model | | | | | | | |
| Silty Topsoil | See above | | | | | | |
| Silt1 | See above | | | | | | |
| Gravelly Sand | See above | | | | | | |
| Silt2 | See above | | | | | | |
| Silty Sand | See above | | | | | | |
| Streambed | See above | | | | | | |
| Sand and Gravel | 86 | 25 | 5.0E-5 | 1.5 | 3.8 | 0.3 | 0.05 |
| Silt3 | See above | | | | | | |
| Clay Lens | 9.7E-4 | 9.8E-4 | 3.0E-3 | 2.0 | 1.2 | 0.5 | 0.1 |

* K = saturated hydraulic conductivity

† Based on Batu (1998), Domenico and Mifflin (1965), and Duffield (2019)

‡ α, n, θs, and θr are van Genuchten parameters (inverse of air entry pressure, fitting parameter, saturated moisture content, and residual moisture content, respectively).

§ Assumed equal to porosity

Table 3.3. Comparison of breakthrough results for 200 days of travel time.

| Event | Solute | Maximum $C/C_0$ | $t_{crit}$ for maximum $C_{sw}$ (days) |
|---|---|---|---|
| Nov 2014 (Simulation N1) | DFR | 5.9E-5* | 142 |
| | Creek | 5.4E-5* | 118 |
| Jul 2017 (Simulation J1) | DFR | 5.6E-6 | -† |
| | Creek | 1.3E-11 | - |
| Nov 2014 Background (Simulation N1NP) | DFR | 1.6E-5 | - |
| Jul 2017 Background (Simulation J1NP) | DFR | 1.0E-17 | - |

* Shaded cells correspond to $C/C_0 > C_{crit,rel}$ for the maximum $C_{sw}$ case.

† "-" signifies "not available" (maximum $C/C_0 < C_{crit,rel}$ for maximum $C_{sw}$)

## 3.7 Figures

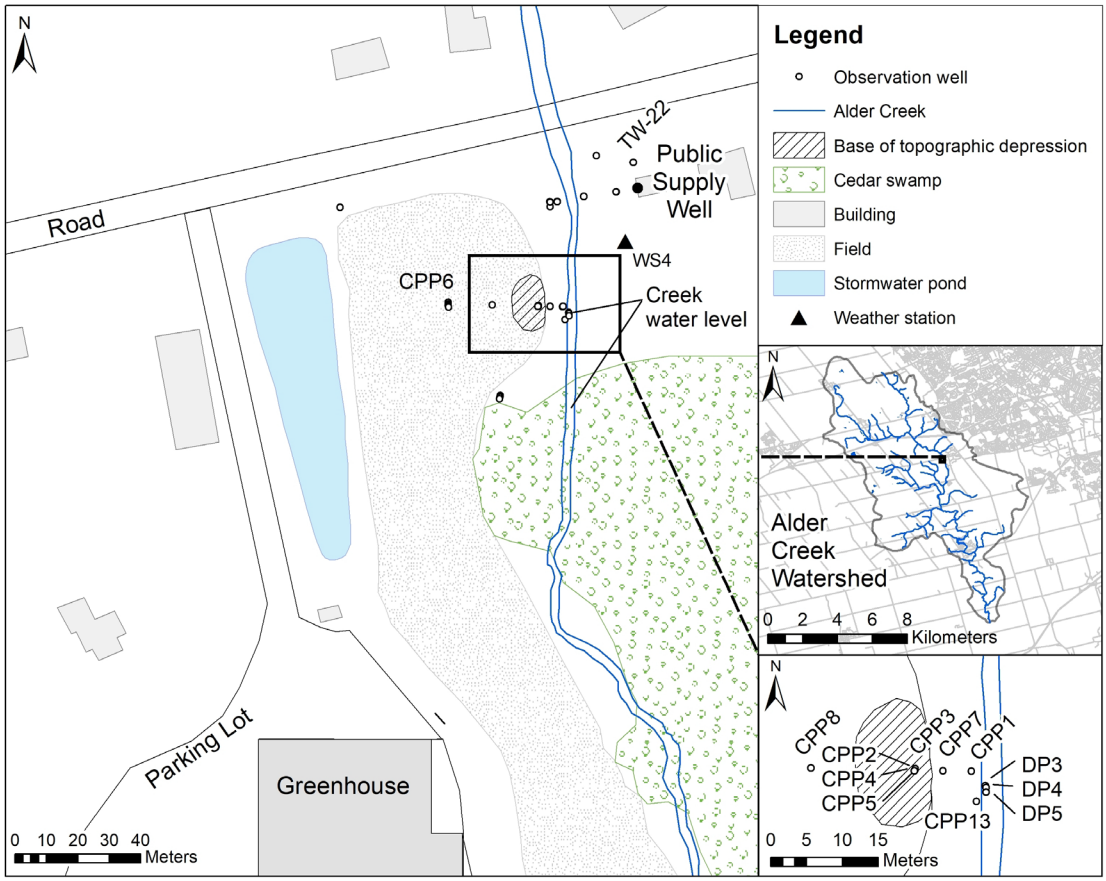


Figure 3.1: Mannheim field site (CH2MHILL and SSPA, 2003; DMTI, 2011; Esri et al., 2013; First Base Solutions, 2006; GRCA, 1998; Menkveld, 2019; Stantec, 2013; Wiebe et al., 2019).

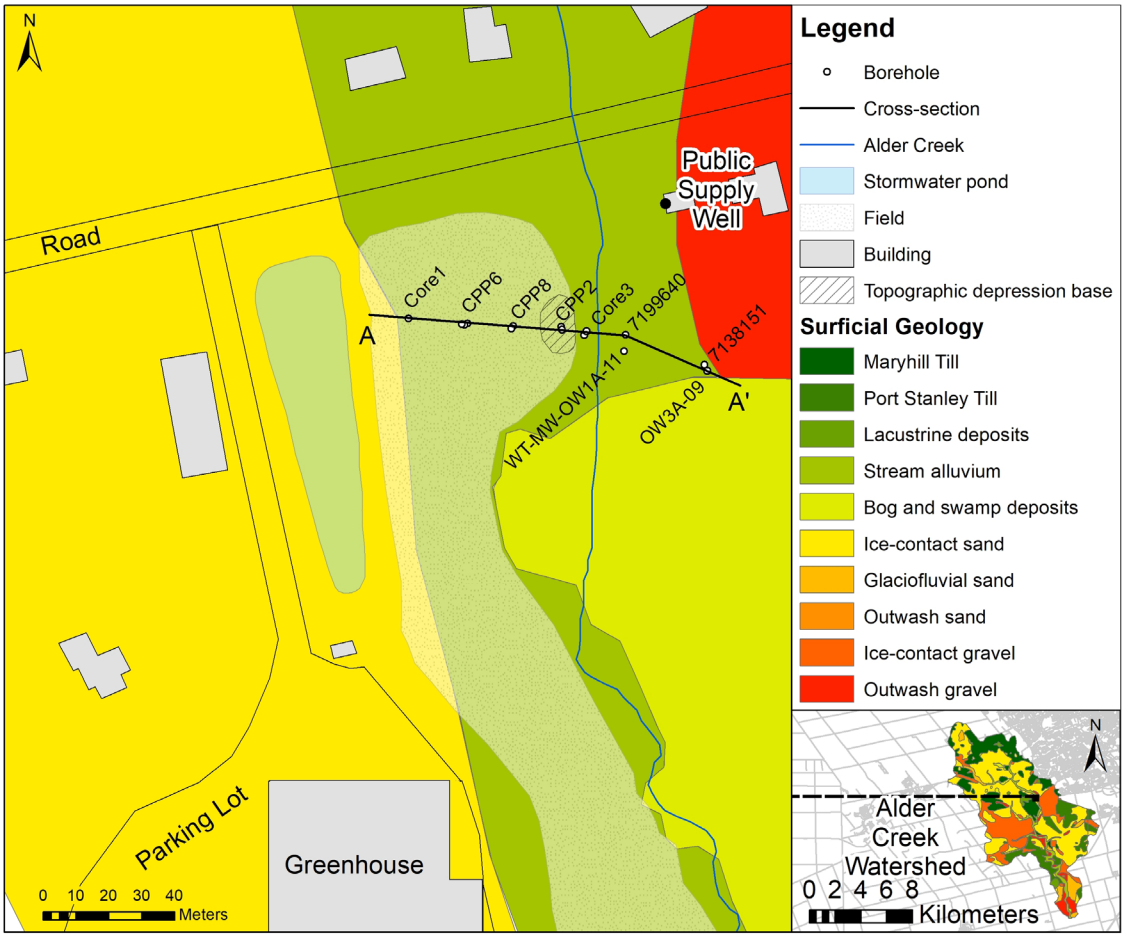


Figure 3.2: Surficial geology (CH2MHILL and SSPA, 2003; DMTI, 2011; Esri et al., 2013; First Base Solutions, 2006; GRCA, 1998; Hillier, 2014; Menkveld, 2019; modifying OGS, 2010; OMECP, 2018).

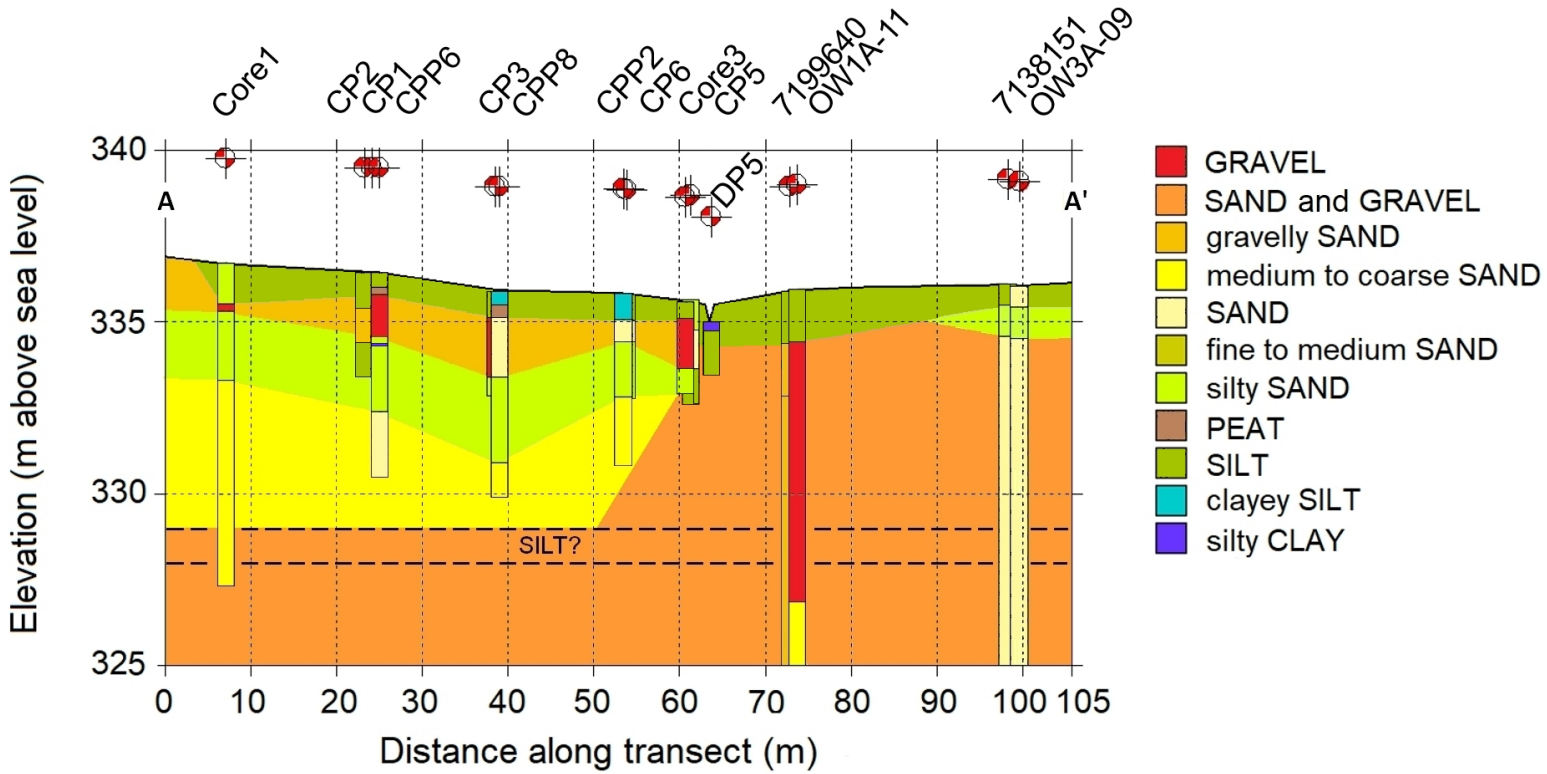


Figure 3.3: Stratigraphic cross-section (Appendix H; Menkveld, 2019; NERC, 2017; BGS Groundhog® Desktop, Copyright © BGS/NERC (2019); OMECP, 2018). Vertical exaggeration = 4.0. Two thin silt layers observed above and below the gravelly sand unit near CPP2 are not shown.

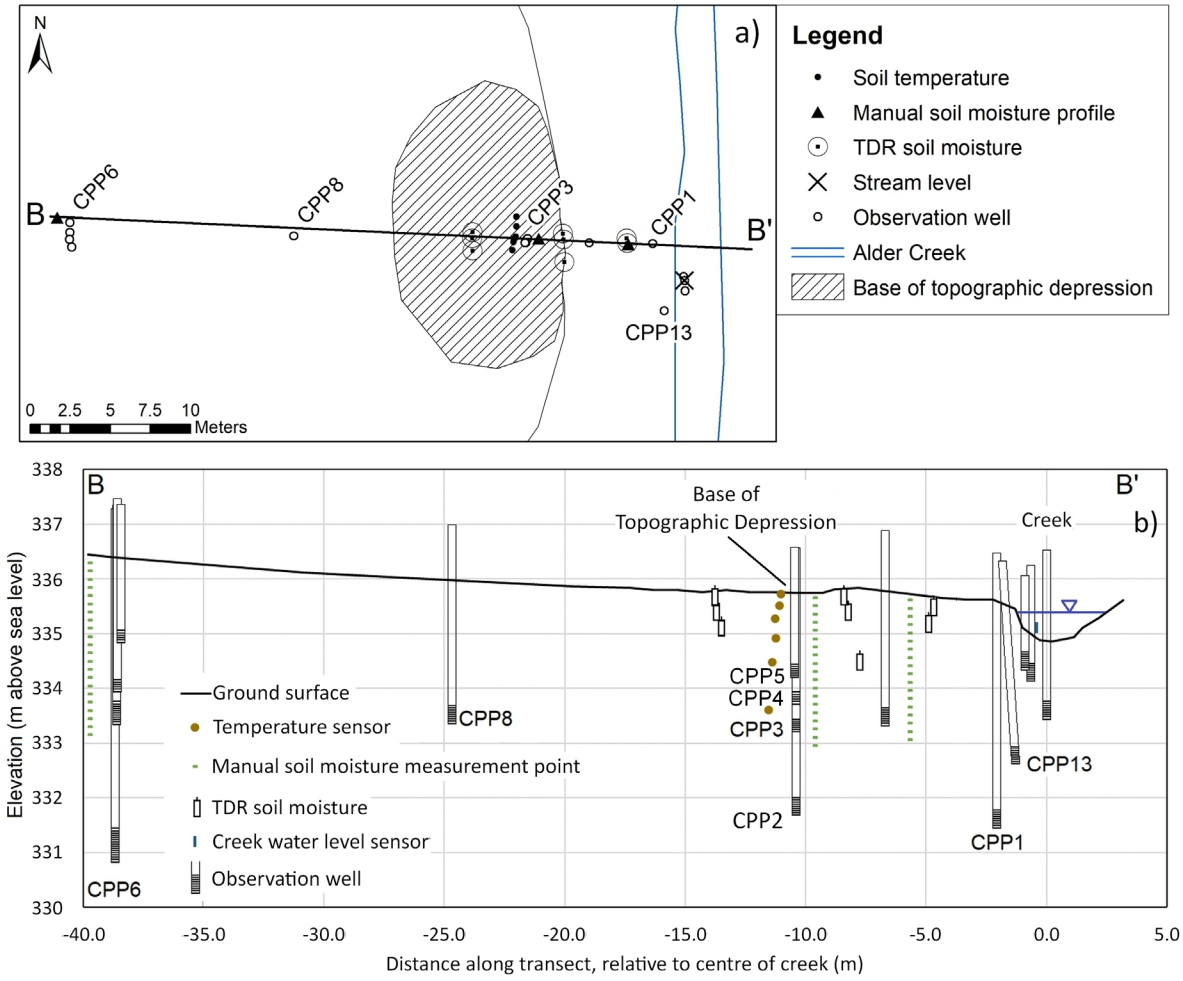


Figure 3.4: Equipment along transect through topographic depression in a) plan view, and b) cross-section (First Base Solutions, 2006; Menkveld, 2019; Wiebe et al., 2019).

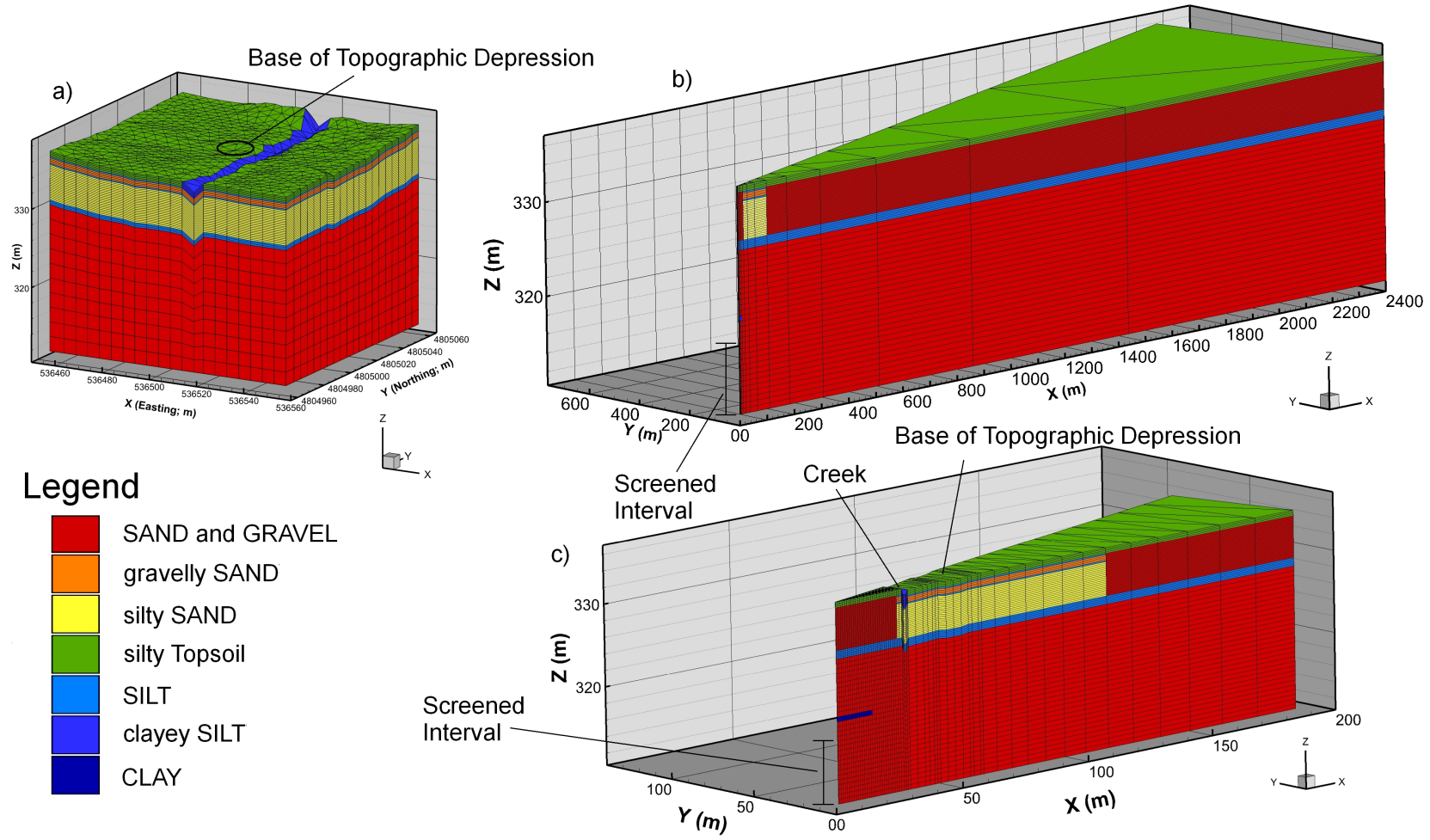


Figure 3.5: Model grids for the (a) Vadose Zone, b) Wedge1, and c) Wedge2 models (McLaren, 2012; Tecplot, 2017).

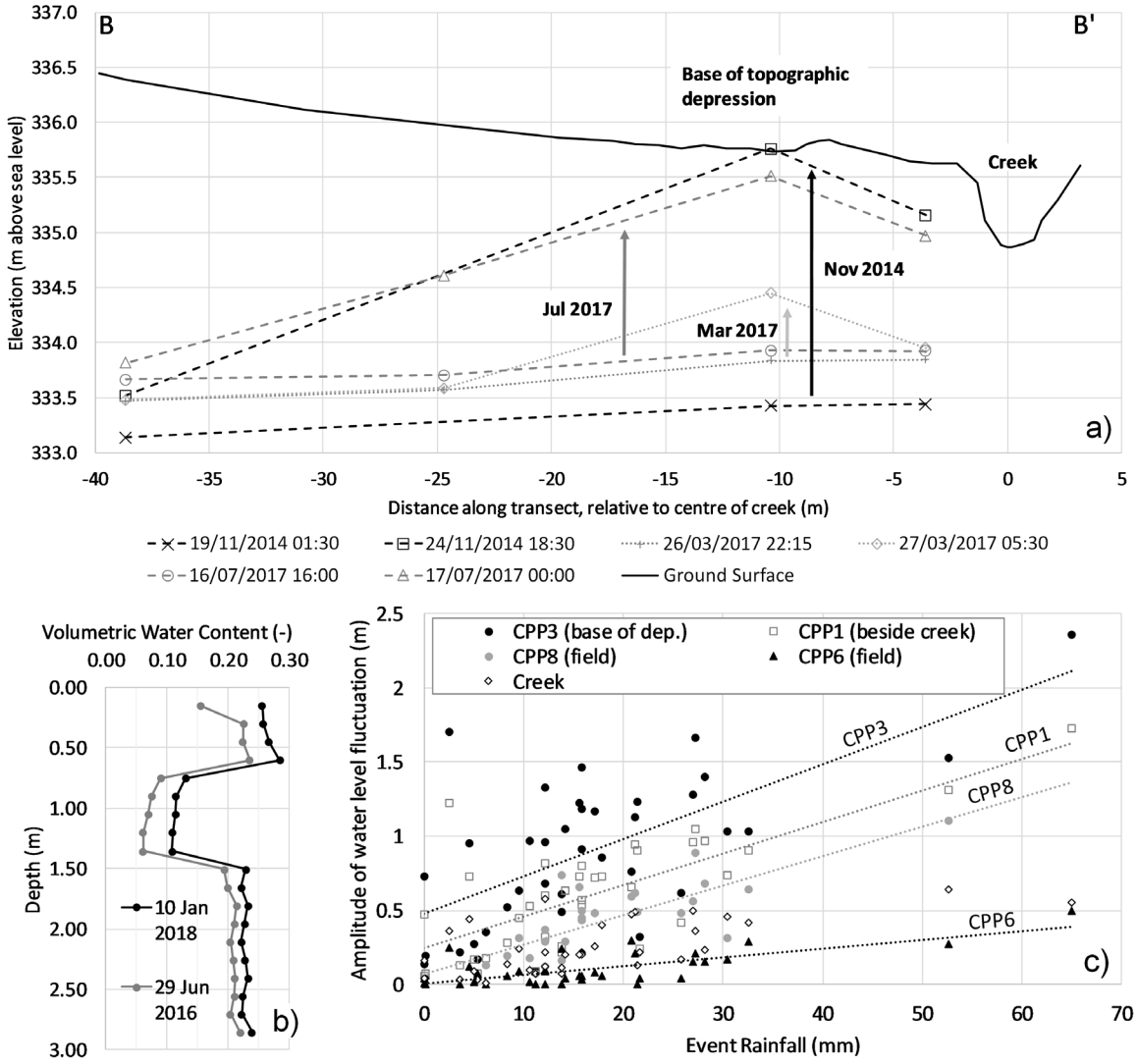


Figure 3.6: Observed event responses at the field site (Appendix I; Wiebe et al., 2019): a) Water levels, b) range of soil moisture profiles under base of topographic depression, and c) relationship between event water level response and rainfall.

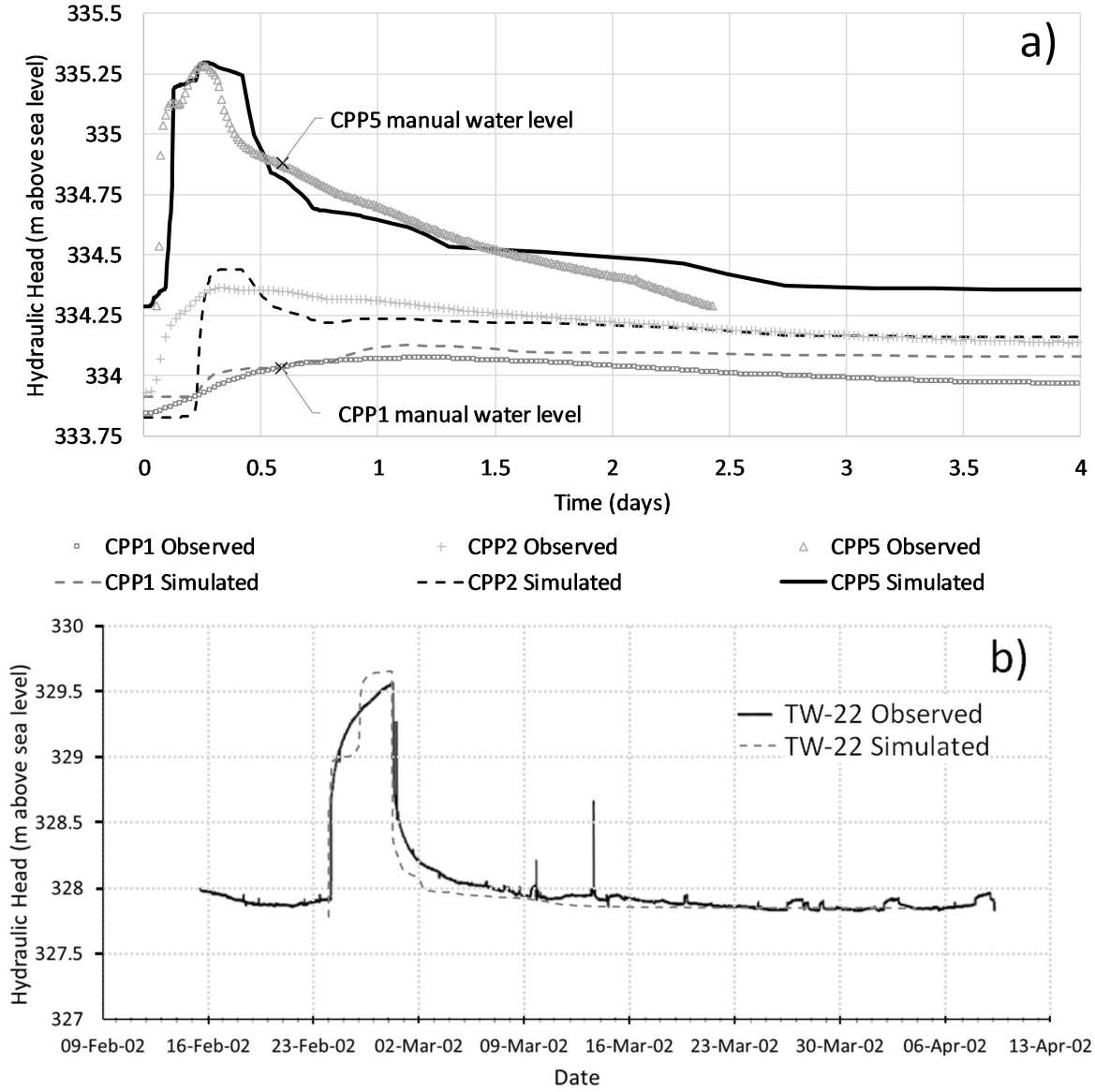


Figure 3.7: Matching of observed water levels: (a) Vadose Zone Model with 26 – 30 Mar 2017 event, (b) pumping test responses with Wedge1 model (after CH2MHILL and SSPA, 2003).

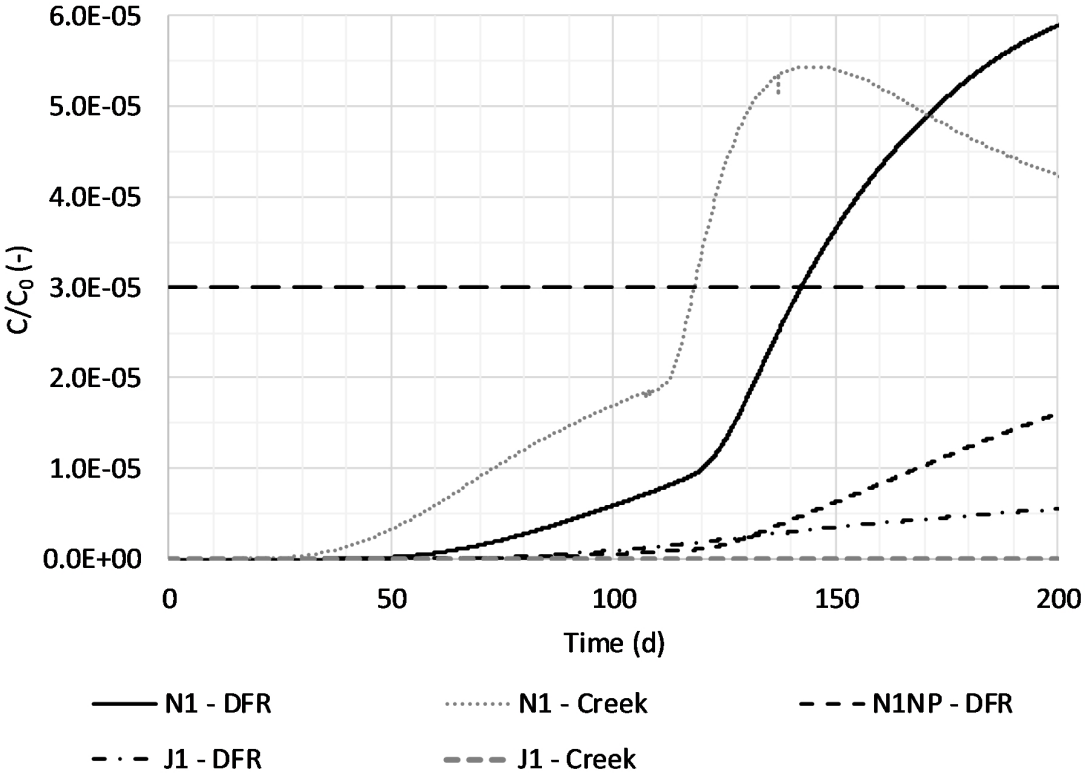


Figure 3.8: Solute breakthrough curves for the November (N1), November background (N1NP), and July (J1) event simulations. Simulation N1NP had no specified event ponding in the base of the topographic depression. The $C_{crit,rel}$ value related to the maximum $C_{sw}$ initial concentration is shown as a dashed horizontal line.

# Chapter 4
# Effects of spatial rainfall variability and actual evapotranspiration estimates on cumulative recharge and the sustainability of public supply wells

## 4.1 Introduction

Precipitation variability has the potential to significantly influence groundwater recharge within a watershed system and confound the estimation of the temporal and spatial recharge distribution for that watershed. As the largest component of the water budget, precipitation generates surface runoff, influences stream baseflow via recharge fluxes, is an important factor affecting the water available for actual evapotranspiration and storage within the subsurface reservoirs, and likely contributes most of the uncertainty in recharge within a water budget (Wiebe and Rudolph, 2020). Though spatial variations in precipitation have repeatedly been studied in streamflow models (Andréassian et al., 2001; Bell and Moore, 2000; Faurès et al., 1995; Obled et al., 1994; Zhao et al., 2013), few studies have looked at impacts on groundwater recharge. Sapriza-Azuri et al. (2015) showed that recharge rates could differ by a factor of 2 between simulations, if stochastic rainfall was applied at different spatial scales over several decades. Mileham et al. (2008) found that recharge rates calculated using a semi-distributed model for SW Uganda were highly sensitive to the precipitation interpolation method. Wiebe and Rudolph (2020) suggested that annual recharge rates could vary by up to 44% in short-term simulations (3 years) using a coupled and fully-distributed watershed model. However, general long-term linkages between the degree of spatial variability of precipitation and the associated potential variability of recharge rate estimates are poorly understood.

It is well known that there are relatively consistent spatial differences in annual precipitation at regional scales. For instance, lake-effect precipitation belts around the Laurentian Great Lakes have been studied by Veals and Steenburgh (2015) and Dewey (1973). Also, the dominant type of precipitation can vary in different areas. Convective rainfall affects smaller areas than frontal systems (Shook and Pomeroy, 2012), and storm track trends may lead to regional or even local differences. Orographic effects on rainfall patterns may be present in some regions, such as the central West Coast of North America (Dingman, 2015). Krajewski et al. (2003) studied the spatial correlation distances of rainfall at five different sites and found that three tropical sites with localized convective rainfall had much lower spatial correlation than two sites in the middle of the contiguous USA, where frontal

storms were more common. One of the main questions for groundwater management is this: at what scale do place-to-place differences in precipitation tend to average out over time such that it is reasonable to assume an average value for that region? Alternatively, at what scales do consistent patterns exist and define regions of microhydrology with observable differences in precipitation over the long term? Further, are precipitation characteristics within a watershed transitioning from being more uniform to more isolated, or vice versa, with climate change (e.g., Shook and Pomeroy, 2012)? A key unknown is whether there exists a spatial scale for a particular geographic region at which long-term average precipitation is sufficiently uniform to lead to minimal differences in recharge.

The existence of microhydrology regions with distinct precipitation signatures could occur in several ways. If precipitation processes are related to repeated patterns, such as storm track trend directions, then conceptualizing precipitation patterns in terms of "belts" could be promoted. However, if precipitation processes may be viewed as largely random, the effect of Poisson clustering could be invoked (Onof et al., 2000; Rodriguez-Iturbe et al., 1999). Poisson clustering describes the tendency of truly random data to contain clusters (Rosenthal, 2005). The idea here is that not only might storm cell development be viewed as a stochastic Poisson clustering process (e.g., Rodriguez-Iturbe et al., 1999), but also spatially variable rainfall trends themselves. Further, other factors could influence precipitation patterns. Urban areas could influence precipitation via a heat island effect, i.e., variations in the land surface thermal regime and wind speed changes due to urban development (Choi, 1998; Renard, 2017). Temporal cycles such as the El Nino-Southern Oscillation, North Atlantic Oscillation, Pacific-North America Oscillation, and North Pacific Oscillation also influence precipitation patterns by modifying the jet stream and storm tracks (Dingman, 2015).

Trends between watershed evapotranspiration and precipitation (P) have been found to exist despite variability in precipitation, geography, and spatial scale. The Budyko curve (Budyko, 1961) is a commonly used empirical tool for conceptualizing the relationship between the ratio of long-term average actual evapotranspiration ($\overline{AET}$) to long-term average total precipitation ($\bar{P}$) as a function of the long-term average index of aridity (Gentine et al., 2012). The index of aridity is the ratio of potential (reference) evapotranspiration ($\overline{PET}$ $or$ $\overline{ET_o}$) to $\bar{P}$. Though the curve was originally developed (Budyko, 1961) using 1,200 watersheds with areas > 1,000 km$^2$, in a different study it was shown to hold for more than 400 watersheds with sizes between 60 and 11,000 km$^2$ and is an example of a hydrological, empirical relationship whose causal mechanism is not completely understood (Gentine et al., 2012). The influence of actual evapotranspiration (AET) estimates on recharge rates is

often not considered, but it could be large because AET is frequently a large water budget component. Annual AET estimates could have uncertainty of ±10% (Kristensen and Jensen, 1975) or more.

AET estimates at the watershed scale over long time periods are difficult to obtain from in situ field sensors. AET methods such as Eddy covariance, Bowen Ratio Energy Balance, scintillometry, and weighing lysimetry have disadvantages such as requiring expensive field instruments, relying on complex data analysis, or having a lack of energy budget closure (Moorhead et al., 2017). Derived AET estimates at individual locations may not be representative of the entire watershed (e.g., Eddy covariance scale ~ $10^4$ $m^2$; Wilson et al., 2001) and may be prohibitively expensive to obtain by monitoring throughout a watershed. Relatively few watersheds have long-term AET estimates derived from such methods. The Budyko curve offers a simple, empirical method to estimate AET for many watersheds, if local measurements related to PET, P, and streamflow (Q) are available.

Sustainable groundwater management in a watershed context essentially involves an accurate historical and ongoing account of the dynamic components of the water budget. One of the main challenges is to quantify groundwater recharge, a vital component of the flow system that is too often solved for as the residual of a water budget (e.g., Wiebe and Rudolph, 2020). Recharge rates are an important factor influencing the dynamic spatial extent of well capture zones, the mass flux of non-point source contaminants to the water table, and the overall sustainability of wells and streams from a quantity perspective. Each of these three metrics – well vulnerability, water quality, and quantity – will be briefly described in the following.

Well vulnerability will be considered in this chapter to refer to the possibility for a well to capture non-point source contaminants, with emphasis on the total area of the land surface that could contribute contaminants to the well. This definition is a subset of the "intrinsic well vulnerability" term defined by Frind et al. (2006) because only the areal extent of the capture zone rather than the entire hydrogeologic pathway is considered, and specific contaminants are not considered. This capture zone area conceptually contributes recharge flux to the drawdown cone of a well pumping under steady state conditions. The delineation of capture zones always involves uncertainty (Martin and Frind, 1998). For example, Piersol (2005) found that three different sets of recharge and hydraulic conductivity distributions with similar degrees of calibration (base case, and upper and lower bounds on its ±95% confidence interval) in FEFLOW yielded different capture zones for a public supply well network in Panama. Total capture zone areas differed by ±30% from the base case, and areas without overlap were about 25% of the base case area. Similarly, Sousa et al. (2013a) found

that three different models of the same watershed, each with a similar degree of calibration, yielded dramatically different capture zones. The areas of the 50% probability of capture zone differed by about ±70% with respect to the simulation with the median area. Capture zones are an important tool for assessing the threats to a well due to land surface activities.

Contaminant migration and capture degrades well water quality and is frequently a major concern for managers of public supply wells. The legacy of non-point source contaminants such as agricultural nutrients and road salt applications can lead to decades of degradation of groundwater quality that threatens the viability of wells (e.g., Bester et al, 2006; Kent and Landon, 2013). Beneficial/best management practices (BMPs) are often developed using numerical models, where recharge rates are a critical factor for estimating mass loadings to the water table (e.g., Chesnaux et al., 2007; Hérivaux et al., 2013; Molénat and Gascuel-Odoux, 2002; Sousa, 2013). For example, Sousa (2013) investigated how nitrate loadings at the water table could vary based on spatially distributed, field-derived, recharge estimates. The level of uncertainty associated with recharge rates may affect the prediction of BMP efficacy (Sousa, 2013), and spatial variations in precipitation are generally not considered. Point source contaminant transport models could be impacted also. Parker et al. (2007) concluded that data from a limited number of weather stations were insufficient to model the dynamic impacts of rainfall on pesticide contamination. The degree to which loadings estimates could vary based on weather station network input data is unknown.

Total recharge within a watershed is important from a broad sustainability perspective (Bruce et al., 2009; Devlin and Sophocleous, 2005). It is an important factor related to the quantity of groundwater and magnitudes of hydraulic gradients that sustain baseflow to streams and replenish amounts extracted for public water supply and irrigation. Total recharge impacts contaminant mass loadings, which influence the concentrations experienced at a well, water treatment, and the exposure time of wells to contaminants (Frind et al., 2006). Variation in recharge may lead to changes in capture zone areas for wells, thus affecting management decisions regarding which land use activities potentially have an impact, and which contaminants are at risk of being captured by the well.

The objective of this study was to quantify the variability of metrics related to well vulnerability, water quality, and overall water quantity in terms of their relation to rainfall and AET variability via recharge rate estimates at the watershed-scale and over a long time period. The results of a short-term, local rainfall variability analysis were projected to multiple decades in order to assess the impact of this variability on the range of possible recharge rates in a typical watershed. A vadose zone water

budget equation was rearranged to solve for cumulative recharge as a function of: P over the watershed, AET estimated from the Budyko curve, and the average surface water component of streamflow. Thousands of random 46-year rainfall time series were generated for virtual stations near the watershed in order to assess a likely range in cumulative recharge estimates. Each realization consisted of three rainfall time series and was assigned annual values of random AET estimates that were normally distributed about the Budyko curve, based on observed variations across 45 US MOPEX (Duan et al., 2006) watersheds having $\overline{PET}/\bar{P}$ ratios similar to the ratio for Alder Creek. It was hypothesized that variability in average recharge among the set of realizations would be non-trivial despite the spatial and temporal averaging of precipitation over the watershed. It was also hypothesized that precipitation would be the dominant contributor to recharge variability when compared to AET because precipitation is a larger component of the water budget. The rainfall time series were selected based on spatial correlation analysis among local weather stations. The average and quantiles outlining the 95% confidence interval from the distribution of cumulative recharge estimates were used to provide a sense of the sensitivity of capture zone areas, non-point source loading estimates, and total recharge to spatial rainfall and watershed AET variability.

## 4.2 Methods

### 4.2.1 Field Site

Alder Creek is a tributary to the Nith River within the Grand River basin (6,800 km$^2$; OMNRF, 2016). The Alder Creek watershed has an area of 78 km$^2$ and is located on the Waterloo Moraine outside of Kitchener-Waterloo, Ontario (Figure 4.1). The Waterloo Moraine consists of inter-bedded sand/gravel layers and silt/clay layers, resulting in a complex stratigraphic system with discontinuous aquifers and aquitards (Bajc et al., 2014; Martin and Frind, 1998). Groundwater recharge to the underlying glaciofluvial aquifers in the watershed provides source water to about seven well fields operated by the Regional Municipality of Waterloo (Brouwers, 2007). An estimated 108 mm per year is pumped by the wells located directly within the watershed (Matrix and SSPA, 2014b). Land use in the watershed is predominantly agricultural (ROW 2010) and coarse-grained sand and gravel deposits are present at the ground surface over about half of the watershed area (OGS, 2010). Total average annual precipitation in the area is around 900 mm per year, with 15% snow on average (Roseville Environment Canada weather station; AquaResource, 2008; Government of Canada, 2019; OMNR,

2007). PET at this station is around 780 mm per year on average, as estimated using the Penman-Monteith method (UNFAO56 ETo Calculator; Raes, 2009) based on daily minimum and maximum temperatures (Government of Canada, 2019) and local wind speed measurements (Wiebe et al., 2019; SOWC weather stations, Figure 4.1; Appendix A; Appendix C). Total streamflow at the Water Survey of Canada (WSC) gauge in the middle of the watershed equates to 140.5 mm per year on average for the area upstream of the gauge (Figure 4.1; WSC, 2019). However, the lower reaches of the creek downstream of the WSC gauge are thought to receive more groundwater discharge than the upper reaches due to the lowering of the water table by the public supply wells in the north and mid-east of the watershed (CH2MHILL and SSPA, 2003). The issue of anthropogenic modifications to the watershed is discussed below.

A network of six local rain gauge stations (WS2 to WS7; Figure 4.1) was installed in and around the watershed by the Southern Ontario Water Consortium (SOWC) to provide greater resolution on rainfall amounts in the area. Rainfall data (Wiebe et al., 2019) were recorded via tipping bucket rain gauges surrounded by Alter-type wind screens. Data were collected from 2014 to 2016 on a 15 min time scale and were aggregated up to daily scale for the correlation analysis described below. Snowfall was not recorded continuously at these stations, so annual sums of the daily snowfall amounts from the Roseville weather station were used (Government of Canada, 2019). Infrequent manual measurements of snowpack thickness near WS4 were within 2 cm of the Roseville measurements (Government of Canada, 2019), and the average difference between Roseville measurements and the average from sonic snow depth readings at all six local stations (Wiebe et al., 2019) was 2.0 cm during the 2014 to 2015 winter season (Nov 2014 to Mar 2015; Appendix D).

This watershed has been modelled many times because of its importance for water supply (e.g., CH2MHILL and SSPA, 2003; Martin and Frind, 1998; Matrix and SSPA, 2014a, 2014b; Sousa et al., 2013a). The current study seeks to build upon previous work by assessing the ranges of plausible variations in rainfall and AET across the watershed and the resulting long-term recharge variability. An increased understanding of the uncertainty of recharge estimates could assist groundwater management in the area with respect to the three management metrics.

### 4.2.2 Analysis

The overall idea for this analysis was to quantify the variability of groundwater recharge based on spatial variation in rainfall and uncertainty in watershed AET estimates via a Monte Carlo framework involving: the generation of thousands of rainfall time series constrained by observed spatial correlation statistics, AET estimates based on the Budyko curve, calculation of the total recharge over several decades, and the estimation of several metrics related to sustainable groundwater management. Rainfall time series were selected from randomly generated time series based on the criterion that daily rainfall spatial Spearman Rank Correlation coefficients were within the range observed among seven weather stations within 3 km of the watershed (six local rain gauges and one national station). The generation of rainfall time series was performed using a parametric approach based on mixed exponential distribution (e.g., Li et al., 2013) fitting to both the observed rainy day spacing and observed rainfall amounts (Appendix N). The range of Spearman coefficients was developed based on the observed daily rainfall rates for the years 2014 to 2016. Scripts (Appendix O) were written for the scientific computation program GNU Octave (Eaton et al., 2011) to perform the calculations for the stochastic water budget analysis.

Both parametric and non-parametric approaches have been used for stochastic rainfall generation (Basinger et al., 2010; Sharma and Mehrotra, 2010). Both types of approaches construct a sequence of rainy and non-rainy days and then generate rainfall amounts for the rainy days (e.g., Lall et al., 1996; Sharma and Mehrotra, 2010). Parametric approaches have the advantages of being simple (Wilks, 1998) and applicable to ungauged locations in sparse data situations (Sharma and Mehrotra, 2010), and the disadvantage of being somewhat less portable than non-parametric approaches (Basinger et al., 2010). Fitting of one of several distributions (e.g., exponential, gamma, Weibull) to the observed rainfall probability distribution is required for parametric models (Vu et al., 2018). Non-parametric approaches do not make assumptions about the statistics of local rainfall, but it is difficult to find an approach that performs well across different climates (Vu et al., 2018). Such approaches typically rely on Markov chain models for the spacing between rainy days (Lall et al., 1996). Non-parametric approaches such as the Neyman-Scott Rectangular Pulse method (Camici et al., 2011, 2014) may employ seasonal statistics derived from observation data. Non-parametric models tend to resample observed rainfall data and thus restrict amounts to those in the historical record (Basinger et al., 2010). The present study selected a parametric approach for simplicity, acknowledging that transferring the approach to another site would require fitting a local rainfall probability distribution for that context. Obtaining rainfall spatial correlation similar to the observed across multiple sites was

accomplished by adjusting the order of rainfall events in the random time series, following the method used by Tarpanelli et al. (2012), which was based on Iman and Conover (1982). Testing conducted by modifying a non-parametric approach (a single site Neyman-Scott Rectangular Pulse method; Camici et al., 2011, 2014) resulted in an underestimate of observed mean annual rainfall by ≥ 25 mm and was rejected in favour of the parametric approach described below.

#### 4.2.2.1 Water Budget

The first step of the analysis employed in the present study was to derive an equation to estimate long-term recharge rates from a combination of measured and stochastic hydrological data. Many studies have used a water budget approach coupled with stochastic methods to estimate recharge (e.g., Baalousha, 2009; Crosbie et al., 2018; Scibek and Allen, 2006; Sene, 1996). Consider a vadose zone (VZ) water budget for the watershed region between the ground surface and the water table (Eqn. 4.1):

$$\Delta S_{VZ} = I - AET_{VZ} - R, \tag{4.1}$$

where $\Delta S_{VZ}$ is storage change in the vadose zone, $I$ is infiltration (the difference between precipitation and overland flow: $I = P - Q_{OL}$), $AET_{VZ}$ is actual evapotranspiration from the vadose zone, and $R$ is recharge flux across the water table. All terms have units of $L^3/L^2$, i.e., length corresponding to a unit area. Substituting for $I$ and rearranging for recharge (Eqn. 4.2):

$$R = P - AET_{VZ} - Q_{OL} - \Delta S_{VZ}. \tag{4.2}$$

This water budget could assume that all recharge occurs following drainage through the vadose zone, and that exchange flux (indirect recharge, $IR$) from surface water bodies to the water table is negligible. Alternatively, $Q_{OL}$, which is stream runoff excluding groundwater baseflow, could be interpreted as the net overland flow into the stream, i.e., $Q_{OL,net} = Q_{OL,Total} - IR$, and the vadose zone drainage assumption would not be necessary. Assuming that steady state conditions are approximated within the watershed after multiple decades, and that the cumulative storage changes approach zero (Eqn. 4.3):

$$R_{tot} = \sum_{yr=1}^{n}\left(P_{yr} - AET_{VZ,yr} - Q_{OL,yr}\right), \quad (4.3)$$

where $R_{tot}$ is the total, cumulative recharge over the watershed over $n$ years, and $yr$ is the index of the year. Re-writing in terms of the ratio of $AET_{VZ}/P$ and expressing the overland flow fraction of total runoff in terms of the baseflow index (BFI) (Eqn. 4.4):

$$R_{tot} = \sum_{yr=1}^{n}\left(P_{yr} - P_{yr}\left(\frac{AET_{VZ,yr}}{P_{yr}}\right) - \left(1 - BFI_{yr}\right)Q_{tot,yr}\right), \quad (4.4)$$

where all terms relate to the watershed overall, $AET_{VZ,yr}/P_{yr}$ may be generated from $AET_{tot}/P$ ratios estimated based on the Budyko curve (e.g., Gentine et al., 2012) and observed variation about it (discussed further below), $BFI_{yr}$ is an annual estimate of baseflow index derived from the WSC stream gauge within the watershed, and $Q_{tot,yr}$ is an estimate of the total annual streamflow (baseflow plus overland flow) that is derived from the measured streamflow at the WSC stream gauge and a scaling factor to account for the ungauged area below the gauge. The precipitation term ($P_{yr}$) here is the annual average precipitation for the watershed that is calculated as the sum of observed snowfall and the weighted average of stochastic rainfall time series. This method assumes the following:

1) Vadose zone storage change over the $n$ years is zero;
2) a time period of $n$ years is sufficient to capture the variability in PET estimates;
3) the watershed is close to its natural state and anthropogenic influences are minor, justifying the use of the Budyko curve to estimate $\overline{AET_{tot}}/\bar{P}$;
4) variation in $AET_{tot,yr}/P_{yr}$ ratios are reasonably represented by normally distributed values about the mean value from the Budyko curve (Gentine et al., 2012) and the maximum standard deviation with respect to the curve for 45 watersheds in the US MOPEX dataset (Duan et al., 2006) with $\overline{PET}/\bar{P}$ ratios similar to (within ±0.05 of) the ratio for Alder Creek;

5) $AET_{VZ}/P$ may be estimated from Budyko curve estimates of $AET_{tot}/P$ values by applying $\overline{PET}$ within the areas of the watershed where the water table is at or close to ground surface (areas mapped as bog, marsh, open water, or swamp; OMNR, 2008; ROW, 2010) and deriving an estimate for a correction factor representing the ratio $\overline{AET_{VZ}}/\overline{AET_{tot}}$ (Appendix P);
6) total streamflow estimates for the watershed outflow may be derived from measurements at the WSC gauge (Figure 4.1) within the watershed and a scaling factor relating watershed outflow to gauged streamflow, based on long-term estimates (Appendix Q);
7) annual BFI values derived from measurements at the WSC gauge are representative for Alder Creek overall; and
8) snowfall is reasonably uniform over the watershed and surrounding area, justifying use of nearby Roseville measurements.

Under these assumptions, Eqn. 4.4 may be used in the context of a stochastic analysis of different rainfall time series interpolated over a watershed, coupled with stochastic AET estimates for the watershed overall.

#### 4.2.2.2 Spatial correlation and stochastic rainfall

The second step in the analysis was to calculate the range of observed spatial correlation coefficients among daily rainfall totals for six local weather stations (five within the Alder Creek watershed, and one < 0.5 km outside) and the Roseville national weather station (< 3 km outside the watershed). The Pearson Product-Moment Correlation coefficient and the Spearman Rank Correlation coefficient were calculated, and the Spearman coefficient was selected for estimation of the observed correlation range because of the non-normality of the rainfall data (e.g., Gibbons and Chakraborti, 1992; Villarini et al., 2010).

The third step in the analysis involved the generation of 19,761 daily rainfall time series of 46 years in length. Stochastic models have been employed often in the analysis of rainfall (e.g., Wilks and Wilby, 1999). The total length of the time series (46 years) was selected based on the amount of data available for the Roseville national weather station (AquaResource, 2008; Government of Canada, 2019; OMNR, 2007). Daily time series for 46 years were generated based on a parametric approach that employed mixed exponential models for the probability distributions of both the observed spacing between rainy days and observed rainfall amounts (Government of Canada, 2019) at the Roseville Environment Canada weather station. The mixed exponential model was (Li et al., 2013):

$$f(x) = \frac{p}{\beta_1}\exp\left(\frac{-x}{\beta_1}\right) + \frac{1-p}{\beta_2}exp\left(\frac{-x}{\beta_2}\right), \quad (4.5)$$

where $f(x)$ is the relative frequency (probability), $x$ is either a time interval between days with rain or a daily rainfall depth, $p$ is the mixing probability ($0 \leq p \leq 1$), and $\beta_1$ and $\beta_2$ are the scale parameters ($\beta_i > 0$) for two different exponential distributions. This approach is similar to the one presented by Rodriguez-Iturbe et al. (1999), except that a mixed exponential model was used instead of an exponential model. A mixed exponential model has the advantage of representing both large and small extremes of the range of rainfall amounts (Li et al., 2013; Wilks, 1998). The values of $p$, $\beta_1$, and $\beta_2$ for the time intervals between rainy days were determined by fitting the probability distribution of gaps (number of days) between rainy days using the Levenberg-Marquardt algorithm (Gavin, 2009, 2019) in the scientific computation program GNU Octave (Eaton et al., 2011) to solve for these parameters. The values of $p$, $\beta_1$, and $\beta_2$ for the probability distribution of daily rainfall depths were estimated in the same way, where rainfall depths were binned by integer values (e.g., the bin for 1 mm included all rainfall amounts, $r$, such that 0 mm $< r \leq 1$ mm, etc.). Time intervals between rainy days and rainfall depths were generated randomly via (Li et al., 2013):

$$x_t = -\beta_t \ln(v_t), \quad (4.6)$$

where $x_t$ is either the time interval or the rainfall amount at time $t$, $\beta_i$ is either $\beta_1$ or $\beta_2$ for the respective distribution (chosen with probability $p$ for the respective distribution), and $v_t$ is a uniform

random number ($0 < v_t < 1$). Appendix N shows the observed (Government of Canada, 2019) probability distributions of time intervals and rainfall depths.

Spearman spatial correlation coefficients were verified to be within the observed range as follows. Sets of six random rainfall time series were adjusted based on the Iman and Conover (1982) method to ensure similarity (Tarpanelli et al., 2012) with the observed Pearson and Spearman correlation matrices. This was conducted using 3- or 4-year subsets of six random time series plus the Roseville time series for consistency with the length of the observed rainfall records (3 years), from which the observed correlation matrices were calculated. Sets of six time series were processed in association with the Roseville observed time series because the Iman and Conover (1982) method required correlation matrices of the same size as the observed matrix (7 x 7). Maximum and minimum Spearman coefficients for the adjusted six random time series were assessed for each 3- or 4- year subset and sets of three time series with coefficients within the observed range were selected.

Next, the Alder Creek watershed was divided into three Thiessen polygon regions (Areas 1 to 3; Figure 4.1), which were drawn for three rain gauge locations (WS5, WS3, and WS7). Each polygon was assigned a virtual rain gauge ("VS1", "VS2", and "VS3"; Figure 4.1), to which stochastic rainfall time series were assigned. Total precipitation was calculated for each station for each year by adding the sum of observed daily Roseville snowfall amounts (Government of Canada, 2019) to the sum of the random daily rainfall amounts for that year. The average precipitation over the watershed was calculated via Thiessen polygon area weighting of the random rainfall time series for each year (Eqn. 4.7):

$$P_{WS,yr} = \sum_{VS=1}^{3} P_{VS,yr} \cdot w_{VS}, \tag{4.7.1}$$

$$w_{VS} = \frac{A_{VS}}{A_{WS}}, \tag{4.7.2}$$

$$P_{VS,yr} = (rain_{VS,yr} + snow_{Roseville,yr}), \tag{4.7.3}$$

where $P_{WS,yr}$ is the average over the entire watershed for year $yr$, $VS$ is the virtual station, $w_{VS}$ is the weight of the virtual station, $A_{VS}$ is the area of the Thiessen polygon for virtual station $VS$, $A_{WS}$ is the overall watershed area, $rain_{VS,yr}$ is the sum of rainfall amounts in the random time series for virtual

station $VS$ for year $yr$, and $snow_{Roseville,yr}$ is the sum of snowfall amounts for the Roseville weather station for year $yr$.

#### 4.2.2.3 AET and Streamflow

Estimates of the annual ratios of $AET_{tot,yr}/P_{WS,yr}$ were obtained from the scatter of observed points around the Budyko curve (Gentine et al., 2012) for 45 US MOPEX watersheds (Duan et al., 2006; Appendix N) similar to Alder Creek for each realization. Similarity was defined as $\overline{PET}/\bar{P}$ within ±0.05 of the ratio derived from the Roseville Environment Canada weather station. $PET_{yr}$ values for the Roseville station were calculated via the Penman-Monteith method (Allen et al., 1998) from the maximum and minimum daily temperatures (Government of Canada, 2019) using the UNFAO56 ETo Calculator (Raes, 2009), where the average wind speed from seven local weather stations over four years was employed (Appendix A; Wiebe et al., 2019). Random $AET_{tot,yr}/P_{WS,yr}$ values were selected from a normal distribution of AET/P ratios about a mean value from the Budyko curve calculated for the $PET_{yr}/P_{WS,yr}$ ratio for the realization. The standard deviation describing this normal distribution was estimated as the maximum value derived from the 45 MOPEX watersheds (Duan et al., 2006) similar to Alder Creek. This process attempts to capture the potential variability in the annual scatter of points about the Budyko curve. Appendix N illustrates the variation of annual AET/P ratios about the Budyko curve for the 45 MOPEX watersheds.

Sensitivity to the AET correction factor for areas where the water table is close to ground surface was tested by adjusting the correction factor, $\overline{AET_{VZ}}/\overline{AET_{tot}}$, by its estimated uncertainty (Appendix P). Calculations were also performed for an alternative scenario that employed the $AET_{tot,yr}/P_{WS,yr}$ ratio directly from the Budyko curve with no random component in order to assess the variability in recharge rates associated solely with precipitation variability.

The annual BFI values for the creek were estimated based on PART (Barlow et al., 2015) hydrograph separation analysis of daily WSC streamflow data (1973 to 2018; WSC, 2019) from the gauge within the Alder Creek watershed. Because the WSC gauge is not located at the outflow of the creek into the Nith River, a scaling factor was derived from long-term water budgets (Appendix Q) to estimate annual total streamflow at the outflow.

Finally, total recharge was calculated via Eqn. 4.4 for each set of three selected rainfall time series. The total number of realizations was determined from the stability of the average recharge over all realizations and the following three water quality, well vulnerability, and water quantity metrics, where stability was defined as the absolute value of average percent change in metric < 0.1% with an additional 400 realizations.

### 4.2.3 Water quality implications in terms of non-point source contamination

Results of the recharge analysis were used to evaluate potential differences in non-point source mass loadings estimates due to rainfall and AET variation. Bekeris (2007) defines mass flux as (Eqn. 4.8):

$$Flux = C_{aq,avg} \cdot R, \tag{4.8}$$

where $Flux$ is the contaminant (e.g., nitrate) mass flux, $C_{aq,avg}$ is the average aqueous concentration below the root zone, and $R$ is the recharge rate. This equation could be applied to different agricultural nutrient or road salt application areas within the watershed to describe the spatial variation. The contaminant concentrations below the root zone were assumed to be the same for source areas in the present study, and average recharge rates for the watershed were assumed representative. Because the mass flux is directly proportional to the recharge rate, the maximum annual percentage difference in non-point source mass flux to the water table within the watershed was estimated via (Eqn. 4.9):

$$PDMF = \pm \frac{max\{|Q_{Ravg}(p) - \bar{R}|\}}{\bar{R}}, \tag{4.9}$$

where $PDMF$ is the percent difference in mass flux, $Q_{Ravg}(p)$ is the $p^{th}$ quantile of the probability distribution of average recharge ($Ravg$) over all realizations, $p$ is the probability of one of the bounds of a 95% confidence interval (2.5% or 97.5%), and $\bar{R}$ is the average annual recharge over all realizations. The overbar indicates an overall average. The worst case $PDMF$ was thus approximated by the maximum absolute difference between the average and either the 0.025- or 0.975-quantile.

### 4.2.4 Well vulnerability implications in terms of capture zone variation

Well vulnerability was assessed based on the possible range of capture zone areas, which were assumed to vary with the watershed's average recharge rate due to rainfall and AET variation. Assuming steady state conditions (Sousa, 2013),

$$\overline{Q_{well}} = \overline{R_{cap\ zone}} \cdot A, \tag{4.10}$$

where $\overline{Q_{well}}$ is the average pumping rate at a well and $\overline{R_{cap\ zone}}$ is the average recharge rate within a capture zone of area $A$. Using the average recharge and the bounds on the 95% confidence range of average recharge rates, the maximum difference in area was estimated via (Eqn. 4.11):

$$\bar{A} = \frac{\overline{Q_{well}}}{\bar{R}}, \text{ and} \tag{4.11.1}$$

$$\text{PDA} = \pm \frac{\max\left\{\left|\bar{A} - \overline{Q_{well}}/Q_{Ravg}(p)\right|\right\}}{\bar{A}}, \tag{4.11.2}$$

where $\bar{A}$ is the average area calculated based on the average annual recharge over all realizations ($\bar{R}$), $Q_{Ravg}(p)$ is the $p^{\text{th}}$ quantile of the probability distribution of average recharge ($Ravg$) over all realizations, $p$ is the probability of one of the bounds of a 95% confidence interval (2.5% or 97.5%), and *PDA* is the percent difference in capture zone area, relative to the average area. Average annual recharge rates within the theoretical capture zone were thus assumed equal to watershed average recharge rates. This assumption is a less robust estimate than using a local average recharge rate for a well capture zone, but it provides a simple estimate where quantifying local average recharge would be a more complex task involving 3D numerical modelling of the watershed. *PDA* was calculated for the watershed's largest public supply well's average pumping rate ($\overline{Q_{well}}$ = 6,756 $m^3$/d; CH2MHILL and SSPA, 2003) over 46 years.

### 4.2.5 Water budget implications due to water quantity uncertainty

Water quantity was assessed by comparing the cumulative recharge totals between the 95% confidence bounds of the probability distribution of total recharge over all realizations:

$$Difference_{Rt} = Q_{Rt}(0.975) - Q_{Rt}(0.025), \quad (4.12.1)$$

$$Avg\ Annual\ Difference_{Rt} = \frac{Difference_{Rt}}{n}, \quad (4.12.2)$$

where $Rt$ is the probability density function of all $R_{tot}$ values over all realizations, and $n$ is the total number of years considered (i.e., 46). The ratio between the maximum and minimum 95% confidence bounds of the $R_{tot}$ distribution was also calculated:

$$Ratio_{Rt} = Q_{Rt}(0.975) / Q_{Rt}(0.025). \quad (4.13)$$

This approximates the worst-case scenario for variability resulting from both rainfall and AET variation. The same calculations were performed for the case of solely rainfall variation when $\overline{AET_{tot}}/\overline{P_{WS}}$ estimates were restricted to the Budyko curve.

## 4.3 Results

The results of the spatial correlation analysis of the observed daily rainfall amounts are shown in Figure 4.2. Spearman spatial correlation coefficients for the seven rainfall stations varied between 0.5 and 0.8. This range in observed coefficients was used to constrain the selection of sets of random time series for the virtual stations. For context, if Pearson Product-Moment Correlation among the Alder Creek rain gauges is compared with the few rainfall correlation studies available in the literature, Alder Creek rainfall is better correlated than rainfall in Florida and Brazil, where intense, convective storms are prevalent (Krajewski et al., 2003), and less well correlated than rainfall in Oklahoma (Villarini and Krajewski, 2007), where frontal rainfall is more common. Alder Creek would be expected to experience a mix of convective and frontal storm systems in the southern Ontario climatic context (e.g., Paixao et al., 2015).

Baseflow separation performed using the PART program (Barlow et al., 2015) on WSC data (WSC, 2019) from a gauge within the Alder Creek watershed (Figure 4.1) yielded a range of BFI values from 0.37 to 0.72 with a mean value of 0.56. Because the creek has been hypothesized to receive increased baseflow into its lower reaches below the WSC gauging station (CH2MHILL and

SSPA, 2003), the average value seems reasonable when compared with the minimum estimate from the Upper Grand River basin (0.6) in a study by Neff et al. (2005). The average annual streamflow for the watershed, $\overline{Q_{tot}}$, was estimated to be 216 mm based on the average total streamflow of 140.5 mm derived from the daily WSC gauge data (WSC, 2019) and long-term water budget component estimates (Appendix Q). The scaling factor for streamflow was 1.54 (Appendix Q).

Figure 4.3 shows the evolution of the water quality, vulnerability, and quantity metrics as the number of realizations increased. The total number of realizations was 16,778, each with a corresponding set of three selected time series for the virtual stations and one time series of watershed $AET_{VZ}$ estimates. The four stability metrics ($\bar{R}$, $PDMF$, PDA, and $Ratio_{Rt}$) met the stability criterion by the total number of realizations (where absolute percent change in each metric was < 0.1% for an additional 400 realizations).

The observed mean total precipitation (AquaResource, 2008; Government of Canada, 2019; OMNR, 2007) and standard deviation at the Roseville station from 1973 to 2018 (Figure 4.4b) were 907 mm and 119 mm, respectively, and the simulated mean annual watershed-averaged precipitation over all realizations was 898 mm, with a standard deviation of 102 mm (Figure 4.4c; Table 4.1). Thus, the magnitude of the average simulated watershed rainfall underestimated the observed average by 9 mm. The observed precipitation at Roseville ranged from 650 to 1140 mm per year (AquaResource, 2008; Government of Canada, 2019; OMNR, 2007), and the simulated (interpolated) annual total precipitation ranged from 707 to 1107 mm over the 95% confidence interval. Mean annual total precipitation values for the individual virtual stations ranged from 649 to 1181 mm over the 95% confidence interval, and their standard deviations each rounded to 136 mm. Figure 4.4a shows an example for VS1; all frequency distributions for the virtual stations were similar. Interpolating annual total precipitation over the watershed resulted in a reduction in range of 25%, compared to the annual ranges at the virtual stations. Averaging simulated total precipitation for the watershed over 46 years resulted in a much smaller 95% confidence range (873 to 923 mm, with a standard deviation of 13 mm; Figure 4.4d).

Figure 4.5 shows the AET estimates derived from the PET values calculated for Roseville and those simulated. $\overline{AET_{VZ}}/\overline{P_{WS}}$ ratios within the 95% confidence interval varied between 0.54 and 0.62, after applying the correction to remove saturated zone AET. The mean ratio of $\overline{AET_{VZ}}/\overline{P_{WS}}$ for the watershed was 0.58, i.e., 9% less than the long-term estimate (0.64) based on locally measured wind speed and Roseville temperature data due to the correction for saturated zone AET. The area of the

watershed covered by wetlands and other features where the water table was expected to be at or close to ground surface was 7% of the total area (OMNR, 2008; ROW, 2010). The $\overline{AET_{VZ}}/\overline{AET_{tot}}$ correction factor was calculated to be 0.91 ±0.02 by applying $\overline{PET}$ to 7% of the watershed area (Appendix P). The standard deviation of $\overline{AET_{VZ}}/\overline{P_{WS}}$ was calculated to be 0.02, and the 95% confidence interval for the magnitude of $\overline{AET_{VZ}}$ varied between 490 and 558 mm, with a mean value of 524 mm (Table 4.1). The standard deviation of $\overline{AET_{VZ}}$ was 17 mm.

Figure 4.6 shows the frequencies of the calculated recharge estimates over all realizations. The average annual recharge over all realizations' averages was 282 mm, and the 95% confidence interval for average recharge ranged from 244 to 321 mm; the standard deviation of average recharge was 20 mm (Table 4.1). These averages were within the range of recharge estimates from previous numerical modelling studies (210 mm – CH2MHILL and SSPA, 2003; 321 mm – M.H. Brouwers, pers. comm., 2017, Matrix and SSPA, 2014a).

The implications of the recharge rate variation due to rainfall and AET variability for the three metrics introduced above are summarized in Table 4.1. Concerning water quality related to non-point source loadings, cumulative differences in mass loadings based on average recharge rates in different scenarios were at worst ±14% different from the average loadings. Regarding well vulnerability, the overall capture zone area for the public supply well was estimated to be 8.74 km$^2$ based on the average annual recharge rate (282 mm). This capture zone area could change by ±1.35 km$^2$ from the annual average in the worst case (Table 4.1). This implies that uncertainty of up to ±15% per year could potentially be associated with capture zone areas due to the combination of spatially variable rainfall and variable AET over several decades. In terms of water quantity, the 95% confidence range in average annual recharge was 77 mm, and cumulative recharge totals over 46 years could differ by up to a factor of 1.31 (Table 4.1). If the impacts of solely the variability of rainfall were considered and $\overline{AET_{tot}}/\overline{P_{WS}}$ estimates were not allowed to deviate from the Budyko curve prior to being adjusting by the AET correction factor (Appendix N), then the difference in mass loadings was ±7.0%, the difference in capture zone area was ±7.4%, average recharge (95% confidence) ranged from 260 to 299 mm, and the ratio of maximum to minimum cumulative recharge was 1.15. Thus, the inclusion of $AET_{tot}$ deviation from the Budyko curve led to a 95% confidence range in recharge (77 mm) that represents 24% of previously estimated steady state recharge (321 mm; M.H. Brouwers, pers. comm., 2017; Matrix and SSPA, 2014a), while solely accounting for rainfall variability led to a

range (39 mm) representing 12% of this. This suggests that spatial rainfall variability and AET uncertainty contribute approximately equal portions to the recharge variability.

The sensitivity of the results to the AET correction factor during the case where the $AET_{tot}/P_{WS}$ estimates were allowed to deviate from the Budyko curve was tested by adjusting the calculated factor of 0.91 by its estimated uncertainty, ±0.02 (Appendix P). A factor of 0.89 produced differences in mass loadings of ±13%, differences in capture zone area of ±15%, and a cumulative recharge ratio of 1.29, while a factor of 0.93 produced differences in mass loadings of ±15%, differences in capture zone area of ±17%, and a cumulative recharge ratio of 1.34. Thus, results were not highly sensitive to the vadose zone correction factor (differences ≤ ±2%). Recharge variability was insensitive to changes in total streamflow.

## 4.4 Discussion

The approach used in the present study applies a new combination of existing ideas using stochastic generation of both rainfall and AET estimates based on the Budyko curve to project watershed scale recharge rates, estimating the surface water fraction of total streamflow via baseflow index, and then applying these to estimate uncertainty in non-point source loadings and capture zone areas. Advantages of this approach include that it is flexible, applicable to the long-term, is at the watershed scale, and does not require complex geological information or hydraulic head measurements – although this latter information can be useful to generate complementary estimates via numerical simulations. The following discusses the methodology and the three management metrics.

AET is the second largest water budget component in this type of setting, and it is difficult to measure or estimate (Hess et al., 2016). AET also has a large impact on recharge rate estimates, similar to the precipitation component. The Budyko curve may be a useful tool for estimating long-term $\overline{AET}/\bar{P}$ ratios, but guidance is needed on two issues. Because the water budget applied in the present study was conducted for the vadose zone, modifications were necessary to estimate and remove the saturated zone AET component. The method of applying $\overline{PET}$ to regions where the water table is known to be at or near ground surface (e.g., wetlands, and open water) was a rough estimate. Modifying the AET correction factor by ±0.02 resulted in changes of ≤ ±2% in terms of mass loadings, capture zone area, and cumulative maximum to minimum recharge ratio. Thus, the results are not very sensitive to the calculated AET correction factor in this case. It is unknown whether this

would be similar for other watersheds. Second, the variability of the $\overline{AET_{tot}}/\bar{P}$ ratio with respect to the average, long-term $\overline{PET}/\bar{P}$ ratio requires further study. The use of the scatter of points about the Budyko curve from the analysis of the MOPEX data (Duan et al., 2006) was based on watersheds in other geographical contexts with $\overline{PET}/\bar{P}$ ratios similar to Alder Creek and verification is needed to determine the possible variation for a specific watershed.

The use of the Budyko curve required the assumption that Alder Creek behaves similarly to the watersheds employed in its development. This entailed assuming that the watershed exchanges a negligible net flow of groundwater with adjacent basins, and that it has experienced minimal human influence (i.e., no significant alterations such as irrigation or reservoirs – Gentine et al., 2012). While maintaining about 70% agricultural land use, the Alder Creek watershed contains some other development in terms of small urban communities (6% by area) and aggregate (sand and gravel) extraction pits (3% by area; OMNR, 2008; ROW, 2010). These gravel pits are expected to facilitate recharge rates that are a relatively larger proportion of total precipitation than in other areas because of the coarse nature of the sediments and the lack of vegetation (Matrix and SSPA, 2014b). Alder Lake, a small reservoir within the watershed, has a spill-over dam and is not considered to constitute a significant anthropogenic change to the watershed (CH2MHILL and SSPA, 2003). Historical pumping within the watershed has lowered the water table in places and may have indirectly influenced AET rates. Whether there is a net flow of groundwater into or out of the watershed is not known. Overall, the $\overline{AET}$ values for the watershed are likely to be lower than they would be in an undeveloped, naturally vegetated watershed.

The replacement of natural vegetation with agricultural crops is likely the largest anthropogenic change to the watershed. Zhang et al. (2001) provide equations for curves similar to the Budyko curve for different vegetation types. Their curves are adjusted by a plant-water availability factor, w, which was proposed to be w = 2.0 for forest and w = 0.5 for pasture/grassland. A value of w = 1.0 was chosen arbitrarily for mixed-vegetation type watersheds (Zhang et al., 2001). For the long-term $\overline{PET}/\bar{P}$ ratio from Roseville, the use of the Zhang et al. (2001) equation with w = 0.5 leads to an $\overline{AET}/\bar{P}$ ratio that is 13.6% less than the value noted above (0.64). This magnitude of change, if applied to the long-term $\overline{AET}$ estimate results in a significant increase in recharge. $\bar{R}$ = 350 mm for w = 0.5, using long-term estimates in the water budget. This seems unreasonable because the previous steady-state Alder Creek modelling studies have estimated $\bar{R}$ to be between 210 and 321 mm. If w = 1.0, the resulting long-term $\overline{AET}/\bar{P}$ ratio would be 3.6% less than the estimate derived in the present

study. This w value would lead to an estimate of $\bar{R}$ of 298 mm. A value of w somewhere between 0.5 and 2.0 seems logical for Alder Creek, a mixed vegetation type watershed, where the lower value of w = 0.5 seems unreasonable and the watershed is only 10% forest. A value of w = 1.2 corresponds to the long-term $\overline{AET}/\bar{P}$ estimate from the present study and a curve that essentially coincides with the Gentine et al. (2012) Budyko curve over the range of $PET/P$ ratios relevant to the Alder Creek area. Further, Istanbulluoglu et al. (2012) discuss the impact of land use change from native vegetation to agricultural crops. These authors state that crops such as corn tend to transpire more than natural grassland, according to another study (Irmak et al., 2008). So, it seems that there could be factors like corn crops (which are grown in the watershed) that increase AET above specifically grassland estimates, and factors such as conversion of native vegetation (e.g., forest) to crop cover that could decrease AET relative to natural vegetation conditions. An effective value of w = 1.2 seems reasonable because the variability of recharge was the focus of the present study rather than the exact average value.

The BFI values and the total streamflow amounts have some uncertainty because the outflow of the creek is not gauged. However, this likely had a minimal influence on the overall recharge results because the overland flow component of the water budget is relatively small (about 10% of average total precipitation). The annual overland flow components of the water budget were consistent in all realizations, whereas the rainfall and AET values differed. The rainfall and AET values thus likely exerted a much larger influence on recharge estimates than the BFI values.

There are several issues to mention related to rainfall. One issue related to the stochastic rainfall generation is whether the correlation coefficients have remained similar over the last 46 years, or if they were different during the three-year analysis period at the local weather stations. Another issue is that the precipitation and AET estimates were generated by a process that ignored potential natural patterns in the relationship between annual AET and precipitation. A third issue is that the variability of average watershed precipitation is likely less than the variability associated with local precipitation within a well capture zone. The method proposed in the present study used watershed scale recharge variability to estimate well capture zone area variations. There was a mismatch in the scales of the two areas, but obtaining water budget component estimates for regions smaller than a watershed is challenging because the Budyko curve does not apply and partitioning of overland flow and baseflow may change throughout the watershed.

Previous studies of the variation of recharge rates due to rainfall spatial variability have reported larger differences in recharge rates than those in the present study. The ratio of cumulative recharge under maximum and minimum conditions for the case of no scatter of $\overline{AET_{tot}}/\bar{P}$ around the Budyko curve (1.15) was less than the factor obtained by Sapriza-Azuri et al. (2015) over a similar time period for a watershed in Spain (~2). The difference in values may be related to the differences in the sizes of these watersheds. The maximum difference in the range of average annual recharge rates in the present study for the case of no scatter of $\overline{AET_{tot}}/\bar{P}$ about the Budyko curve (39 mm) was smaller than most of the differences between annual scenarios comparing different rain gauge networks as inputs within a fully-distributed model of the Alder Creek watershed (Wiebe and Rudolph, 2020). This may be due to the difference in time scale.

The worst-case capture zone area change (±15%) was smaller than the results of Piersol (2005) and smaller than would be predicted by the water budget derived uncertainty from Wiebe and Rudolph (2020). Piersol (2005) generated capture zones for the city of Aguadulce, Panama, using steady state particle tracking under different uniform recharge rates. The author found that recharge rate variation from the base case by factors of +50% and -30% resulted in a capture zone whose area differed from the base case by -33% and +43%, respectively, under uniform pumping rates. Such variation in recharge rates (≥ 30%) would be outside the 95% confidence interval of the present study. Wiebe and Rudolph (2020) estimated the water-budget derived uncertainty on recharge to be ±100 mm or about ±30% of a previous steady state recharge estimate (321 mm; M.H. Brouwers, pers. comm., 2017; Matrix and SSPA, 2014a). A change in recharge of ±100 mm would lead to a capture zone area change of up to around ±54% of the average area via equations Eqn. 4.11.1 and Eqn. 4.11.2. The worst-case capture zone area change from the present study, ±15%, is significantly less than this value. However, this estimate does not incorporate the 25% larger variability of the local virtual rain gauges because of the difference in spatial scale mentioned above. Also, local sediment types and vegetation play key roles that were not accounted for by the watershed-scale recharge estimates generated by the present study. The present analysis assumed that well capture zones contain soil and vegetation types representative of the entire watershed, which may not be the case. This would be more likely to be true for a well with a larger capture zone, which may potentially sample a broader range of soil types. Despite this, guidance is needed to assess the uncertainty of the capture zone concept, which is extremely important from a source water protection perspective (Sousa et al., 2013a). The method employed in the present study could be used to provide a rough estimate of the uncertainty boundaries for the challenging task (Frind and Molson, 2018; Rayne et al., 2014) of

delineating transient capture zones. The capture zone concept has also been extended to the contribution area for gaining stream reaches (Chow et al., 2016). A similar change in stream contribution areas would be possible based on variation in recharge rate estimates due to spatially variable rainfall. The $\overline{Q_{well}}$ term in equations Eqn. 4.10 and Eqn. 4.11 could be replaced with the groundwater discharge flow rate into the stream reach of interest.

Guidance is also needed in terms of understanding the uncertainty in non-point source mass loadings for watershed management. There is a large amount of uncertainty associated with road salt and nitrogen concentrations and mass loadings to the water table. Variations in daily road salt application are currently recorded by municipalities (Perera et al., 2013). However, the fraction of salt that is ploughed with snow to the side of the road to be retained by the soil is unknown (Denby et al., 2016). Historical municipal salt application rates are likely less well known than current rates. In terms of nitrogen loadings, the applied mass is quantified according to provincial regulations (e.g., Province of Ontario, 2002). The proportion of nitrogen that leaches below the root zone has considerable uncertainty and has been estimated via coefficient of variation (standard deviation / mean) as up to 40% in one study (Hansen et al., 1999), and +59% or -79% in another (Schmidt et al., 2008). The coefficient of variation for non-point source mass loadings due to the combined variability of watershed-averaged rainfall and AET in the present study would be 7.1%. This suggests that water budget uncertainty is a minor component of overall mass loadings estimates and efforts to reduce uncertainty should focus on quantifying the fraction of applied mass retained by the soil more accurately.

Climatic change may result in changing trends and statistics (e.g., DeBeer et al., 2016; Gregersen et al., 2013), including the spatial correlation of rainfall rates. An increase in the number of intense storms would likely be associated with changes in the spatial distribution of rainfall at different scales (Marvel and Bonfils, 2013; Simonovic et al., 2017; Trenberth, 2011). The present study's approach could be a useful tool to project potential changes in recharge rates for watersheds undergoing climatic change, if key parameters (e.g., rainfall spatial correlation, streamflow, and BFI) were measured. It may be possible to apply to urban watersheds if the Budyko curve estimate of $AET/P$ could be revised for the decrease in $AET$ caused by the replacement of vegetation with impermeable surfaces. Other water budget components such as recharge from leaky water (Jang et al., 2019) or sewer pipes (Vystavna et al., 2018) would likely need to be accounted for in the water budget.

Generally, the method of the present study could be used as context for distributed numerical model results, or a comparison for uncertainty analyses from such models.

Quantifying uncertainty is difficult without measurements of rainfall or AET across a watershed. Correlation coefficients are a valuable tool to constrain spatial rainfall variability. The results of the present study suggested that AET uncertainty and spatial rainfall variability contributed nearly equivalently to estimated recharge variability, and, by extension, to non-point source loadings and capture zone areas. These error bars may be helpful for the sustainable management of well fields from a quality and quantity perspective.

Five recommendations are offered here to improve confidence in recharge rate estimates, and therefore in capture zone and non-point source mass loadings estimates. First, reducing uncertainty on long-term average watershed rainfall may be as important as reducing the uncertainty of $AET$ estimates. Verifying the validity of and scatter of points about the Budyko curve for a certain area would be a useful step. Care should be taken because the watersheds of some regions may not fall along the Budyko curve (e.g., some arid regions – Donohue et al., 2007, 2010; Gentine et al., 2012; areas affected by afforestation or deforestation – Zhang et al., 2001; and possibly peatlands – Hwang et al., 2018). Second, the influence of soil texture in association with rainfall variability may lead to increasing uncertainty on average watershed estimates. Third, it may also become increasingly necessary to track changing rainfall trends and correlation statistics as climatic changes occur. Fourth, guidance is needed to downscale AET and baseflow results from the watershed scale to the subwatershed scale, a scale at which precipitation may be more variable and a scale that may be similar to the area of public supply well capture zones. Fifth, spatial snowfall variability should be addressed. While this is on average a smaller component of the water budget in the Alder Creek watershed (about 15% of total precipitation; Government of Canada, 2019; OMNR, 2007), this could be a larger component in other watersheds. The present study assumed uniform snowfall based on limited data, but this is a second source of spatial precipitation uncertainty whose impact on recharge should be considered further.

## 4.5 Conclusions

This study used three years of observed rainfall data from the Alder Creek watershed to calculate spatial correlation coefficients that were then used to constrain a stochastic vadose zone water budget

to estimate the variability of watershed scale recharge rates over 46 years. Stochastic AET estimates for the watershed were developed based on: i) the Budyko curve (Gentine et al., 2012), ii) observed PET/P ratios at a weather station near the watershed, iii) observed annual variations from the Budyko curve for 45 US MOPEX (Duan et al., 2006) watersheds, and iv) applying PET to regions within the watershed where the water table is known to be at or close to ground surface. Annual streamflow from a gauge within the watershed and derived BFI values were used to estimate the overland flow component of streamflow.

The average recharge rate across all realizations was estimated to be 282 mm per year, a value within the range of previous steady state estimates determined by numerical modelling (M.H. Brouwers, pers. comm., 2017; CH2MHILL and SSPA, 2003; Matrix and SSPA, 2014a). The 95% confidence interval for recharge ranged from around 244 to 321 mm per year over all realizations, and the total variability represented by this range was derived nearly equivalently from the uncertainty of AET estimates and the spatial variability of stochastic rainfall.

The 95% confidence interval derived for long-term recharge rates was applied to three water management metrics. The water quality implications of the results suggest that non-point source contaminant loadings estimates could vary from the average by up to ±14%. Well vulnerability was evaluated in terms of capture zone area uncertainty, which was estimated to vary by up to ±15% from the average. Water quantity was assessed via the ratio of maximum to minimum cumulative recharge over 46 years. This ratio was estimated to vary by a factor of up to 1.31. Impacts of rainfall spatial variability alone with $\overline{AET_{tot}}/\bar{P}$ ratios estimated strictly based on the Budyko curve resulted in variations in contaminant loadings of up to ±7.0%, capture zone area percentage differences of up to ±7.4%, and a ratio of maximum to minimum recharge of 1.15. These results provide a sense of the uncertainty related to groundwater management that may be present in typical water budget analyses (e.g., most steady state numerical models) due to the spatial variability of rainfall and the uncertainty of AET, and the approach is applicable to watersheds where the Budyko curve is either representative or the influence of land use changes on the curve may be estimated. Variability in contaminant loadings and capture zone areas may be increased for partial areas of the watershed because local rainfall variation was damped by 25% by interpolating over the watershed. Further work is needed on the expected degree of variability of the ratio of $AET/P$ about the Budyko curve, based on geographical area or watershed characteristics.

## 4.6 Tables

Table 4.1. Stochastic water budget results for 16,778 realizations, considering the influence of both rainfall and AET variability.

| Category | Result |
|---|---|
| **Water Budget** | |
| Average annual weighted average watershed total P | 898 mm |
| Average annual $AET_{VZ}$ | 524 mm |
| Average annual watershed recharge (over 46 years, all realizations) | 282 mm |
| Standard deviation for average annual watershed recharge | 20 mm |
| 0.025-quantile annual watershed recharge | 244 mm |
| 0.975-quantile annual watershed recharge | 321 mm |
| **Water Quality** | |
| Percent difference in mass loadings over 46 years, PDMA* | ±14% |
| **Well Vulnerability** | |
| Percent difference in capture zone area for 46 years, PDA* | ±15% |
| **Water Quantity** | |
| 0.975-quantile – 0.025-quantile difference, average annual recharge† | 77 mm |
| 0.975-quantile cumulative recharge / 0.025-quantile cumulative recharge† | 1.31 |

* Maximum 95% confidence interval difference with respect to the average

† Worst case approximation using 95% confidence interval bounds

## 4.7 Figures

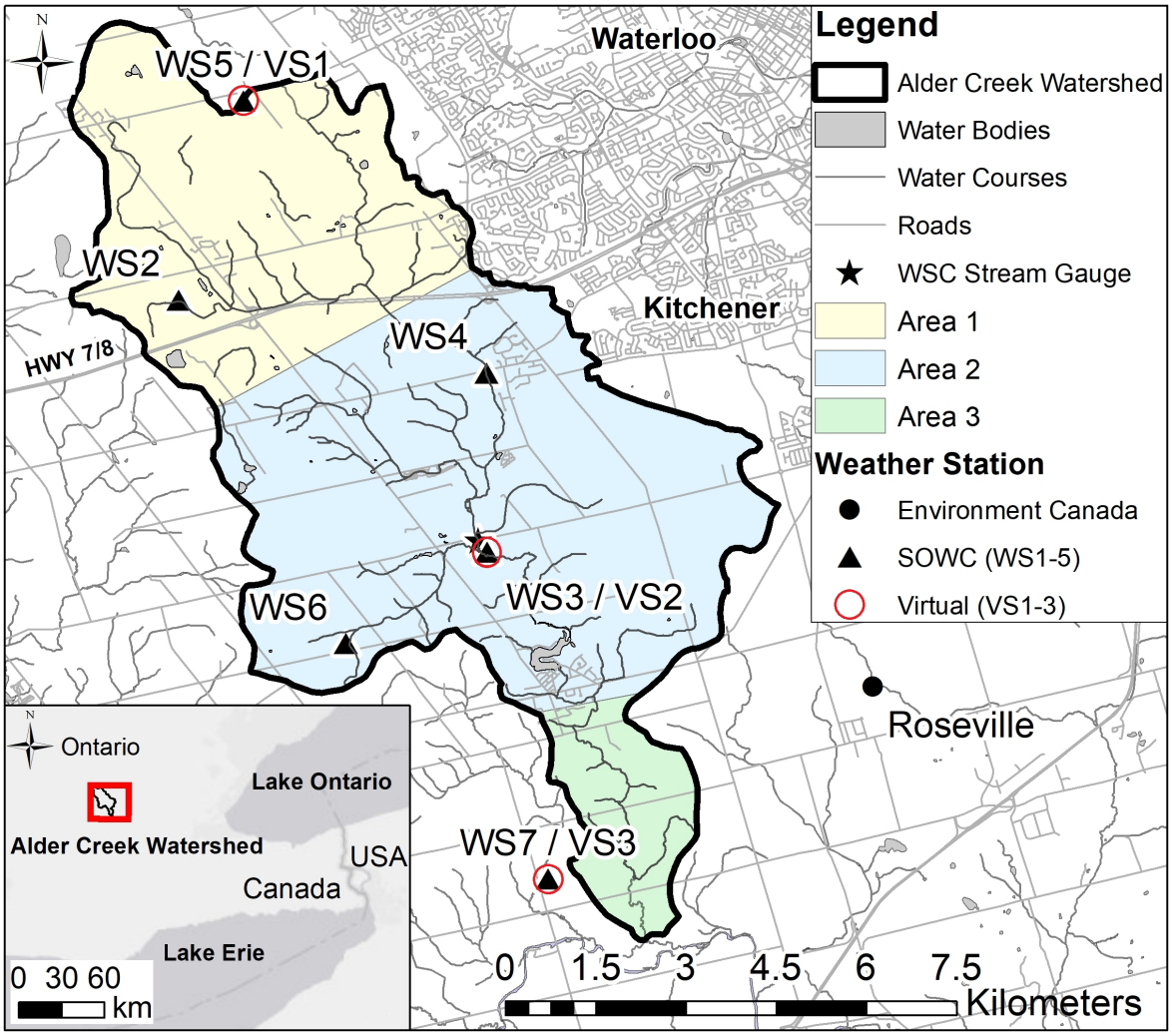


Figure 4.1: Study site and Thiessen polygons (Areas 1 – 3) for virtual rain gauges (DMTI, 2011; Esri et al., 2019a; Government of Canada, 2019; GRCA, 1998; WSC, 2019).

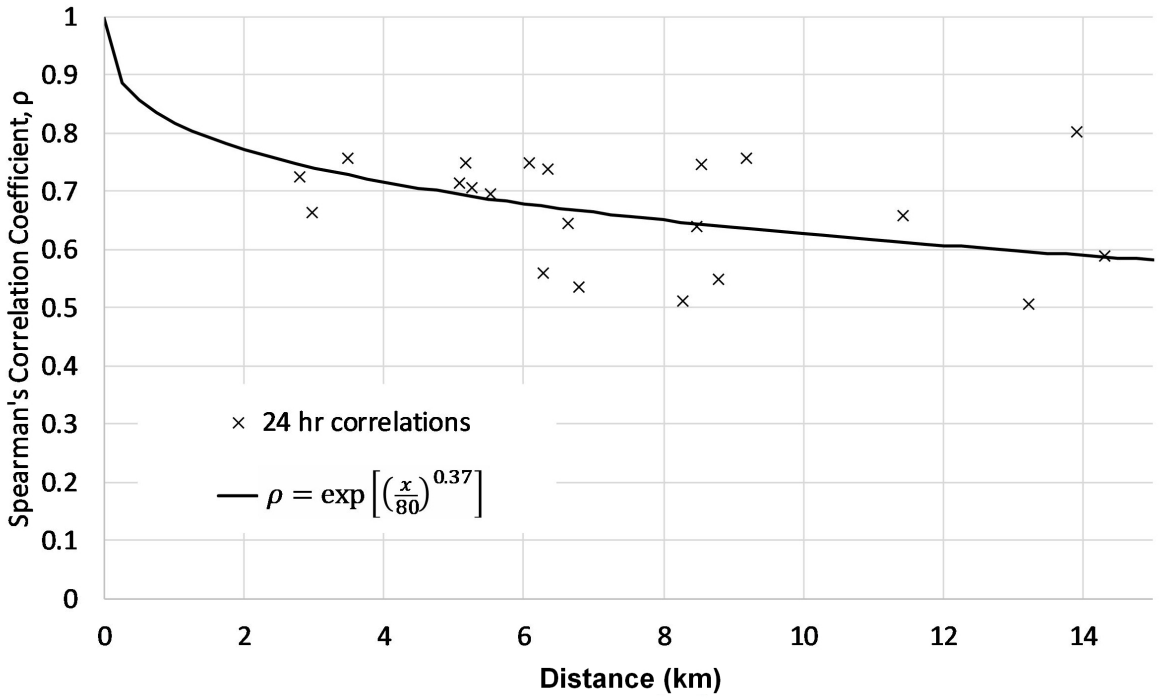


Figure 4.2: Spearman correlation between six local rain gauges and the nearest national station (Gavin, 2009, 2019; Government of Canada, 2019; Wiebe et al., 2019).

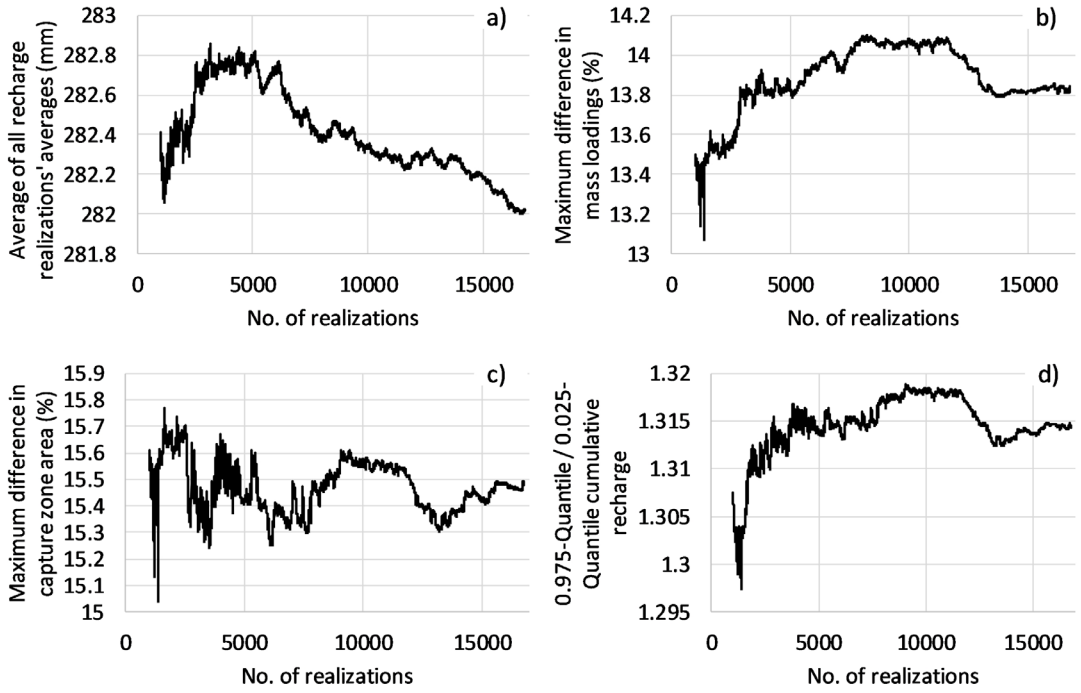


Figure 4.3: Variation of metrics with the number of realizations: a) Average recharge ($\bar{R}$), b) maximum 95% confidence percentage difference in mass loadings ($PDMF$), c), maximum 95% confidence percentage difference in capture zone area (PDA), and d) ratio of 95% confidence maximum to minimum cumulative recharge ($Ratio_{Rt}$).

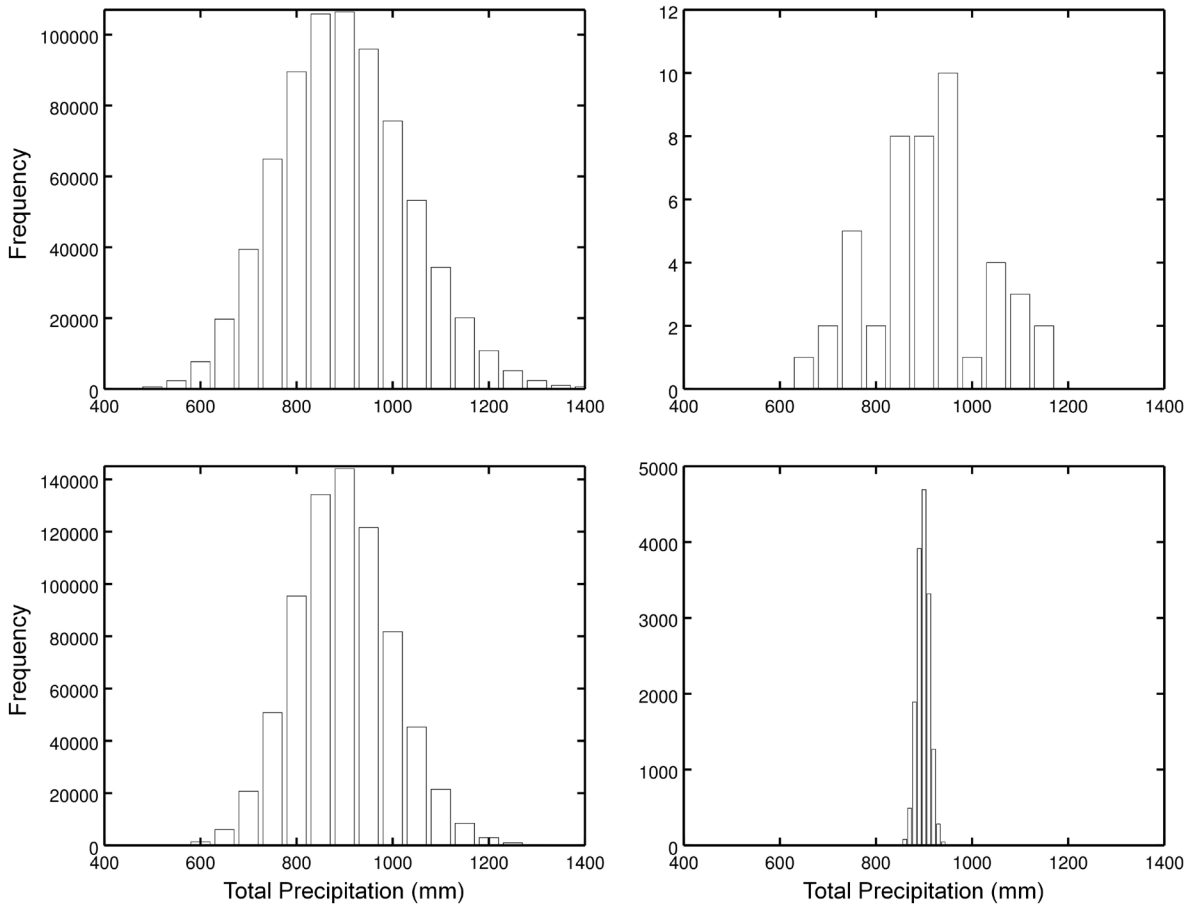


Figure 4.4: Frequency distribution of total precipitation for: a) Virtual Station 1 over all realizations (annual values), b) Roseville annual values for 1973 to 2018 (Government of Canada, 2019), c) the watershed, over all realizations and in terms of interpolated annual values, and d) the watershed, where interpolated annual values were averaged over 46 years for each realization. The bin size was 50 mm for a), b), and c), and 10 mm for d).

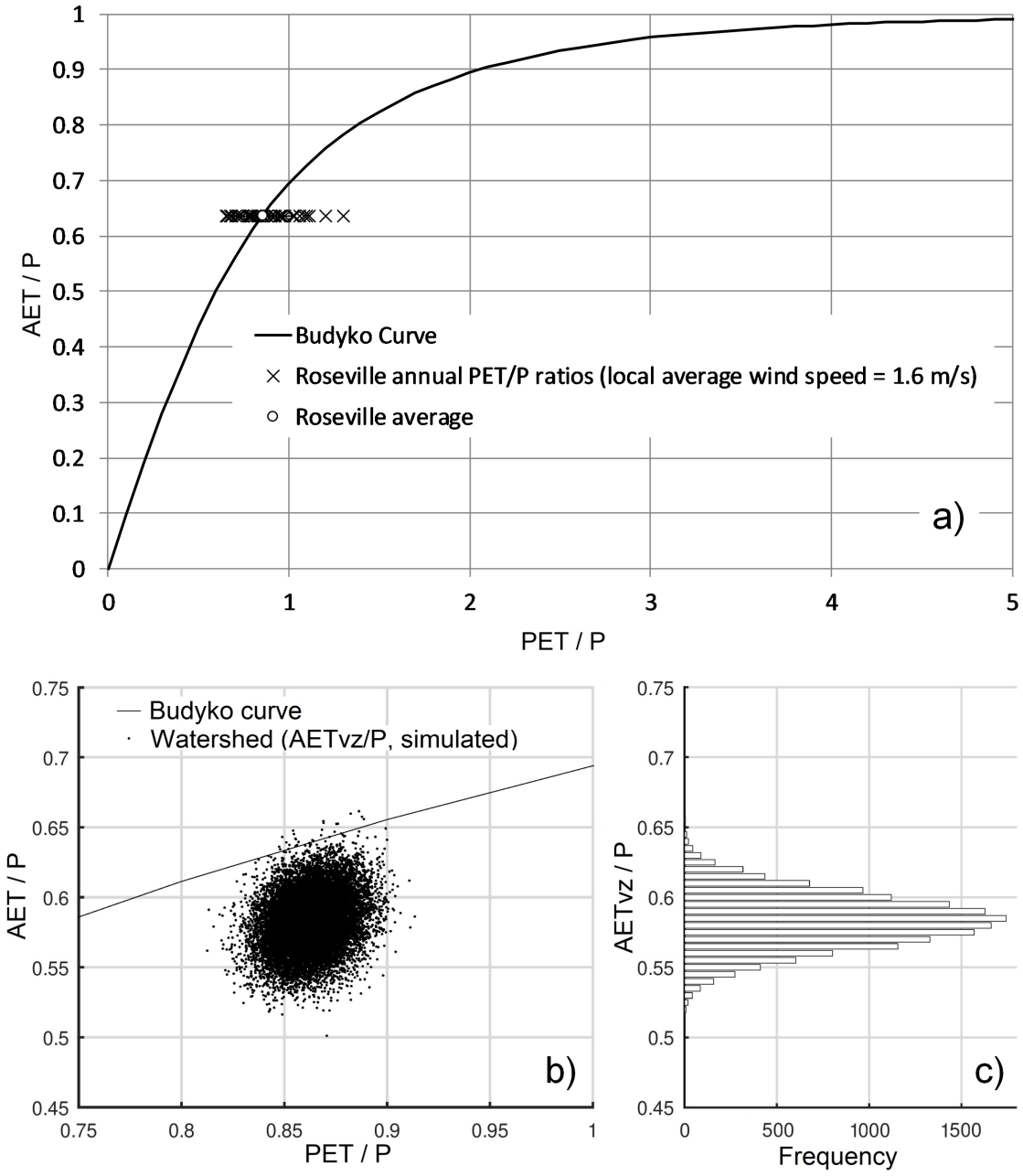


Figure 4.5: AET/P and PET/P ratios: a) observed Roseville (Government of Canada, 2019) annual variations in PET/P and average $\overline{AET}/\bar{P}$ value along the Budyko curve (Gentine et al., 2012), b) simulated $\overline{AET_{VZ}}/\overline{P_{WS}}$ ratios, and c) frequency distribution of $\overline{AET_{VZ}}/\overline{P_{WS}}$ ratios from all realizations.

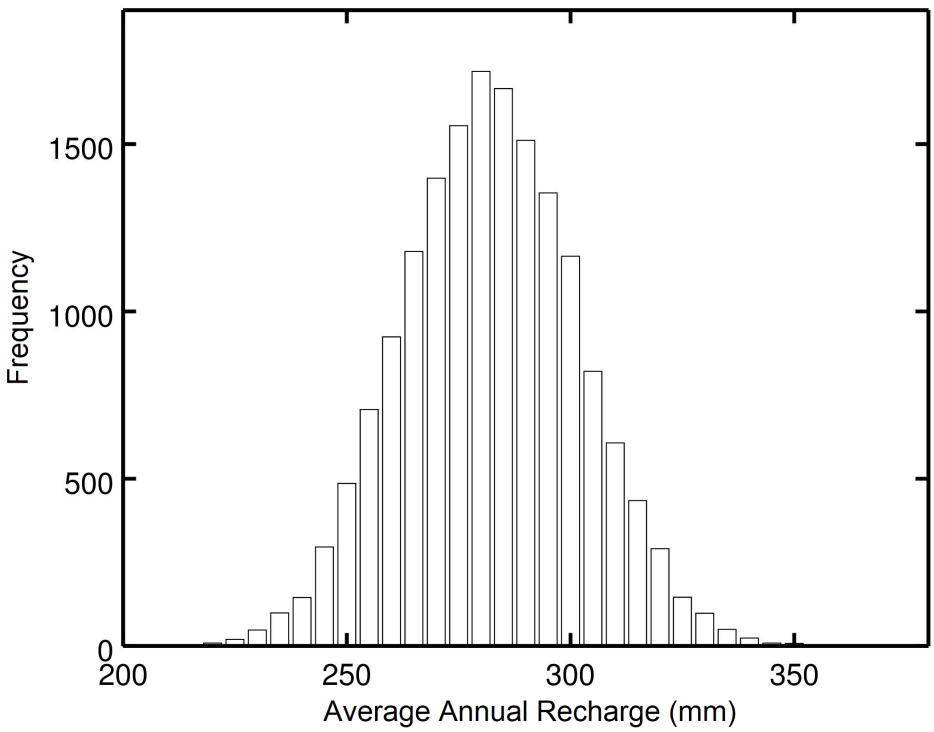


Figure 4.6: Frequency of 46-year average recharge rates over all realizations.

# Chapter 5
# Conclusions and Recommendations

The present study explored the impact of the spatial variation of rainfall on groundwater recharge and the impact of DFR on well vulnerability in the Alder Creek watershed, a typical watershed in southwestern Ontario that provides source water for multiple well fields. Field data were collected within a network of six local weather stations (five within the watershed) and at one DFR site. Regional data were obtained for a network of six rainfall stations within 30 km of the watershed, and for one national station within 3 km of the watershed. Daily spatial correlation coefficients for local and regional rain gauge networks, and for the local network plus one national weather station, were < 0.8, suggesting that rainfall is generally not very well correlated in the area.

Chapter 2 explored how annual recharge rates could be affected by the choice of rain gauge network in a fully-distributed, watershed-scale, coupled model for three calendar years. Overall average recharge rates differed by up to 141 mm per year in the worst-case comparison of simulations employing either national or regional rainfall with local rain gauge network input data. This constituted 44% of previously estimated steady state recharge (321 mm; M.H. Brouwers, pers. comm., 2017; Matrix and SSPA, 2014a) for the Alder Creek watershed. The cumulative streamflow for the local rainfall scenario appeared to be a closer match with observations. These results suggest that the calibration of transient models of watersheds with similar rainfall correlation would be likely to compensate for rainfall differences by adjusting hydraulic conductivity values to match observed hydraulic heads and streamflow. Ultimately, adjustments to such near-surface soil properties based on imprecise rainfall information could negatively impact recharge estimates and management decisions related to capture zone delineation and net baseflow into streams.

Chapter 3 addressed focused recharge and well vulnerability to potential microbial contaminants at the site scale. Creek water levels, groundwater levels, soil moisture, and rainfall were monitored at a site within the Alder Creek watershed where surficial ponding had been observed to occur in the base of a topographic depression. This ponding occurred around 50 m (Menkveld, 2019) from a public supply well that is screened > 15 m below ground in glacial overburden sediments (CH2MHILL, 2002). Numerical modelling was conducted to examine the hypothesis that contaminants originating in the ponded water in the topographic depression during a large-magnitude rainfall or snowmelt event could reach the well at relative concentrations of concern within 50 days, a time frame related

to microbial risks to water quality. Two fully-integrated, surface water–groundwater (HydroGeoSphere) models were used to calibrate shallow soil properties based on an observed ponding event, and the main aquifer soil properties to a pumping test. A smaller version of the second model represented the radial flow field through the base of the topographic depression and the creek toward the well and was used to simulate two large hydrologic events (> 40 mm of rain over 4 days; Nov 2014, Jul 2017) and subsequent transport of solute tracers from the depression and the creek to the well. Breakthrough curves did not reach a critical value corresponding to "detection" (1 cfu/100 mL) at the well for median initial concentrations in surface water (220 cfu/100 mL). However, critical travel times associated with maximum initial concentrations in surface water (31,000 cfu/100 mL) were 118 and 142 days for the creek solute and the DFR solute, respectively, in the most extreme case (Nov 2014). Breakthrough results for the DFR solute in a background scenario with no event ponding did not reach critical relative concentrations within 200 days. This suggests that event ponding could reduce critical travel time by at least58 days, indicating a potential concern for the well. The phenomenon of ponding, sharp increases in effective precipitation, and creek overbank flow events seemed to be important factors for breakthrough at the well.

Chapter 4 extended the analysis of the influence of spatially varying rainfall on recharge rates to several decades (46 years) using a stochastic vadose zone water budget. The influence of variable actual evapotranspiration (AET) estimates was also examined. Stochastic rainfall time series were generated via a parametric, mixed exponential method and then adjusted based on the observed range of rainfall correlation coefficients. Stochastic annual vadose zone AET estimates for the Alder Creek watershed were based on factors including: the Budyko curve, PET calculated for a long-term weather station < 3 km from the watershed, observed annual variations about the Budyko curve for 45 US MOPEX watersheds, and applying PET estimates to watershed regions where the water table is at or close to ground surface. The overland flow component of streamflow was estimated based on baseflow index values derived from the gauging station within the watershed. The 95% confidence interval results for combined rainfall and AET variability suggested that non-point source contaminant loadings could differ from the average by up to ±14%. Capture zone areas were estimated to vary up to ±15% with respect to the average. The ratio of maximum to minimum cumulative recharge over 46 years was at most 1.31. When only rainfall spatial variability was considered, contaminant loadings were estimated to differ from the average by up to ±7.0%, capture zone areas were estimated to differ from the average by up to ±7.4%, and the ratio of maximum to minimum cumulative recharge was 1.15. This latter value is smaller than the ratio found during a

previous study by Sapriza-Azuri et al. (2015) of spatially variable rainfall in a larger watershed in Spain. In contrast to Chapter 2, rainfall spatial variability over several decades could lead to a range of recharge estimates that differ by up to 12% of a previously estimated steady state estimate (321 mm; M.H. Brouwers, pers. comm., 2017; Matrix and SSPA, 2014a). The variability calculated for water quality, well vulnerability, and water quantity provides a sense of the potential influence of spatial rainfall variation over the long term at the watershed scale, though the variability of local rainfall might increase the variability of contaminant loadings and well capture zone area estimates beyond the above percentages. The results of Chapter 4 suggest that the contributions of AET uncertainty and spatial rainfall variability to recharge variability may be nearly equivalent at the watershed scale.

The present study has implications for transient, coupled or integrated watershed modelling and for well vulnerability assessments. Previous studies (Mileham et al., 2008; Sapriza-Azuri et al., 2015) that assessed the sensitivity of recharge rates to spatial rainfall variability focused on watersheds at a much larger scale. Chapter 2 suggests that recharge rates and streamflow estimates for a small to medium sized watershed (~70 $km^2$) can be quite sensitive to the spatial scale of input rainfall data at an annual time scale. The transient calibration of land use planning or water resources models assessing baseflow to streams may be affected by the amount of available rainfall data. Local rainfall data may improve confidence in groundwater recharge estimates and provide more accurate estimates of discharge to streams. The installation of rain gauges would likely be less expensive than drilling operations to collect soil cores and install new groundwater monitoring points. Appendix A identified wind speed as an important supplementary parameter for constraining $ET_o$ estimates when only temperature data are available, though $ET_o$ variation was found to exert less impact on recharge estimates than rainfall variation. Chapter 3 illustrated the possibility for extreme hydrological events to reduce microbial contaminant travel times to a public supply well when ponding occurs at the ground surface. Chapter 4 introduced an approach to estimate the uncertainty of non-point source loadings to the water table, capture zone areas, and cumulative recharge rates that could be used to provide context for modelling results in watersheds where the Budyko curve applies.

Recommendations for future study are offered here in closing. A long-term comparison of modelled recharge rates based on rain gauges and on radar-derived rainfall estimates would complement the work in Chapter 2. Radar may integrate rainfall over space differently than interpolation algorithms but is still subject to ground-truthing with rain gauges. The spatial variability

of snowpack thicknesses could be assessed in watersheds where this is expected to be significant. An assessment of the sensitivity of recharge rates within watersheds with greater and lesser degrees of spatial rainfall correlation could establish a general relationship between the degree of spatial rainfall correlation and associated differences in recharge estimates. The work described in Chapter 3 suggests that sediment core logging, especially near regions of localized infiltration and in greater detail than is usually available (e.g., one soil type for intervals spanning multiple metres; OMECP, 2018), would be helpful for modelling large-magnitude hydrological events. Site-specific information on longitudinal dispersivity and fecal indicator concentrations in surface water during events would be needed to reduce uncertainty in transport modelling. Cameras could assist with the monitoring of hydrological events and rain gauge data, in addition to hydrological sensors. Estimates of the variability of AET based on geographical or watershed characteristics are needed to confirm the expected degree of variability of the ratio of AET/P about the Budyko curve for a given watershed. Verification of the method used to adjust $AET_{tot}$ estimates to remove AET from the saturated zone would also be useful.

# References


Abbott, M.B., Bathurst, J.C., Cunge, J.A., O'Connell, P.E., Rasmussen, J., 1986. An introduction to the European Hydrological System-Système Hydrologique Européen, SHE, 2: Structure of a physically-based, distributed modelling system. J. Hydrol. 87, 61-77. https://doi.org/10.1016/0022-1694(86)90115-0.

Adam, J.C., Lettenmaier, D.P., 2003. Adjustment of global gridded precipitation for systematic bias. J. Geophys. Res. 108(D9), 4257. https://doi.org/10.1029/2002JD002499.

Ahmed, A., Emelko, M., Mutti, D., Sokolowski, O., 2019. The complete draft GUDI terms of reference: Guidance document to determine minimum treatment for municipal residential drinking water systems using subsurface raw water supplies. Webinar slides. Professional Geoscientists Ontario. 24 Sep 2019. https://www.pgo.ca/files/events/webinar-mecp-2019-gudi-terms-of-reference.pdf. (Accessed 01.05.2020).

Aksoy, U., Akisu, C., Sahin, S., Usluca, S., Yalcin, G., Kuralay, F., Oral, A.M, 2007. First reported waterborne outbreak of cryptosporidiosis with Cyclospora co-infection in Turkey. EuroSurveillance 12(7), 3142. https://www.eurosurveillance.org/content/10.2807/esw.12.07.03142-en.

Allen, R.G., Pereira, L.S., Raes, D., Smith, M., 1998. Crop evapotranspiration – Guidelines for computing crop water requirements – FAO Irrigation and drainage paper. FAO (Food and Agriculture Organization of the United Nations), Rome, IT. http://www.fao.org/docrep/X0490E/X0490E00.htm. (Accessed 05.05.2017).

Anderson, M.P., Woessner, W.W., 1992. Applied Groundwater Modeling: Simulation of Flow and Advective Transport. Academic Press, San Diego, CA, USA.

Andréassian, V., Perrin, C., Michel, C., Usart-Sanchez, I., Lavabre, J., 2001. Impact of imperfect rainfall knowledge on the efficiency and the parameters of watershed models. J. Hydrol. 250, 206-233. https://doi.org/10.1016/S0022-1694(01)00437-1.

Aquanty Inc. (Aquanty), 2015a. HGS Reference Manual. Manual for HydroGeoSphere code. Aquanty, Inc. Waterloo, ON. https://www.aquanty.com/. (Accessed 12.02.2018).

Aquanty Inc (Aquanty), 2015b. HGS User Manual. Manual for HydroGeoSphere code. Aquanty Inc. Waterloo, ON. https://www.aquanty.com/. (Accessed 12.02.2018).

AquaResource Inc. (AquaResource), 2008. Technical Memorandum Re: MNR Climate Data Gap Filling Project – Data Review. Summary of Ontario Ministry of Natural Resources (MNR) precipitation data analysis. August 2008. Obtained from Matrix Solutions Inc., controlled access.

Baalousha, H., 2009. Stochastic water balance model for rainfall recharge quantification in Ruataniwha Basin, New Zealand. Environ. Geol. 58, 85-93. https://doi.org/10.1007/s00254-008-1495-6.

Bajc, A.F., Russell, H.A.J., Sharpe, D.R., 2014. A three-dimensional hydrostratigraphic model of the Waterloo Moraine area, southern Ontario, Canada. Can. Water Resour. J. 39(2), 95-119. https://doi.org/10.1080/07011784.2014.914794.

Baldursson, S., Karanis, P., 2011. Waterborne transmission of protozoan parasites: Review of worldwide outbreaks - An update 2004-2010. Water Res. 45, 6603-6614. https://doi.org/10.1016/j.watres.2011.10.013.

Bales, R.C., Li, S., Yeh, T.-C.J., Lenczewski, M.E., Gerba, C.P., 1997. Bacteriophage and microsphere transport in saturated porous media: Forced-gradient experiment at Borden, Ontario. Water Resour. Res. 33(4), 639-648. https://doi.org/10.1029/97WR00025.

Barlow, P.M., Cunningham, W.L., Zhai, T., and Gray, M., 2015. U.S. Geological Survey Groundwater Toolbox, a graphical and mapping interface for analysis of hydrologic data (version 1.0) – User guide for estimation of base flow, runoff, and groundwater recharge from streamflow data. U.S. Geological Survey Techniques and Methods, book 3, chap. B10, 27 p. https://doi.org/10.3133/tm3B10.

Barthel, R., Banzhaf, S., 2016. Groundwater and surface water interaction at the regional-scale – A review with focus on regional integrated models. Water Resour. Manage. 30,1-32. https://doi.org/10.1007/s11269-015-1163-z.

Basinger, M., Montalto, F., Lall, U., 2010. A rainwater harvesting system reliability model based on nonparametric stochastic rainfall generator. J. Hydrol. 392, 105-118. https://doi.org/10.1016/j.jhydrol.2010.07.039.

Batu, V., 1998. Aquifer Hydraulics: A Comprehensive Guide to Hydrogeologic Data Analysis. John Wiley & Sons, New York. 727p.

Bekeris, L., 2007. Field-scale evaluation of enhanced agricultural management practices using a novel unsaturated zone nitrate mass load approach. Unpublished MSc. thesis. University of Waterloo, Waterloo, ON. http://hdl.handle.net/10012/2701.

Bell, V.A., Moore, R.J., 2000. The sensitivity of catchment runoff models to rainfall data at different spatial scales. Hydrol. Earth System Sci 4(4), 653-667. https://doi.org/10.5194/hess-4-653-2000.

Berthold, S., Bentley, L.R., Hayashi, M., 2004. Integrated hydrogeological and geophysical study of depression-focused groundwater recharge in the Canadian prairies. Water Resour. Res. 40, W06505. https://doi.org/10.1029/2003WR002982.

Besmer, M.D., Epting, J., Page, R.M., Sigrist, J.A., Huggenberger, P., Hammes, F., 2016. Online flow cytometry reveals microbial dynamics influenced by concurrent natural and operational events in groundwater used for drinking water treatment. Sci. Rep. 6, 38462. https://doi.org/10.1038/srep38462.

Bester, M.L., Frind, E.O., Molson, J.W., Rudolph, D.L., 2006. Numerical investigation of road salt impact on an urban wellfield. Ground Water 44(2), 165-175. https://doi.org/10.1111/j.1745-6584.2005.00126.x.

Blackport Hydrogeology Inc. (Blackport), Blackport and Associates Ltd., AquaResource Inc., 2009. Review of the State of Knowledge for the Waterloo and Paris/Galt Moraines. Prepared for: Land and Water Policy Branch, Ontario Ministry of the Environment. 92p. https://guelph.ca/wp-content/uploads/Moraines_Report_May2009.pdf.

Blackport, R.J., Meyer, P.A., Martin, P.J., 2014. Toward an understanding of the Waterloo Moraine hydrogeology. Can. Water Resour. J. 39(2), 120-135. https://doi.org/10.1080/07011784.2014.914795.

Bouwer, H., Rice, R.C., 1976. A slug test for determining hydraulic conductivity of unconfined aquifers with completely or partially penetrating wells. Water Resour. Res., 12(3), 423-428.

Bradshaw, J.K., Snyder, B.J., Oladeinde, A., Spidle, D., Berrang, M.E., Meinersmann, R.J., Oakley, B., Sidle, R.C., Sullivan, K., Molina, M., 2016. Characterizing relationships among fecal indicator bacteria, microbial source tracking markers, and associated waterborne pathogen occurrence in

stream water and sediments in a mixed land use watershed. Water Res. 101, 498-509. https://doi.org/10.1016/j.watres.2016.05.014.

Bridgman, S.A., Robertson, R.M.P., Syed, Q., Speed, N., Andrews, N., Hunter, P.R., 1995. Outbreak of Cryptosporidiosis associated with disinfected groundwater supply. Epidemiol. Infect. 115(3), 555-566. https://doi.org/10.1017/S0950268800058726.

Brocca, L., Liersch, S., Melone, F., Moramarco, T., Volk, M., 2013. Application of a model-based rainfall-runoff database as efficient tool for flood risk management. Hydrol. Earth Syst. Sci. Discuss. 10, 2089-2115. https://doi.org/10.5194/hessd-10-2089-2013.

Brook, J.M., 2012. Evaluating Innovative nutrient management options and seasonal groundwater recharge dynamics in an agricultural source water protection area. Unpublished MSc. thesis. University of Waterloo, Waterloo, Ontario. http://hdl.handle.net/10012/7070.

Brouwers, M.H., 2007. A case study for assessing the hydrologic impacts of climate change at the watershed scale. Unpublished MASc. thesis, University of Waterloo, Waterloo, ON, Canada. 121p. http://hdl.handle.net/10012/3514.

Brouwers, M.H., 2017. Personal communications from Groundwater Modelling Specialist at Matrix Solutions Inc. Tier Three recharge results shapefile exported from FEFLOW, Sim836 (Sim836_Rch.shp).

Bruce, J.P., Cunningham, W., Freeze, A., Gillham, R., Gordon, S., Holysh, S., et al., 2009. The sustainable management of groundwater in Canada. The Canadian Council of Canadian Academies, Ottawa, Canada. https://www.scienceadvice.ca/reports/the-sustainable-management-of-groundwater-in-canada/.

Budyko, M., 1961. The heat balance of the Earth's surface. Natl. Weather Serv., U.S. Dep. of Commer., Washington, D.C., USA.

Burr, S.E., 2000. An assessment of seven methods to measure nitrogen leaching under agricultural practices. Unpublished MSc. thesis, University of Guelph, Guelph, ON, Canada. 79pp.

Burn, D.H., Whitfield, P.H., 2015. Changes in floods and flood regimes in Canada. Can. Water Resour. J. 41(1-2), 139-150. https://doi.org/10.1080/07011784.2015.1026844.

Butler Jr., J.J., 1998. The design, performance, and analysis of slug tests. CRC Press LLC, Boca Raton, FL, USA.

Camici, S., Tarpanelli, A., Brocca, L., Melone, F., Moramarco, T., 2011. Design soil moisture estimation by comparing continuous and storm-based rainfall-runoff modelling. Water Resour. Res. 47, W05527. https://doi.org/10.1029/2010WR009298.

Camici, S., Brocca, L., Tarpanelli, A., 2014. Neyman-Scott Rectangular Pulse Model (Matlab code - updated). https://www.researchgate.net/publication/260219802_Neyman-Scott_Rectangular_Pulse_Model_Matlab_code_-_updated. (Accessed 04.07.2019).

Camporese, M., Paniconi, C., Putti, M., Orlandini, S., 2010. Surface-subsurface flow modeling with path-based runoff routing, boundary condition-based coupling, and assimilation of multisource observation data. Water Resour. Res. 46, W02512. https://doi.org/10.1029/2008WR007536.

Canadell, J., Jackson, R.B., Ehleringer, J.R., Mooney, H.A., Sala, O.E., Schulze, E.-D., 1996. Maximum rooting depth of vegetation types at the global scale. Oecologia 108, 583-595. https://doi.org/10.1007/BF00329030.

Cey, E.E., Rudolph, D.L., Passmore, J., 2009. Influence of macroporosity on preferential solute and colloid transport in unsaturated field soils. J. Contam. Hydrol. 107, 45-57. https://doi.org/10.1016/j.jconhyd.2009.03.004.

Champagne, O., Arain, M.A., Leduc, M., Coulibaly, P., McKenzie, S., 2020. Future shift in winter streamflow modulated by the internal variability of climate in southern Ontario. Hydrol. Earth Syst. Sci. 24, 3077-3096. https://doi.org/10.5194/hess-24-3077-2020.

Chen, F.-W., Liu, C.-W., 2012. Estimation of the spatial rainfall distribution using inverse distance weighting (IDW) in the middle of Taiwan. Paddy Water Environ. 10, 209-222. https://doi.org/10.1007/s10333-012-0319-1.

Chesnaux, R., Allen, D.M., Graham, G., 2007. Assessment of the impact of nutrient management practices on nitrate contamination in the Abbotsford-Sumas aquifer. Environ. Sci. Technol. 41, 7229-7234. https://doi.org/10.1021/es0704131.

Chik, A., 2020. Personal communications from PhD candidate, University of Waterloo.

Chin, D.A., 2006. Water-Resources Engineering. 2nd Ed. Pearson Prentice Hall, Upper Saddle River, NJ, USA.

Choi, Y., 1998. Urban effects on precipitation in the southern United States of America. Unpublished PhD dissertation. Louisiana State University and Agricultural and Mechanical College, Baton Rouge, LA, USA. https://digitalcommons.lsu.edu/gradschool_disstheses/6621.

Chow, R., Frind, M.E., Frind, E.O., Jones, J.P., Sousa, M.R., Rudolph, D.L., Molson, J.W., Nowak, W., 2016. Delineating baseflow contribution areas for streams – A model and methods comparison. J. Contam. Hydrol. 195, 11-22. https://doi.org/10.1016/j.jconhyd.2016.11.001.

Christie, M., Rudolph, D.L., Payment, P., Locas, A., 2009. Monitoring the occurrence of microbial contaminants within the wellhead protection area of a municipal well field in an agricultural setting. Microbial Transport and Survival in the Subsurface: First International Conference, Niagara-on-the-Lake, Ontario, Canada, 10-13 May 2009.

CH2MHILL, 2002. Final Report: Hydrogeological study to evaluate the GUDI status of the Mannheim West, Mannheim East, and Peaking well fields. Prepared for: The Regional Municipality of Waterloo. Oct 2002.

CH2MHILL, S.S. Papadopulos and Associates Inc. (SSPA), 2003. Alder Creek Groundwater Study: Final Report. Prepared for: The Regional Municipality of Waterloo, Kitchener, ON.

Collins, M., Knutti, R., Arblaster, J., Dufresne, J.-L., Fichefet, T., Friedlingstein, P., Gao, X., Gutowski Jr., W.J., Johns, T., Krinner, G., Shongwe, M., Tebaldi, C., Weaver, A.J., Wehner, M., 2013. Long-term Climate Change: Projections, Commitments and Irreversibility, in: Stocker, T.F., Qin, D., Plattner, G.-K., Tignor, M., Allen, S.K., Boschung, J., Nauels, A., Xia, Y., Bex, V., Midgley, P.M. (Eds.), Climate Change 2013: The Physical Science Basis. Contribution of Working Group I to the Fifth Assessment Report of the Intergovernmental Panel on Climate Change. Cambridge University Press, Cambridge, United Kingdom and New York, NY, USA. http://www.ipcc.ch/report/ar5/wg2/.

CPN International (CPN), 2013. CPN 503 Elite Hydroprobe: Operating manual. Dec 2013. V1.1. http://www.instrotek.com.

Crosbie, R.S., Peeters, L.J.M., Herron, N., McVicar, T.R., Herr, A., 2018. Estimating groundwater recharge and its associated uncertainty: Use of regression kriging and the chloride mass balance method. J. Hydrol. 561, 1063-1080. https://doi.org/10.1016/j.jhydrol.2017.08.003.

Crosbie, R.S., Scanlon, B.R., Mpelasoka, F.S., Reedy, R.C., Gates, J.B., Zhang, L., 2013. Potential climate change effects on groundwater recharge in the High Plains Aquifer, USA. Water Resour. Res. 49, 3936-3951. https://doi.org/10.1002/wrcr.20292.

Cubasch, U., Meehl, G.A., Boer, G.J., Stouffer, R.J., Dix, M., Noda, A., Senior, C.A., Raper, S., Yap, K.S., 2001. Projections of Future Climate Change, in: Houghton, J.T., Ding, Y., Griggs, D.J., Noguer, M., van der Linden, P.J., Dai, X., Maskell, K., Johnson, C.A. (Eds.), Climate Change 2001: The Scientific Basis. Contribution of Working Group I to the Third Assessment Report of the Intergovernmental Panel on Climate Change. Cambridge University Press, Cambridge, UK, pp. 525-582. https://www.ipcc.ch/report/ar3/wg1/.

Curriero, F.C., Patz, J.A., Rose, J.B., Lele, S., 2001. The association between extreme precipitation and waterborne disease outbreaks in the United States, 1948-1994. Am. J. Public Health 91(8), 1194-1199. https://doi.org/10.2105/AJPH.91.8.1194.

Dai, A., Trenberth, K.E., Qian, T., 2004. A global dataset of Palmer drought severity index for 1870-2002: Relationship with soil moisture and effects of surface warming. J. Hydrometeorol. 5(6), 1117-1130. https://doi.org/10.1175/JHM-386.1.

Daus, A.D., Frind, E.O., Sudicky, E.A., 1985. Comparative error analysis in finite element formulations of the advection-dispersion equation. Adv. Water Resour. 8(2), 86-95. https://doi.org/10.1016/0309-1708(85)90005-3.

DeBeer, C.M., Wheater, H.S., Carey, S.K., Chun, K.P., 2016. Recent climatic cryospheric, and hydrological changes over the interior of western Canada: a review and synthesis. Hydrol. Earth Syst. Sci. 20, 1573-1598. https://doi.org/10.5194/hess-20-1573-2016.

Delin, G.N., Healy, R.W., Landon, M.K., Böhlke, J.K., 2000. Effects of topography and soil properties on recharge at two sites in an agricultural field. J. Amer. Water Resour. Assoc. 36(6), 1401-1416. https://doi.org/10.1111/j.1752-1688.2000.tb05735.x.

Denby, B.R., Ketzel, M., Ellermann, T., Stojiljkovic, A., Kupiainen, K., Niemi, J.V., Norman, M., Johansson, C., Gustafsson, M., Blomqvist, G., Janhäll, S., Sundvor, I., 2016. Road salt emissions: A comparison of measurements and modelling using the NORTRIP road dust emission model. Atmos. Environ. 141, 508-522. https://doi.org/10.1016/j.atmosenv.2016.07.027.

Devlin, J.F., Sophocleous, M., 2005. The persistence of the water budget myth and its relationship to sustainability. Hydrogeol. J. 13: 549-554. https://doi.org/10.1007/s10040-004-0354-0.

de Vries, J.J., Simmers, I., 2002. Groundwater recharge: an overview of processes and challenges. Hydrogeol. J. 10, 5-17. https://doi.org/10.1007/s10040-001-0171-7.

Dewey, K.F., 1973. An analytical study of lake-effect snowfall. Unpublished PhD dissertation. University of Toronto, Toronto, ON.

DHI, 2017a. MIKE SHE Volume 2: Reference guide. Hørsholm, Denmark.

DHI, 2017b. MIKE SHE Online Help Files. http://doc.mikepoweredbydhi.help/webhelp/2017/mikeshe/index.htm. (Accessed 15.05.2017).

DHI, 2017c. MIKE SHE Volume 1: User guide. Hørsholm, Denmark.

DHI-WASY, 2011. FEFLOW 6.0 – Finite Element Subsurface Flow and Transport Simulation System. WASY GmbH. Berlin, Germany.

Dingman, S.L., 2015. Physical Hydrology, 3rd ed., Waveland Press Inc., Long Grove, IL, USA.

DMTI Spatial Inc. (DMTI), 2011. CanMap Streetfiles, major water regions, and minor water regions [computer files]. University of Waterloo Geospatial Centre, controlled access. GIS digital mapping data. (Accessed 29.03.2012).

Doherty, J., 2015. Calibration and uncertainty analysis for complex environmental models. Watermark Numerical Computing, Brisbane, Australia. ISBN: 978-0-9943786-0-6.

Domenico, P.A., Mifflin, M.D., 1965. Water from low-permeability sediments and land subsidence. Water Resour. Res. 1(4), 563-576. https://doi.org/10.1029/WR001i004p00563.

Domenico, P.A., Schwartz, F.W., 1998. Physical and chemical hydrogeology, second ed. John Wiley & Sons, Inc., New York.

Donohue, R.J., Roderick, M.L., McVicar, T.R., 2007. On the importance of including vegetation dynamics in Budyko's hydrological model. Hydrol. Earth Syst. Sci. 11, 983-995. https://doi.org/10.5194/hess-11-983-2007.

Donohue, R.J., Roderick, M.L., McVicar, T.R., 2010. Can dynamic vegetation information improve the accuracy of Budyko's hydrological model? J. Hydrol. 390, 23-34. https://doi.org/10.1016/j.jhydrol.2010.06.025.

Duan, Q., et al., 2006. Model Parameter Estimation Experiment (MOPEX): An overview of science strategy and major results from the second and third workshops. J. Hydrol. 320, 3-17. https://doi.org/10.1016/j.jhydrol.2005.07.031.

Duffield, G.M., 2019. Representative Values of Hydraulic Properties. HydroSOLVE, Inc. http://www.aqtesolv.com/aquifer-tests/aquifer_properties.htm.

Eaton, J.W., Bateman, D., Hauberg, S., 2011. GNU Octave. Edition 3 for Octave version 3.6.4. Manual for high-level interactive language for numerical computations. https://www.gnu.org/software/octave/download.html. (Accessed 03.08.2013).

Eberts, S.M., Böhlke, J.K., Kauffman, L.J., Jurgens, B.C., 2012. Comparison of particle-tracking and lumped-parameter age-distribution models for evaluating vulnerability of production wells to contamination. Hydrogeol. J. 20, 263-282. https://doi.org/10.1007/s10040-011-0810-6.

Eisenhauer, I.F., Hoover, C.M., Remais, J.V., Monaghan, A., Celada, M., Carlton, E.J., 2016. Estimating the risk of domestic water source contamination following precipitation events. Am. J. Trop. Med. Hyg. 94(6), 1403-1406. https://doi.org/10.4269/ajtmh.15-0600.

Enzenhoefer, R., Nowak, W., Helmig, R., 2012. Probabilistic exposure risk assessment with advective-dispersive well vulnerability criteria. Adv. Water Resour. 36, 121-132. https://doi.org/10.1016/j.advwatres.2011.04.018.

Espinosa, A.C., Mazari-Hiriart, M., Espinosa, R., Maruri-Avidal, L., Méndez, E., Arias, C.F., 2008. Infectivity and genome persistence of rotavirus and astrovirus in groundwater and surface water. Water Res. 42, 2618-2628. https://doi.org/10.1016/j.watres.2008.01.018.

Esri, HERE, Garmin, Intermap, increment P Corp., GEBCO, USGS, FAO, NPS, NRCAN, GeoBase, IGN, Kadaster NL, Ordnance Survey, Esri Japan, METI, Esri China (Hong Kong), swisstopo, © OpenStreetMap contributors, the GIS User Community, 2013. World topographic map. Obtained using ArcMap 10.3 software. http://goto.arcgisonline.com/maps/World_Topo_Map. (Accessed 06.05.2019).

Esri, HERE, Garmin, © OpenStreetMap contributors, the GIS user community, 2019a. World map. Obtained using ArcMap 10.3 software. http://goto.arcgisonline.com/maps/World_Light_Gray_Base. (Accessed 26.06.2019, 07.10.2019).

Esri, HERE, Garmin, © OpenStreetMap contributors, the GIS user community, 2019b. World map. Obtained using ArcMap 10.3 software. http://goto.arcgisonline.com/maps/World_Light_Gray_Reference. (Accessed 07.10.2019)

Faurès, J.-M., Goodrich, D.C., Woolhiser, D.A., Sorooshian, S., 1995. Impact of small-scale spatial rainfall variability on runoff modeling. J. Hydrol. 173, 309-326. https://doi.org/10.1016/0022-1694(95)02704-S.

Ferguson, C., de Roda Husman, A.M., Altavilla, N., Deere, D., Ashbolt, N., 2003. Fate and transport of surface water pathogens in watersheds. Crit. Rev. Environ. Sci. Technol. 33(3), 299-361. https://doi.org/10.1080/10643380390814497.

Ferré, T. 2016. Personal communications from Distinguished Professor, University of Arizona, Tucson, AZ, USA.

Fetter, C.W., 2001. Applied hydrogeology, 4th ed. Prentice Hall, Upper Saddle River, NJ, USA.

First Base Solutions Inc. (First Base Solutions), 2006. SWOOP: Orthophotography 2006. GIS digital mapping data. Obtained from University of Waterloo Geospatial Centre, controlled access. (Accessed 20.10.2015).

Freeze, A., Cherry, J., 1979. Groundwater. Prentice-Hall Inc., Englewood Cliffs, NJ, USA. 604p.

Frind, E.O., Molson, J. W., 2018. Issues and options in the delineation of well capture zones under uncertainty. Ground Water 56(3), 366-376. https://doi.org/10.1111/gwat.12644.

Frind, E.O., Molson, J.W., Rudolph, D.L., 2006. Well vulnerability: A quantitative approach for source water protection. Ground Water 44(5), 732-742. https://doi.org/10.1111/j.1745-6584.2006.00230.x.

Frind, E.O., Muhammad, D.S., Molson, J.W., 2002. Delineation of three-dimensional well capture zones for complex multi-aquifer systems. Ground Water 40(6), 586-598. https://doi.org/10.1111/j.1745-6584.2002.tb02545.x.

Gavin, H.P., 2009. MATLAB files for the Levenberg-Marquardt algorithm for nonlinear least squares curve-fitting problems. lm.m, lm_examp.m, lm_func.m, and lm_plots.m [computer files]. CE 281: Experimental Systems course, Department of Civil and Environmental Engineering, Duke University, Durham, NC, USA. Updated 12 Jan 2009. http://people.duke.edu/~hpgavin/ce281/. (Accessed 12.01.2019).

Gavin, H.P., 2019. The Levenberg-Marquardt algorithm for nonlinear least squares curve-fitting problems. Tutorial for CE 281: Experimental Systems course, Department of Civil and Environmental Engineering, Duke University, Durham, NC, USA. http://people.duke.edu/~hpgavin/ce281/. (Accessed 12.01.2019).

Gelhar, L.W., Welty, C., Rehfeldt, K.R., 1992. A critical review of data on field-scale dispersion in aquifers. Water Resour. Res. 28(7), 1955-1974. https://doi.org/10.1029/92WR00607.

Gentine, P., D'Odorico, P., Lintner, B.R., Sivandran, G., Salvucci, G., 2012. Interdependence of climate, soil, and vegetation as constrained by the Budyko curve. Geophys. Res. Lett. 39, L19404. https://doi.org/10.1029/2012GL053492.

Gibbons, J.D., Chakraborti, S., 1992. Nonparametric statistical inference. 3rd ed. Marcel Dekker, New York, NY, USA. 544pp.

Ginn, T.R., Wood, B.D, Nelson, K.E., Scheibe, T.D., Murphy, E.M., Clement, T.P., 2002. Processes in microbial transport in the natural subsurface. Adv. Water Resour. 25(8-12), 1017-1042. https://doi.org/10.1016/S0309-1708(02)00046-5.

Government of Canada, 2013. Weather Tools – FAQ: Frequently asked questions. https://ec.gc.ca/meteo-weather/default.asp?lang=En&n=108C6C74-1#ws41070341. Date modified: 5 Jul 2013. (Accessed 19.07.2017).

Government of Canada, 2017. Historical Data: Rainfall, snowfall, and temperature data for Ontario weather stations at Fergus, Roseville, Foldens, Waterloo Wellington 2, Woodstock, and Stratford. Computer files. http://climate.weather.gc.ca/historical_data/search_historic_data_e.html. (Accessed 07.11.2017).

Government of Canada, 2019. Historical Data: Rainfall, snowfall, and temperature data for the Roseville, ON, weather station [computer files]. http://climate.weather.gc.ca/historical_data/search_historic_data_e.html. (Accessed 18.01.2017, 05.05.2017, 07.07.2017, 15.01.2019).

Graham, D., 2017. Personal communications from senior engineer at DHI, Denmark.

Graham, D.N., Butts, M.B., 2005. Flexible integrated watershed modelling with MIKE SHE, in: Singh, V.P., Frevert, D.K. (Eds.), Watershed Models, CRC Press, Boca Raton, FL, USA, pp.245-272.

Grand River Conservation Authority (GRCA), 1998. Grand River Watershed data [computer file]. Subcatchment basins. Cambridge, Ontario: Grand River Conservation Authority. https://maps.grandriver.ca/data-gis.html. GIS digital mapping data. (Accessed 29.03.2012).

Grand River Conservation Authority (GRCA), 2017a. Daily rainfall and average temperature data from the Paris, Cambridge (Shades Mill), Baden, Burford, Laurel Creek, and Wellesley Dam climate stations [computer files]. https://data.grandriver.ca/downloads-monitoring.html. (Accessed 23.11.2017, 15.12.2017).

Grand River Conservation Authority (GRCA), 2017b. HEC2 cross-section files from "Alder Creek Floodline Mapping Study," Jan. 1997 [computer files]. Produced using information under License with the Grand River Conservation Authority. Copyright © Grand River Conservation Authority, 2017.

Greenwood, W.J., Buttle, J.M., 2018. Land cover controls on depression-focused recharge on the Oak Ridges Moraine, southern Ontario, Canada. Hydrol. Process. 32, 1909-1926. https://doi.org/10.1002/hyp.13130.

Gregersen, I.B., Madsen, H., Rosbjerg, D., Arnbjerg-Nielsen, K., 2013. A spatial and nonstationary model for the frequency of extreme rainfall events. Water Resour. Res. 49, 127-136. https://doi.org/10.1029/2012WR012570.

Guay, C., Nastev, M., Paniconi, C., Sulis, M., 2013. Comparison of two modeling approaches for groundwater–surface water interactions. Hydrol. Process. 27, 2258-2270. https://doi.org/10.1002/hyp.9323.

Gurdak, J.J., Roe, C.D., 2010. Review: Recharge rates and chemistry beneath playas of the High Plains aquifer, USA. Hydrogeol. J. 18, 1747-1772. https://doi.org/10.1007/s10040-010-0672-3.

Hamada, A., Murayama, Y., Takayabu, Y.N., 2014. Regional characteristics of extreme rainfall extracted from TRMM PR measurements. J. Clim. 27, 8151-8169. https://doi.org/10.1175/JCLI-D-14-00107.1.

Hansen, S., Thorsen, M., Pebesma, E.J., Kleeschulte, S., Svendsen, H., 1999. Uncertainty in simulated nitrate leaching due to uncertainty in input data. A case study. Soil Use and Manage. 15, 167-175. https://doi.org/10.1111/j.1475-2743.1999.tb00083.x.

Harvey, R.W., George, L.H., Smith, R.L., LeBlanc, D.R., 1989. Transport of microspheres and indigenous bacteria through a sandy aquifer: results of natural- and forced-gradient tracer experiments. Environ. Sci. Technol. 23(1), 51-56. https://doi.org/10.1021/es00178a005.

Hayashi, M., van der Kamp, G., Rosenberry, D.O., 2016. Hydrology of prairie wetlands: Understanding the integrated surface-water and groundwater processes. Wetlands 36(Suppl 2), S237-S254. https://doi.org/10.1007/s13157-016-0797-9.

He, X., Refsgaard, J.C., Sonnenborg, T.O., Vejen, F., Jensen, K.H., 2011. Statistical analysis of the impact of radar rainfall uncertainties on water resources modeling. Water Resour. Res. 47, W09526. https://doi.org/10.1029/2011WR010670.

He, X., Sonnenborg, T.O., Refsgaard, J.C., Vejen, F., Jensen, K.H., 2013. Evaluation of the value of radar QPE data and rain gauge data for hydrological modeling. Water Resour. Res. 49, 5989-6005. https://doi.org/10.1002/wrcr.20471.

Healy, R.W., 2010. Estimating groundwater recharge. Cambridge University Press, Cambridge, UK.

Healy, R.W., Cook, P.G., 2002. Using groundwater levels to estimate recharge. Hydrogeol. J. 10, 91-109. https://doi.org/10.1007/s10040-001-0178-0.

Hérivaux, C., Orban, P., Brouyère, S., 2013. Is it worth protecting groundwater from diffuse pollution with agri-environmental schemes? A hydro-economic modeling approach. J. Environ. Manage 128, 62-74. https://doi.org/10.1016/j.jenvman.2013.04.058.

Herschy, R.W., 1973. The magnitude of errors at flow measurements stations. Proc. of the Koblenz Symp. on Hydrometry (1970). IAHS Publ. 99, pp. 109-131. https://iahs.info/uploads/dms/099013.pdf.

Hess, T., Daccache, A., Daneshkhah, A., Knox, J., 2016. Scale impacts on spatial variability in reference evapotranspiration. Hydrol. Sci J. 61(3), 601-609. https://doi.org/10.1080/02626667.2015.1083105.

Hillier, C.E., 2014. Establishing metrics to quantify the vulnerability of municipal supply wells to contaminants from surface water sources. Unpublished MSc. thesis, University of Waterloo, Waterloo, ON. http://hdl.handle.net/10012/8683.

Hrudey, S.E., Huck, P.M., Payment, P., Gillham, R.W., Hrudey, E.J., 2002. Walkerton: Lessons learned in comparison with waterborne outbreaks in the developed world. J. Environ. Eng. Sci. 1, 397-407. https://doi.org/10.1139/s02-031.

Hrudey, S.E., Payment, P., Huck, P.M., Gillham, R.W., Hrudey, E.J., 2003. A fatal waterborne disease epidemic in Walkerton, Ontario: comparison with other waterborne outbreaks in the developed world. Water Sci. Technol. 47(3), 7-14. https://doi.org/10.2166/wst.2003.0146.

Huff, F.A., 1970. Sampling errors in measurement of mean precipitation. J. Appl. Meteorol. 9(1), 35-44. https://doi.org/10.1175/1520-0450%281970%29009%3C0035%3ASEIMOM%3E2.0.CO%3B2.

Huff, F.A., Schickedanz, P.T., 1972. Space-time uncertainties in precipitation measurement. Proc. Int. Symp. on Uncertainties in Hydrol. and Water Resour. Syst., 11-14 Dec 1972. Vol. I, 395-409. Univ. of Arizona, Tucson, AZ.

Hunter, P.R., 2003. Climate change and waterborne and vector-borne disease. J. Appl. Microbiol. 94(S1), 37-46. https://doi.org/10.1046/j.1365-2672.94.s1.5.x.

Hvorslev, M.J., 1951. Time lag and soil permeability in ground-water observations. U.S. Army Corps of Engrs. Waterways Exper. Sta. Bull no. 36.

Hwang, H.-T., Park, Y.-J., Sudicky, E.A., Berg, S.J., McLaughlin, R., Jones, J.P., 2018. Understanding the water balance paradox in the Athabasca River Basin, Canada. Hydrol. Process. 32, 729-746. https://doi.org/10.1002/hyp.11449.

Hydrological Services PTY LTD, 2013. Instruction Manual: Tipping Bucket Raingauge Model TB3. Issue 11: 12 Mar 2013. http://www.hydrologicalservices.com. (Accessed 14.07.2014)

Iman, R.L., Conover, W.J., 1982. A distribution-free approach to inducing rank correlation among input variables. Commun. Statist.-Simula. Computa. 11(3), 311-334. https://doi.org/10.1080/03610918208812265.

IPCC, 2013. Summary for policymakers, in: Stocker, T.F., Qin, D., Plattner, G.-K., Tignor, M., Allen, S.K., Boschung, J., et al. (Eds.), Climate Change 2013: The Physical Science Basis. Contribution of Working Group I to the Fifth Assessment Report of the Intergovernmental Panel on Climate Change. Cambridge University Press, Cambridge, UK. https://www.ipcc.ch.

Irmak, S., Istanbulluoglu, E., Irmak, A., 2008. An evaluation of evapotranspiration model complexity against performance in comparison with Bowen ratio energy balance latent heat measurements. Trans. ASABE 51, 1295-1310. https://doi.org/10.13031/2013.25246.

Isensee, A.R., Sadeghi, A.M., 1995. Long-term effect of tillage and rainfall on herbicide leaching to shallow groundwater. Chemosphere. 30 (4), 671-685. https://doi.org/10.1016/0045-6535(94)00433-U.

Istanbulluoglu, E., Wang, T., Wright, O.M., Lenters, J.D., 2012. Interpretation of hydrologic trends from a water balance perspective: The role of groundwater storage in the Budyko hypothesis. Water Resour. Res. 48, W00H16. https://doi.org/10.1029/2010WR010100.

Jang, D., Choi, G., Park, H., 2019. Adaptation of multiple regression analysis to identify effective factors of water losses in water distribution systems. Smart Water 4:1. https://doi.org/10.1186/s40713-018-0013-6.

Jiang, C., Shaw, K.S., Upperman, C.R., Blythe, D., Mitchell, C., Murtugudde, R., Sapkota, A.R., Sapkota, A., 2015. Climate change, extreme events and increased risk of salmonellosis in Maryland, USA: Evidence for coastal vulnerability. Environ. Int. 83, 58-62. https://doi.org/10.1016/j.envint.2015.06.006.

Ju, J. 2016. Fate and transport of land applied waste greenhouse feed water during field infiltration experiments. Unpublished MSc. thesis, University of Waterloo, Waterloo, ON, Canada. 161pp. http://hdl.handle.net/10012/10428.

Jyrkama, M.I., Sykes, J.F., 2007. The impact of climate change on spatially varying groundwater recharge in the Grand River Watershed (Ontario). J. Hydrol. 338, 237-250. https://doi.org/10.1016/j.jhydrol.2007.02.036.

Kampf, S.K., Burges, S.J., 2010. Quantifying the water balance in a planar hillslope plot: Effects of measurement errors on flow prediction. J. Hydrol. 380, 191-202. https://doi.org/10.1016/j.jhydrol.2009.10.036.

Kent, R., Landon, M.K., 2013. Trends in concentrations of nitrate and total dissolved solids in public supply wells of the Bunker Hill, Lytle, Rialto, and Colton groundwater subbasins, San Bernardino County, California: Influence of legacy land use. Sci. Total Environ. 452-453, 125-136. https://doi.org/10.1016/j.scitotenv.2013.02.042.

Knappett, P.S.K., Du, J. Liu, P., Horvath, V., Mailloux, B.J., Feighery, J., van Geen, A., Culligan, P.J., 2014. Importance of reversible attachment in predicting *E. coli* transport in saturated aquifers from column experiments. Adv. Water Resour. 63, 120-130. https://doi.org/10.1016/j.advwatres.2013.11.005.

Koch, J., 2009. Evaluating regional aquifer vulnerability and BMP performance in an agricultural environment using a multi-scale data integration approach. Unpublished MSc. thesis, University of Waterloo, Waterloo, ON. http://hdl.handle.net/10012/4492.

Krajewski, W.F., Ciach, G.J., Habib, E., 2003. An analysis of small-scale rainfall variability in different climatic regions. Hydrol. Sci. J. 48(2), 151-162. https://doi.org/10.1623/hysj.48.2.151.44694.

Kristensen, K.J., Jensen, S.E., 1975. A model for estimating actual evapotranspiration from potential evapotranspiration. Nordic Hydrol. 6, 170-188. https://doi.org/10.2166/nh.1975.0012.

Kvitsand, H.M., Ilyas, A., Østrhus, S.W., 2015. Rapid bacteriophage MS2 transport in an oxic sandy aquifer in cold climate: Field experiments and modeling. Water Resour. Res. 51, 9725-9745. https://doi.org/10.1002/2015WR017863.

Lall, U., Rajagopalan, B., Tarboton, D.G., 1996. A nonparametric wet/dry spell model for resampling daily precipitation. Water Resour. Res. 32(9), 2803-2823. https://doi.org/10.1029/96WR00565.

Leij, F.J., Alves, W.J., van Genuchten, M.Th., Williams, J.R., 1996. The UNSODA Unsaturated Soil Hydraulic Database: User's Manual Version 1.0. U.S. Environmental Protection Agency, Cincinnati, OH, USA. EPA/600/R-96/095 (NTIS 97-149496). https://cfpub.epa.gov/si/.

Lerner, D.N., Issar, A.S., Simmers, I., 1990. Groundwater recharge. A guide to understanding and estimating natural recharge. International contributions to hydrogeology, Volume 8. International Association of Hydrogeologists. Heise, Hannover, Germany. https://iah.org/education/professionals/out-of-print-books.

Li, Z., Brissette, F., Chen, J., 2013. Finding the most appropriate precipitation probability distribution for stochastic weather generation and hydrological modelling in Nordic watersheds. Hydrol. Process. 27, 3718-3729. https://doi.org/10.1002/hyp.9499.

Linsley, R.K., Kohler, M.A., 1951. Variations in storm rainfall over small areas. Trans. Amer. Geophys. Union. 32(2), 245-250. https://doi.org/10.1029/TR032i002p00245.

Loschko, M., Wöhling, T., Rudolph, D.L., Cirpka, O.A., 2016. Cumulative relative reactivity: A concept for modeling aquifer-scale reactive transport. Water Resour. Res. 52, 8117-8137. https://doi.org/10.1002/2016WR019080.

Mallén, G., Maloszewski, P., Flynn, R., Rossi, P., Engel, M., Seiler, K.-P., 2005. Determination of bacterial and viral transport parameters in a gravel aquifer assuming linear kinetic sorption and desorption. J. Hydrol. 306, 21-36. https://doi.org/10.1016/j.jhydrol.2004.08.033.

Martin, P.J., Frind, E.O., 1998. Modeling a complex multi-aquifer system: The Waterloo Moraine. Ground Water 36(4), 679-690. https://doi.org/10.1111/j.1745-6584.1998.tb02843.x.

Marvel, K., Bonfils, C., 2013. Identifying external influences on global precipitation. PNAS 110(48), 19301-19306. https://doi.org/10.1073/pnas.1314382110.

Matrix Solutions Inc. (Matrix), S.S. Papadopulos and Associates Inc. (SSPA), 2014a. Region of Waterloo Tier Three Water Budget and Local Area Risk Assessment, Model Calibration and Water Budget Report. Prepared for: The Regional Municipality of Waterloo. Waterloo, ON. Aug. 2014.

Matrix Solutions Inc. (Matrix), S.S. Papadopulos and Associates Inc. (SSPA), 2014b. Region of Waterloo Tier Three Water Budget and Local Area Risk Assessment. Final Report, Sep. 2014. Prepared for: Region of Waterloo. https://www.sourcewater.ca/en/source-protection-areas/resources/Documents/Grand/RMOW-September-2014-WQRA_chpt-1-10.pdf.

McDonnell, J.J., Sivapalan, M., Vaché, K., Dunn, S., Grant, G., Haggerty, R., Hinz, C., Hooper, R., Kirchner, J., Roderick, M.L., Selker, J., Weiler, M., 2007. Moving beyond heterogeneity and process complexity: A new vision for watershed hydrology. Water Resour. Res. 43, W07301. https://doi.org/10.1029/2006WR005467.

McLaren, R.G., 2012. Grid Builder: A pre-processor for 2-D, triangular element, finite element programs. University of Waterloo Groundwater Simulations Group. Code Revision 35, Build Date 30.04.2012. User manual revised 15.12.2011. https://www.aquanty.com/hgs-download/. (Accessed 28.08.2018).

Menkveld, P.G., 2017. Personal communications from MSc. Candidate, University of Waterloo.

Menkveld, P.G., 2019. A field study of event based, seasonally affected, depression focused recharge in glaciated terrain. Unpublished MSc. thesis. University of Waterloo, Waterloo, ON, Canada. 144p. http://hdl.handle.net/10012/14568.

Menkveld, P.G., Wiebe, A.J., Rudolph, D.L., 2015. Monitoring of event-based, depression focussed recharge to a shallow unconfined aquifer near a municipal well in the Alder Creek Subwatershed, SW Ontario. Presentation at: IAH-CNC 2015 Waterloo Conference, Waterloo, ON, Canada, 27-30.10.2015.

Metcalfe, J.R., Routledge, B., Devine, K., 1997. Rainfall measurement in Canada: Changing observational methods and archive adjustment procedures. J. Clim. 10(1), 92-101. https://doi.org/10.1175/1520-0442(1997)010<0092:RMICCO>2.0.CO;2.

Meyer, P., Martin, P., Brouwers, B., Wootton, R., Hodgins, E., 2017. Using source water protection models to manage an unexpected water supply shutdown; A case study from the Region of Waterloo. Proc. GeoOttawa 2017: 70th Canadian Geotechnical Conference and 12th CGS/IAH-CNC Groundwater Conference, Ottawa, ON, Canada, 1-4 Oct 2017.

Mileham, L., Taylor, R., Thompson, J., Todd, M., Tindimugaya, C., 2008. Impact of rainfall distribution on the parameterization of a soil-moisture balance model of groundwater recharge in equatorial Africa. J. Hydrol. 359, 46-58. https://doi.org/10.1016/j.jhydrol.2008.06.007.

Missori, C., 2015. Study of hydrogeologic characterization of a glaciofluvial aquifer of Ontario (CANADA): A comparison of field and laboratory methods to estimate hydraulic conductivity in heterogeneous porous media. Unpublished MSc. thesis. Sapienza University of Rome, Rome, Italy. 164p.

Molénat, J., Gascuel-Odoux, C., 2002. Modelling flow and nitrate transport in groundwater for the prediction of water travel times and of consequences of land use evolution on water quality. Hydrol. Process. 16, 479-492. https://doi.org/10.1002/hyp.328.

Moorhead, J.E., Marek, G.W., Colaizzi, P.D., Gowda, P.H., Evett, S.R., Brauer, D.K., Marek, T.H., Porter, D.O., 2017. Evaluation of sensible heat flux and evapotranspiration estimates using a surface layer scintillometer and a large weighing lysimeter. Sensors 17, 2350. https://doi.org/10.3390/s17102350.

Murphy, H.M., Prioleau, M.D., Borchardt, M.A., Hynds, P.D., 2017. Review: Epidemiological evidence of groundwater contribution to global enteric disease, 1948-2015. Hydrogeol. J. 25, 981-1001. https://doi.org/10.1007/s10040-017-1543-y.

Myers, D.N., Stoeckel, D.M., Bushon, R.N., Francy, D.S., Brady, A.M.G., 2014. Fecal indicator bacteria. U.S. Geol. Surv. Tech. of Water-Resour. Invest., 09-A7.1 (version 2.1). https://doi.org/10.3133/twri09A7.1.

Nalarajan, N. A., Govindarajan, S.K., Nambi, I.M., 2019. Numerical modeling on flow of groundwater energies in transient well capture zones. Environ. Earth Sci. 78, 142. https://doi.org/10.1007/s12665-019-8176-5.

Nandakumar, N., Mein, R.G., 1997. Uncertainty in rainfall-runoff model simulations and the implications for predicting the hydrologic effects of land-use change. J. Hydrol. 192, 211-232. https://doi.org/10.1016/S0022-1694(96)03106-X.

Neff, B.P., Day, S.M., Piggott, A.R., Fuller, L.M., 2005. Base flow in the Great Lakes basin. Date Posted: 29 Nov 2005. U.S. Geological Survey Sci. Inv. Rep. 2005-5217. https://pubs.usgs.gov/sir/2005/5217/pdf/SIR2005-5217.pdf.

Natural Environment Research Council (NERC), 2017. BGS Groundhog® Desktop Copyright © BGS/NERC (2019). Version 1.10.0. British Geological Survey, UK. Computer program. http://www.bgs.ac.uk/research/environmentalmodelling/.

Obled, Ch., Wendling, J., Beven, K., 1994. The sensitivity of hydrological models to spatial rainfall patterns: an evaluation using observed data. J. Hydrol. 159, 305-333. https://doi.org/10.1016/0022-1694(94)90263-1.

O'Connor, D.R., 2002. Report of the Walkerton Inquiry. Part 1. The events of May 2000 and related issues. The Walkerton Inquiry, Toronto, ON. http://www.archives.gov.on.ca/en/e_records/walkerton/index.html.

Onof, C., Chandler, R.E., Kakou, A., Northrop, P., Wheater, H.S., Isham, V., 2000. Rainfall modelling using Poisson-cluster processes: a review of developments. Stoch. Environ. Res. Risk Assess. 14, 384-411. https://doi.org/10.1007/s004770000043.

Ontario Geological Survey (OGS), 2010. Surficial geology of Southern Ontario. Ontario Geological Survey, Miscellaneous Release--Data 128-REV. ISBN 978-1-4435-2482-7. Obtained from Matrix Solutions Inc., controlled access. (Accessed 29.06.2016).

Ontario Geological Survey (OGS), 2017. Geotechnical Boreholes. Computer file. https://www.mndm.gov.on.ca/en/mines-and-minerals/applications/ogsearth/geotechnical-boreholes. Last modified: 23.05.2017. (Accessed 14.08.2017).

Ontario Ministry of Natural Resources (OMNR), 2007. Daily weather data [computer file]. Digital Archive of Canadian Climatological Data. Obtained from Matrix Solutions Inc., controlled access. (Accessed 28.04.2016).

Ontario Ministry of Natural Resources (OMNR), 2008. Southern Ontario Land Resource Information System (SOLRIS) Land Use Data [computer files]. Obtained from University of Waterloo Geospatial Centre, Waterloo, ON, controlled access. (Accessed 03.06.2009).

Ontario Ministry of Natural Resources (OMNR), 2010. Natural Resources and Values Information System: Spot Heights. Topography elevations, 30 m resolution. GIS digital mapping data. Obtained from University of Waterloo Map and Design Library, controlled access.

Ontario Ministry of Natural Resources and Forestry (OMNRF), 2016. Watershed, Quaternary [computer file]. Revised 4 Jan 2010. https://www.ontario.ca/page/land-information-ontario. (Accessed 01.02.2017).

Ontario Ministry of the Environment, Conservation, and Parks (OMECP), 2018. Well records. https://www.ontario.ca/environment-and-energy/map-well-records. Updated 28.06.2018. (Accessed 25.07.2018).

Ontario Ministry of the Environment, Conservation, and Parks (OMECP), 2019. Guide for applying for drinking water works permit amendments, licence amendments. https://www.ontario.ca/page/guide-applying-drinking-water-works-permit-amendments-licence-amendments. Updated 05.04.2019. (Accessed 29.04.2019).

Oudin, L., Perrin, C., Mathevet, T., Andréassian, V, Michel, C. 2006. Impact of biased and randomly corrupted inputs on the efficiency and the parameters of watershed models. J. Hydrol. 320, 62-83. https://doi.org/10.1016/j.jhydrol.2005.07.016.

Paixao, E., Monirul Qader Mirza, M., Shephard, M.W., Auld, H., Klaassen, J., Smith, G., 2015. An integrated approach for identifying homogeneous regions of extreme rainfall events and estimating IDF curves in southern Ontario, Canada: Incorporating radar observations. J. Hydrol. 528, 734-750. https://doi.org/10.1016/j.jhydrol.2015.06.015.

Parker, R., Arnold, J.G., Barrett, M., Burns, L., Carrubba, L., Neitsch, S.L., Snyder, N.J., Srinivasan, R., 2007. Evaluation of three watershed-scale pesticide environmental transport and fate models. J. Am. Water Resour. Assoc. 43(6), 1424-1443. https://doi.org/10.1111/j.1752-1688.2007.00101.x.

Pasha, E., 2018. Quantifying groundwater recharge during dynamic seasonality in cold climates. Unpublished MSc. thesis, University of Waterloo, Waterloo, ON. 141p. http://hdl.handle.net/10012/12883.

Paturel, J.E., Servat, E., Vassiliadis, A., 1995. Sensitivity of conceptual rainfall-runoff algorithms to errors in input data – case of the GR2M model. J. Hydrol. 168, 111-125. https://doi.org/10.1016/0022-1694(94)02654-T.

Peckenham, J.M., Thornton, T., Whalen, B., 2009. Sand and gravel mining: effects on ground water resources in Hancock county, Maine, USA. Environ. Geol. 56, 1103-1114. https://doi.org/10.1007/s00254-008-1210-7.

Peel, M.C., Finlayson, B.L., McMahon, T.A., 2007. Updated world map of the Köppen-Geiger climate classification. Hydrol. Earth Syst. Sci. 11, 1633-1644. https://doi.org/10.5194/hess-11-1633-2007.

Perera, N., Gharabaghi, B., Howard, K., 2013. Groundwater chloride response in the Highland Creek watershed due to road salt application: A re-assessment after 20 years. J. Hydrol. 479, 159-168. https://doi.org/10.1016/j.jhydrol.2012.11.057.

Piersol, J., 2005. Evaluating groundwater supply sustainable capacity and pollution threats for an urban well field in a semi-arid coastal region: Aguadulce, Panama. Unpublished MSc. thesis, University of Waterloo, Waterloo, ON. 147p.

Province of Ontario, 2002. Nutrient Management Act. O. Reg. 267/03: General. S.O. 2002, c.4. https://www.ontario.ca/laws/regulation/030267. Updated 14.04.2020. (Accessed 31.08.2020).

Province of Ontario, 2006. Clean Water Act. S.O. 2006, c 22. https://www.ontario.ca/laws/statute/06c22. Updated 22.03.2017. (Accessed 11.02.2019).

Province of Ontario, 2018. 2017 Technical rules under the Clean Water Act. https://www.ontario.ca/page/2017-technical-rules-under-clean-water-act. Updated 28.06.2018. (Accessed 11.02.2019).

Raes, D., 2009. The ETo Calculator: Evapotranspiration from a reference surface. Reference Manual Version 3.1. Food and Agriculture Organization of the United Nations, Land and Water Division, Rome, IT. http://www.fao.org/land-water/databases-and-software/eto-calculator/en/. (Accessed 01.02.2018).

Rayne, T.W., Bradbury, K.R., Zhen, C., 2014. Correct delineation of capture zones using particle tracking under transient conditions. Ground Water 52(3), 332-334. https://doi.org/10.1111/gwat.12141.

Refsgaard, J.C., Storm, B., 1995. MIKE SHE, in: Singh, V.P. (Ed.), Computer Models of Watershed Hydrology. Water Resour. Publ., Highlands Ranch, CO, USA. pp.809-846.

Region of Waterloo (ROW), 2010. Land use data for Kitchener (2010-08-31), Waterloo (2009-09-24), and Wilmot (2009-09-24) [computer files]. Region of Waterloo, Kitchener, ON. Obtained from Matrix Solutions Inc., controlled access. (Accessed 21.06.2016).

Renard, F., 2017. Local influence of south-east France topography and land cover on the distribution and characteristics of intense rainfall cells. Theor. Appl. Climatol. 128, 393-405. https://doi.org/10.1007/s00704-015-1698-1.

Rizak, S., Hrudey, S.E., 2007. Achieving safe drinking water – risk management based on experience and reality. Environ. Rev. 15, 169-174. https://doi.org/10.1139/A07-005.

Rockhold, M.L., Zhang, Z.F., Bott, Y.-J., 2016. Scale-dependent solute dispersion in variably saturated porous media. Pacific Northwest National Laboratory, Richland, WA, USA. PNNL-25146. https://beta11.pnnl.gov/publications/scale-dependent-solute-dispersion-variably-saturated-porous-media.

Rodriguez-Iturbe, I., Porporato, A., Ridolfi, L., Isham, V., Cox, D.R., 1999. Probabilistic modelling of water balance at a point: The role of climate, soil, and vegetation. Proc. R. Soc. Lond. A. 455, 3789-3805. https://doi.org/10.1098/rspa.1999.0477.

Rosenthal, J.S., 2005. Struck by lightning: The curious world of probabilities. HarperCollins, Toronto, ON.

Ryan, J.N., Elimelech, M., 1996. Review: Colloid mobilization and transport in groundwater. Colloid. Surf. A 107, 1-56. https://doi.org/10.1016/0927-7757(95)03384-X.

Sadeghi, A.M., Isensee, A.R., 1994. Spatial distribution of atrazine residues in soil and shallow groundwater: effect of tillage and rainfall timing. Agric. Ecosyst. Environ. 48, 67-76. https://doi.org/10.1016/0167-8809(94)90076-0.

Sanderson, M.E.L., 1998. The Grand climate: weather & water in the Grand River Basin. Grand River Foundation, Cambridge, ON.

Sandvik, B., 2009. World borders dataset. GIS digital mapping data. http://thematicmapping.org/downloads/world_borders.php.

Sapriza-Azuri, G., Jódar, J., Navarro, V., Slooten, L.J., Carrera, J., Gupta, H.V., 2015. Impacts of rainfall spatial variability on hydrogeological response. Water Resour. Res. 51, 1300-1314. https://doi.org/10.1002/2014WR016168.

Scanlon, B.R., Goldsmith, R.S., 1997. Field study of spatial variability in unsaturated flow beneath and adjacent to playas. Water Resour. Res. 33(10), 2239-2252. https://doi.org/10.1029/97WR01332.

Schaake, J., Cong, S., Duan, Q., 2006. The US MOPEX data set. IAHS Publ. 307. https://iahs.info/uploads/dms/13600.04-9-28-SCHAAKE.pdf.

Schaap, M.G., Liej, F.J., van Genuchten, M. Th., 1999. A Bootstrap-neural network approach to predict soil hydraulic parameters, in: M. Th. van Genuchten, et al. (Eds.), Characterization and Measurements of the Hydraulic Properties of Unsaturated Porous Media, University of California at Riverside, Riverside, CA, USA. pp. 1237-1250.

Schijven, J.F., Hassanizadeh, S.M., 2000. Removal of viruses by soil passage: Overview of modeling, processes, and parameters. Crit. Rev. Environ. Sci. Technol. 30(1), 49-127. https://doi.org/10.1080/10643380091184174.

Schijven, J.F., Hassanizadeh, S.M., de Roda Husman, A.M., 2010. Vulnerability of unconfined aquifers to virus contamination. Water Res. 44(4), 1170-1181. https://doi.org/10.1016/j.watres.2010.01.002.

Schijven, J.F., Hoogenboezem, W., Hassanizadeh, S.M., Peters, J.H., 1999. Modeling removal of bacteriophages MS2 and PRD1 by due recharge at Castricum, Netherlands. Water Resour. Res. 35(4), 1101-1111. https://doi.org/10.1029/1998WR900108.

Schmidt, T.G., Franko, U., Meissner, R., 2008. Uncertainties in large-scale analysis of agricultural land use – A case study for simulation of nitrate leaching. Ecol. Model. 217, 174-180. https://doi.org/10.1016/j.ecolmodel.2008.06.020.

Schuurmans, J.M., Bierkens, M.P.F., 2007. Effect of spatial distribution of daily rainfall on interior catchment response of a distributed hydrological model. Hydrol. Earth Sys. Sci. 11, 677-693. https://doi.org/10.5194/hess-11-677-2007.

Scibek, J., Allen, D.M., 2006. Modeled impacts of predicted climate change on recharge and groundwater levels. Water Resour. Res. 42, W11405. https://doi.org/10.1029/2005WR004742.

Scurlock, J.M.O., Asner, G.P., Gower, S.T., 2001. Worldwide Historical Estimates of Leaf Area Index, 1932-2000. ORNL Tech. Memo. TM-2001/268. Oak Ridge National Laboratory, Oak Ridge, TN, USA. https://doi.org/10.2172/814100.

Seglenieks, F., 2017. University of Waterloo Weather Station Data Archives [computer files]. http://weather.uwaterloo.ca/data.html. (Accessed 05.05.2017).

Sene, K.J., 1996. Meteorological estimates for the water balance of a sparse vine crop growing in semiarid conditions. J. Hydrol. 179, 259-280. https://doi.org/10.1016/0022-1694(95)02828-5.

Sharma, A., Mehrotra, R., 2010. Rainfall generation, in: Testik, F.Y., Gebremichael, M. (Eds.), Rainfall: State of the Science. Geophysical Monograph 191. American Geophysical Union, Washington, DC, USA. pp. 215-246. https://doi.org/10.1029/GM191.

Shifflett, S., 2018. Personal communications from Water Resources Engineer, Grand River Conservation Authority.

Shook, K., Pomeroy, J., 2012. Changes in the hydrological character of rainfall on the Canadian prairies. Hydrol. Process. 26, 1752-1766. https://doi.org/10.1002/hyp.9383.

Simonovic, S.P., Schardong, A., Sandink, D., 2017. Mapping extreme rainfall statistics for Canada under climate change using updated intensity-duration-frequency curves. J. Water Resour. Plann. Manage. 143(3): 04016078. https://doi.org/10.1061/(ASCE)WR.1943-5452.0000725.

Singh, V.P., 1992. Elementary Hydrology. Prentice Hall, Englewood Cliffs, NJ, USA.

Sinton, L.W., Finlay, R.K., Pang, L., Scott, D.M., 1997. Transport of bacteria and bacteriophages in irrigated effluent and through and alluvial gravel aquifer. Water Air Soil Pollut. 98, 17-42. https://doi.org/10.1007/BF02128648.

Sousa, M.R., 2013. Using numerical models for managing water quality in public supply wells. Unpublished PhD dissertation. University of Waterloo, Waterloo, ON. 149p. http://hdl.handle.net/10012/7801.

Sousa, M.R., Frind, E.O., Rudolph, D.L., 2013a. An integrated approach for addressing uncertainty in the delineation of groundwater management areas. J. Contam. Hydrol. 148, 12-24. https://doi.org/10.1016/j.jconhyd.2013.02.004.

Sousa, M.R., Jones, J.P., Frind, E.O., Rudolph, D.L., 2013b. A simple method to assess unsaturated zone time lag in the travel time from ground surface to receptor. J. Contam. Hydrol. 144(1), 138-151. https://doi.org/10.1016/j.jconhyd.2012.10.007.

Sousa, M.R., Rudolph, D.L., Frind, E.O., 2014. Threats to groundwater resources in urbanizing watersheds: The Waterloo Moraine and beyond. Can. Water Resour. J., 39:2, 193-208. https://doi.org/10.1080/07011784.2014.914801.

Stantec Consulting Ltd. (Stantec), 2012. Nitrate management study: Production Well K26. Prepared for: Regional Municipality of Waterloo. December 2012.

Stantec Consulting Ltd. (Stantec), 2013. Mannheim West well field performance and water quality evaluation: Production Well K22A. Prepared for: Regional Municipality of Waterloo. April 2013.

Stisen, S., Tumbo, M., 2015. Interpolation of daily raingauge data for hydrological modelling in data sparse regions using pattern information from satellite data. Hydrolog. Sci. J. 60(11), 1911-1926. https://doi.org/10.1080/02626667.2014.992789.

Sudicky, E., 2019. Personal communications from Professor Emeritus, Quantitative Hydrogeology, University of Waterloo.

Suriano, Z.J., Leathers, D.J., 2017. Synoptic climatology of lake-effect snowfall conditions in the eastern Great Lakes region. Int. J. Climatol. 37, 4377-4389. https://doi.org/10.1002/joc.5093.

Tarpanelli, A., Franchini, M., Brocca, L., Camici, S., Melone, F., Moramarco, T., 2012. A simple approach for stochastic generation of spatial rainfall patterns. J. Hydrol 472-473, 63-76. https://doi.org/10.1016/j.jhydrol.2012.09.010.

Taylor, J.R., 1997. An Introduction to Error Analysis: The Study of Uncertainties in Physical Measurements, second ed. University Science Books, Sausalito, CA, USA.

Tecplot, Inc. (Tecplot), 2017. Tecplot 360 EX: User's manual. Release 3. Data visualization and analysis software. www.tecplot.com.

Thodal, C.E., 1997. Hydrogeology of Lake Tahoe Basin, California and Nevada, and results of a ground-water quality monitoring network, water years 1990–92. U.S. Geological Survey Water-Resour. Inv. Rep. 97-4072. https://pubs.usgs.gov/wri/1997/4072/report.pdf.

Tosomeen, C.A.S., 1991. Modeling the effects of depression focusing on groundwater recharge. Unpublished MSc. thesis, University of Minnesota, Minneapolis, MN.

Trenberth, K.E., 2011. Changes in precipitation with climate change. Clim. Res. 47, 123-138. https://doi.org/10.3354/cr00953.

Tsanis, I.K., Gad, M.A., 2001. A GIS precipitation method for analysis of storm kinematics. Environ. Modell. Softw. 16, 273-281. https://doi.org/10.1016/S1364-8152(00)00068-2.

Unc, A., Goss, M.J., 2003. Movement of faecal bacterial through the Vadose zone. Water Air Soil Pollut. 149(1-4), 327-337. https://doi.org/10.1023/A:1025693109248.

van der Kamp, G., Hayashi, M., 2009. Groundwater-wetland ecosystem interaction in the semiarid glaciated plains of North America. Hydrogeol. J. 17, 203-214. https://doi.org/10.1007/s10040-008-0367-1.

Van Dyke, M.I., Morton, V.K., McLellan, N.L., Huck, P.M., 2010. The occurrence of *Campylobacter* in river water and waterfowl within a watershed in southern Ontario, Canada. J. Appl. Microbiol. 109, 1053-1066. https://doi.org/10.1111/j.1365-2672.2010.04730.x.

Veals, P.G., Steenburgh, W.J., 2015. Climatological characteristics and orographic enhancement of lake-effect precipitation east of Lake Ontario and over the Tug Hill Plateau. Mon. Weather Rev. 143, 3591-3609. https://doi.org/10.1175/MWR-D-15-0009.1.

Villarini, G., Krajewski, W.F., 2007. Evaluation of the research version TMPA three-hourly 0.25° × 0.25° rainfall estimates over Oklahoma. Geophys. Res. Lett. 34, L05402. https://doi.org/10.1029/2006GL029147.

Villarini, G., Mandapaka, P.V., Krajewski, W.F., Moore, R.J., 2008. Rainfall and sampling uncertainties: A rain gauge perspective. J. Geophys. Res. 113, D11102. https://doi.org/10.1029/2007JD009214.

Villarini, G., Smith, J.A., Baeck, M.L., Sturdevant-Rees, P., Krajewski, W.F., 2010. Radar analyses of extreme rainfall and flooding in urban drainage basins. J. Hydrol. 381, 266-286. https://doi.org/10.1016/j.jhydrol.2009.11.048.

Vu, T.M., Mishra, A.K., Konapala, G., Liu, D., 2018. Evaluation of multiple stochastic rainfall generators in diverse climatic regions. Stoch. Environ. Res. Risk Assess. 32, 1337-1353. https://doi.org/10.1007/s00477-017-1458-0.

Vystavna, Y., Diadin, D., Rossi, P.M., Gusyev, M., Hejzlar, J., Mehdizadeh, R., Huneau, F., 2018. Quantification of water and sewer leakages from urban infrastructure into a shallow aquifer in East Ukraine. Environ. Earth Sci. 77:748. https://doi.org/10.1007/s12665-018-7936-y.

Wang, X., Huang, G., Liu, J., Li, Z., Zhao, S., 2015. Ensemble projections of regional climatic changes over Ontario, Canada. J. Climate 28, 7327-7346. https://doi.org/10.1175/JCLI-D-15-0185.1.

Water Survey of Canada (WSC), 2019. Daily discharge data for Alder Creek near New Dundee (02GA030)[ON]. https://wateroffice.ec.gc.ca/mainmenu/historical_data_index_e.html. (Accessed 13.07.2017, 07.03.2018, 10.05.2018. 12.03.2019).

Waterloo Hydrogeologic, 2016. AquiferTest 7.0. Computer software. https://www.waterloohydrogeologic.com/.

Waterloo Hydrogeologic, 2018. Hydro GeoAnalyst, Version 8.0. Computer software. https://www.waterloohydrogeologic.com/.

Werner, A.D., Gallagher, M.R., Weeks, S.W., 2006. Regional-scale, fully coupled modelling of stream–aquifer interaction in a tropical catchment. J. Hydrol. 328, 497-510. https://doi.org/10.1016/j.jhydrol.2005.12.034.

Wiebe, A.J., Conant Jr., B., Rudolph, D.L., Korkka-Niemi, K., 2015. An approach to improve direct runoff estimates and reduce uncertainty in the calculated groundwater component in water balances of large lakes. J. Hydrol. 531, 655-670. https://doi.org/10.1016/j.jhydrol.2015.10.061.

Wiebe, A.J., Menkveld, P.G., Hillier, C.E., Mesec, E., Rudolph, D.L., 2019. Meteorological and hydrological data from the Alder Creek watershed, Grand River basin, Ontario. https://doi.org/10.20383/101.0178.

Wiebe, A.J., Rudolph, D.L., 2020. On the sensitivity of modelled groundwater recharge estimates to rain gauge network scale. J. Hydrol. 585, 124741. https://doi.org/10.1016/j.jhydrol.2020.124741.

Wilks, D.S., 1998. Multisite generalization of a daily stochastic precipitation generation model. J. Hydrol. 210, 178-191. https://doi.org/10.1016/S0022-1694(98)00186-3.

Wilks, D.S., Wilby, R.L., 1999. The weather generation game: a review of stochastic weather models. Prog. Phys. Geog. 23(3), 329-357. https://doi.org/10.1177/030913339902300302.

Wilson, K.B., Hanson, P.J., Mulholland, P.J., Baldocchi, D.D., Wullschleger, S.D., 2001. A comparison of methods for determining forest evapotranspiration and its components: sap-flow, soil water budget, eddy covariance and catchment water balance. Agric. For. Meteorol. 106(2), 153-168. https://doi.org/10.1016/S0168-1923(00)00199-4.

Winter, T.C., 1981. Uncertainties in estimating the water balance of lakes. Water Resour. Bull. 17(1), 82-115. https://doi.org/10.1111/j.1752-1688.1981.tb02593.x.

Wood, W.W., Sanford, W.E., 1995. Chemical and isotopic methods for quantifying ground-water recharge in a regional, semiarid environment. Ground Water 33(3), 458-468. https://doi.org/10.1111/j.1745-6584.1995.tb00302.x.

Worthington, S.R.H., Smart, C.C., 2017. Transient bacterial contamination of the dual-porosity aquifer at Walkerton, Ontario, Canada. Hydrogeol. J. 25, 1003-1016. https://doi.org/10.1007/s10040-016-1514-8.

Worthington, S.R.H., Smart, C.C., Ruland, W., 2012. Effective porosity of a carbonate aquifer with bacterial contamination: Walkerton, Ontario, Canada. J. Hydrol. 464-465, 517-527. https://doi.org/10.1016/j.jhydrol.2012.07.046.

Wu, Y., Xu, Y., 2005. Snow impact on groundwater recharge in Table Mountain Group aquifer systems with a case study of the Kommissiekraal River catchment in South Africa. Water SA 31(3), 275-282. http://hdl.handle.net/10566/820.

Xu, M., Eckstein, Y., 1995. Use of weighted least-squares method in evaluation of the relationship between dispersivity and field scale. Ground Water 33(6), 905-908. https://doi.org/10.1111/j.1745-6584.1995.tb00035.x.

Yin, Y., Sykes, J.F., Normani, S.D., 2015. Impacts of spatial and temporal recharge on field-scale contaminant transport model calibration. J. Hydrol. 527, 77-87. https://doi.org/10.1016/j.jhydrol.2015.04.040.

Zebarth, B.J., De Jong, E., Henry, J.L., 1989. Water flow in a hummocky landscape in central Saskatchewan, Canada, II. Saturated flow and groundwater recharge. J. Hydrol. 110, 181-198. https://doi.org/10.1016/0022-1694(89)90243-6.

Zhang, L., Dawes, W.R., Walker, G.R., 2001. Response of mean annual evapotranspiration to vegetation changes at catchment scale. Water Resour. Res. 37(3), 701-708. https://doi.org/10.1029/2000WR900325.

Zhao, F., Zhang, L., Chiew, F.H.S., Vaze, J., Cheng, L., 2013. The effect of spatial rainfall variability on water balance modelling for south-eastern Australian catchments. J. Hydrol. 493, 16-29. https://doi.org/10.1016/j.jhydrol.2013.04.028.

Zhou, J., Hu, B.X., Chen, G., Wang, G., Li, X., 2011. Development of a three-dimensional watershed modelling system for water cycle in the middle part of the Heihe rivershed, in the west of China. Hydrol. Process. 25, 1964-1978. https://doi.org/10.1002/hyp.7952.

# Appendix A

# The influence of $ET_o$ variation on modelled recharge results

## A.1 Methods

Daily Penman-Monteith reference evapotranspiration ($ET_o$) values were calculated for both the regional and local networks for 2014 to 2016 using the ETo Calculator program (Raes, 2009). Daily maximum and minimum temperatures were used to estimate daily $ET_o$ values for the national station and the regional network. Air temperature, relative humidity, wind speed, and incoming solar radiation data were incorporated into the $ET_o$ estimates for the local network. The Wellesley station (regional network) was omitted from the $ET_o$ analysis due to missing data. $ET_o$ values for both the "light winds" (0.5 m/s) and "light to moderate winds" (2.0 m/s) options were calculated for comparison. These wind speeds correspond to a height of 2 m above ground. An intermediate value based on the average of observed wind speeds at the local network stations was also used for comparison. Pearson and Spearman spatial correlation coefficients were calculated for $ET_o$ using pairs from the set of all thirteen available stations, rather than separating the results among the local and regional networks.

The Actual ET (AET) estimate by Sanderson (1998) of 540 mm per year was assessed by using the Budyko curve (Budyko, 1961; Gentine et al., 2012), which represents the relationship between long-term averages of the ratio of AET to precipitation (P) and the ratio of potential ET (PET, identical to $ET_o$) to P for a watershed with minimal anthropogenic influences. Averages from long-term (1973 – 2018) temperature and P data from Roseville (AquaResource, 2008; Government of Canada, 2019) were used to explore the influence of wind speed on $ET_o$ and AET.

The sensitivity of modelled recharge rates to the scale of point $ET_o$ estimates was explored during two scenarios in addition to the three described in Wiebe and Rudolph (2020) (Chapter 2): Scenario 4 employed rainfall interpolated from the local network, with spatially variable $ET_o$ interpolated from the regional network; and Scenario 5 employed rainfall interpolated from the local network, with spatially variable $ET_o$ interpolated from the local network. These two scenarios were compared with Scenario 3, which employed rainfall interpolated from the local network and spatially uniform $ET_o$ from the national network. Scenarios 4 and 5 were started from the same initial conditions as Scenario 3 in all three years. $ET_o$ for Scenarios 4 and 5 was interpolated using the inverse distance squared technique and a 250 m by 250 m grid in MIKE SHE (Abbott et al., 1986; Graham and Butts, 2005; Refsgaard and Storm, 1995).

## A.2 Results

Annual $ET_o$ totals are shown in Table A.1 for each of the three networks' weather stations for the "light to moderate winds" option. Figure A.1 shows the annual $ET_o$ totals for all stations for both the "light to moderate winds" and "light winds" options. The "light to moderate winds" option (2 m/s) yielded annual $ET_o$ estimates for Roseville that were near the upper end of the range of values generated by the local stations using more measured parameters. The use of the "light winds" option (0.5 m/s) generated $ET_o$ estimates near the lower end of the local range. The spatial correlation of the Penman-Monteith $ET_o$ estimates was found to be very high, with coefficients essentially above 0.9 in all daily comparisons among all available stations (Figure A.2). Correlation lengths for the curves on Figure A.2 were > 400 km. Some of the annual coefficients were slightly lower, but still higher than 0.8. Thus, $ET_o$ was found to be much more spatially correlated than rainfall in the study area.

Table A.1. Annual $ET_o$ totals for the local, regional, and national networks.

| Weather Station | $ET_o$ (mm) | | |
|---|---|---|---|
| | 2014 | 2015 | 2016 |
| WS1* | 722 | 793 | 808 |
| WS2* | 756 | 783 | 837 |
| WS3* | 699 | 726 | 779 |
| WS4* | 653 | 720 | 774 |
| WS5* | N/A† | 683 | 731 |
| WS6* | 698 | 729 | 783 |
| WS7* | 776 | 819 | 891 |
| Baden‡ | 846 | 904 | 954 |
| Laurel Creek‡ | 723 | 762 | 803 |
| Cambridge‡ | 781 | 813 | 846 |
| Paris‡ | 842 | 892 | 946 |
| Burford‡ | 818 | 874 | 946 |
| Roseville§ | 756 | 816 | 857 |

* Local (SOWC) weather station (Wiebe et al., 2019)

† N/A – not available. WS5 data collection started in June 2014.

‡ Grand River Conservation Authority weather station (GRCA, 2017a)

§ Environment Canada weather station (Government of Canada, 2019)

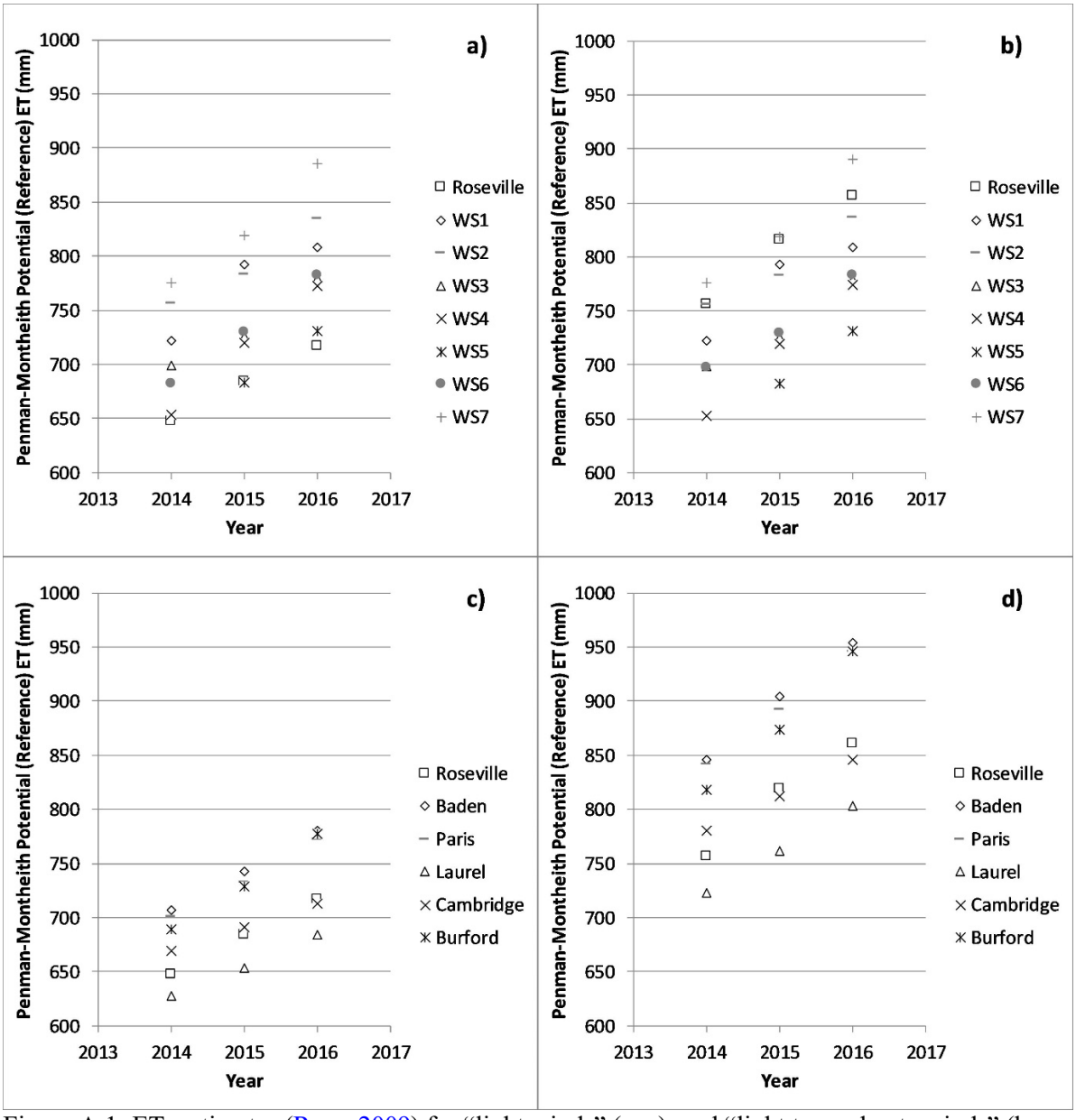


Figure A.1: $ET_o$ estimates (Raes, 2009) for "light winds" (a, c), and "light to moderate winds" (b, d). Local stations are shown in a) and b); regional stations are in c) and d). The one national station is included on all plots.

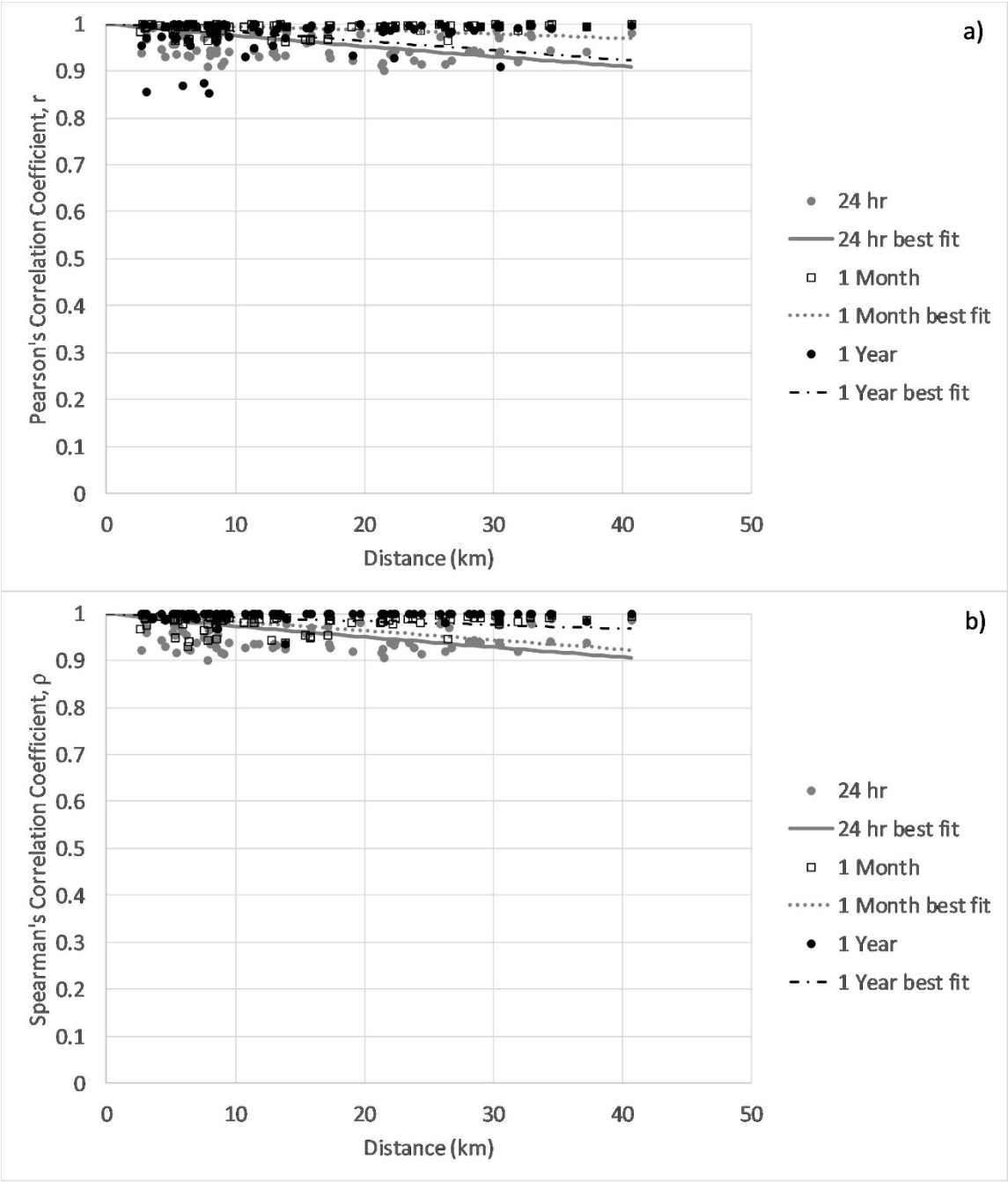


Figure A.2: Pearson (a) and Spearman (b) spatial correlations among $ET_o$ estimates for all stations (Raes, 2009). Best fit curves were calculated using the Levenberg-Marquardt algorithm coded by Gavin (2009).

Observed wind speeds at the local stations, corrected for 2 m height above ground surface, ranged between 0 and 14.6 m/s; the average of all recorded values was 1.6 m/s (Wiebe et al., 2019).

Figure A.3 shows $\overline{AET}/\bar{P}$ results along the Budyko curve for estimates of $ET_o$ based on different wind speeds (Budyko, 1961; Gentine et al., 2012). The "light winds" option for $ET_o$ yielded an average annual $ET_o$ value of 680 mm. Based on an average annual total precipitation of 907 mm and the resulting index of aridity of 0.75, $\overline{AET}/\bar{P}$ was 0.59, and $\overline{AET}$ was calculated to be 532 mm/yr. This result was very similar to the 540 mm/yr noted by Sanderson (1998). For comparison, the "light to moderate winds" option yielded an aridity index of 0.89, an annual average $ET_o$ value of 806 mm, an average $\overline{AET}/\bar{P}$ ratio of 0.65, and an $\overline{AET}$ value of 590 mm. Employing an average wind speed value over about 4 years from the seven local weather stations (1.6 m/s) yielded an aridity index of 0.85, an annual average $ET_o$ value of 775 mm, an $\overline{AET}/\bar{P}$ ratio of 0.64, and an $\overline{AET}$ of 577 mm. The "light to moderate winds" estimate is therefore closer to the estimate derived using wind speed data from the local stations.

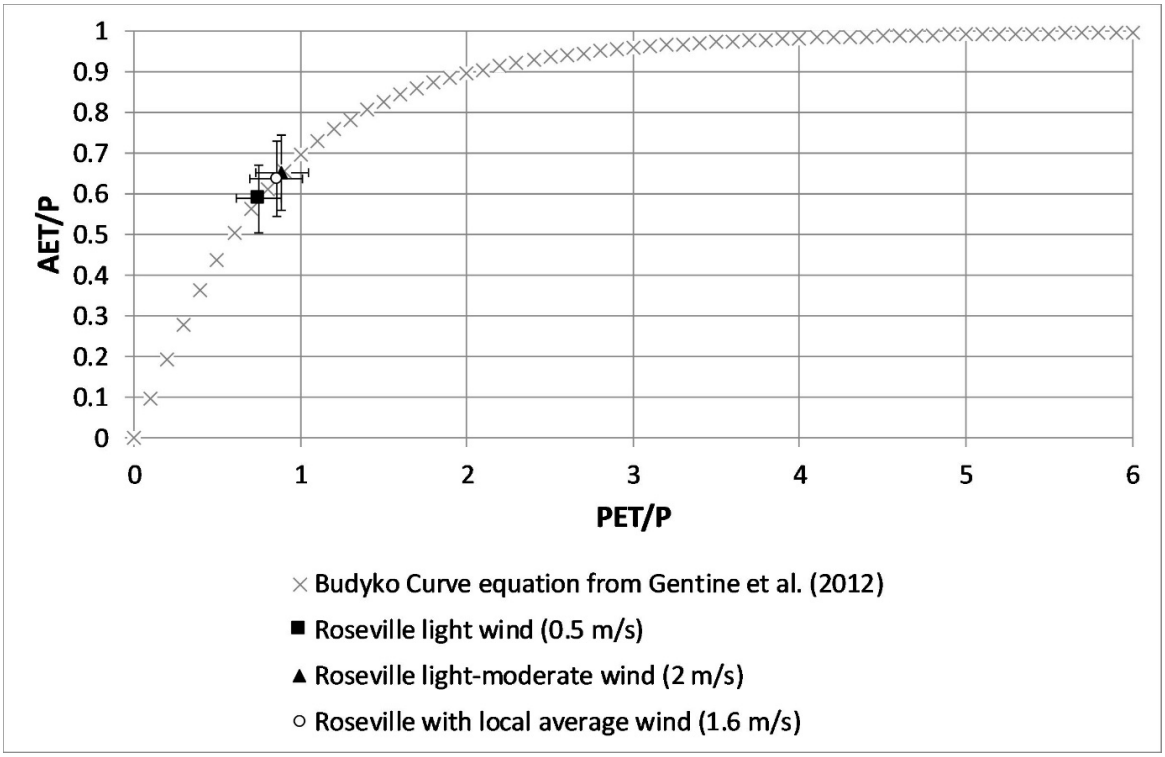


Figure A.3: Budyko curve and AET/P estimates for the Roseville weather station for different average wind speed estimates. Error bars were derived based on relative uncertainty values of P ± 10%, PET ± 15%, and AET ± 10%.

Figure A.4 suggests that the three $ET_o$ scenarios (3, 4, and 5) from the MIKE SHE model are in closer agreement than the three rainfall scenarios (1, 2, and 3). Like the differences between the

regional and national rainfall scenarios (Figure 2.7, g - i), there is a similar shift in recharge rates for large numbers of cells between scenarios. Recharge rates varied among Scenarios 3, 4, and 5 by up to around 50 mm in 2014, up to 40 mm in 2015, and up to 16 mm in 2016 (Table A.2). Thus, the maximum difference in recharge rates for a given year was 51 mm, or 16% of previously estimated steady state recharge (M.H. Brouwers, pers. comm., 2017; Matrix and SSPA, 2014a). The three ET scenarios thus varied much less than the rainfall scenarios, which varied up to 44% of previously estimated stead state recharge.

Streamflow totals showed a maximum difference of 26 mm (in 2014) for the $ET_o$ scenarios, varying within a range of about ±20% of long-term average streamflow at the WSC gauge (Figure A.5, Table A.2). Table A.2 shows that all components of the water budget were similar for these three scenarios. This indicates that the choice of network for $ET_o$ input to the model had much less influence on the variability of the recharge results than the choice of rain gauge network. The variation between the recharge distributions of Scenarios 3, 4, and 5 (analogous to Figure 2.6) was slight and is not presented here.

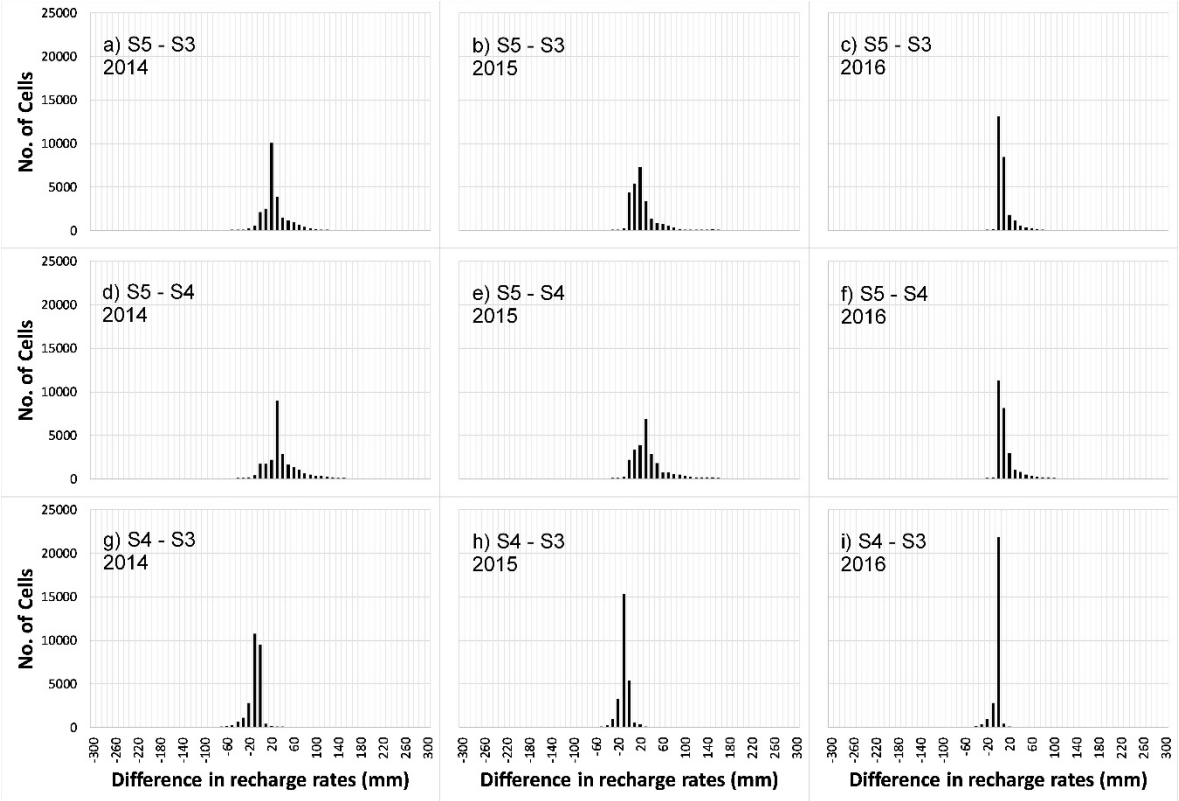


Figure A.4: Frequency of differences in recharge rates between $ET_o$ scenarios (3, 4, and 5). "S5 – S3" implies a cell-by-cell subtraction of *Scenario 5 minus Scenario 3*, etc.

Table A.2. Numerical model water budget results and comparisons (results in mm per $m^2$ per yr).

| Year | Component | Scenario | | | | |
|---|---|---|---|---|---|---|
| | | 1 | 2 | 3 | 4 | 5 |
| 2014 | Precipitation | 849 | 895 | 1048 | 1048 | 1048 |
| | Evapotranspiration* | 392 | 376 | 381 | 398 | 316 |
| | Overland Runoff† | 91 | 96 | 124 | 119 | 144 |
| | Storage change‡ | -53 | -33 | -20 | -21 | -15 |
| | Recharge§ | 421 | 456 | 562 | 550 | 601 |
| | Streamflow at node representing WSC gauge¶ | 107 | 112 | 148 | 143 | 174 |
| | Total Streamflow** | 121 | 127 | 157 | 152 | 178 |
| 2015 | Precipitation | 789 | 714 | 897 | 897 | 897 |
| | Evapotranspiration* | 425 | 421 | 428 | 445 | 385 |
| | Overland Runoff† | 68 | 61 | 85 | 82 | 93 |
| | Storage change‡ | 7 | -9 | 20 | 17 | 26 |
| | Recharge§ | 288 | 241 | 364 | 352 | 392 |
| | Streamflow at node representing WSC gauge¶ | 84 | 75 | 101 | 98 | 110 |
| | Total Streamflow** | 97 | 88 | 116 | 112 | 125 |
| 2016 | Precipitation | 879 | 756 | 771 | 771 | 771 |
| | Evapotranspiration* | 444 | 382 | 338 | 345 | 316 |
| | Overland Runoff† | 78 | 64 | 93 | 91 | 97 |
| | Storage change‡ | 13 | 25 | -10 | -11 | -3 |
| | Recharge§ | 344 | 285 | 349 | 345 | 361 |
| | Streamflow at node representing WSC gauge¶ | 96 | 79 | 112 | 110 | 116 |
| | Total Streamflow** | 107 | 91 | 122 | 118 | 125 |
| Recharge Estimate from Previous Study (Tier Three††) | | | | 321 | | |
| Streamflow estimates from WSC gauge‡‡ | | 2014 | | | 153 | |
| | | 2015 | | | 112 | |
| | | 2016 | | | 139 | |

* AET excluding AET from the saturated zone. Total AET values were: 493, 476, 496, 511, and 442 mm, respectively, for scenarios 1 to 5 for 2014; 521, 505, 533, 547, and 495 mm, respectively, for scenarios 1 to 5 for 2015; and 540, 466, 439, 445, and 419 mm, respectively, for scenarios 1 to 5 for 2016.

† Overland flow into stream.

‡ Includes storage changes in both sat. and unsat. zones, as well as boundary flows out of unsat. zone.

§ Recharge can be calculated via Eqn. (2.2).

¶ Area above gauge = 47.4 $km^2$ (WSC, 2019).

** Area of model domain = 68.2 $km^2$ (GRCA, 1998).

†† Results from calibrated, steady state, saturated zone FEFLOW simulation for Regional Municipality of Waterloo Tier Three Assessment (M.H. Brouwers, pers. comm., 2017; Matrix and SSPA, 2014a).

‡‡ WSC (2019). There were twelve days with missing data at the start of 2016.

Cumulative streamflow patterns for the $ET_o$ scenarios were similar. Scenario 4 results were 7% smaller, 13% smaller, and 21% smaller than observed in 2014, 2015, and 2016, respectively. Scenario 5 results were 14% larger, 2% smaller, and 17% smaller than observed for the three years, respectively. Scenario 3 results were 3% smaller, 10% smaller, and 19% smaller, respectively. Scenarios 3 and 4 yielded very similar streamflow results. Scenario 5 sometimes differed to a slightly greater extent but was still closer to the observed cumulative streamflow than Scenarios 1 and 2.

The reasonably good spatial correlation between $ET_o$ values near the study area was associated with smaller discrepancies in recharge rates and cumulative streamflow totals, compared to rainfall results (Wiebe and Rudolph, 2020; Chapter 2). These results suggest that rainfall variation is greater and has a larger impact on recharge rates. Therefore, incorporating rainfall variation seems more important than capturing $ET_o$ variation for the area around the study site.

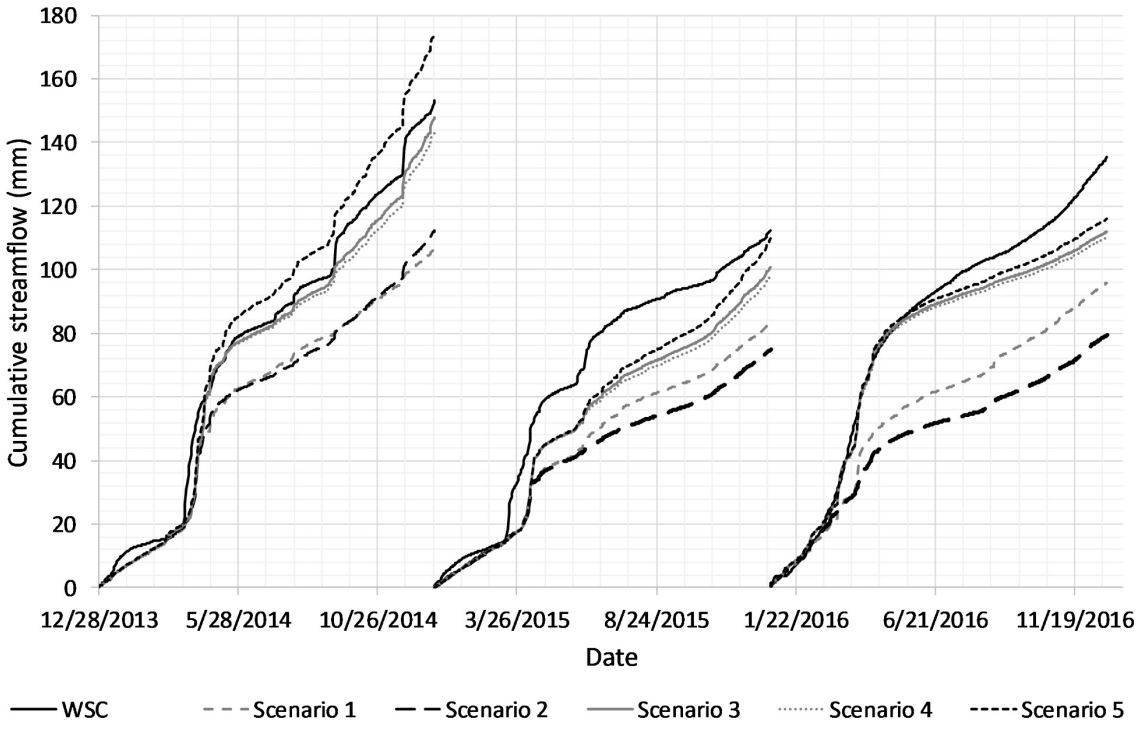


Figure A.5: Comparison of cumulative streamflow results for all simulations with recorded flows at the Water Survey of Canada (WSC) gauge (WSC, 2019). The WSC gauge was missing 12 days of data at the start of 2016.

## A.3 Discussion

The relatively short-term results of the present study are an important initial analysis because of the costs associated with the long-term operation of a network of weather stations. The choice of $ET_o$ network had a smaller influence on overall annual recharge rates (≤ 51 mm per year, or ≤16% of steady state recharge) than the choice of rainfall network (variation up to 44% of steady state recharge). Hydrological modelling (streamflow) studies have similarly found less sensitivity to evaporation variation than to rainfall variation (Nandakumar and Mein, 1997; Oudin et al., 2006; Paturel et al., 1995).

Despite the high degree of correlation of the $ET_o$ estimates, there was initially some uncertainty regarding which wind speed option to choose in the ETo calculator for stations with only temperature data. The "light to moderate winds" (2 m/s) option was employed for modelling by Wiebe and Rudolph (2020) (Chapter 2) and was considered more reasonable than the "light winds" (0.5 m/s) option based on the range of $ET_o$ estimates for the local network, where the average of all recorded wind speed values was 1.6 m/s. Whether the "light to moderate winds" option (2 m/s) in the ETo Calculator is used, or an average value of 1.6 m/s is entered as input, the index of aridity and average $\overline{\mathrm{AET}}/\bar{P}$ ratio are quite similar.

## A.4 Conclusions

$ET_o$ values were very well correlated, with daily, monthly, and annual Pearson and Spearman coefficients > 0.8 among all thirteen stations. The three $ET_o$ scenarios were all quite similar, and overall average recharge rates varied by up to ±51 mm, or ±16% of a previous estimate of steady state recharge for the watershed. Results indicate that the rainfall differences between networks could lead to much larger differences than those displayed by $ET_o$ scenarios.

Care is needed for selecting the wind speed option or value for $ET_o$ calculations when local wind data are unavailable.

# Appendix B
# Background information on the meteorological observation networks

### National (Environment Canada) Network

Figure B.1 shows the Environment Canada weather stations closest to the Alder Creek watershed, and Table B.1 shows the number of missing days of data at each station. Because so many observations were missing from many of these stations, only the Roseville station was used to represent national network precipitation. Missing precipitation and temperature data for the Roseville station during 2014 to 2016 were filled in using either WS4 in the local network (Wiebe et al., 2019; 8 km from the station), or the University of Waterloo weather station (Seglenieks, 2017; 16 km from the station).

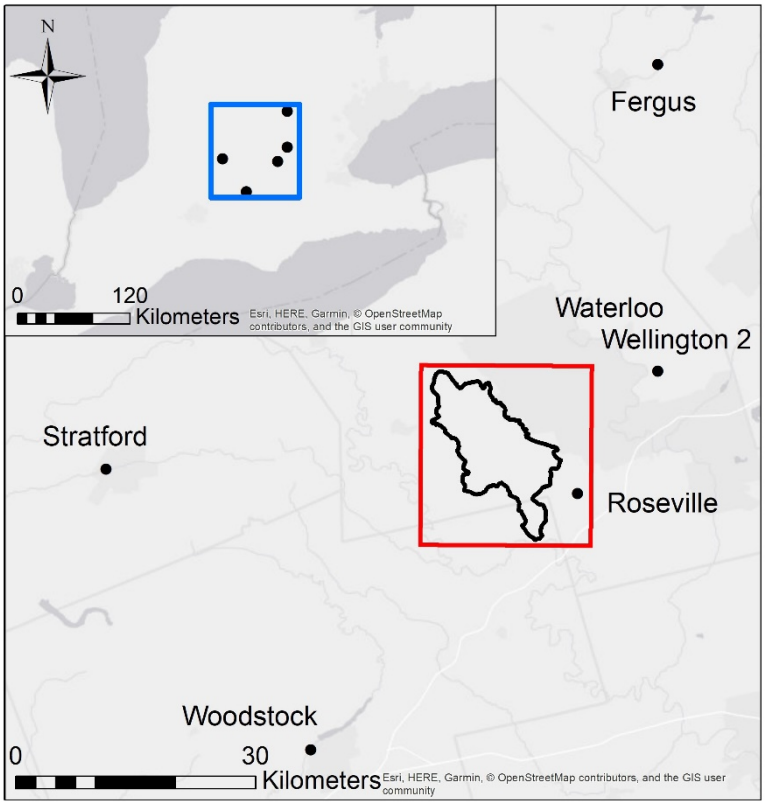


Figure B.1: Environment Canada weather stations with rainfall observations near the Alder Creek watershed (Esri et al., 2019a, 2019b; Government of Canada, 2017; GRCA, 2017a).

Table B.1. Data gaps for the national weather stations near the Alder Creek watershed*.

| Station | Number of days with missing data per year | | |
|---|---|---|---|
| | 2014 | 2015 | 2016 |
| Fergus | 3 | 6 | 3 |
| Roseville | 22 | 15 | 32 |
| Foldens | 2 | 28 | 202 |
| Waterloo Wellington 2 | 200 | 200 | 201 |
| Woodstock | 218 | 218 | 213 |
| Stratford | 125 | 125 | 325 |

* Government of Canada (2017)

**Regional (GRCA) Network**

The GRCA rain gauges were installed for flood forecasting purposes (S. Shifflett, pers. comm., 2018). They represent the only regionally available gauges with continuous data for the time period of interest. Wellesley temperature data were incomplete for 2014 and 2015, so this station was only used as a source of rainfall data and not for $ET_o$ calculations.

**Local (SOWC) Network**

The rainfall data were analyzed for anomalous readings that could be due to snow accumulating on the gauge and then melting in a short period of time. Each rain gauge was installed following factory-calibration, and all gauges were tested and calibrated to within ± 5% (if necessary) between Dec 2015 and Jul 2016. Errors were found to be < 10% during multiple lab trials, though errors for the WS2 gauge were < 20% during one trial. The lab trials employed an intensity of around 8 mm/hour for about one hour, representing a locally heavy rainfall rate exceeded ≤ 2.2% of the time by gauges of the local network. The manufacturer (Hydrological Services PTY LTD, 2013) recommended a more rapid rate of water addition during calibration (653 mL for 12 min, i.e., 100 mm / hr). While not as high, the rate used during calibration seems appropriate for the rainfall rates observed in the Alder Creek watershed. Observed hourly rainfall intensities in the local network were only greater than 37 mm/hr on two occasions (51.75 mm/hr at WS7; 44.75 mm/hr at WS6). Maximum rainfall intensities for all three networks are listed in Table B.2.

Table B.2. Maximum rainfall rates observed in the three networks (2014 – 2016).

| Network | Station | Maximum hourly rainfall rate (mm/hr) | Maximum daily rainfall rate (mm/day) |
|---|---|---|---|
| Local* | WS2 | 39.2 | 61.6 |
| | WS3 | 46.4 | 58.4 |
| | WS4 | 37.0 | 69.6 |
| | WS5 | 34.2 | 53.0 |
| | WS6 | 39.8 | 75.6 |
| | WS7 | 58.0 | 88.4 |
| Regional† | Wellesley | 52.4 | 78.8 |
| | Baden | 39.5 | 59.0 |
| | Laurel Creek | 28.8 | 41.0 |
| | Cambridge | 48.5 | 90.4 |
| | Paris | 41.5 | 67.8 |
| | Burford | 31.0 | 109.6 |
| National‡ | Roseville | N/A | 67.1 |

* Local (SOWC) weather station (Wiebe et al., 2019)

† Grand River Conservation Authority weather station (GRCA, 2017a)

‡ Environment Canada weather station (Government of Canada, 2019)

# Appendix C
# The Alder Creek field observatory

## C.1 Introduction and Objectives

The Alder Creek Field Observatory is one of three watershed monitoring initiatives of the Southern Ontario Water Consortium (SOWC; Wiebe et al., 2019).[6] The SOWC is a collaboration of 10 universities and colleges supported by the federal and provincial governments and private companies. Its mandate is to spur economic growth through providing a platform for the development and testing of new technologies in a broad range of water-related disciplines. Alder Creek represents a middle member along a trajectory from agricultural (Hopewell Creek, east of Kitchener) to fully urbanized (Mimico Creek, Toronto) watersheds, and is important from a water supply perspective. As many as seven of the well fields of the Regional Municipality of Waterloo capture water recharged within the 78 km$^2$ Alder Creek watershed, which is located on the Waterloo Moraine (Brouwers, 2007).

There were several objectives for the setup of a hydrological monitoring network within the Alder Creek watershed, including to: 1) expand the body of knowledge generated by previous studies; 2) measure rainfall variation; 3) assess reference evapotranspiration (ET) variation; 4) monitor surface water; 5) develop systems to record hydrological events, including depression focused recharge; and 6) estimate recharge rates in different locations.

### C.1.1 Network Setup and Instrumentation

Locations of the field stations are shown on Figure C.1. Efforts were made to find well-distributed locations in and around the watershed for the seven weather stations. A typical weather station is shown in Figure C.2, and typical sensors for the different types of stations are listed in Table C.1. Weather data collection became a focus of the project because of questions about the sensitivity of coupled or fully integrated (surface flow, vadose zone, and saturated groundwater flow), watershed-scale hydrological models to various input data imposed on the upper domain surface. Beyond this, two sites were instrumented to monitor groundwater recharge, three sites were instrumented with surface water sensors, and several wells were drilled. Groundwater recharge sites included: bromide tracer applications; groundwater level, soil moisture, temperature, and electrical conductivity

[6] Renamed as the Ontario Water Consortium, Aug 2019.

monitoring; and tensiometer testing. Soil tension was a missing element in previous, similar studies in Woodstock on groundwater recharge rates (e.g., Bekeris, 2007; Koch, 2009). Multi-level tensiometers were developed for the two recharge stations.

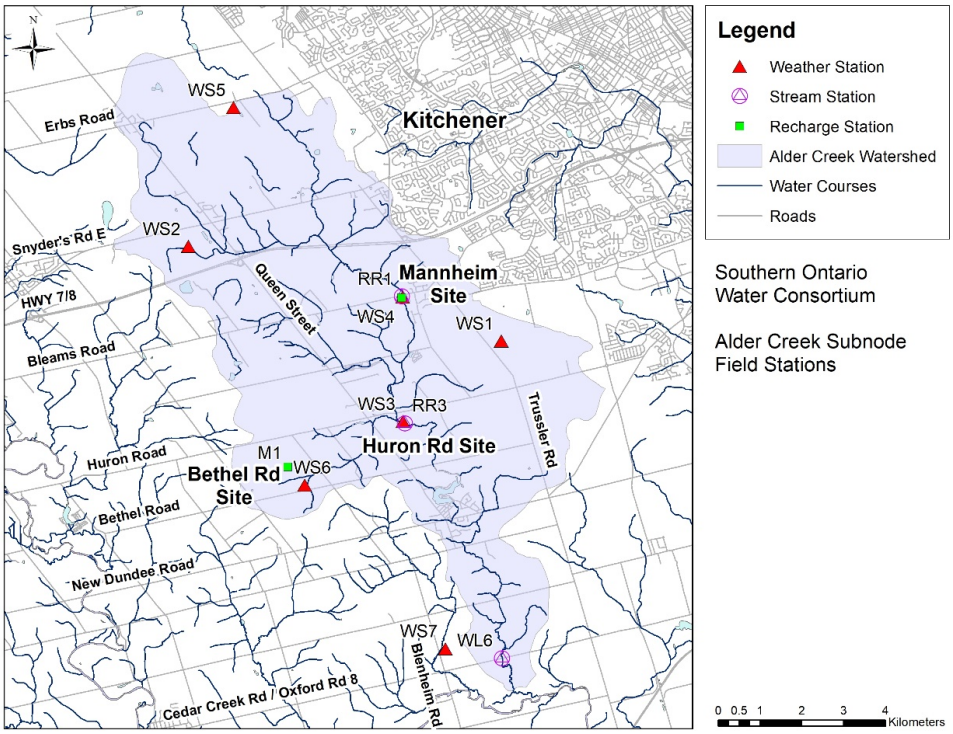


Figure C.1: Locations of the SOWC Alder Creek field stations (DMTI, 2011; GRCA, 1998).

Figure C.2: Photo of typical station setup (WS2). Not shown: an Alter-type windscreen (1 m radius), which was installed around the rain gauge after this photo was taken.

Table C.1. Typical instrumentation and supplementary equipment at field stations.

| | |
|---|---|
| **Weather Stations** | **Sensors** |
| | Tipping bucket rain gauge |
| | Temperature |
| | Relative humidity |
| | Incoming solar radiation* |
| | Wind speed and direction |
| | Snow depth sensor |
| | |
| | **Supplementary equipment** |
| | Alter-type wind screen for rain gauge, 1 m radius† |
| | |
| **Stream Stations** | **Sensors** |
| | Water level (pressure transducer) |
| | Creek (water) Temperature |
| | Multi-parameter water quality sonde – pH, dissolved oxygen, electrical conductivity, temperature |
| | Automatic water sampler |
| | Well (water) temperature |
| | |
| | **Supplementary equipment** |
| | Radio relay system with secondary station |
| | |
| **Recharge stations** | **Sensors** |
| | Soil moisture |
| | Soil temperature |
| | Soil electrical conductivity |
| | Well water levels |
| | Soil tension |
| | |
| **All Stations** | **Supplementary equipment** |
| | Datalogger |
| | Deep cycle battery |
| | Solar panel |
| | Cell network modem |

* WS7 alternatively had sensors to measure incoming short-wave solar radiation and outgoing long-wave radiation.

† WS6 had a second rain gauge with two concentric Alter-type wind screens at radii of 1 m and 2 m.

The surface water stations included monitoring of water level and temperature, and options to deploy multi-parameter water quality instruments and automatic water samplers. The automatic water samplers were configured with the ability to collect creek or groundwater samples either on a

schedule or based on hydrological triggers such as water levels rising in exceedance of a specified rate. Two of the surface water stations employed radio-relay technology, allowing multiple sensors deployed remotely at smaller stations tens of metres from the master station to send their data periodically to the master station via line-of-sight radio link.

Nearly all stations could periodically (e.g., hourly) communicate sensor readings via modems to a central server at the University of Waterloo over the cellular telephone network, though a couple of stations experienced poor reception.

Following a review of the maintenance history and detailed examination of the data from each weather station, WS1 rainfall data were suspected to be unreliable due to an equipment malfunction and were not used.

### C.1.2 Bromide Tracer Tests

Bromide tracer tests were conducted at the Mannheim and Bethel Road sites following the procedure of Bekeris (2007) with modifications by Ju (2016) for composite soil sampling (Figure C.3). One tracer application was conducted at the Mannheim site, while two experiments were carried out at the Bethel Road site; one of these plots was within an active agricultural field with coarse sand and gravel sediments, and the other in a woodlot with sandy soil and deciduous and coniferous trees nearby (Figure C.3). A known mass of sodium bromide (5 kg) was dissolved in 20 L of deionized water and applied to a 3 m by 3 m area by hand using watering cans at each of three recharge plots in June 2016. Sampling was conducted by hand using a soil auger after 97 days at both sites, and after 369 days at the Bethel Road site. Sampling was later conducted using a Geoprobe 7720DT drill rig at the Bethel Road site after 524 days. Multiple soil cores (up to nine by hand, or three with the drill rig) were collected during each sampling event, and soil from equivalent depth intervals from across all cores at a tracer plot were combined, mixed, and subsampled for submission to a commercial laboratory for bromide mass analysis. Background soil cores were collected outside the Mannheim and Bethel Road-Woodlot plots after 97 days. Soil samples were submitted in filled 50 g (approximately 300 mL volume) jars on ice. Sampling by hand could only obtain soil samples from depths of up to about 1 m. Coring with the drill rig obtained samples down to 4.2 m (Bethel Road site - field plot) or 7.3 m (Bethel Road site - woodlot plot). Soil cores were only collected once at the Mannheim site due to

suspected non-vertical migration of tracer during a snowmelt event with high local water table conditions under the tracer plot.

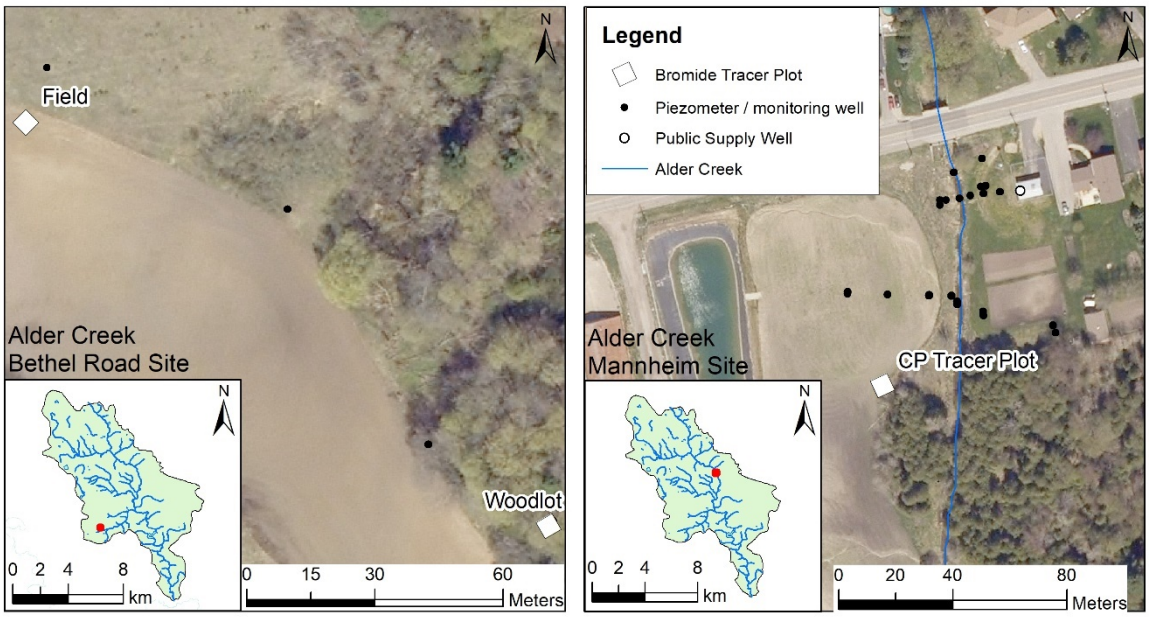


Figure C.3: Locations of the tracer application plots at the two recharge sites (DMTI, 2011; First Base Solutions, 2006; GRCA, 1998).

### C.1.3 Manual Operation Multi-Level Tensiometers

Pressure head measurements in the vadose zone may be used for calculating drainage or evapotranspiration rates via the zero-flux plane method (Healy, 2010). Tensiometers are one of the few types of instruments able collect pressure head measurements in the vadose zone. However, data collection can be challenging because of either the need to maintain a vacuum, or the tendency for entrapped air bubbles to impact pressure measurements due to the high compressibility of air. Burr (2000) found that tensiometer pressures in the second year of a field study yielded unreasonable recharge rates. P. Menkveld (pers. comm., 2017) found tensiometer measurements unreliable, possibly due to small amounts of air entering the tensiometer each time the needle of the vacuum gauge was used to collect pressure measurements.

The manual-operation, porous cup tensiometer that has been deployed in the past (e.g., Burr, 2000; Healy, 2010) typically consists of a water-filled PVC pipe with a porous ceramic cup at the lower end and a rubber septum at the top. Such a device is: installed into unsaturated soil with an appropriate

slurry of fine-grained sediment to assure a good hydraulic connection between the ceramic and the native soil, filled to the top with de-aired water, capped with a rubber septum, and then allowed to equilibrate with soil pressures. During equilibration, the water in the PVC pipe will be drawn into the soil by the tension of the unsaturated soil around the ceramic cup and the water level will decrease until the vacuum tension in the head space at the top of the PVC pipe is the same as the tension in the soil around the ceramic cup. Following this, the pressure head (tension, in the vadose zone above the water table) in the soil region in contact with the ceramic cup may be measured by inserting the needle of a vacuum gauge through the rubber septum into the vacuum in the head space above the water column in the PVC pipe and taking a reading.

Due to the difficulties in maintaining a vacuum under field conditions for long periods of time, and as an alternative to the cost associated with purchasing large numbers of electronic tensiometers in order to obtain vertical profiles of pressure measurements in the vadose zone at multiple locations, a variation on a porous cup tensiometer design was deployed in the field at two sites within the Alder Creek watershed. The variation was based on Figure 2.12 in Freeze and Cherry (1979), where a pressure head profile in the vadose zone is depicted as a series of point measurements connected to manometer (U-shaped) tubes containing water. One side of the "U" is hydraulically connected to the soil, and the other side is open to the atmosphere; the bottom of the "U" is below the elevation of the measurement point and ideally the distance between the measurement point and the ceramic cup would be equal to the greatest expected tension, in terms of water column height. When the measurement point (e.g., porous ceramic cup) is above the water table and experiencing negative pressure (tension), the water level in the side of the "U" that is open to the atmosphere is below the elevation of the measurement point. The magnitude of the tension experienced at the measurement point is the difference between the elevation of the measuring point (ceramic) and the elevation of the water level on the other side of the "U", which is a pressure in units of water column height.

If a series of tubes, each connected to a porous ceramic cup on one end, and open on the other end, are installed in a borehole with the ceramic cups at different depths, the system is a multi-level tensiometer (MLT) in which vadose zone pressure heads at the depths of the ceramics may be measured manually using a small diameter water tape. Table C.2 lists advantages and disadvantages of such a system.

The first generation of MLTs employed a design consisting of six moderate-flow ceramic discs attached to 6 mm diameter Teflon tubing via custom PVC brackets with fittings. Each fitting was

installed into the side-wall of a hollow 5 cm diameter PVC tube. The maximum depth of the bottoms of the tubes was designed to be the typical water table depth at prospective installation locations.

Concern about the lag time between soil pressure changes and the response in the water column of the manometer due to the hydraulic conductivity of the "Generation 1" MLT (moderate-flow) disks, a second design was developed. The second generation of MLTs used high-flow ceramic cups and a central 1 cm diameter PVC piezometer, to which was fastened all tubing and cups. Custom fittings were again built to connect the ceramics to the 6 mm tubing.

MLTs were prepared for field installation as follows, using a procedure that minimized the risk of air entrapment within the porous ceramics. Each ceramic disk or cup was soaked in de-aired water overnight prior to installation. For the "Generation 1" MLTs, the assembly was set up horizontally and each of the ceramic disks was placed in a de-aired water bath. While the ceramic disk was in the bath, a syringe was used to draw water through the ceramic in order to fill the tubing. Measurement ends of the tubes were capped once filled, and a wet sponge was taped across each ceramic disk overnight. For the "Generation 2" MLTs, the entire ~ 5 m long assembly was set vertically in a larger PVC tube. This larger tube was filled with de-aired water and then a syringe was used to draw water through each ceramic cup until all manometer tubing was filled with water. Each measurement tube end was capped once filled and the ceramics were left to soak overnight.

Installation of the "Generation 1" and "Generation 2" MLTs in the field involved drilling with a track mounted Geoprobe 7720DT rig. For the "Generation 1" MLTs, a borehole of approximately 2 inches in diameter was drilled (while collecting a soil core), then a 3.25-inch metal casing was driven into the pilot hole, and then the 2-inch PVC casing was installed and the metal casing was removed. Attempts were made to align the side of the casing with the ceramic disks against the borehole wall, while silty fine sand was backfilled in the borehole annulus space on the opposite side. The sand was occasionally tamped while backfilling. For the "Generation 2" MLTs, a pilot hole was first hammered down to a depth near the water table, and then 3.5-inch diameter augers were used to create a borehole of sufficient size for the MLT assembly. The MLT assembly was installed in the borehole, and silty fine sand was backfilled and periodically tamped up to a depth of around 1 or 1.5 m below ground surface. Bentonite chips were then backfilled until near ground surface, and native topsoil was used to fill the remaining space.

Table C.2. Advantages and disadvantages of the manual operation multi-level tensiometers.

| Advantages |
|---|
| • pressure head in the vadose zone (i.e., tension) may be measured manually, similar to collecting piezometer or well water levels<br>• measurement equipment consists of only a small diameter water tape with no weights; no other specialized equipment is needed<br>• no need to maintain a vacuum; measurement side of the manometer tube allowed to de-gas; air entry not a problem if hydraulic connection maintained between soil, ceramic material, and water column on soil side of the manometer tube<br>• no moving parts<br>• after initial equilibration, no need to reset tensiometer by adding water (e.g., Burr, 2000)<br>• intuitive design (promotes conceptual understanding)<br>• MLT may be removed using a manual jack during decommissioning |
| Disadvantages |
| • currently lacking a method for continuous data collection*<br>• difficult to verify hydraulic connection between native soil and fine sediment fill around the ceramic cups†<br>• pressure range dictated by depth of installation of the bottom of the manometer tube<br>• insufficient tamping could lead to preferential vertical pathways for drainage to occur through the soil† |

* Would require a small diameter (≤6 mm) pressure transducer of suitable (mm scale) accuracy

† This is a potential issue with all tensiometers.

### C.1.4 Challenges

Finding landowners to host the field stations was an initial challenge. Partnership with the Regional Municipality of Waterloo provided one site (part of the Mannheim site). The Grand River Conservation Authority (GRCA) recommended three land-owners who agreed to host weather stations and wells. Four businesses (a greenhouse operation adjacent to the Regional Municipality of Waterloo site, an organic farm, a farm market, and a golf course) also agreed to host weather stations or other equipment. The County of Oxford provided access to the right-of-way beside a bridge over the lower reach of Alder Creek, where permission from landowners could not be obtained. It was not possible to install monitoring equipment within about one kilometre of the confluence of Alder Creek and the Nith River due to this lack of permission.

Another challenge was the development of rating curves for the stream stations. While low to moderate flow rates in the creek could be gauged manually by wading and using a flow meter, large-magnitude events such as those generated during mid-winter snowmelt events with rainfall could not be measured for safety reasons. Such events were observed to include streamflow in the riparian zone beside the creek at the Mannheim site, putting equipment at risk. A related challenge was damage to steel drivepoint piezometers installed in the creek. Ice movement associated with mid-winter snowmelt events bent some piezometers and pulled one completely out of the streambed.

The gravelly sand unit at the Mannheim site made sampling for the bromide tracer difficult for depths greater than about 1 m. This unit dictated the maximum depth of sampling via hand-auger and tended to yield reduced soil recovery over its thickness during soil coring via drill rig.

## C.2 Results and Discussion

### C.2.1 Tracer Tests

Soil sampling results from the Mannheim site confirmed the hypothesis that composite soil sampling, (i.e., collecting multiple cores and then combining similar depth intervals to create a composite core) provides a more complete analysis of the tracer migration than is given by one core (Figure C.4; Ju, 2016).

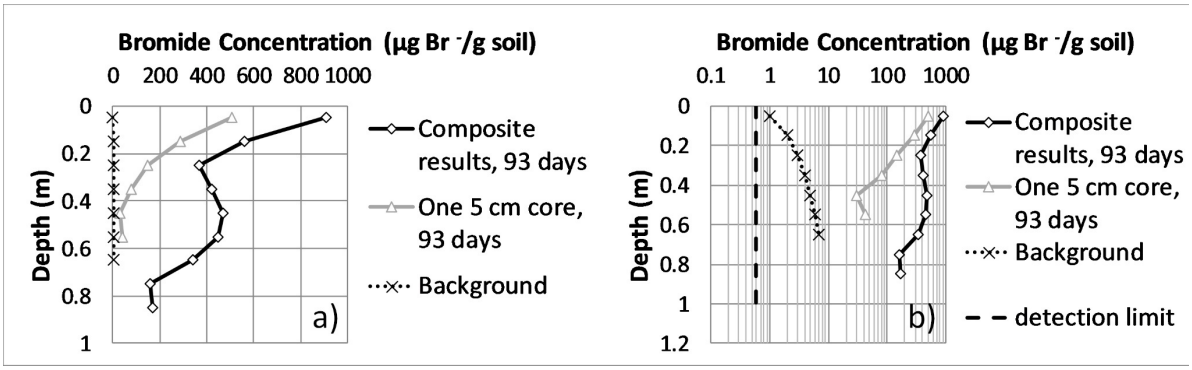


Figure C.4: Soil sampling results after 93 days of tracer migration at the Mannheim tracer plot: a) linear concentration scale; b) logarithmic concentration scale.

Figure C.5 shows the bromide tracer results from the woodlot plot. Results for none of the three sampling events show a decline to near the detection limit as depth increases. The first and second sampling events (at 93 and 369 days of travel time), may have failed to capture the centre of mass of the tracer due to their shallow sampling depth, and the increase in concentration at the bottom of the profile for the third sampling event (524 days) suggests that some amount of the tracer had reached the water table prior to sampling. Thus, any vadose zone drainage rate approximations or recharge estimates based on these results are likely to be underestimates (Table C.3).

Figure C.6 shows that the sampling event at 93 days at the field plot resulted in concentrations much higher than the detection limit at the bottom of the profile. Samples collected after 524 days were near or below the detection limit, suggesting that most of the tracer mass had been flushed through the system.

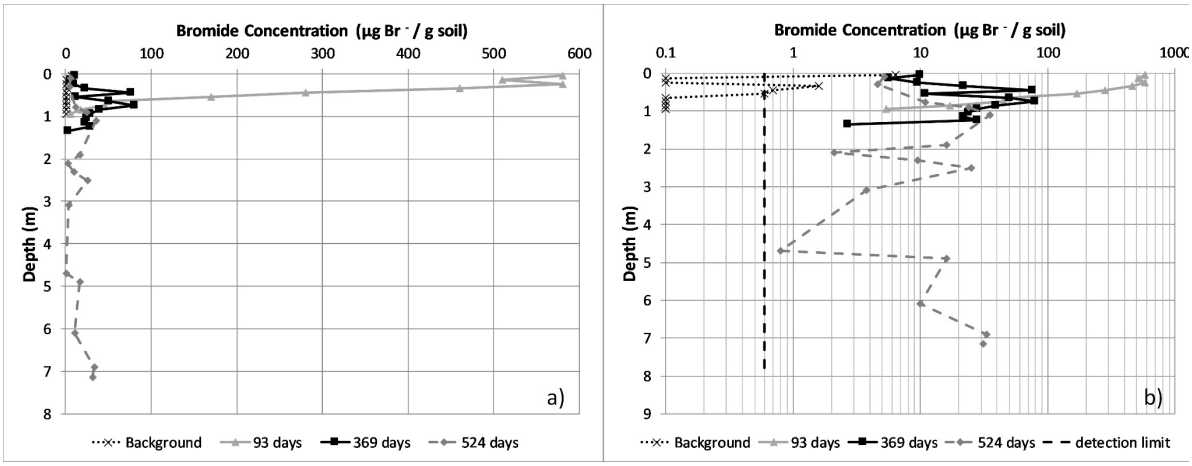


Figure C.5: Bromide tracer results for the Bethel Road site – Woodlot plot: a) linear concentration scale; b) logarithmic concentration scale.

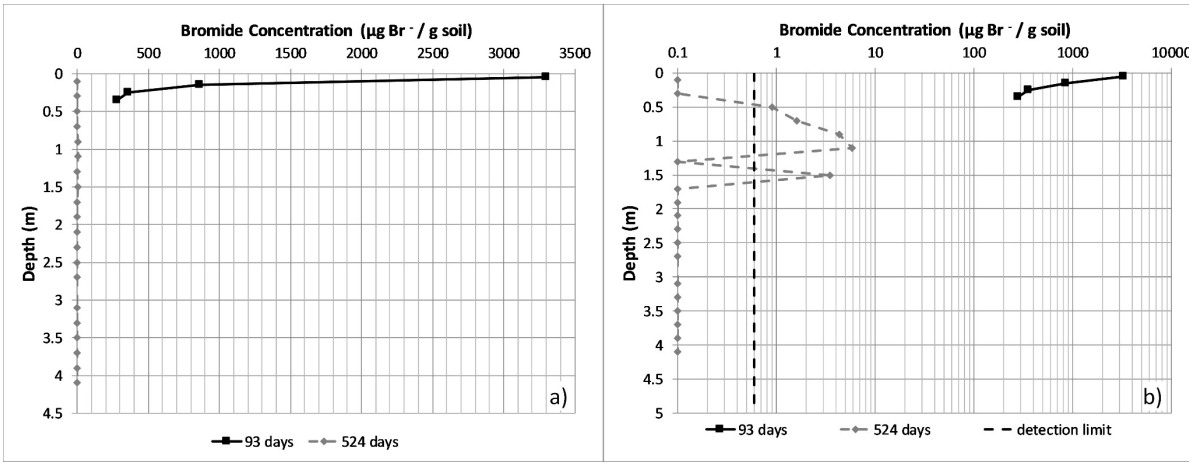


Figure C.6: Bromide tracer results for the Bethel Road site – Field plot: a) linear concentration scale; b) logarithmic concentration scale.

Table C.3. Recharge estimates based on bromide tracer results.

| Location (Soil sampling method, no. of samples) | Maximum Sampling Depth (m) | Depth of Centre of Mass (m) | Travel time (yr) | Average Volumetric Water Content ($m^3/m^3$) | Drainage rate estimate [§] (m/yr) |
|---|---|---|---|---|---|
| CP – Grass plot (Composite, 9) | 0.9 | 0.34 | 0.27 | 0.16[*] | 0.20 |
| CP – Grass plot (2" core, 1) | 0.7 | 0.16 | 0.27 | 0.16[*] | 0.09 |
| Bethel Rd. – Woodlot (Composite, 7) | 1.0 | 0.27 | 0.27 | 0.15[†] | 0.15 |
| Bethel Rd – Field (Composite, 4) | 0.4 | 0.10 | 0.27 | 0.07[‡] | 0.03 |
| Bethel Rd – Woodlot (Composite, 5) | 1.4 | 2.48 | 1.02 | 0.15[†] | 0.36 |
| Bethel Rd – Woodlot (Composite, 3) | 7.6 | 3.50 | 1.44 | 0.15[†] | 0.36 |
| Bethel Rd – Field (Composite,3) | 3.8 | 1.06 | 1.44 | 0.07[‡] | 0.05 |

[*] VWC calculated via overall calibration equation (y = 0.3112x + 0.1398), Appendix H.

[†] VWC calculated via silty topsoil and silty SAND equation (y = 0.1795x + 0.3839), Appendix H.

[‡] VWC calculated via gravelly SAND equation (y = 0.0991x – 0.0005), Appendix H.

[§] Drainage rate calculated via $d = \frac{\Delta z}{\Delta t}\theta_{avg}$ (Bekeris, 2007)

### C.2.2 Multi-Level Tensiometers

Early readings (shortly after installation) for each MLT were likely influenced by the initial equilibration of pressure between the two sides of the manometer. Each tube was initially filled with water on the measurement side, and this water would flow out of the ceramic ports into the soil until equilibration.

The deeper MLTs at the Mannheim site do not suggest the presence of a zero-flux plane, except possibly on a few days at MLT3 (Figures C.11 and C.13). This may be due to shallow transpiration by vegetation (grass) near MLT2 and MLT3 ("Generation 2" MLTs). Conversely, MLT1 ("Generation 1") was located closer to several trees and suggests the presence of a zero-flux plane (sink) at a depth of about 2 m during some parts of the year (Figure C.9). However, some of the hydraulic head profiles with troughs at the 1.84 m deep port occur during winter.

Some studies assume that a zero-flux plane will develop in the vadose zone soil profile beneath agricultural fields (e.g., Bekeris, 2007). Despite the use of "Generation 1" low flow ceramic ports in the Bethel Road site's MLTs, Figure C.15 suggests that a zero-flux plane may frequently be present under the agricultural field. The peak in the total hydraulic head suggests that water is moving away from the zero-flux plane both upward (due to evapotranspiration) and downward (due to gravity drainage of soil moisture) (Healy, 2010). Two of the three complete sets of hydraulic head estimates for the woodlot tensiometer (Figure C.17) show a zero-flux plane that is a trough (sink) in middle of the profile. Water appears to be moving toward an intermediate depth somewhere between the ports at depths of 1.3 m and 3.4 m. This occurs on 27 Sep 2016 and 4 Oct 2016, possibly indicating that the roots of the nearby deciduous trees draw water from this depth range. The only other complete set of measurements for this tensiometer shows a snapshot of the tension profile in late October. This profile suggests drainage between all measurement ports and does not contain a zero-flux plane. Deciduous trees may have stopped transpiring by this time, allowing drainage to occur more continuously. Measurements could not routinely be made at the deepest port of MLT2 at the Bethel Road site, likely due to constriction of the tubing. The water tape could not pass a certain point.

Pressure should theoretically equilibrate between native soil and the backfilled soil around the ceramics at pseudo-steady state. This is expected to be reasonable under conditions where changes are not too rapid. The amount of water migration into and out of the tensiometer could be a concern (T. Ferré, pers. comm., 2016). While the amount of water between the ceramic and the bottom of the manometer is constant, the size of the tubing on the open side of the "U" dictates the volume of water that must be exchanged with the soil pores for a unit change in pressure. Another issue is that

installation of tubing extending below the water table would require casing to be driven below the water table, which was not possible with the auger system on the drill rig. This limits the depth of installation and the maximum pressure range. MLT measurements suggest that the installation depths used in the present study (5 or 5.5 m) were suitable for the local soil tensions experienced.

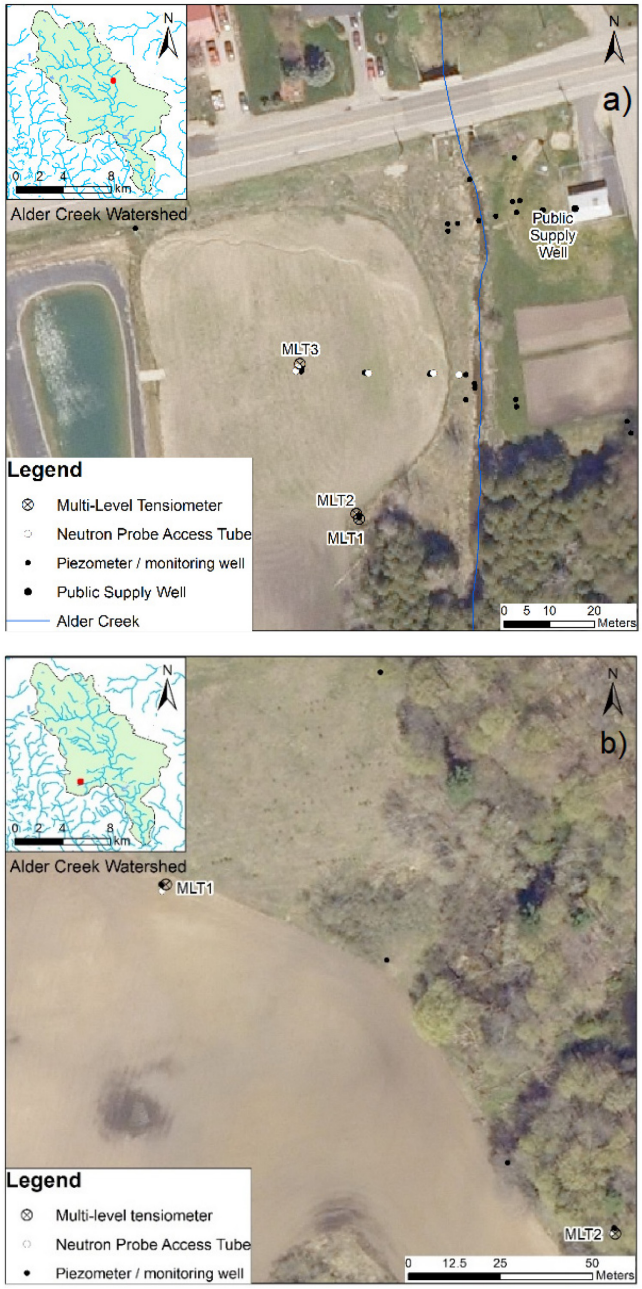


Figure C.7: Locations of the three multi-level tensiometers at: a) the Mannheim site, and b) the Bethel Road site (DMTI, 2011; First Base Solutions, 2006; GRCA, 1998).

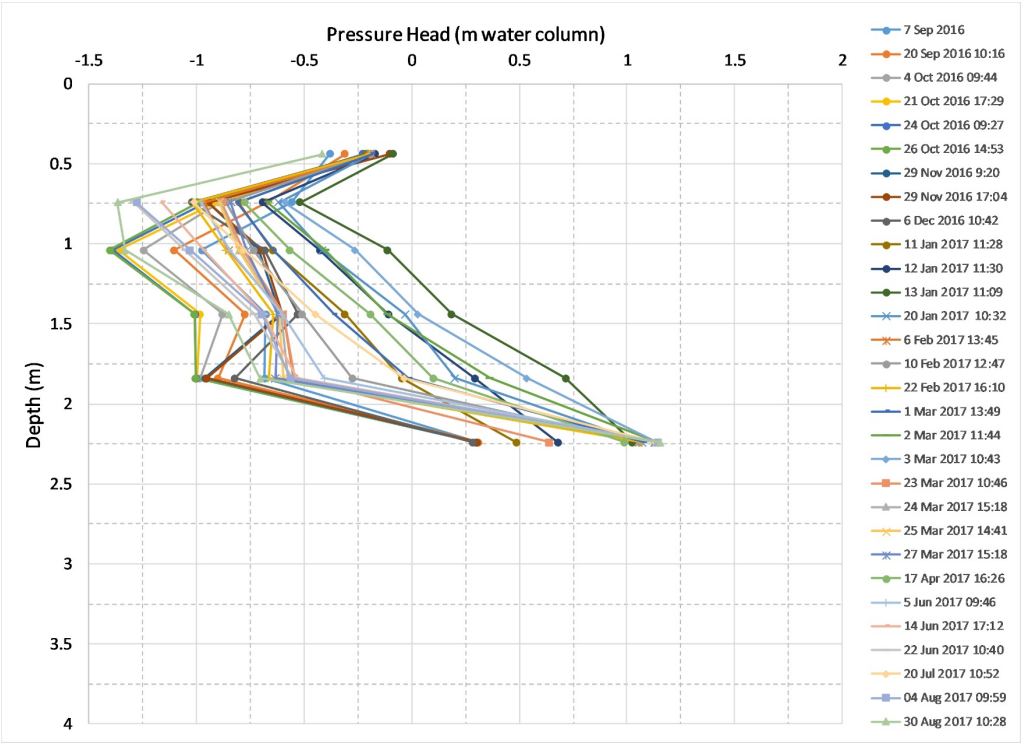

Figure C.8: Pressure head profiles for Mannheim MLT1.

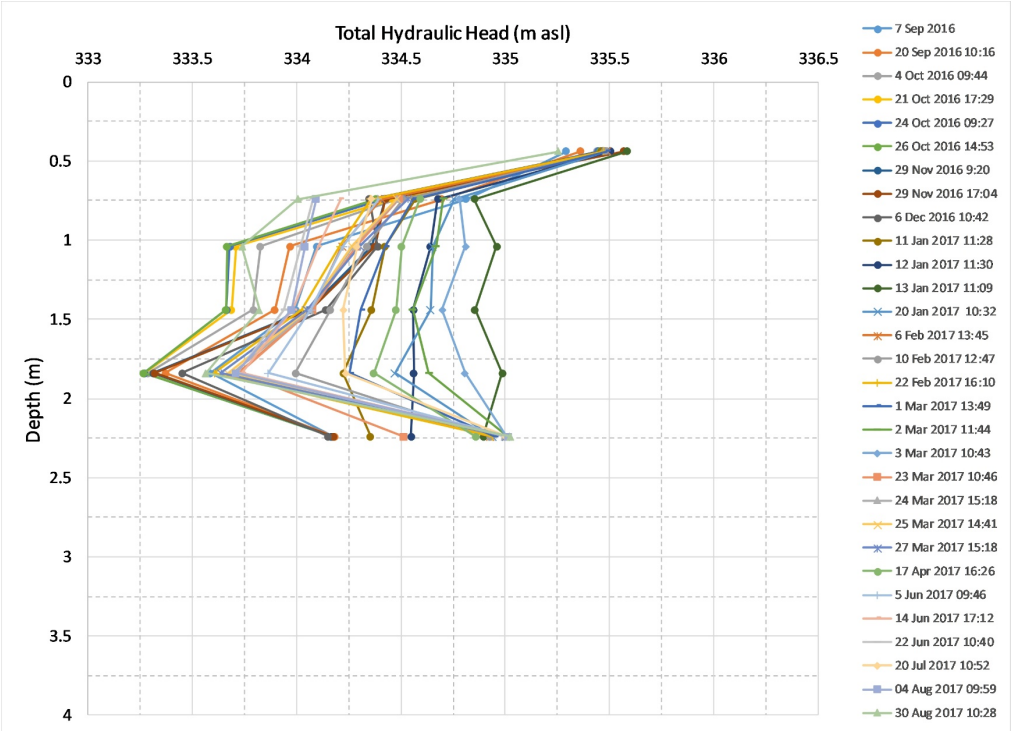

Figure C.9: Hydraulic head profiles for Mannheim MLT1.

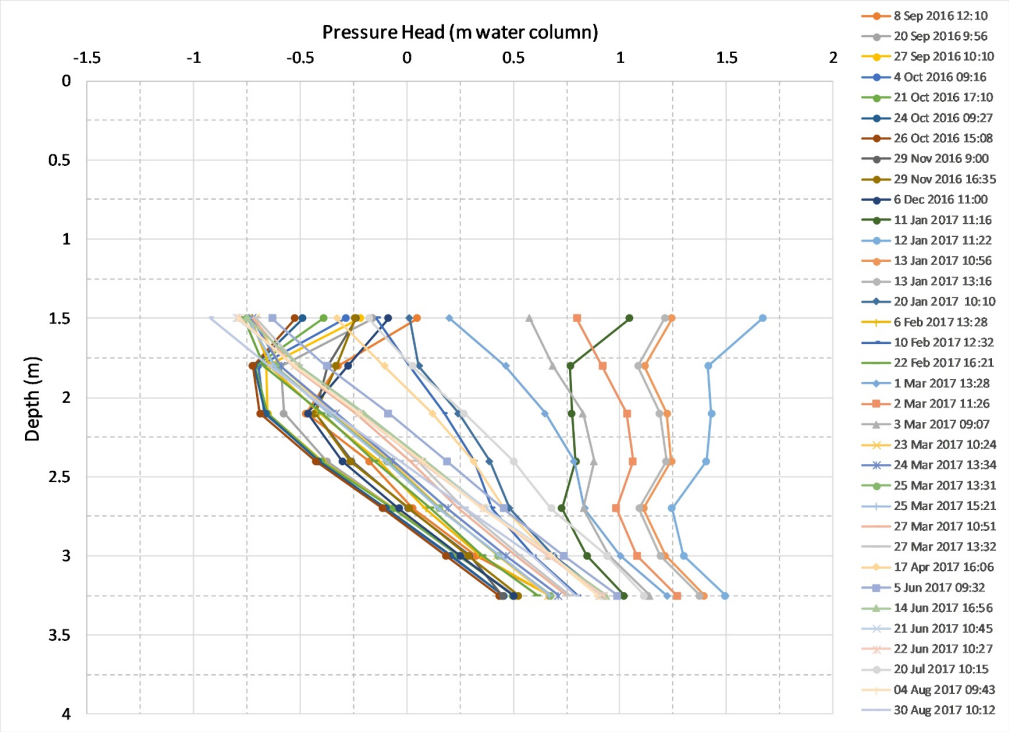

Figure C.10: Pressure head profiles for Mannheim MLT2.

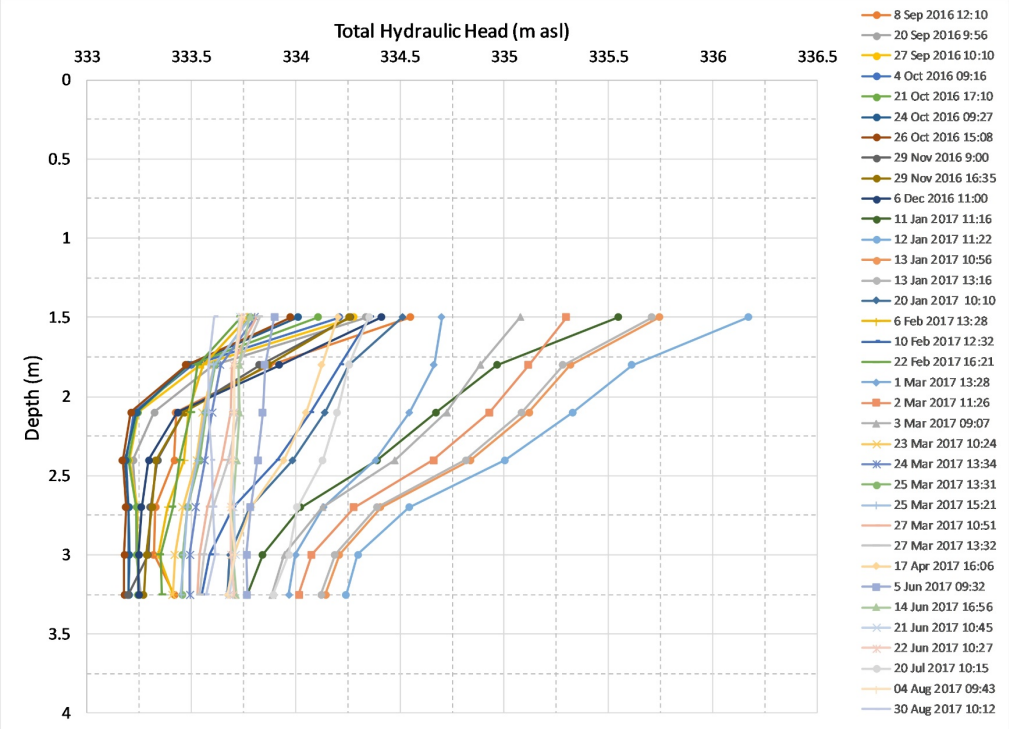

Figure C.11: Hydraulic head profiles for Mannheim MLT2.

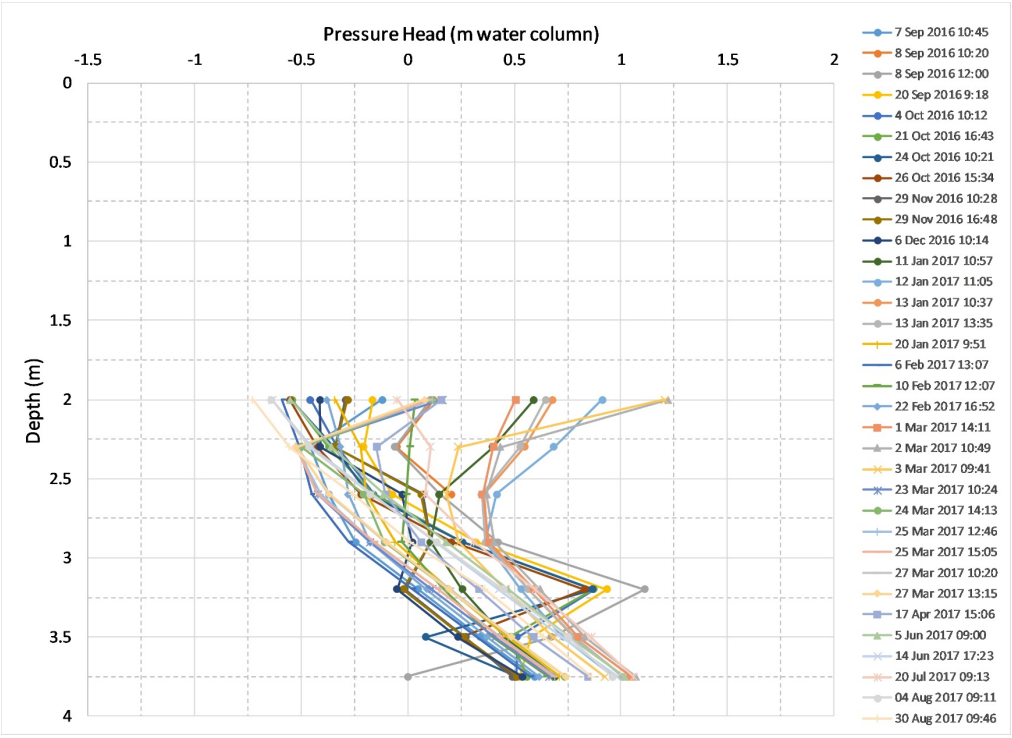

Figure C.12: Pressure head profiles for Mannheim MLT3.

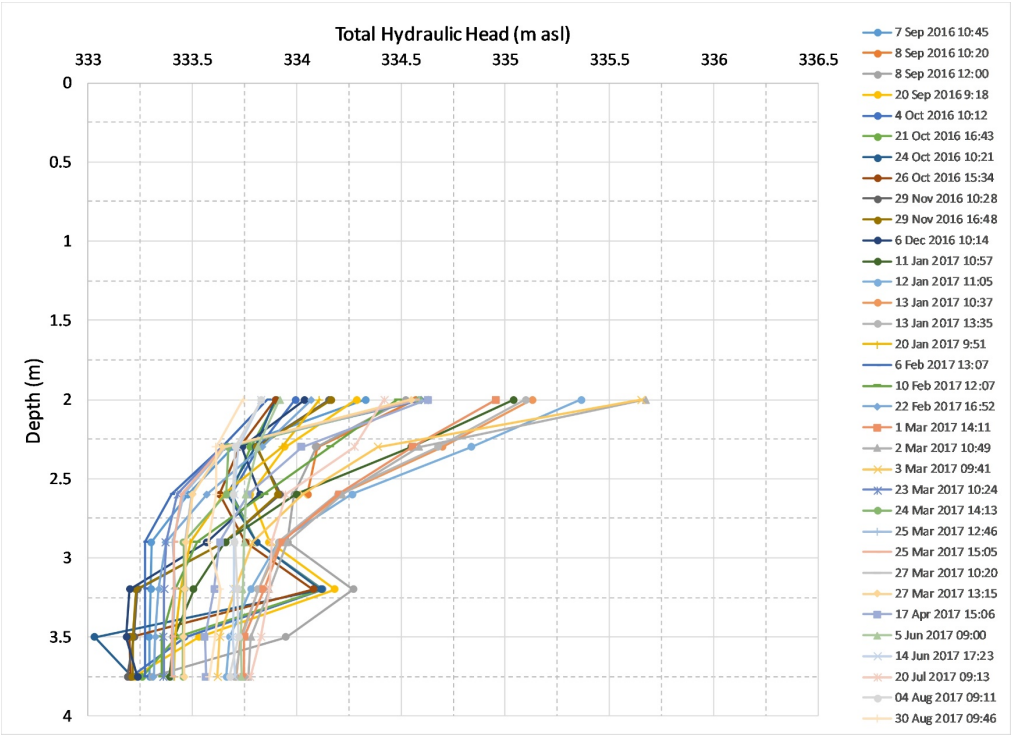

Figure C.13: Hydraulic head profiles for Mannheim MLT3.

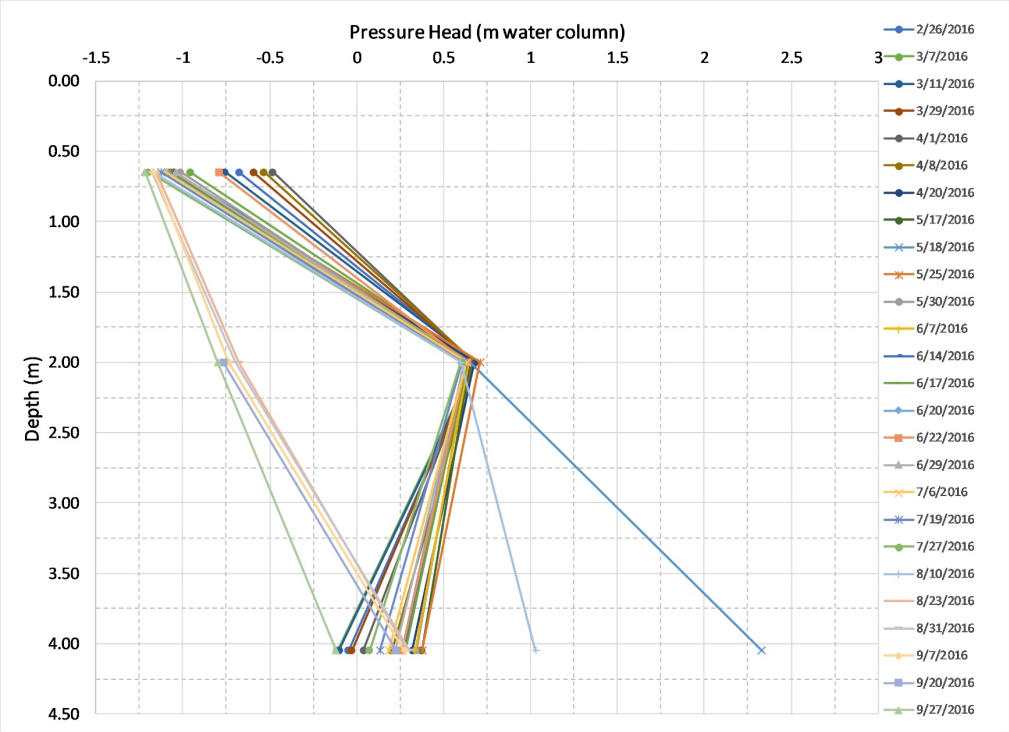

Figure C.14: Pressure head profiles for Bethel Road MLT1.

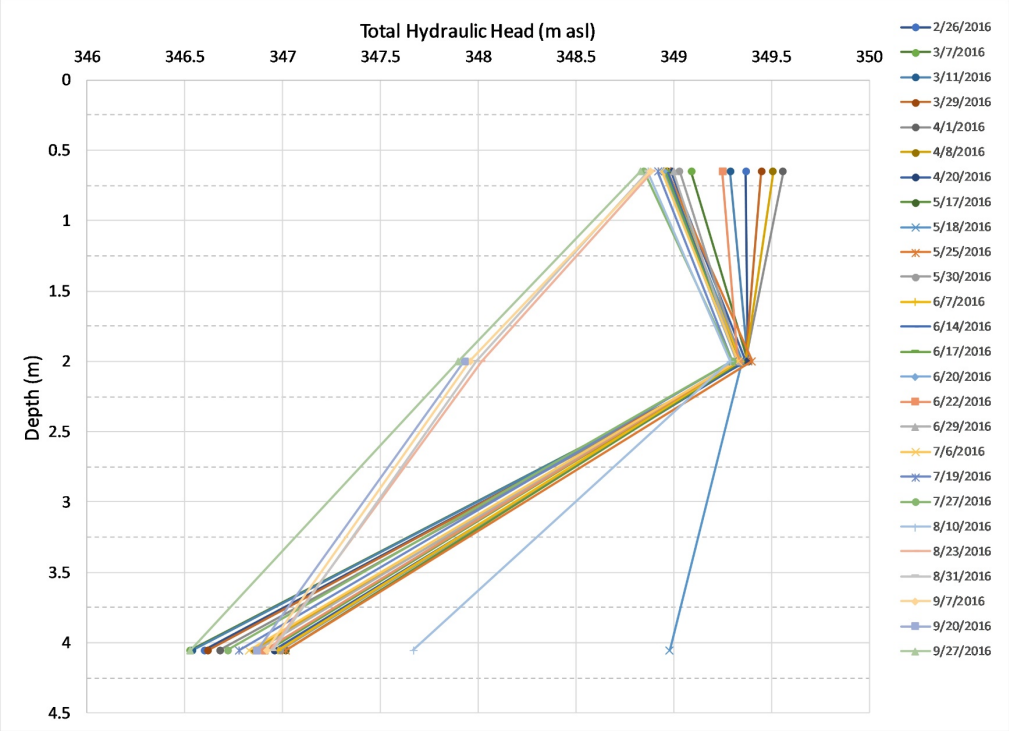

Figure C.15: Hydraulic head profiles for Bethel Road MLT1.

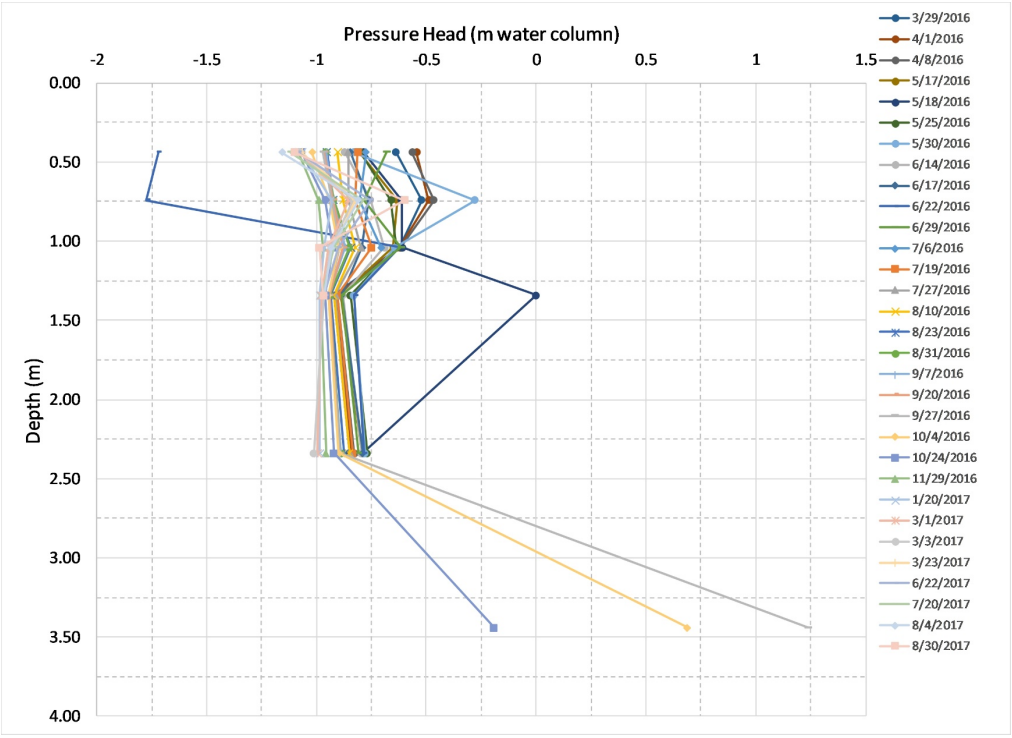

Figure C.16: Pressure head profiles for Bethel Road MLT2.

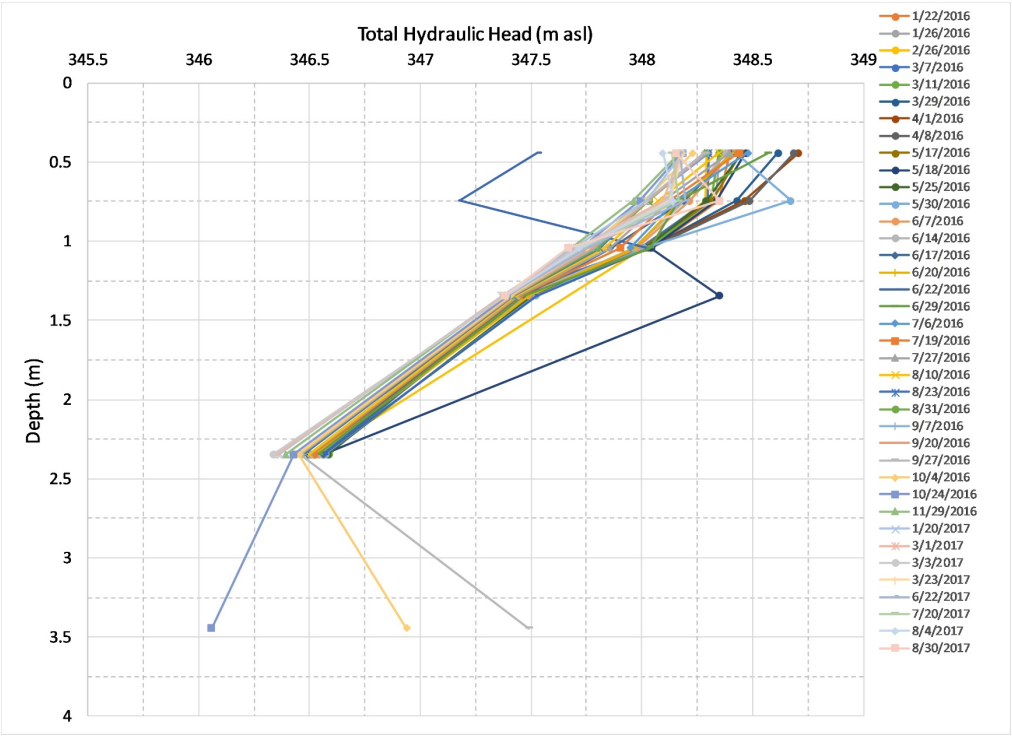

Figure C.17: Hydraulic head profiles for Bethel Road MLT2.

### C.2.3 Data from the Alder Creek field observatory

Most of the meteorological and hydrological data collected are available - see Wiebe et al. (2019).

## C.3 Recommendations

Rain Gauges

- Install at least two rain gauges at each weather station. This is similar to the recommendation by Krajewski et al. (2003). Having multiple rain gauges was beneficial at WS6, where one of the gauges had electrical connection problems.
- Collect rainwater from each gauge in a container for volume checking. It may be advantageous to store this water underground, where temperature fluctuations would be damped, and evaporation will be less likely. The collection system must account for freezing, however.

Weather Stations

- More regular maintenance checks are advised. For example, a suitable schedule could involve a maintenance check of each weather station every two months. Items to check include battery voltage, battery wiring connections, rain gauge funnel, and rain gauge wiring continuity. It is important to check battery wiring because corrosion can lead to poor connections or the disconnection of wires from the battery terminals. Debris should be cleaned out of the rain gauge funnel to avoid build-up that could lead to clogging. Rain gauge wiring continuity testing should be performed using a voltmeter on the wires that plug into the datalogger. The gauge should be disconnected from the datalogger to avoid erroneous readings, and then the bucket should be tipped manually to test the signal transmission.
- Acoustic snow sensors should be retrieved after snowfall is unlikely in the spring and the internal desiccant should be replaced prior to re-installation in the fall.
- Venting strategies for pressure transducers connected to dataloggers within enclosures should be assessed. Vented pressure transducers were found to have a slight offset of up to about 10 cm from the manual water level measurements, and this may be due to the vent tubes terminating within the enclosure, despite the enclosure having a waterproof air vent.

Solute Tracer Tests

- More frequent sampling is recommended, especially in coarse-grained unsaturated soils, with a drill rig. Drilling soil cores when soil is moist may maximize soil recovery in coarse soils. Tracer applications should target areas without coarse gravel units in the vadose zone, thereby avoiding soil layers likely to yield poor soil recovery.

Soil Moisture Block Sensors

- The soil moisture block sensors for matric potential did not function well at the Mannheim site. Testing of these devices under controlled or well-monitored conditions should be conducted, and installation techniques should be reviewed.

Multi-Level Tensiometers

- Improvements to the MLT design are recommended. An alternative installation method is suggested by Figure 6.2 in Fetter (2001). Porous ceramic cups could be attached to tubing as in the "Generation 2" MLTs discussed above but installed right-way up (tubing going up to ground surface), and then the tubing could form a manometer "U" inside the casing of a nearby well. This would decrease the depth of drilling required specifically for the tensiometers, and the maximum pressure range (in metres of water column) would be dictated by the difference in elevation between the ceramic cup and the bottom of the well. Thus, the pressure range could be extended beyond the limitations of the auger system.
- Bentonite chips could be backfilled with care in between the measurement ports and above the upper measurement port to limit preferential vertical flow through the disturbed borehole. Each ceramic cup would need a suitable silt/sand pack extending above and below it to ensure a good hydraulic connection with native soil.

# Appendix D
# Alder Creek climate and precipitation

## D.1 Introduction

This appendix describes introduces the climate of the Alder Creek watershed, presents monthly graphs of rainfall and snowfall, and notes how rainfall and snowfall were combined to produce total precipitation time series. Data may be obtained from the URLs associated with the Wiebe et al. (2019), GRCA (2017a), and Government of Canada (2019) references.

The Alder Creek watershed is located within a region of southern Ontario that is classified as "humid continental" within the Köppen-Geiger climate classification system (Peel et al., 2007). The area has a cold climate with a warm summer, relative to regions across the globe. Precipitation in southern Ontario tends to be around 1,000 mm/yr with about 20% falling as snow (Champagne et al., 2020; Wang et al., 2015). Storms may be frontal or convective (Paixao et al., 2015); the lack of mountainous terrain nearby precludes orographic storms. Alder Creek is located far enough from the nearby Great Lakes (Lake Huron and Lake Erie) to avoid direct lake-effect precipitation much of the time. Maps in Suriano and Leathers (2017) suggest that lake-effect snow does impact the region around Alder Creek occasionally, under certain weather conditions.

Figure D.1 shows the average monthly total precipitation at the Roseville Environment Canada weather station. Precipitation is reasonably well distributed throughout all months of the year (Champagne et al., 2020; Wang et al., 2015), with 20 mm less than the monthly average in February and 15 mm more in July. The $ET_o$ curve superimposed on the precipitation amounts in Figure D.1 suggests that precipitation and ET are *in phase*, i.e., that maximum precipitation and maximum ET occur in the same season. Figure D.1 also shows that peak streamflows occur in winter to early spring, between February and April, which is common for southern Ontario (Burn and Whitfield, 2015; Champagne et al., 2020).

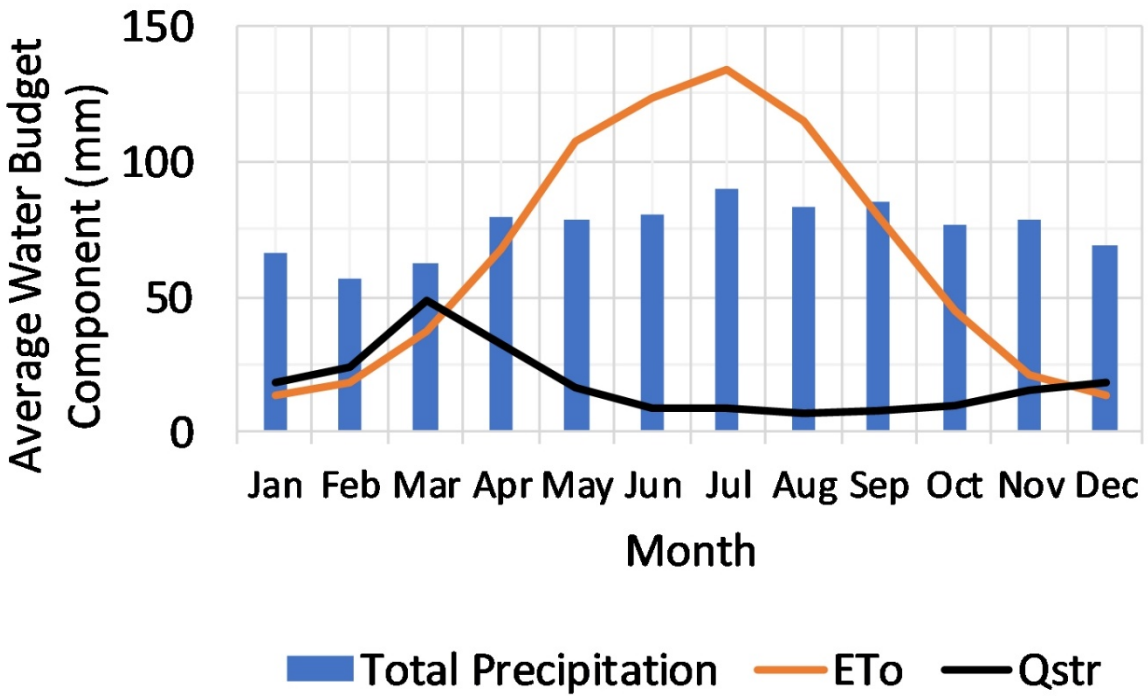


Figure D.1: Precipitation (Government of Canada, 2019), reference ET (ETo; Penman-Monteith method via ETo Calculator program, Raes, 2009; temperature data from Government of Canada, 2019; average wind speed from Wiebe et al., 2019), and estimated streamflow (Qstr; WSC, 2019) for the Alder Creek watershed. Average values are shown for each month based on analysis of daily data from 1973 to 2018. A scaling factor of 1.54 ($Q_{total,\ average,\ estimated}$ / $Q_{WSC,\ average}$; see Appendix Q), was used to adjust the measured streamflow at the WSC gauge within the watershed to be an estimate relevant for the entire watershed.

## D.2 Rainfall

### D.2.1 Local Rainfall

Figures D.2 to D.7 show monthly rainfall totals at the local SOWC rain gauges. The low rainfall amounts (< 15 mm per month) at WS2 (Figure D.2) and WS6 (Figure D.6) from May to Dec 2016 are likely related to equipment problems, though both stations exhibited this pattern in the data. The gauges were still recording non-zero rainfall amounts at times, so the electronics were at least partially operational. The reason for the low rainfall amounts is unclear. The rainfall data from these two stations were used in: 1) the correlation analysis shown in Figure 2.4, 2) the MIKE SHE model simulation Scenario 3, and 3) the correlation analysis shown in Figure 4.2. If the May to Dec 2016 time period was omitted from correlations between WS2 or WS6 and the other local gauges, nine of the SOWC points would shift upward (show increased correlation) for each of the three time intervals on Figure 2.4. If the May to Dec 2016 time period for these two stations was omitted from the rainfall interpolations in Scenario 3, the total precipitation and average recharge for Scenario 3 would increase in 2016. This would not be likely to change the conclusions in Chapter 2. Omission of the May to Dec 2016 data from the WS2 and WS6 stations would increase the Spearman Rank Correlation coefficients of 11 of the 21 points on Figure 4.2 by $\leq 0.05$.

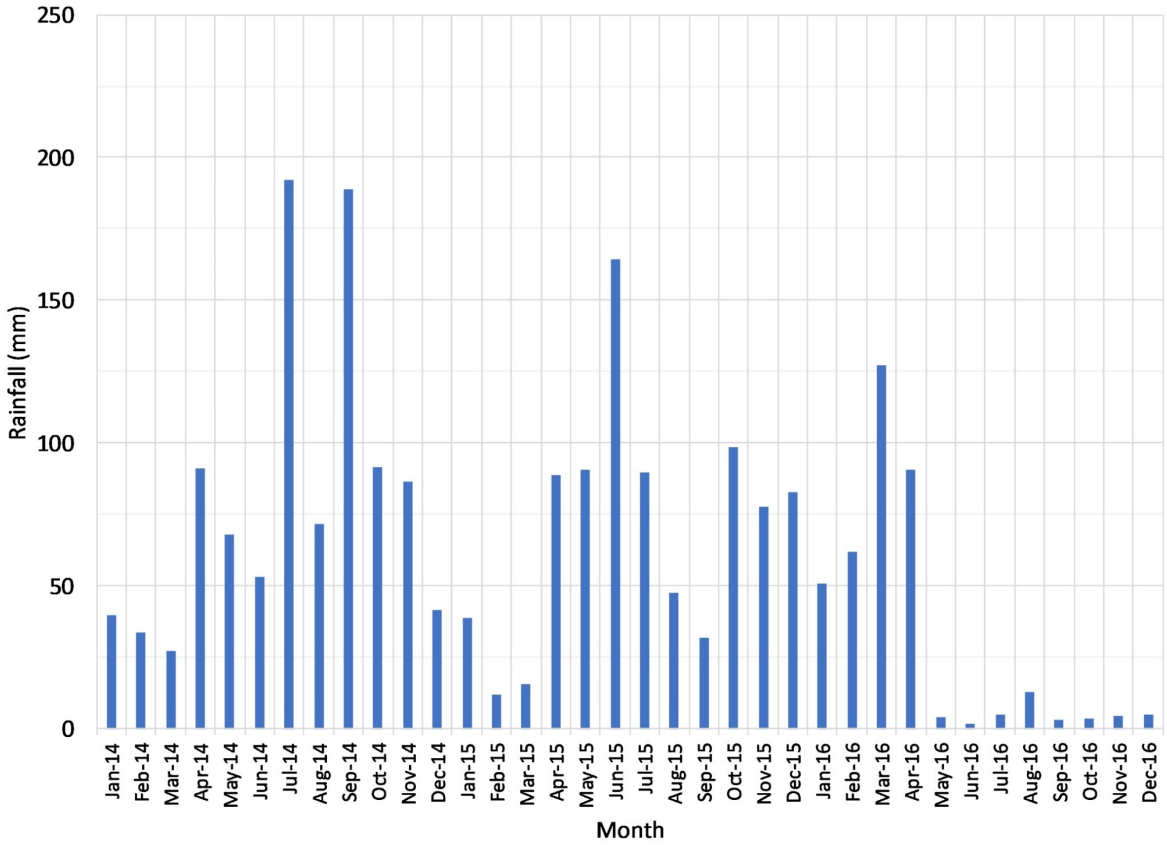


Figure D.2: Monthly rainfall at the WS2 local station (Wiebe et al., 2019).

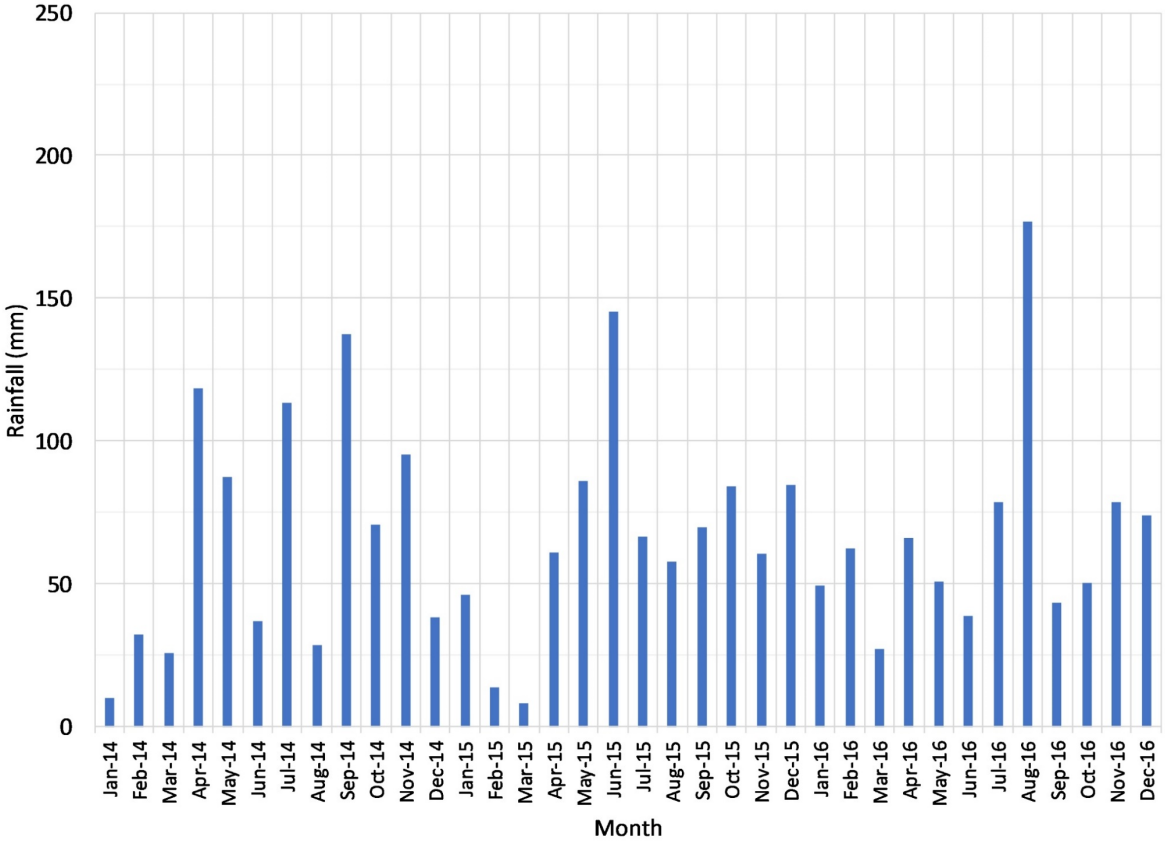


Figure D.3: Monthly rainfall at the WS3 local station (Wiebe et al., 2019).

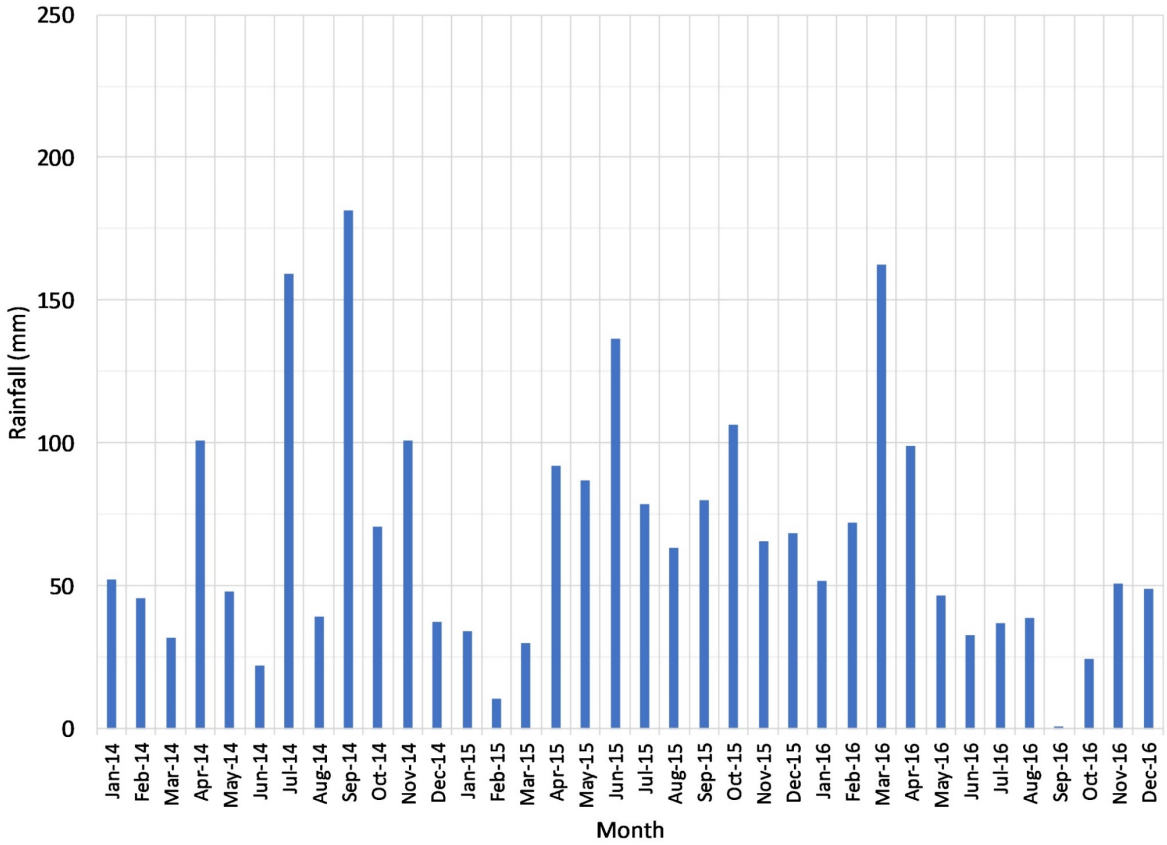


Figure D.4: Monthly rainfall at the WS4 local station (Wiebe et al., 2019).

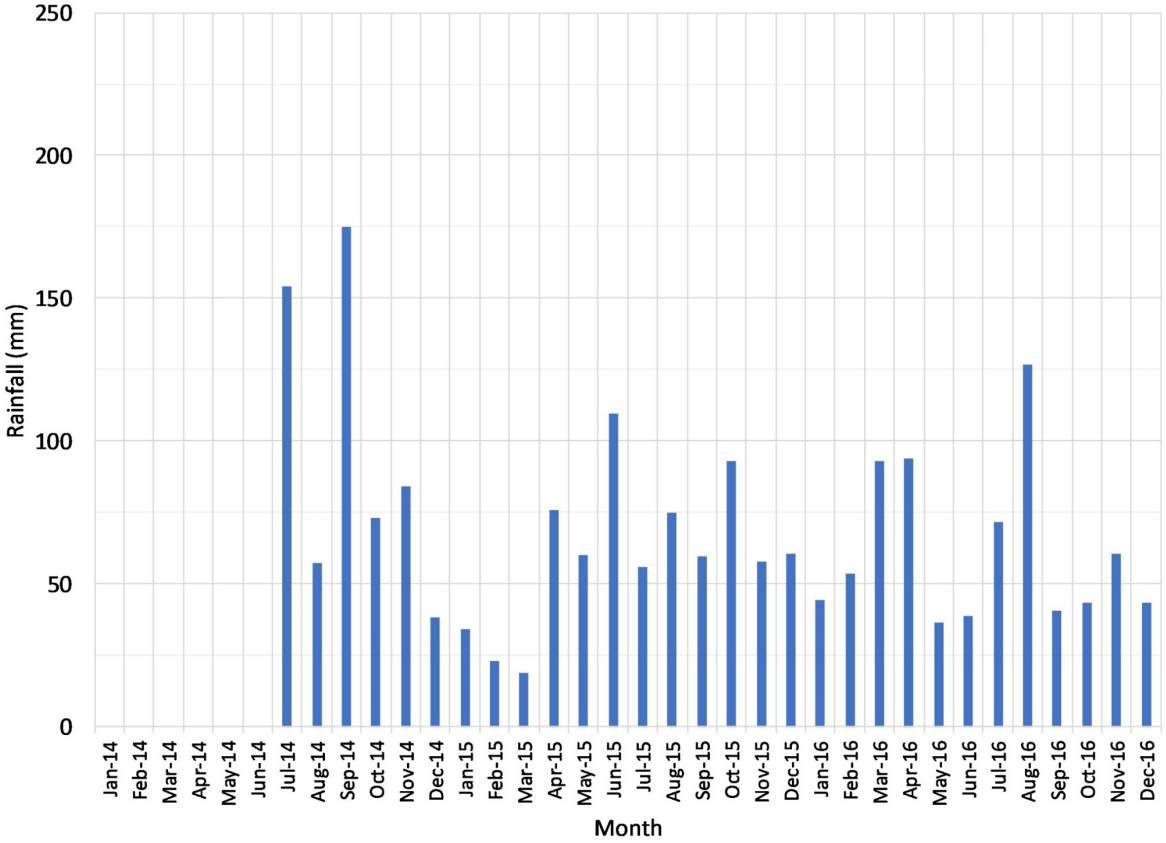


Figure D.5: Monthly rainfall at the WS5 local station (Wiebe et al., 2019). Data collection at WS5 started on 20 June 2014. The graph omits the incomplete month of June 2014.

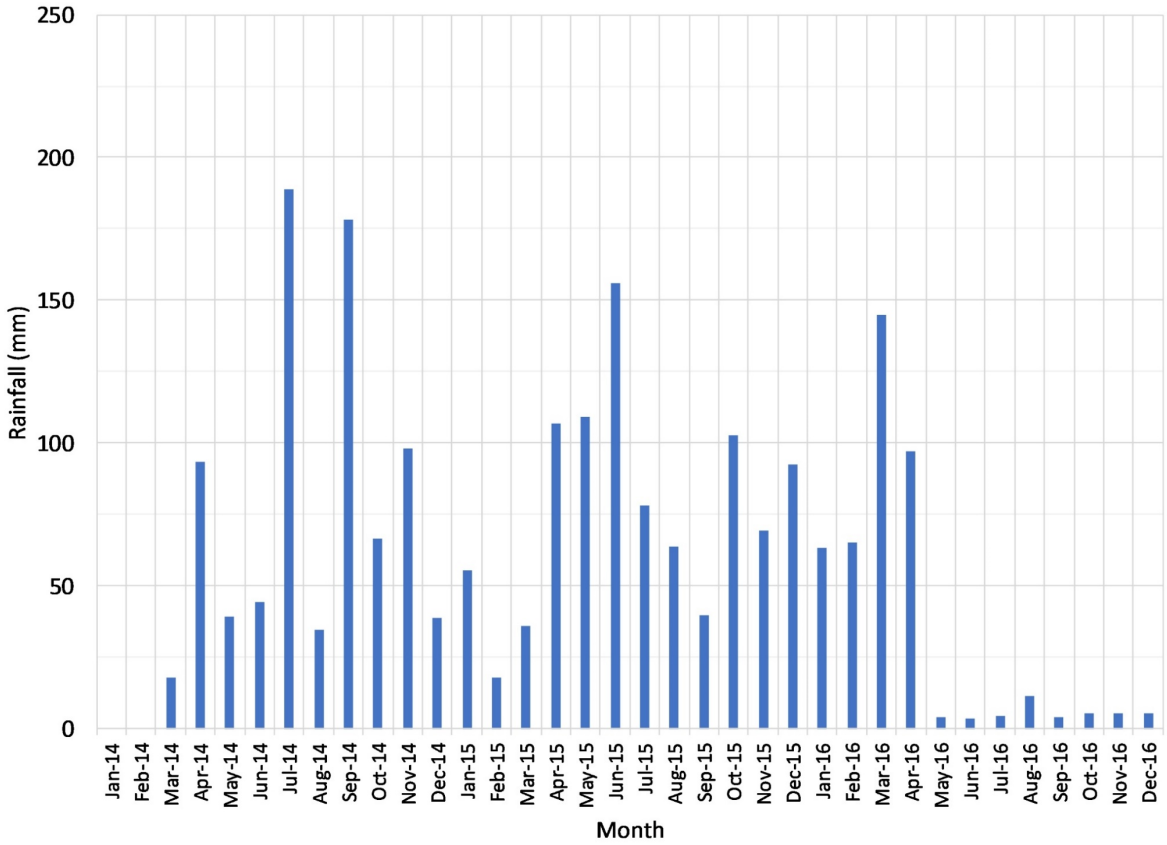


Figure D.6: Monthly rainfall at the WS6 local station (Wiebe et al., 2019). The data shown are a composite of data from two rain gauges at the site.

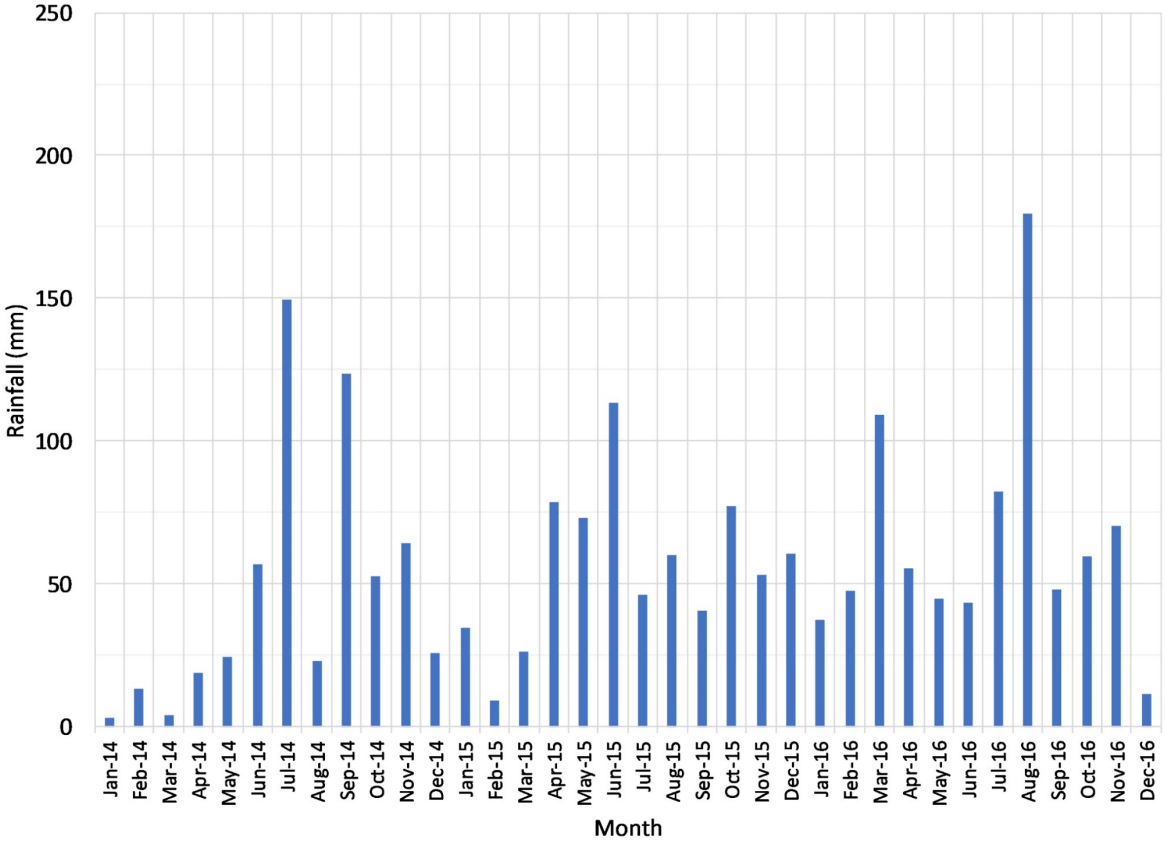


Figure D.7: Monthly rainfall at the WS7 local station (Wiebe et al., 2019).

### D.2.2 Regional Rainfall

Figures D.8 to D.13 show monthly rainfall totals at the regional GRCA rain gauges. There appear to be some missing data (Jan to Apr 2014; Jul to Dec 2016) from the Burford rain gauge (Figure D.9). The rainfall data from this station were used in: 1) the correlation analysis shown in Figure 2.4, and 2) the MIKE SHE model simulation Scenario 2. Omission of these time periods would lead to increased correlation for five of the GRCA points in each of the three time intervals on Figure 2.4. If these time periods were omitted from the rainfall interpolation, Scenario 2 would have higher total precipitation and recharge in 2014 and in 2016. This would not change the conclusions of Chapter 2.

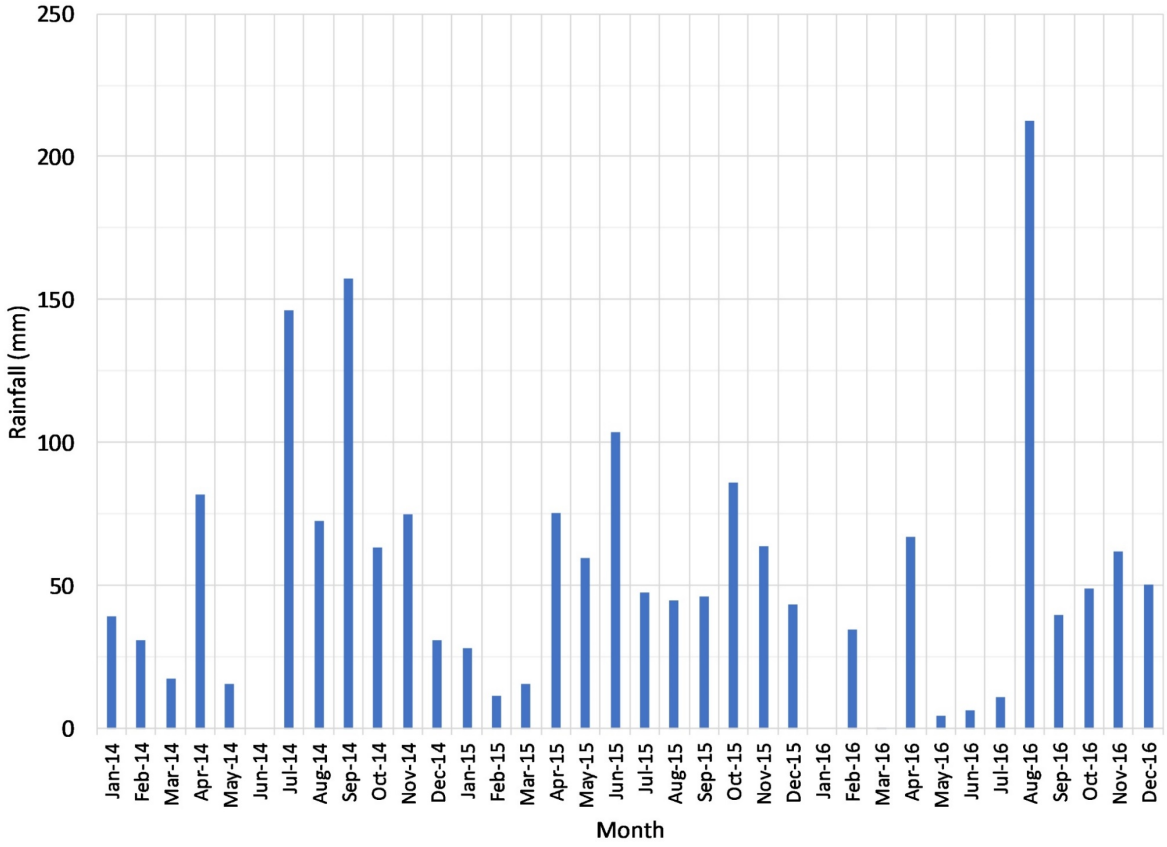


Figure D.8: Monthly rainfall at the Baden GRCA station (GRCA, 2017a).

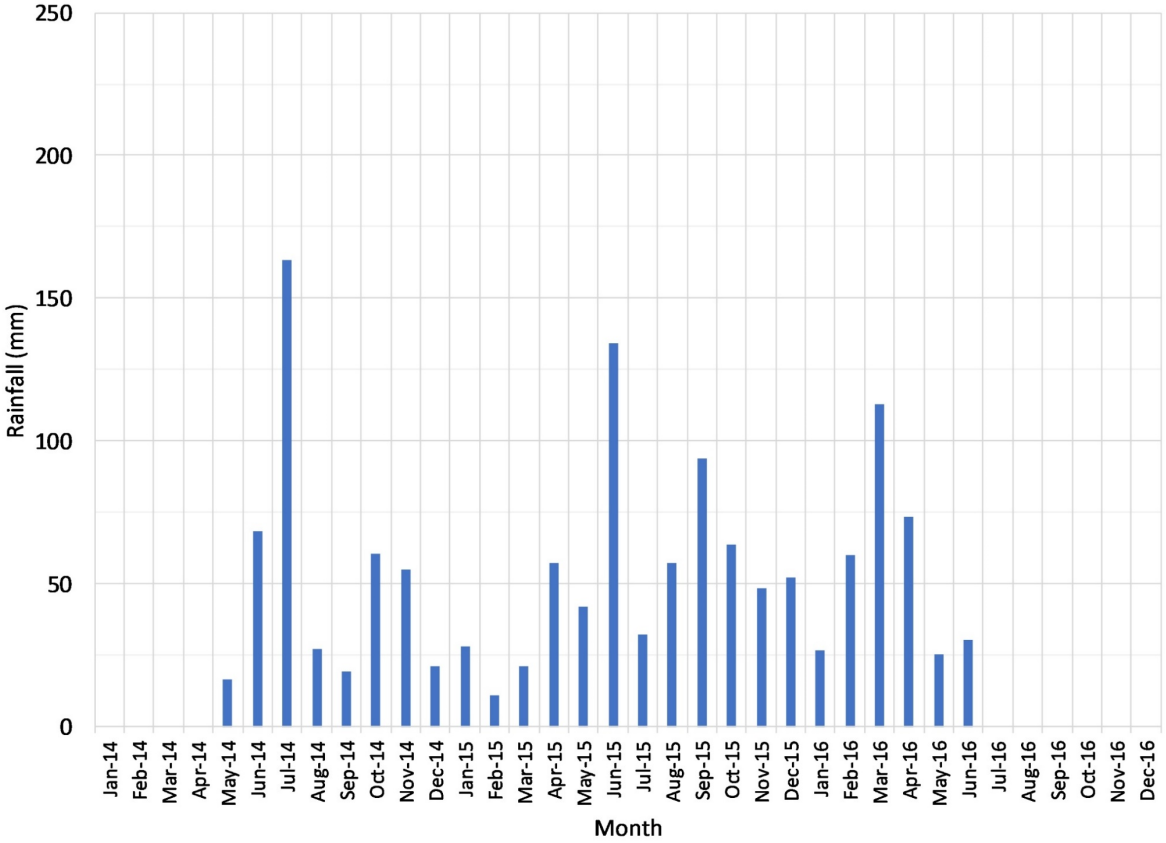


Figure D.9: Monthly rainfall at the Burford GRCA station (GRCA, 2017a). An anomalously high hourly reading of 219.4 mm on 26 May 2014 at 18:00 was considered erroneous and was removed.

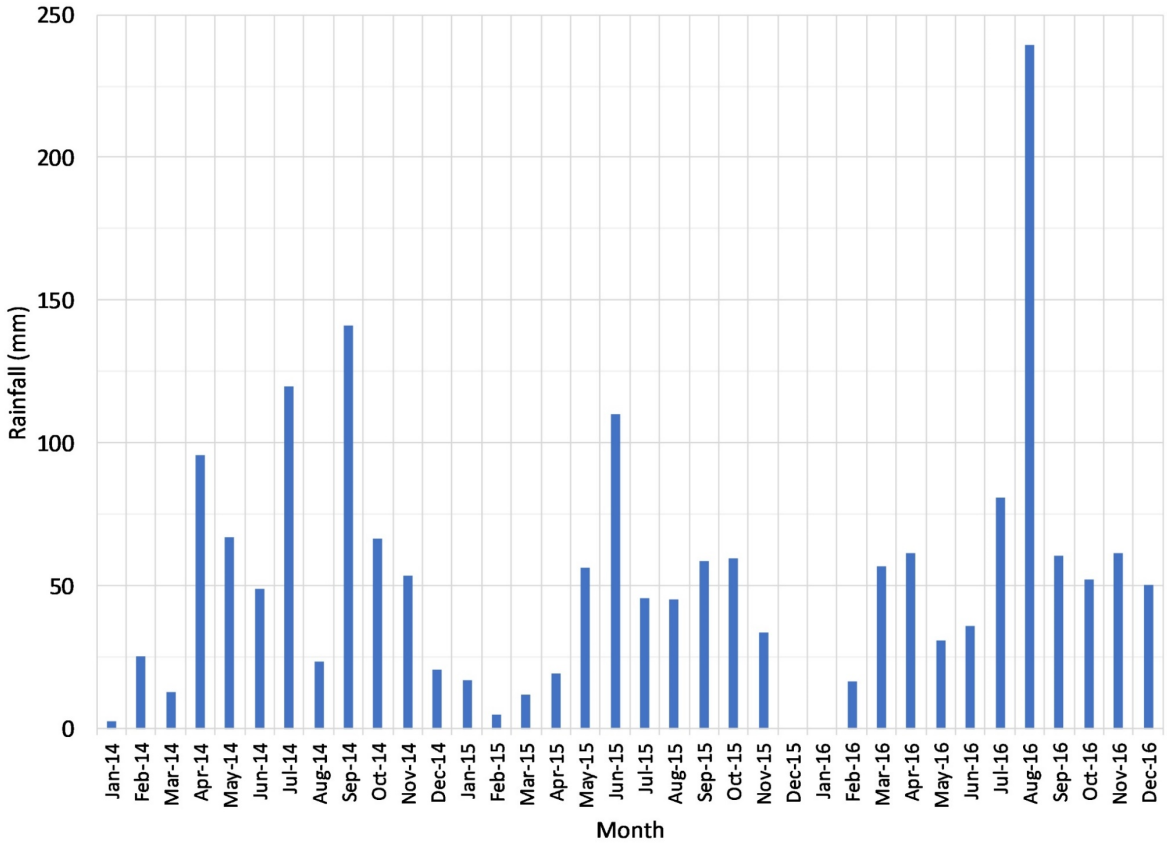


Figure D.10: Monthly rainfall at the Cambridge GRCA station (GRCA, 2017a).

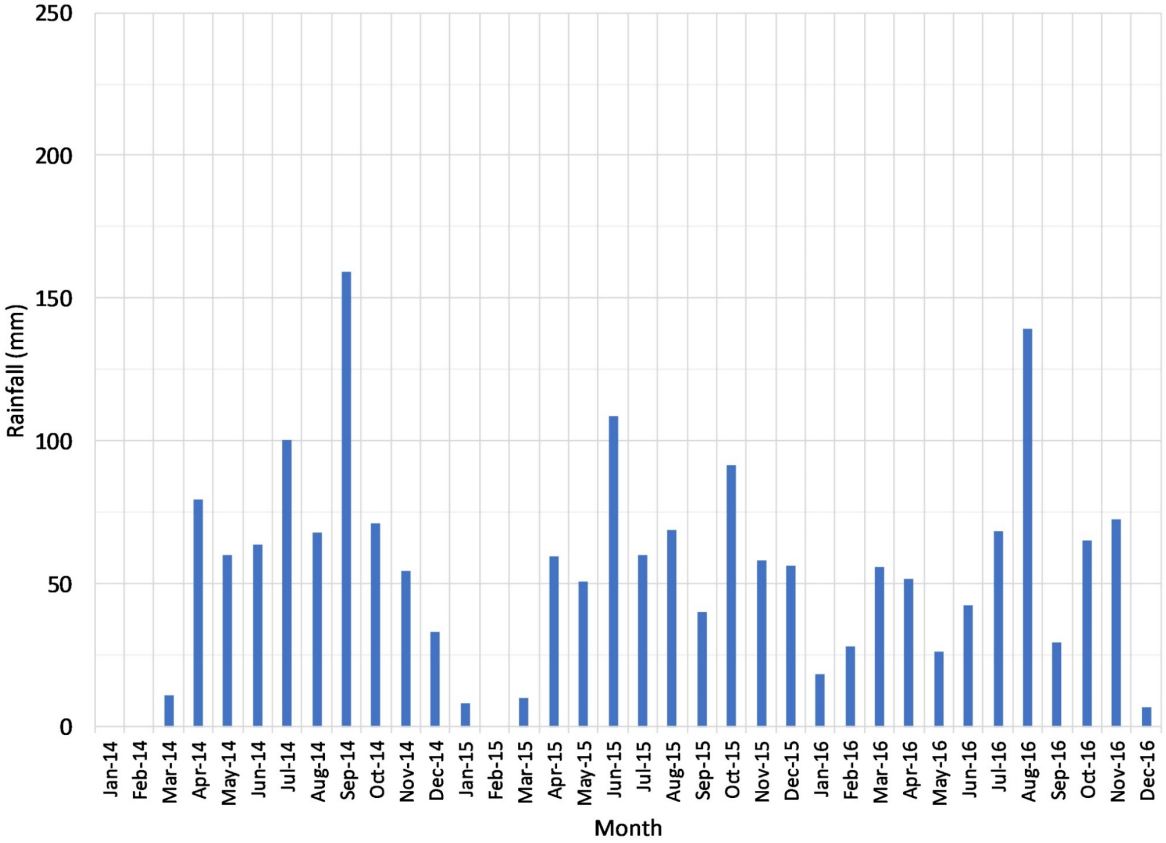


Figure D.11: Monthly rainfall at the Laurel GRCA station (GRCA, 2017a).

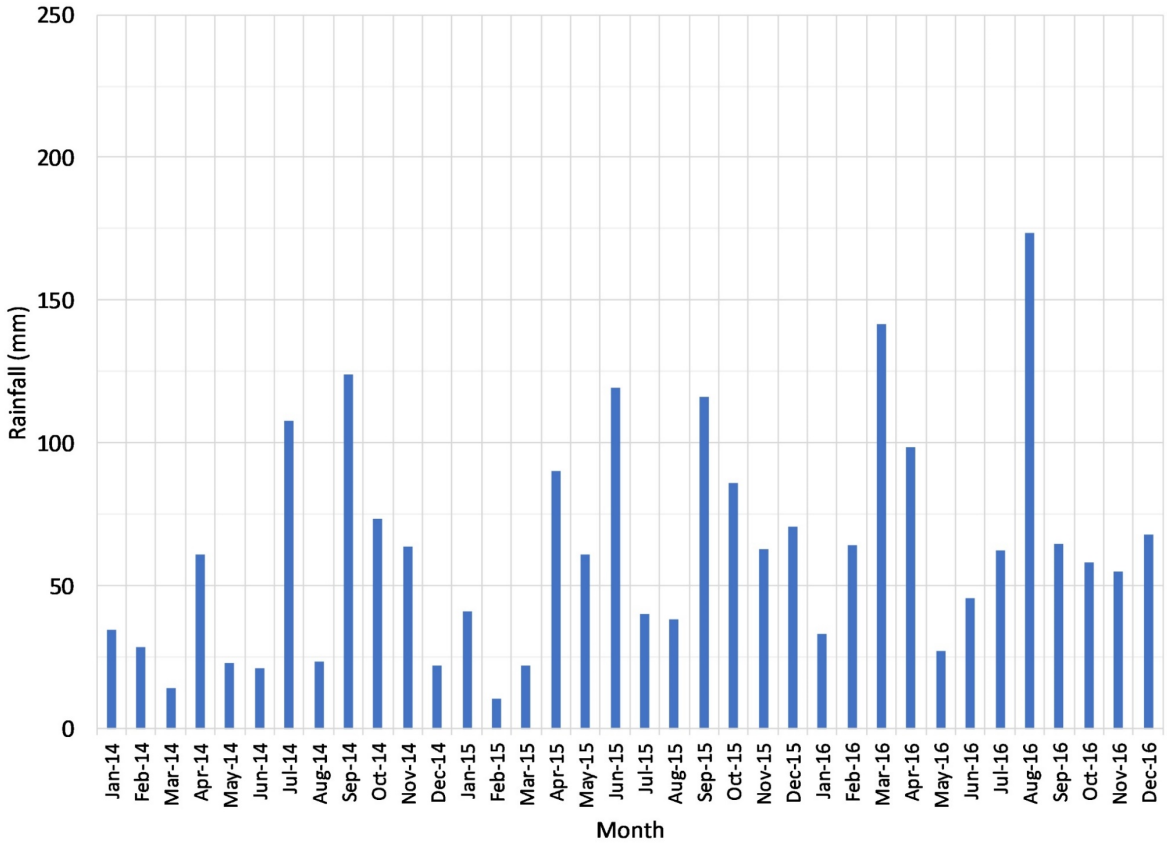


Figure D.12: Monthly rainfall at the Paris GRCA station (GRCA, 2017a).

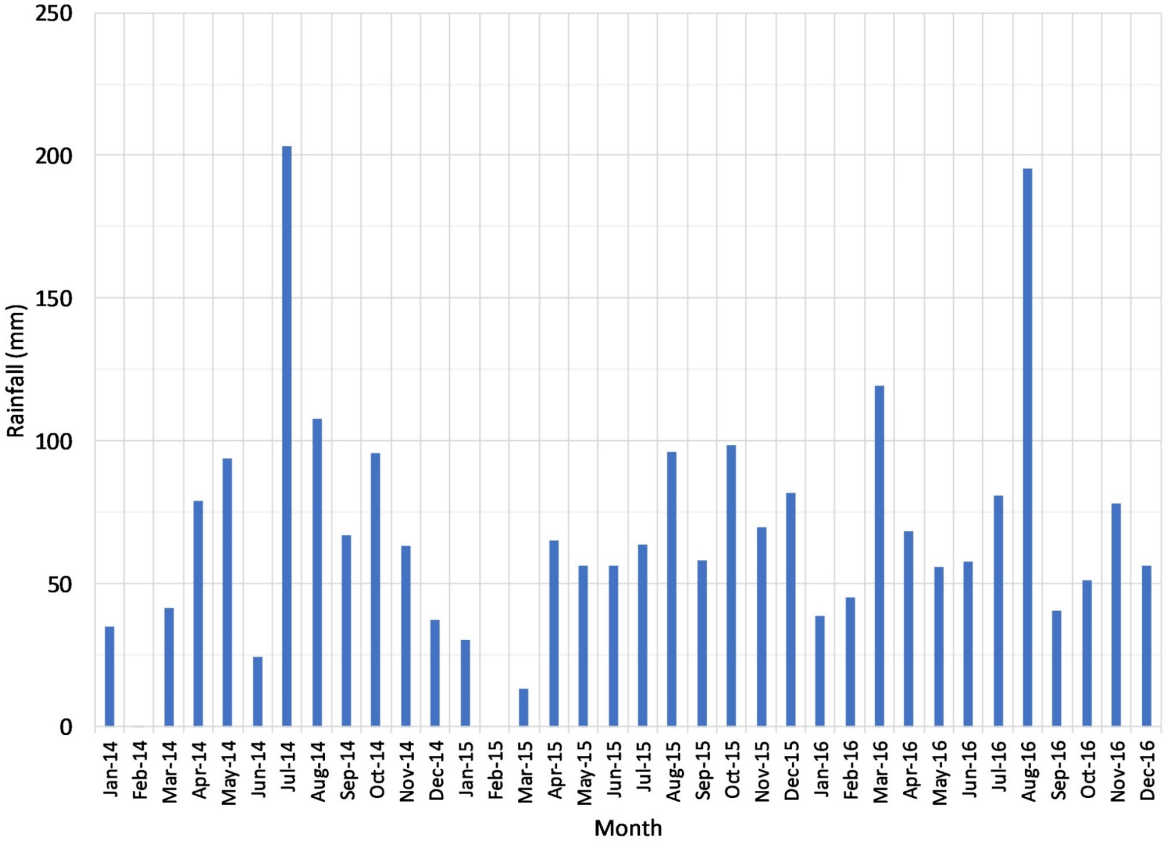


Figure D.13: Monthly rainfall at the Wellesley GRCA station (GRCA, 2017a).

### D.2.3 National Rainfall

Figure D.14 shows monthly rainfall totals at the Roseville rain gauge for 2014 to 2016. The long-term Roseville precipitation dataset (1973 to 2018) was composed of two different parts. Data from 1973 to 2005 were obtained from OMNR (2007), where missing data were filled in using data from the nearby Preston Environment Canada station (AquaResource, 2008; 6.9 km from the Roseville station). Data from 2006 to 2018 were obtained from Government of Canada (2019) and no fill-in was conducted over this time period. Testing was conducted to determine whether the results of Chapter 4 would change if the online Environment Canada data (Government of Canada, 2019) for 1973 to 2018 were used with no fill-in. The variability of recharge and the three groundwater management metrics was essentially the same as when the dataset with fill-in from 1973 to 2005 was used, though mean precipitation and mean recharge were each around 20 mm lower with no fill-in.

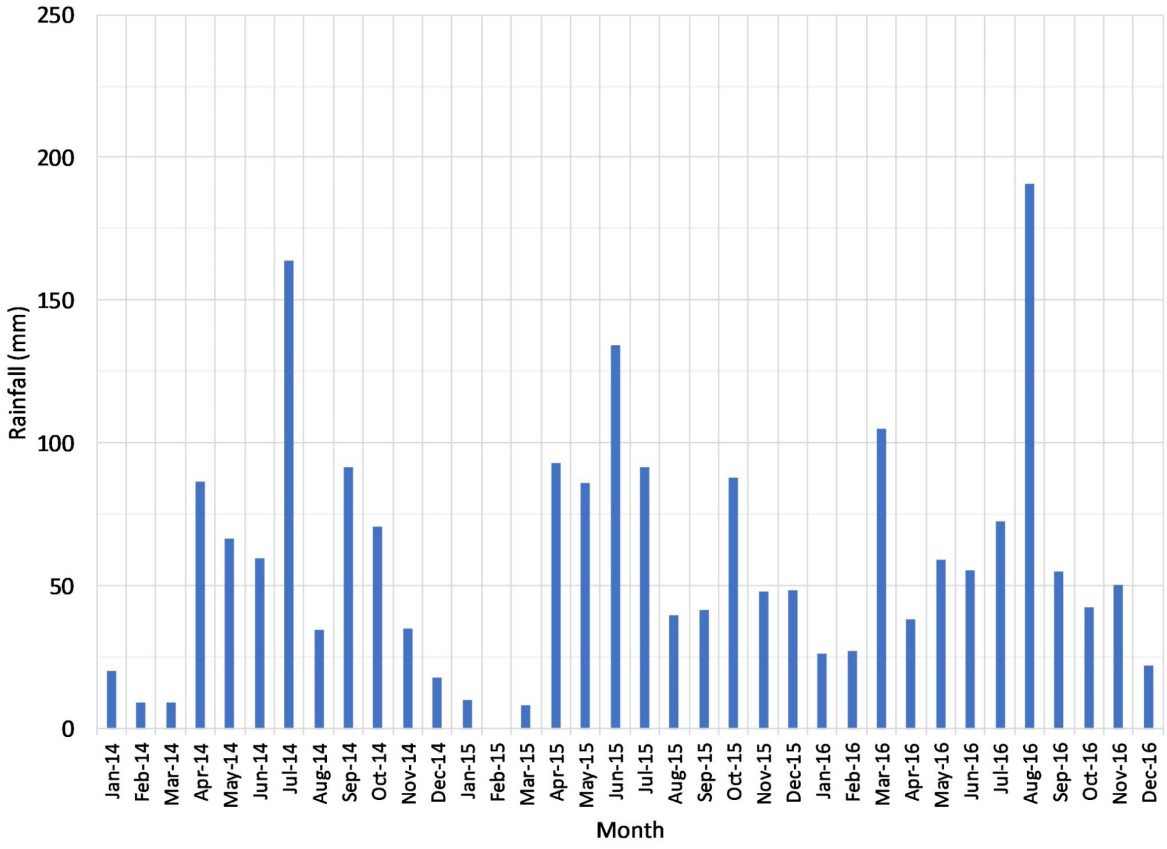


Figure D.14: Monthly rainfall at the Roseville Environment Canada weather station (Government of Canada, 2019).

### D.2.4 Comparison of All Stations

Figure D.15 shows annual rainfall totals at all stations.

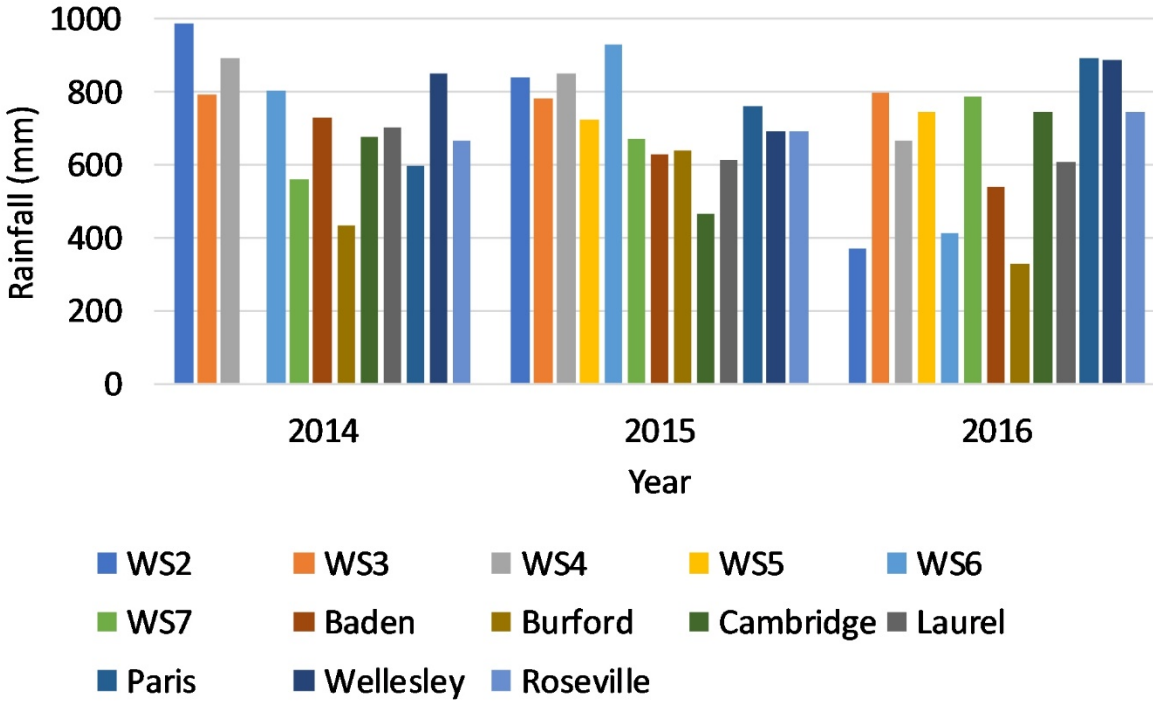


Figure D.15: Annual rainfall at all stations of the local (Wiebe et al., 2019), regional (GRCA, 2017a), and national (Government of Canada, 2019) networks. The WS5 total is omitted from 2014 because data were only collected from 20 June to 31 Dec at that station.

## D.3 Snowfall

Sonic snow sensors (Campbell Scientific SR50A) were installed to monitor the 2014 to 2015 winter season. The available local snowfall data (Wiebe et al., 2019) are shown in Figure D.16 and Figure D.17 along with snow depth measurements at the Roseville station (Government of Canada, 2019). Sonic snow depth estimates were corrected for air temperature using the Vaisala HMP155 or Campbell Scientific HMP45C temperature/relative humidity sensor at each local weather station. Maintenance issues (regarding desiccant pack replacement) led to unreasonable results during the winter of 2015 to 2016. The sensors were not re-deployed after this second winter.

Manual spot checks of snowpack thickness at the Mannheim field site corresponded very well to the Roseville (Government of Canada, 2019) records (within 2 cm) on several occasions. Similarly, the average difference between the reported snow depth at Roseville (Government of Canada, 2019) and the arithmetic average of all local sonic snow depths (Wiebe et al., 2019) was 2.0 cm (Figure D.17). Monthly snowfall observations at the Roseville weather station (Government of Canada, 2019) over the time period of 2014 to 2016 are shown in Figure D.18.

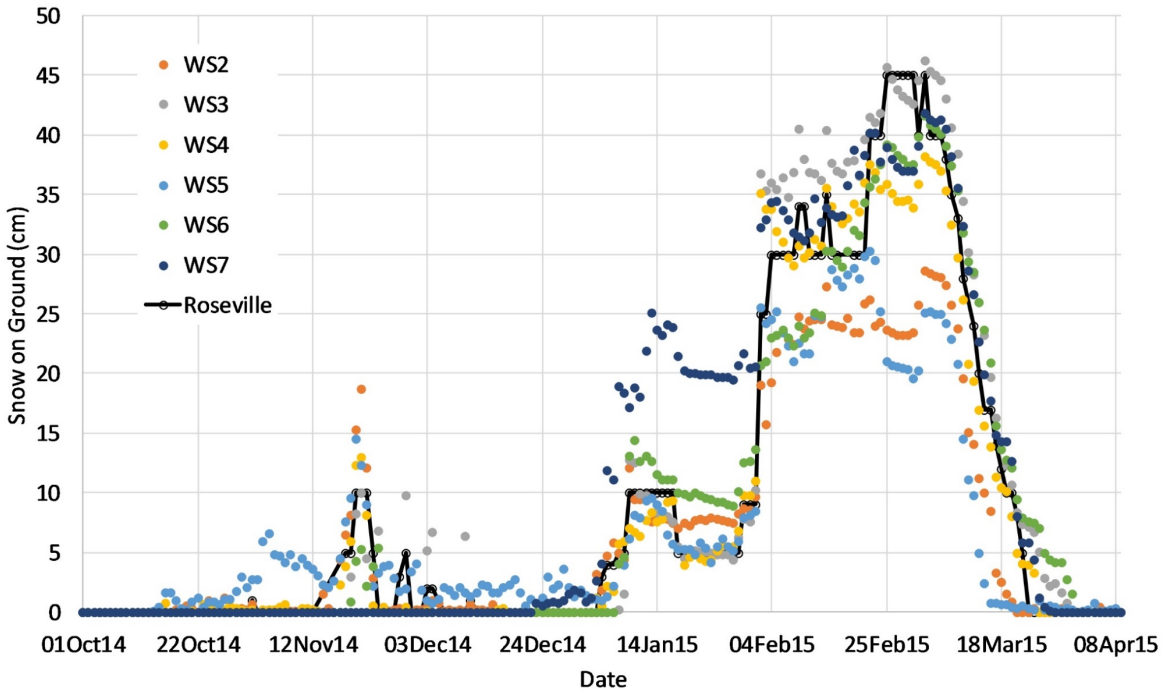


Figure D.16: Sonic snow depth readings over time at the local SOWC stations (Wiebe et al., 2019), compared with snow depth measurements reported at the Roseville Environment Canada weather station (Government of Canada, 2019).

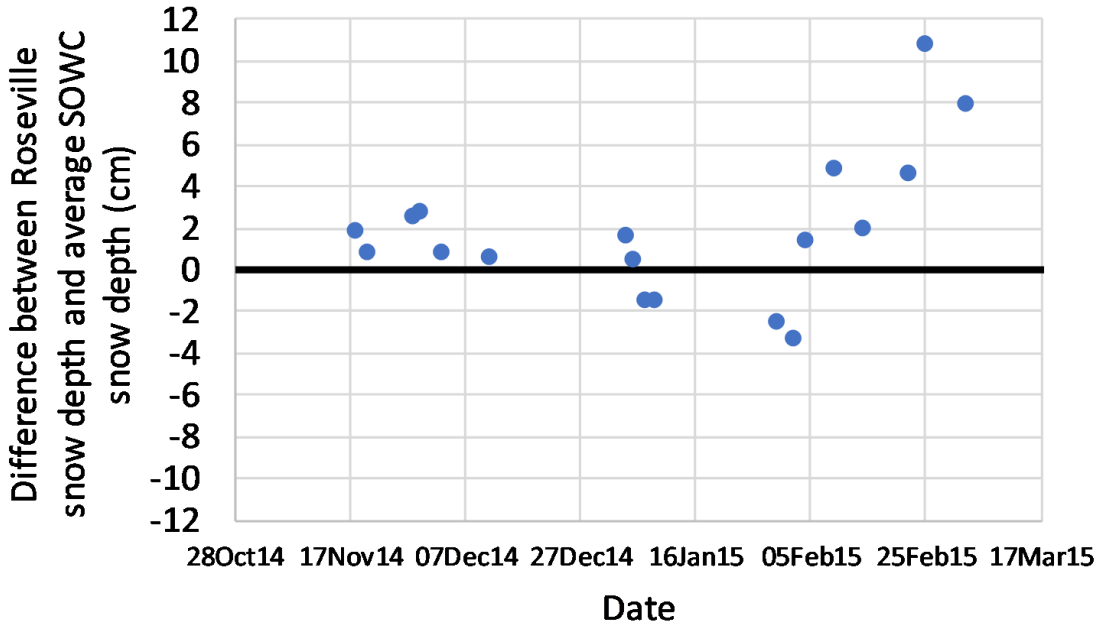


Figure D.17: Differences between the snow depth measurements reported at the Roseville Environment Canada weather station (Government of Canada, 2019) and the arithmetic average of the sonic snow depth readings at the local SOWC stations (Wiebe et al., 2019). Points are shown only for those days when snow depth increased at the Roseville station, indicating a snowfall event. Other days were excluded from this analysis because of the possibility of redistribution of snow by wind, or differences in snowpack melting at the different sites. The average of all differences shown was 2.0 cm.

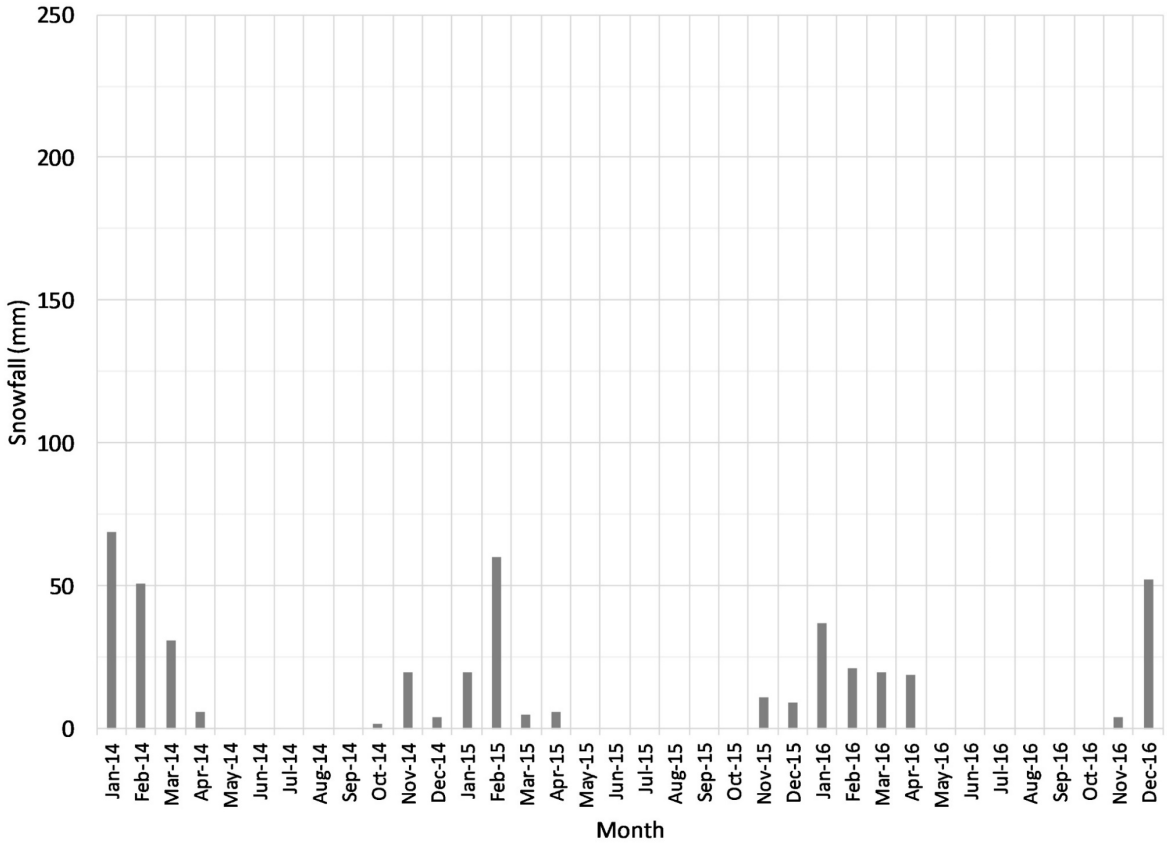


Figure D.18: Monthly snowfall at the Roseville Environment Canada weather station (Government of Canada, 2019).

## D.4 Total Precipitation

Rainfall and snowfall occur on the same day frequently in the precipitation records at the Roseville station (Government of Canada, 2019), and this fact was preserved during the total precipitation calculations. Daily total precipitation for each local SOWC station was calculated by adding the local rainfall time series (Wiebe et al., 2019) to the Roseville snowfall time series (Government of Canada, 2019; OMNR, 2007) on a day by day basis. Similarly, daily total precipitation for the regional or national stations was calculated by adding their respective rainfall time series (GRCA, 2017a; Government of Canada, 2019) to the Roseville snowfall time series (Government of Canada, 2019). This procedure assumes uniform snowfall across the watershed and no melting of snow into the tipping bucket rain gauges. Local rainfall data were checked to minimize the possibility of counting large snowmelt-derived amounts as rainfall. Amounts > 10 mm during times of potential snowmelt in the local network data were verified to be associated with other rainy time steps at the same station

and at other local stations during the same day. This was interpreted to indicate that rainfall was occurring around those time periods rather than isolated snowmelt occurring into the gauges, but the analysis is not conclusive because of the possibility for snow to melt on top of the gauges on a day with rainfall. Possible double counting of melting snow on top of the rain gauges was assumed to be a minimal source of error because: 1) snowfall constitutes only 15% of total precipitation in the area on average (Government of Canada, 2019; OMNR, 2007), 2) the number of snowmelt events during each year is limited (e.g., there were perhaps eight major snowmelt events during the 2014 to 2015 winter based on the Roseville data in Figure D.16), and 3) it is not likely that snow accumulation would be present on top of the gauges during all snowmelt events (due to the possibility for sublimation or wind to remove snow from the tops of the gauges).

# Appendix E

# MIKE SHE model settings

Table E.1 and Table E.2 list settings for the MIKE SHE model, including its surface water model component (MIKE HYDRO).

Table E.1. MIKE SHE Settings

| Heading | Category | Parameter | Option/Value |
|---|---|---|---|
| Simulation specification | Water movement | Overland flow (OL) | Finite difference |
| | | Rivers and lakes (OC) | Yes |
| | | Unsaturated flow (UZ) | Richards equation |
| | | Evapotranspiration (ET) | Yes |
| | | Saturated flow (SZ) | Finite difference |
| Time step control | General settings | Initial basic time step | 0.25 hrs |
| | | Maximum allowed OL time step | 0.5 hrs |
| | | Maximum allowed UZ time step | 2 hrs |
| | | Maximum allowed SZ time step | 24 hrs |
| | | Increment of reduced time step length | 0.05 |
| | Parameters for precipitation-dependent time step control | Maximum precipitation depth per time step | 10 mm |
| | | Maximum infiltration amount per time step | 2.5 mm |
| | | Input precipitation rate requiring its own time step | 5 mm/hr |
| OL Computational Control Parameters | Solver Type and Solver-specific parameters | Solver type | Explicit |
| | | Maximum Courant number (for adaptive time step) | 0.8 |
| | Common stability parameters | Threshold water depth for overland flow | 0.0001 m |
| | | Threshold gradient for applying low-gradient flow reduction | 0.0001 |
| | Overland-river exchange calculation | Manning Equation | use OL flow Manning numbers (OL to River only) |
| UZ computational control parameters | UZ-SZ coupling control | Maximum profile water balance error | 0.001 m |
| | Richards equation parameters | Iteration control – maximum number of iterations | 150 |
| | | Iteration stop criteria (fraction of Psi) | 0.002 |
| | Timestep reduction control (UZ restart) | Maximum water balance error in one node (fraction) | 0.03 |

Table E.1. MIKE SHE Settings (Continued)

| Heading | Category | Parameter | Option/Value |
|---|---|---|---|
| SZ computational control parameters | Solver | Solver type | Preconditioned conjugate gradient, transient |
| | Iteration control | Maximum number of iterations | 200 |
| | | Maximum head change per iteration | 0.01 m |
| | | Maximum residual error | 0.001 m/d |
| | Sink de-activation in drying cells | Saturated thickness threshold | 0.05 m |
| | Advanced settings | Gradual drain-activation | Yes |
| | | Horizontal conductance averaging between iterations | Yes |
| | | Under-relaxation? | No |
| | Maximum exchange from river during one time step | Max. fraction of H-point volume | 0.9 |
| Model domain and grid | General | Number of cells in x-direction | 250 |
| | | Number of cells in y-direction | 250 |
| | | Cell size (length = width) | 50 m |
| | | Rotation (degrees counter-clockwise) | 0° |
| | | $x_0$ | 529600 |
| | | $y_0$ | 4799700 |
| | | Coordinate system | UTM-17 (N) |
| Climate | Snow melt | Include snow melt? | Yes |
| | | Factor reducing sublimation rate from dry snow | 0 |
| | Threshold melting temperature | Spatial distribution | Uniform |
| | | Value | 0 °C |
| | Snow melt degree-day melting or freezing coefficient | Spatial distribution | Uniform |
| | | Temporal distribution | Constant |
| | | Value | 2 mm/°C/d |
| | Minimum snow storage for full area coverage | Spatial distribution | Uniform |
| | | Value | 0 mm |
| | Maximum wet snow fraction in snow storage | Spatial distribution | Uniform |
| | | Value | 0 |
| | Initial total snow storage | Spatial distribution | Uniform |
| | | Value | 0 mm |
| | Initial wet snow fraction | Spatial distribution | Uniform |
| | | Value | 0 |

Table E.1. MIKE SHE Settings (Continued)

| Heading | Category | Parameter | Option/Value |
|---|---|---|---|
| Land use | Irrigation | Include irrigation? | No |
| | Vegetation | Spatial distribution | Station based |
| | Leaf Area Index (LAI) (Maximum values from: Canadell et al., 1996; Scurlock et al., 2001) | Urban | 0 (Oct-Apr), 3 (May-Sep) |
| | | Forest | 0 (Oct-Apr), Linear increase (May), 5.06 (Jun-15Sep), Linear decrease (16Sep-30Sep) |
| | | Aggregate extraction | 0 |
| | | Wetlands | 0 (Oct-Apr), Linear increase (May), 6.34 (Jun-15Sep), Linear decrease (16Sep-30Sep) |
| | | Open water | 0 |
| | | Row crops and green space | 0 (Oct-Apr), Linear increase (May), 3.62 (Jun-15Sep), Linear decrease (16Sep-30Sep) |
| | | Roads | 0 |
| Overland flow | General | Separated overland flow areas? | No |
| | | Surface-subsurface exchange – reduced vertical exchange in specified areas? | No |
| | | Include ponded drainage? | No |
| | Manning number (M) | Spatial distribution | Uniform |
| | | Value (Note: $M_{Manning} = 1/n_{Manning}$) | 3.33 $m^{1/3}s^{-1}$ |
| | Detention storage | Urban | 3.0 mm |
| | | Forest | 7.6 mm |
| | | Aggregate extraction | 4.0 mm |
| | | Wetlands | 0.0 mm |
| | | Open water | 0.0 mm |
| | | Row crops and green space | 5.0 mm |
| | | Roads | 1.5 mm |
| | Initial water depth | Spatial distribution | Uniform |
| | | Value | 0 m |

Table E.1. MIKE SHE Settings (Continued)

| Heading | Category | Parameter | Option/Value |
|---|---|---|---|
| Unsaturated flow | Initial conditions | Initial conditions | Equilibrium pressure profile (based on field capacity) |
| | Macropores | Macropore flow | None |
| | Soil profile definitions (All soil types except regions noted immediately below) | Uppermost cells' height | 0.1 m |
| | | Number of cells in uppermost category | 100 |
| | | Intermediate cells' height | 0.2 |
| | | Number of cells in intermediate category | 100 |
| | | Deepest cells' height | 0.5 |
| | | Number of cells in deepest category | 50 |
| | Soil profile definitions (Ice-Contact Gravel and Maryhill Till, eastern part of watershed only) | Uppermost cells' height | 0.1 m |
| | | Number of cells in uppermost category | 100 |
| | | Intermediate cells' height | 0.2 |
| | | Number of cells in intermediate category | 100 |
| | | Deepest cells' height | 0.5 |
| | | Number of cells in deepest category | 100 |
| Saturated zone | General | Include pumping wells? | Yes |
| | | Include subsurface drainage? | No |
| | | Hydrogeologic parameter distribution | Assign parameters via geological layers |
| | | Specific yield in SZ computational layer 1 | Derive from UZ soil parameters when UZ included |
| | | Geological lenses? | No |
| | Computational layers | Type of numerical vertical discretization | Explicit definition of lower levels |
| | Bottom elevation correction | Minimum layer thickness | 0.1 m |
| | | Adjust top SZ layer thickness to the initial water table? | No |
| | Pumping rates (Matrix and SSPA, 2014b) | W7 and W8 (combined; same cell; screen = 329.10 to 345.30 m above sea level (asl)) | 9713 $m^3/d$ |
| | | K23 (screen = 311.64 to 325.37 masl) | 2256 $m^3/d$ |
| | | K24 (screen = 307.0 to 313.20 masl) | 2562 $m^3/d$ |
| | | K26 (screen = 303.47 m 326.4 masl) | 6841 $m^3/d$ |

Table E.1. MIKE SHE Settings (Continued)

| Heading | Category | Parameter | Option/Value |
|---|---|---|---|
| Storing of results | General | Internal MIKE SHE units | Yes |
| | Water movement and output | Store water balance | Yes |
| | | Store hot start data | Yes |
| | | Hot start storing interval | 8736 hrs |
| | Storing interval for grid series output | Overland | 168 hrs |
| | | Precipitation, SM, ET, UZ | 168 hrs |
| | | SZ-heads | 168 hrs |
| | | SZ-fluxes | 168 hrs |
| | Detailed river time series output | Minimum output time step | 0.5 hrs |
| | Extra Parameters | Strict retention curve adjustment? | true |

Table E.2. MIKE HYDRO Settings

| Heading | Category | Parameter | Option/Value |
|---|---|---|---|
| Simulation specifications | General | Model type | River |
| | | River modules (data, simulation) | Hydrodynamic |
| | Time step length | Fixed time step | 30 min |
| Computational control parameters | Grid spacing | Maximum dx (global value) | 500 m |
| | Wave approximation | Wave approximation (global value) | Dynamic, high order friction |
| Computation parameters | Shallow water equation parameters | Time centering coefficient for gravity term | 0.5 |
| | | Velocity distribution coefficient | 1 |
| | | Weighting factor, momentum equation | 1 |
| | | Threshold water level slope for diffusive wave approximation | 0.0001 |
| | | Enhanced formulation of convective suppression? | No |
| | | Alternative utilization of the convective suppression? | No |
| Computation parameters (Continued) | Structure parameters | Threshold water level difference below which flow is linearized | 0.01 m |
| | | Minimum head loss coefficient | 0.1 |
| | | Maximum number of iterations at structures | 10 |
| | | Use pre-processed h-Q-h files for bridges generated from previous simulations? | No |
| | Miscellaneous | Threshold depth for slot creation | 0.1 m |
| | | Number of iterations at each time step | 1 |
| | | Maximum exceedance factor for depth above bank level | 100 |

Table E.2. MIKE HYDRO Settings (Continued)

| Heading | Category | Parameter | Option/Value |
|---|---|---|---|
| Map configurations | Coord. system | Coordinate system | UTM-17 (N) |
| | Digital Elevation Model (DEM) | Use DEM for cross-section creation | Yes |
| | | Use DEM for river tracing and catchment delineation | Yes |
| | | Background layer | (choose .DFS2 file from PreProcessed MIKE SHE model) |
| | Cross-sections | Cross-sections – interpolation | Bilinear interpolation |
| | | Cross-sections – spacing between points | Half cell size |
| | | Maximum number of points | 100 |
| | River tracing and catchment delineation | Spatial extent | whole DEM |
| | | Resampling factor | 1 |
| | | Assume internal undefined areas as local depressions | Yes |
| Hydrodynamic parameters | Bed resistance | Resistance formula | Manning (n) |
| | | Resistance number | 0.0333333 |
| Boundary conditions | Standard boundaries | HD boundary | Include |
| | | Input type | Constant |
| | | Scale | 1 |
| | | HD value | 318 m |
| Groundwater leakage | General | Include groundwater leakage? | No |
| MIKE SHE couplings | General | Include MIKE SHE coupling? | Yes |
| | River-aquifer exchange | conductance | Aquifer + river bed |
| | | Leakage coefficient | 1E-5 |
| | | Linear reservoir exchange | Gaining river |
| | Overland-river exchange | Weir coefficient | 1.838 |
| | | Weir exponential coefficient | 1.5 |
| | | Minimum upstream height above bank for full weir width | 0.1 m |
| | | Allow overbank spilling from river to overland domain? | No |
| | Inundation | Flood area option | No flooding |
| HD initial conditions | General | type | User defined |
| | | Level type | Water level; 0.1 m |
| | | Discharge type | Natural flow |

# Appendix F
# Rainfall interpolation

One scenario was considered in addition to the national, regional, and local rainfall scenarios presented. This scenario was conceptualized as a reference scenario in which rainfall was interpolated from the set of all thirteen available rain gauges (Table 2.1). Interpolations were made at the daily time scale using the inverse distance squared method.

Figure F.1 suggests that the reference scenario results were very similar to those of the local scenario for several larger rainfall events and contain only minor differences. Table F.1 shows the individual stations' readings for these examples. The cumulative streamflow results of the reference scenario were similar to (within about 20 mm of) the cumulative streamflow results of the regional and national scenarios in 2014, and very similar to (within a few mm of) those from the local rainfall scenario in 2015 and 2016 (Figure F.2). Results for the water budget components of the reference scenario were intermediate values between the local and regional scenarios' results, but the values were generally closer to the local scenario. This is likely because of the immediate impacts of the local gauges within the watershed through the interpolated precipitation distribution. The minimal differences between the reference scenario and the local rainfall scenario, and the poorer match between the reference scenario and the observed streamflow results suggest that this reference scenario does not constitute an improvement with respect to the results of the local scenario.

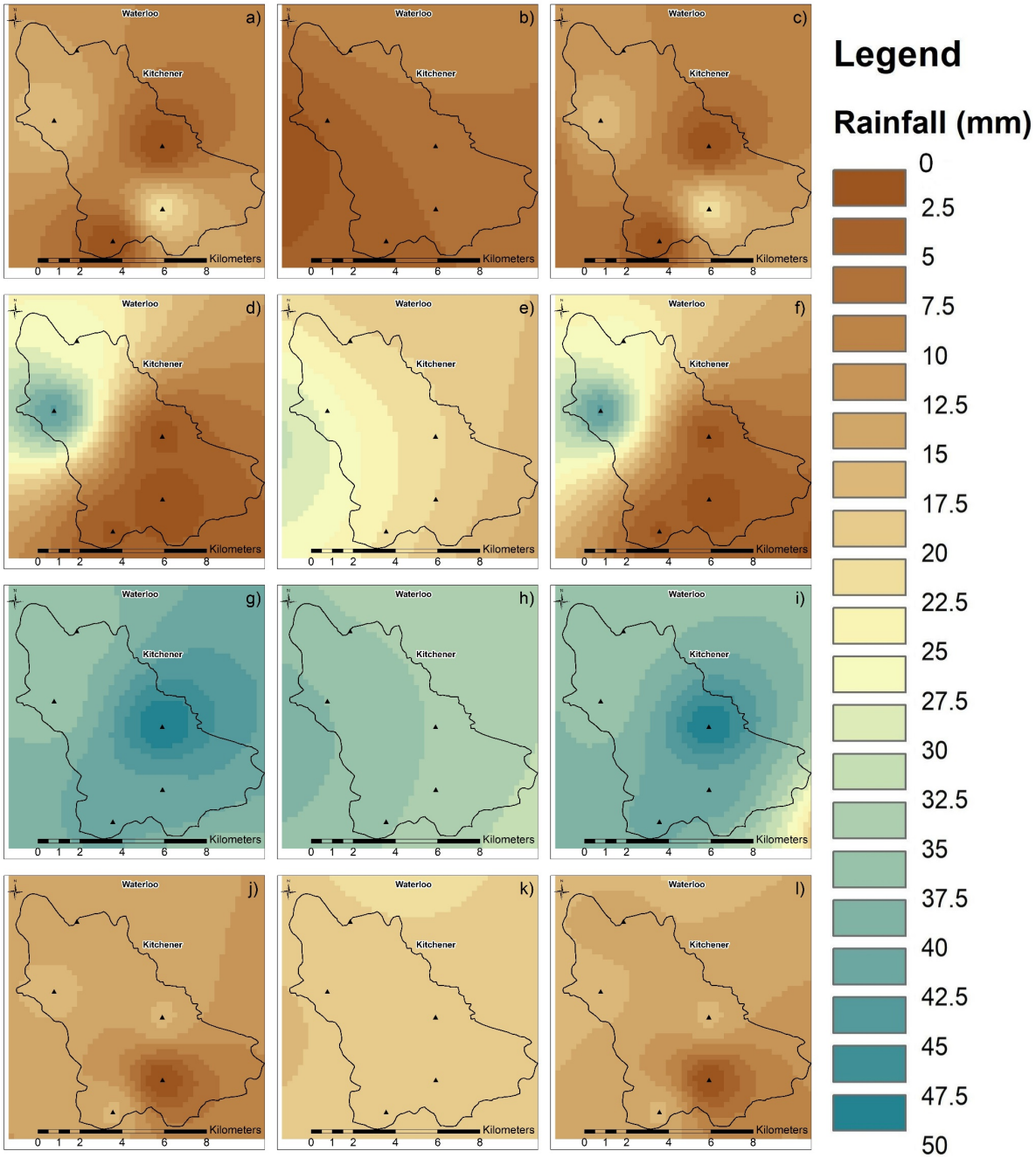


Figure F.1: Examples of rainfall interpolations for 20 May 2014 (a, b, c), 15 Jul 2014 (d, e, f), 24 Nov 2014 (g, h, i), and 20 Apr 2015 (j, k, l).[7] The first column (a, d, g, j) shows results for the local network, the second column (b, e, h, k) shows results for the regional network, and the third column (c, f, i, l) shows results for the reference scenario (all networks).

[7] The interpolation shown in subplot (c) is a corrected version of the subplot in Figure A.1 of Wiebe and Rudolph (2020), Appendix A.

Table F.1. Daily rainfall (mm) on the four days portrayed in Figure F.1 (Government of Canada, 2019; GRCA, 2017a; Wiebe et al., 2019).

| Weather Station | Rainfall | | | |
|---|---|---|---|---|
| | 20-May-14 | 15-Jul-14 | 24-Nov-14 | 20-Apr-15 |
| WS2 | 16.8 | 42.8 | 35.6 | 15.8 |
| WS3 | 21.2 | 0.0 | 42 | 0 |
| WS4 | 0.0 | 1.6 | 50.2 | 15.6 |
| WS5 | N/A | 26.0 | 35.8 | 14 |
| WS6 | 0.0 | 2.2 | 41 | 15.4 |
| WS7 | 15.2 | 0.6 | 25.6 | 11 |
| Wellesley | 22 | 14.6 | 34.2 | 17.2 |
| Baden | 0 | 31.4 | 39.2 | 17.2 |
| Laurel | 10 | 18.6 | 34.4 | 20.8 |
| Cambridge | 6.2 | 0.4 | 26.2 | 14.4 |
| Paris | 0.8 | 0.6 | 25.6 | 22.8 |
| Burford | 0 | 0.6 | 20.4 | 19 |
| Roseville | 15.2 | 0 | 3.7 | 0.6 |

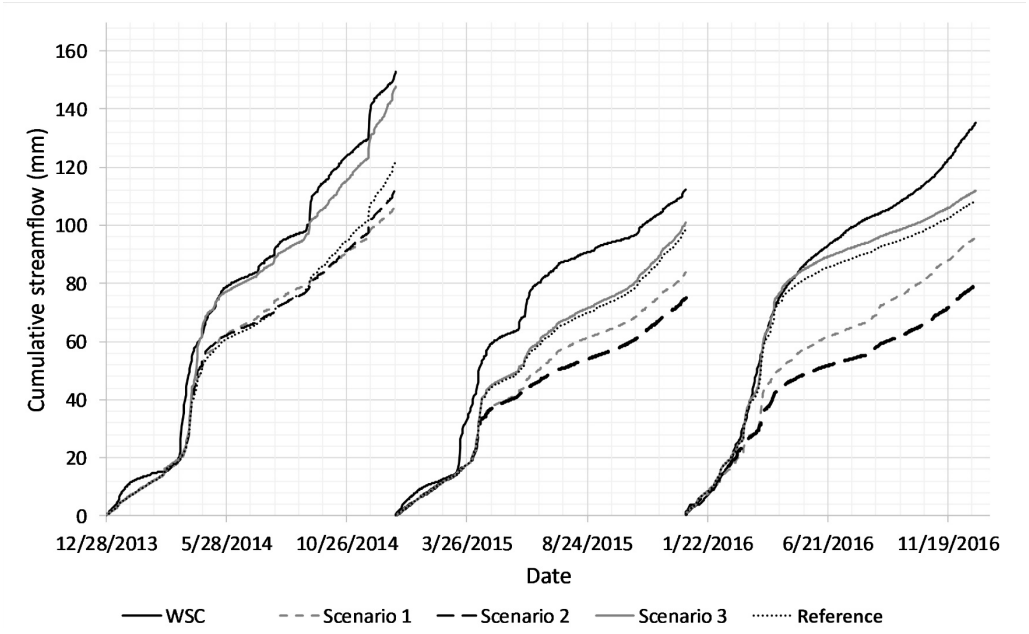


Figure F.2: Cumulative streamflow results from all scenarios including the reference scenario (WSC, 2019).

Figure F.3 shows the simulated and observed rainfall frequencies for depths less than 20 mm. The simulated frequencies tend to be similar or slightly higher than the observed regional and local values. The simulated frequencies follow the same pattern as the local and regional frequencies, unlike what was observed during rainfall analysis by Mileham et al. (2008), where the simulated and observed frequency patterns differed to a greater extent.

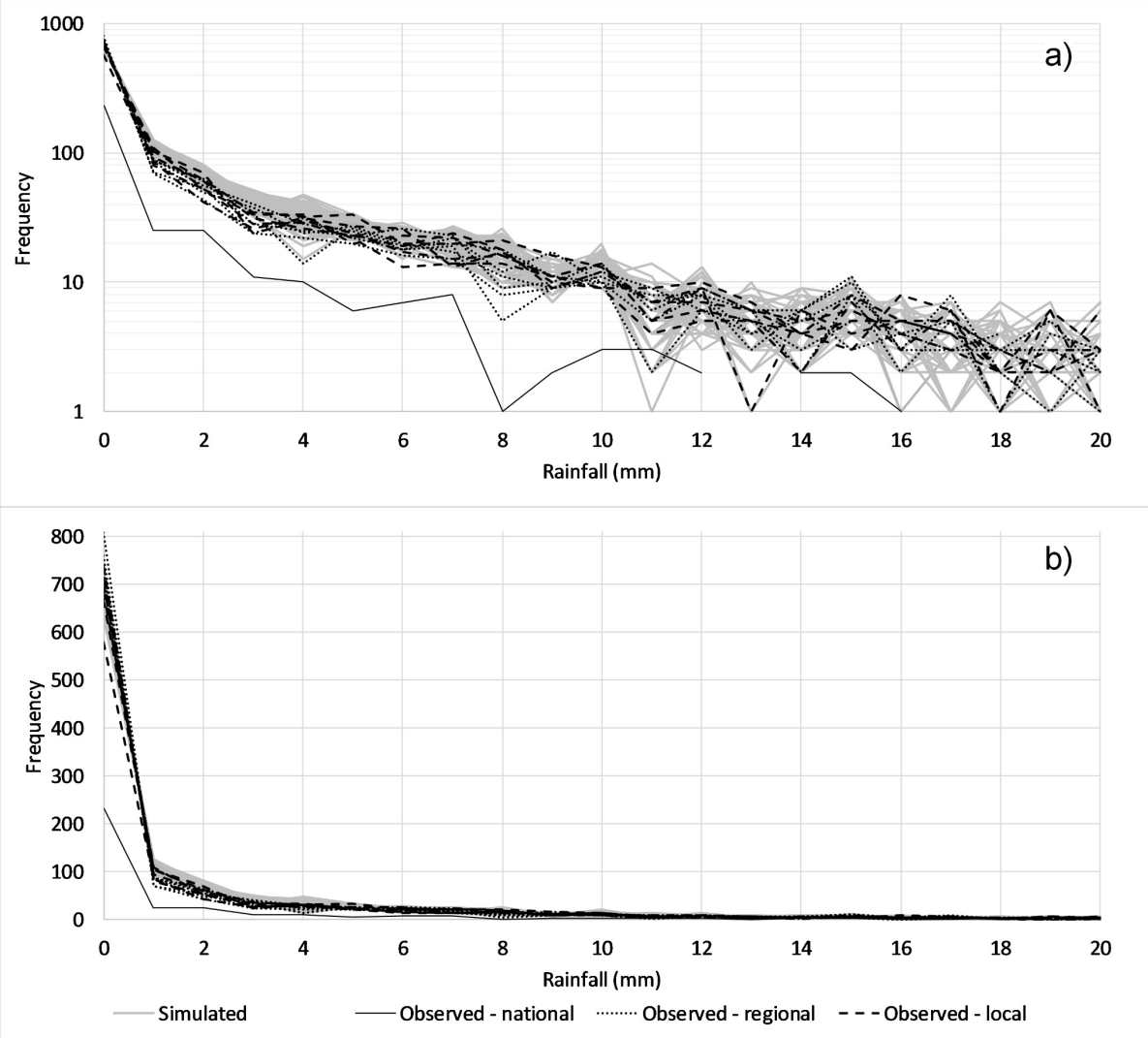


Figure F.3: Frequency distributions of observed and simulated daily rainfall: a) log scale for frequency, b) linear scale for frequency (Government of Canada, 2019; OMNR, 2007; GRCA, 2017a; Wiebe et al., 2019). The simulated rainfall time series were extracted from 36 grid cells for both the regional and local rainfall scenarios.

# Appendix G

# Borehole logs

Figure G.1 shows the locations of sediment cores collected during the present study, and Figures G.2 to G.7 show the logs (created in HydroGeoAnalyst – Waterloo Hydrogeologic, 2018).

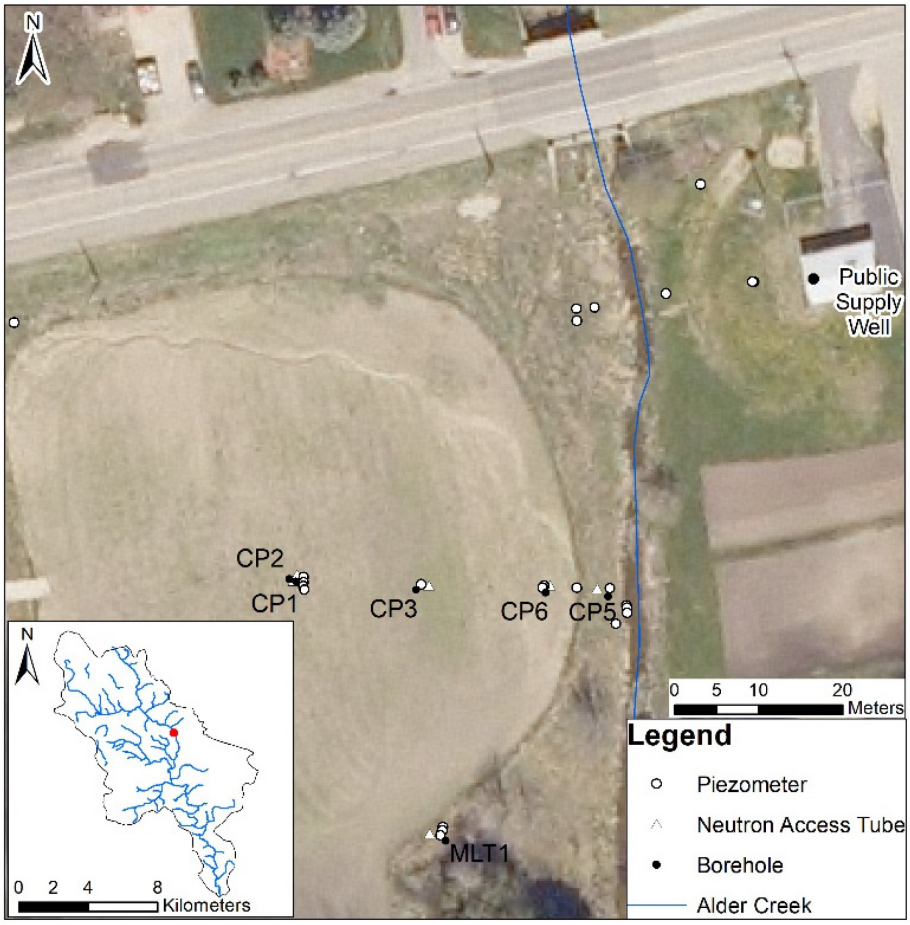


Figure G.1: Locations of sediment cores (CH2MHILL and SSPA, 2003; DMTI, 2011; First Base Solutions, 2006; GRCA, 1998; Hillier, 2014; Menkveld, 2019).

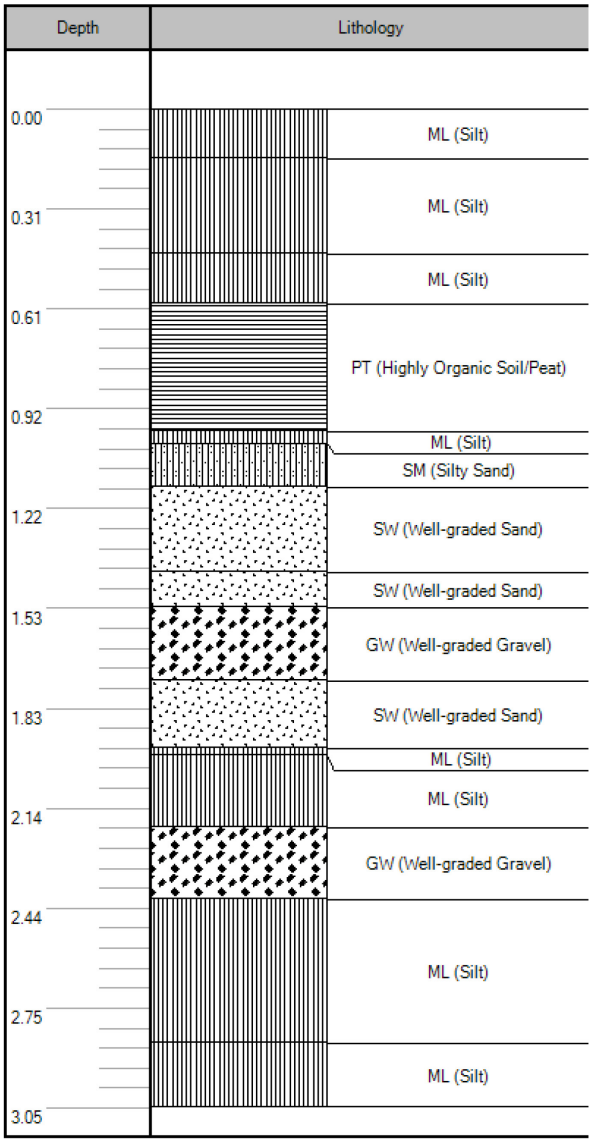


Figure G.2: CP1 borehole log.

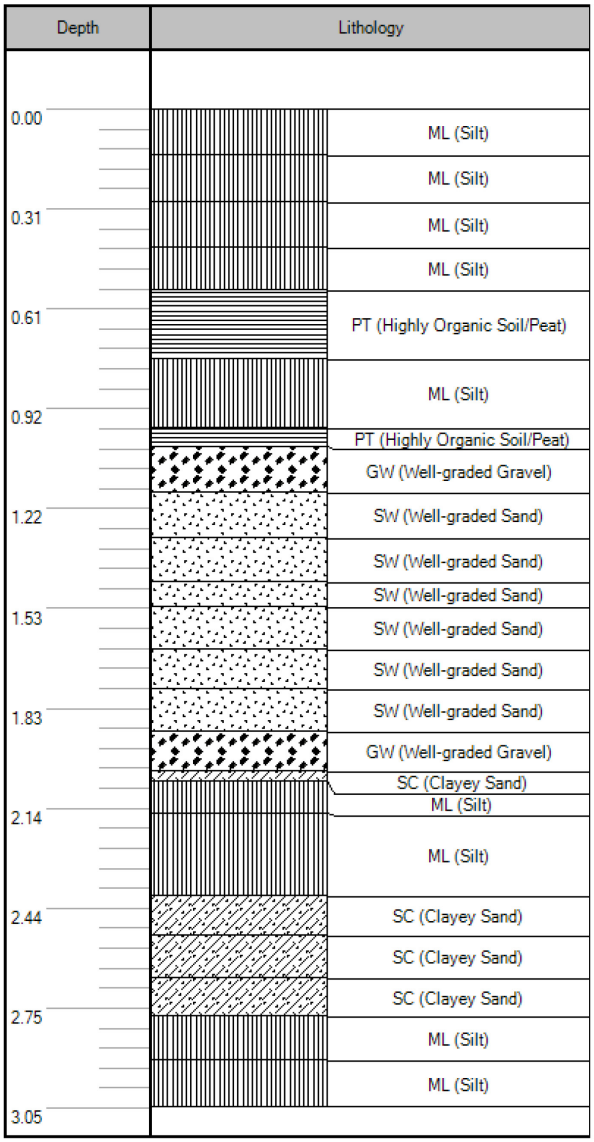


Figure G.3: CP2 borehole log.

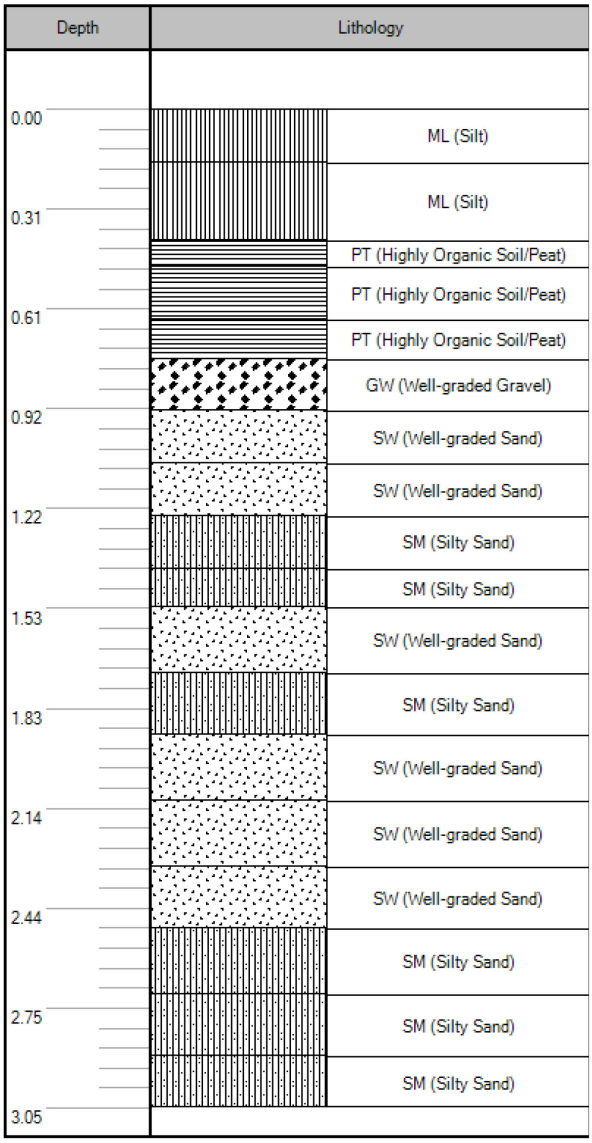


Figure G.4: CP3 borehole log.

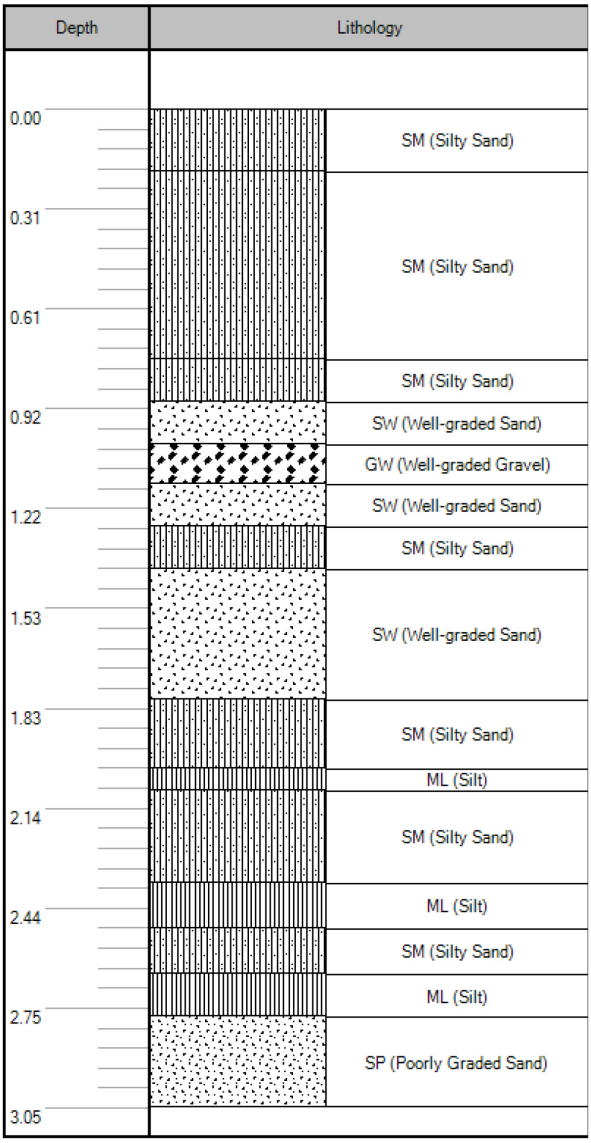


Figure G.5: CP5 borehole log.

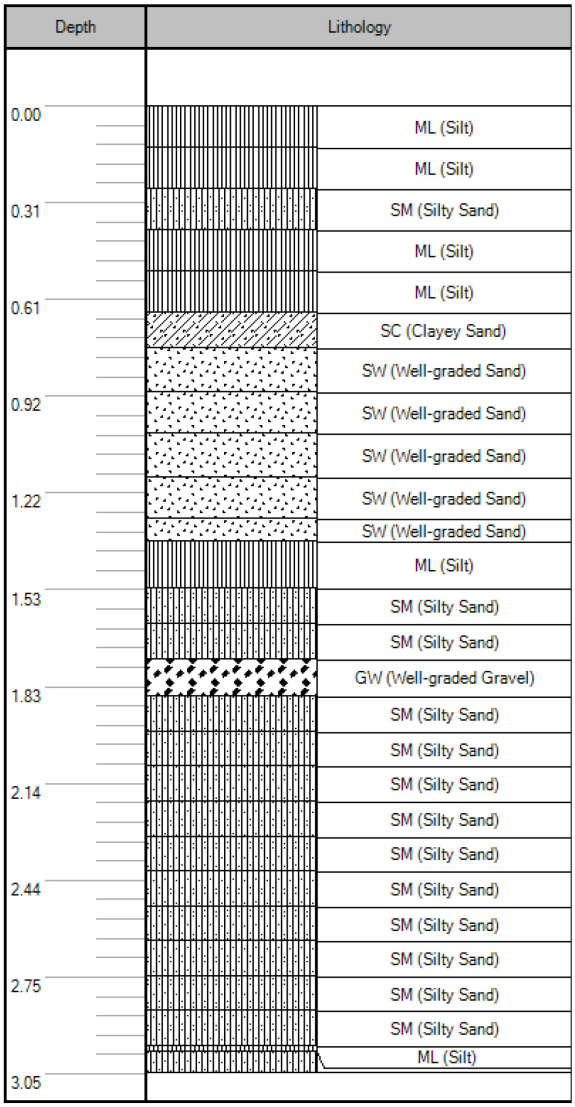


Figure G.6: CP6 borehole log.

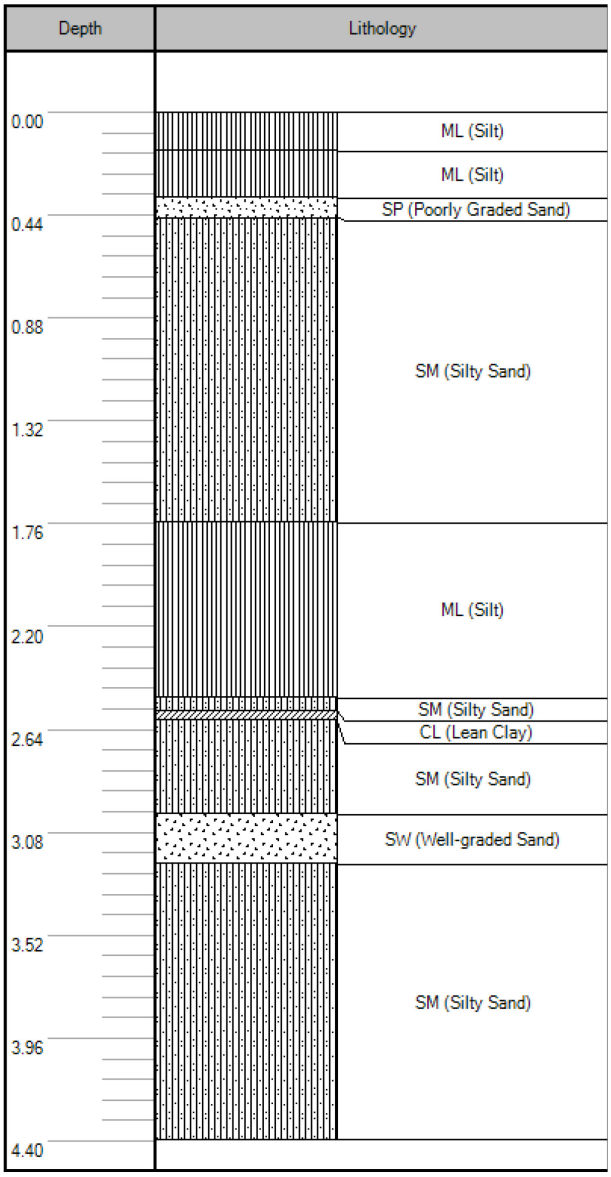


Figure G.7: MLT1 borehole log.

# Appendix H
# Soil moisture

Figure H.1 and Figure H.2 show the locations of the six 2-inch PVC access tubes ("AT1", "AT2", etc.) where neutron probe soil moisture data were collected at the Mannheim site. Calibration results for neutron probe "C" (i.e., University of Waterloo neutron probe "C"; CPN, 2013; employed starting in February 2016) are shown on Figure H.3. Volumetric water content (VWC) estimates derived from the neutron probe are included on Figures H.4 to H.9.

Figure H.10 shows the locations of eight 30 cm-long time domain reflectometry (TDR) sensors. Figure H.11 shows maximum and minimum TDR soil moisture (i.e., VWC) conditions.

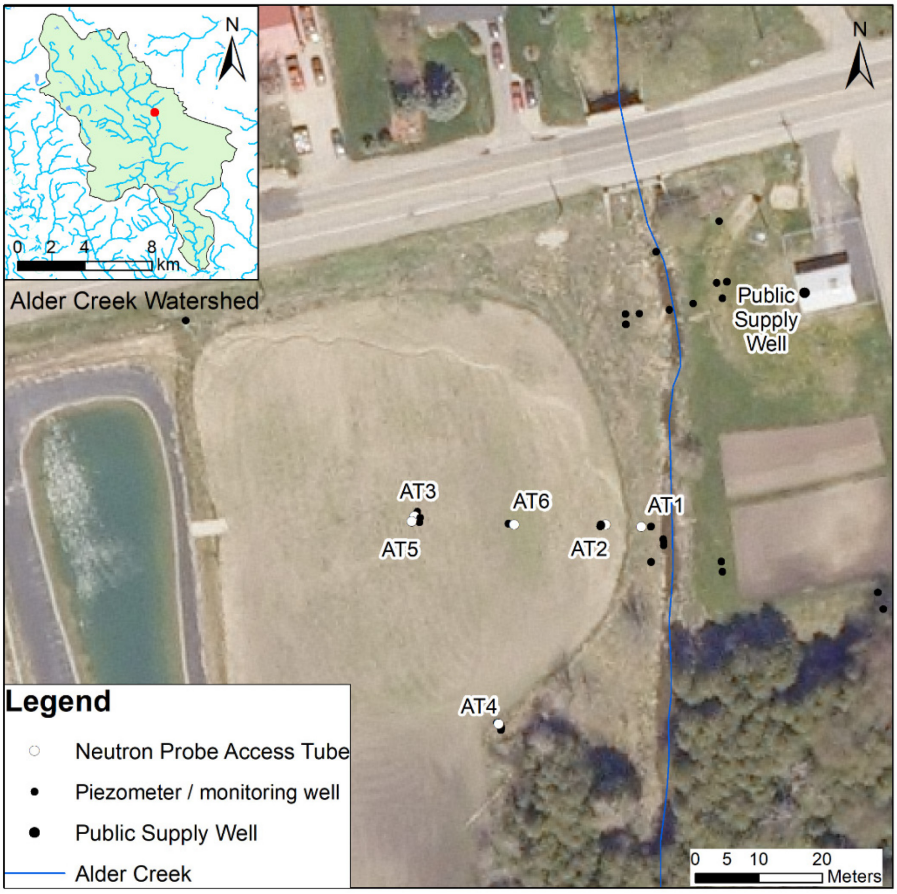


Figure H.1: Locations of 2-inch diameter neutron probe access tubes at the Mannheim site (CH2MHILL and SSPA, 2003; DMTI, 2011; First Base Solutions, 2006; GRCA, 1998; Hillier, 2014; Wiebe et al., 2019).

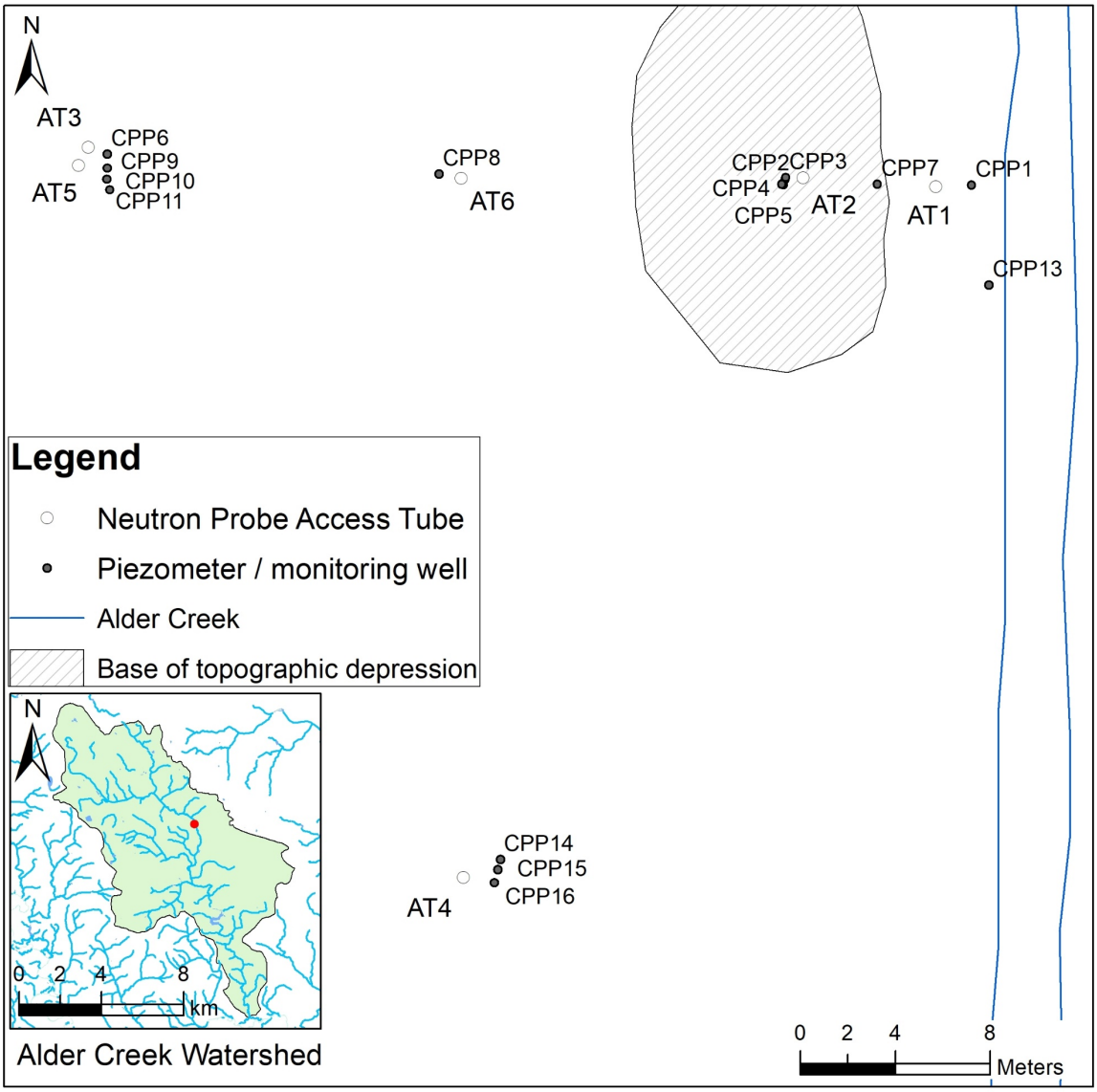


Figure H.2: Locations of neutron probe access tubes and monitoring wells at the Mannheim site (DMTI, 2011; GRCA, 1998; Wiebe et al., 2019).

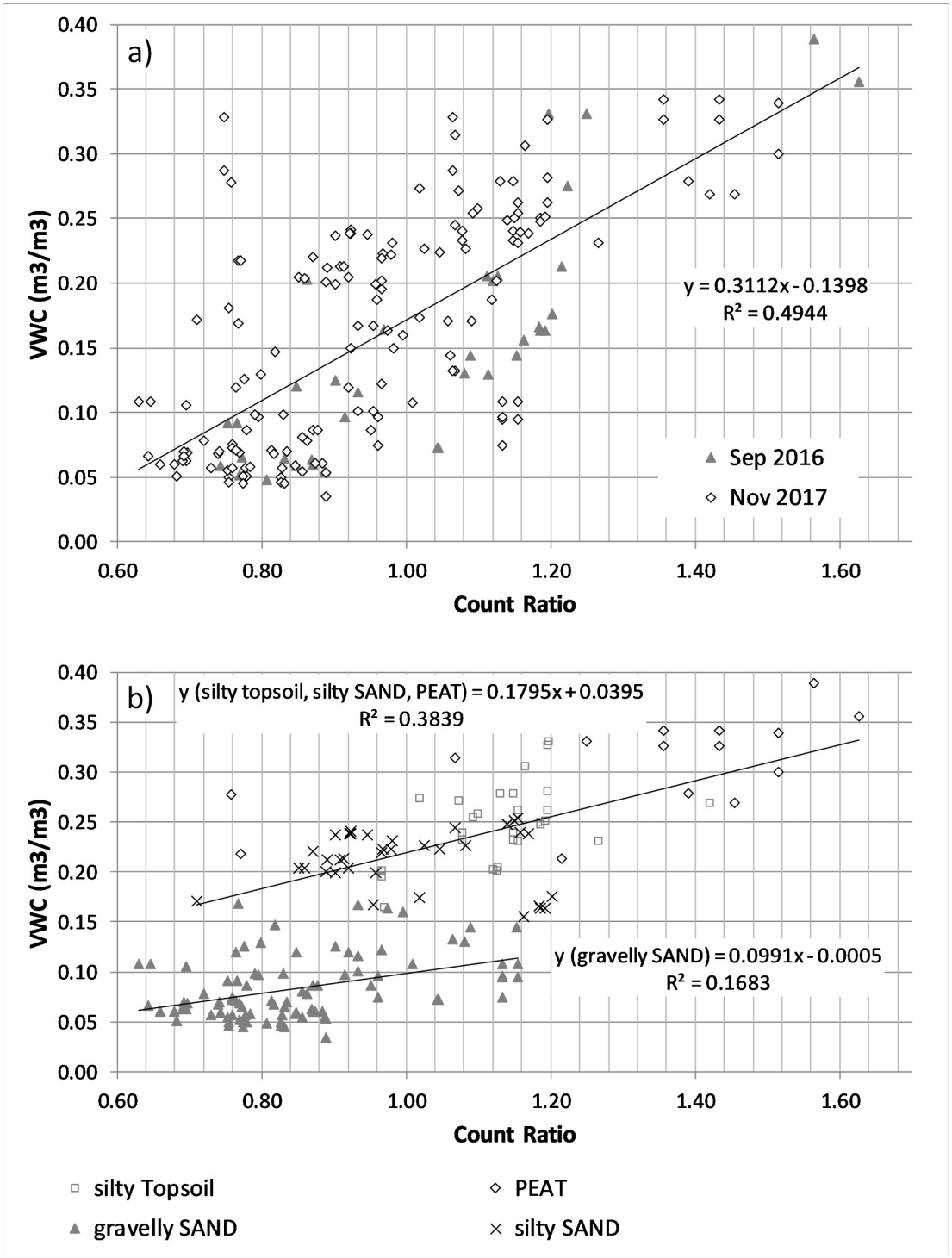


Figure H.3: Calibration relationship for neutron probe "C" based on gravimetric analysis of soil cores for: a) all core intervals, and b) core intervals sorted by soil type. Soil cores were collected within 1 m of all six access tubes for the Nov 2017 dataset, and at AT4 and AT5 for the Sep 2016 dataset. Outliers for the two categories in (b) were likely related to the interface between categories and were removed.

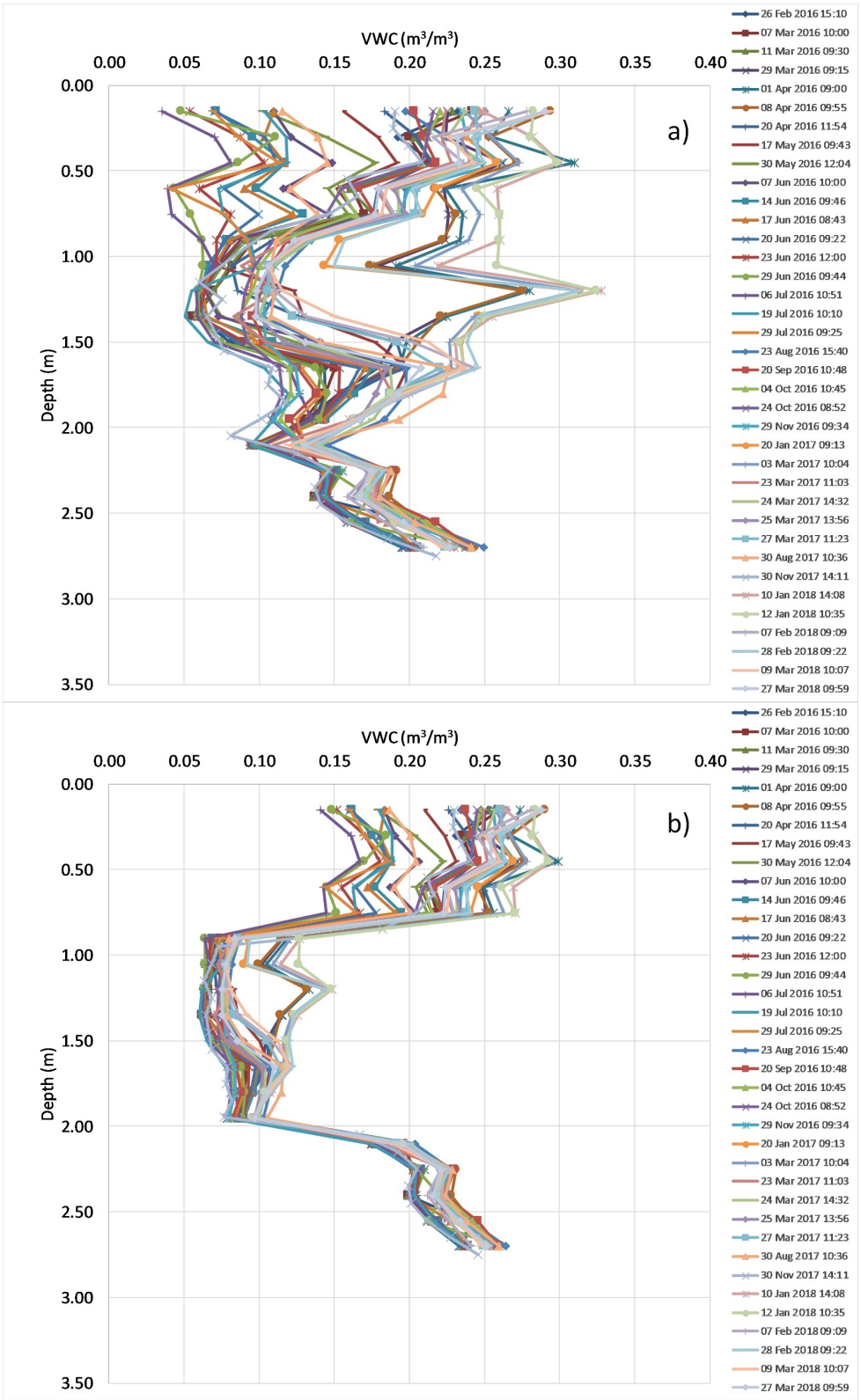


Figure H.4: Calculated VWC at AT1 based on equation for a) all or b) sorted core intervals.

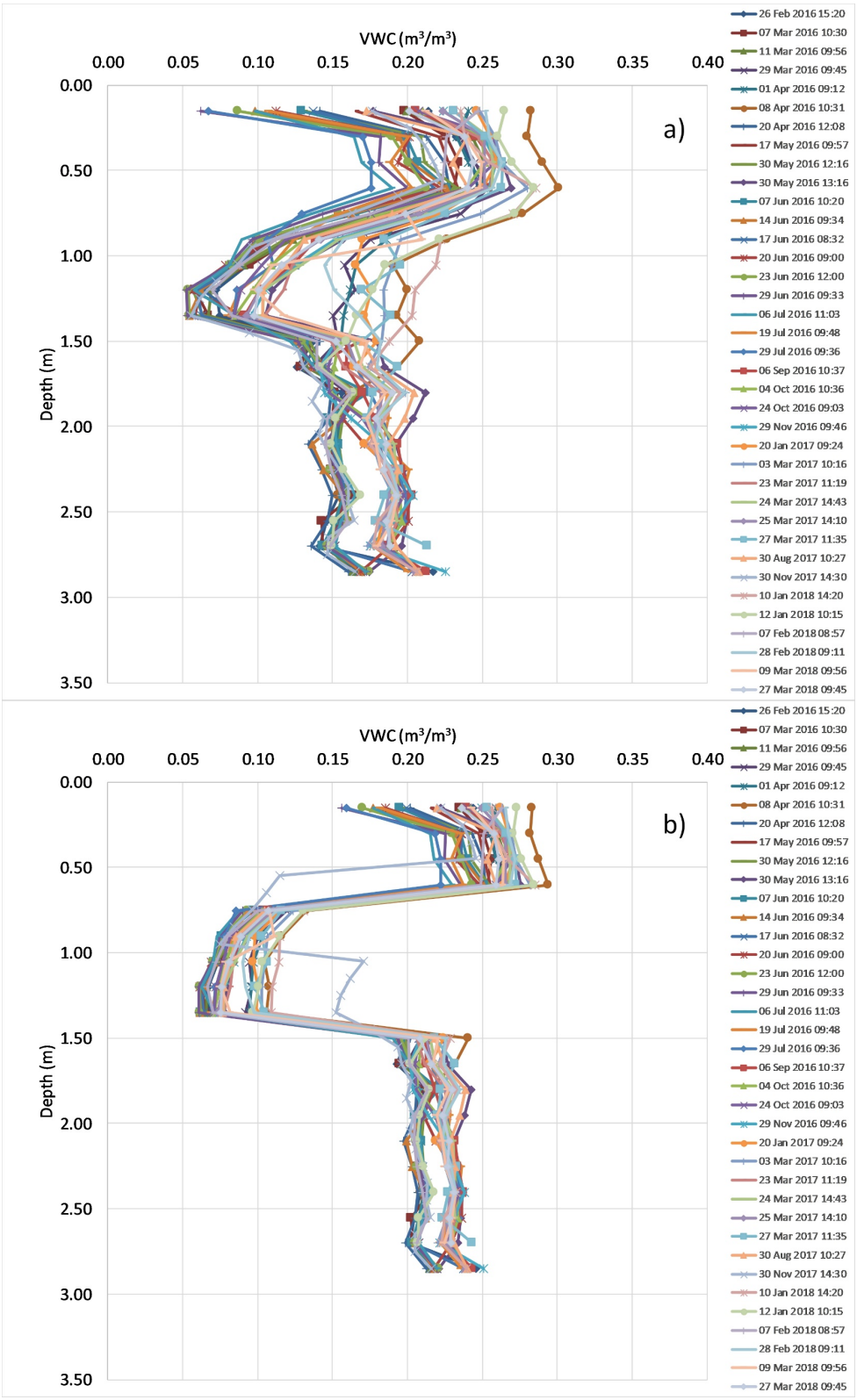


Figure H.5: Calculated VWC at AT2 based on equation for a) all or b) sorted core intervals.

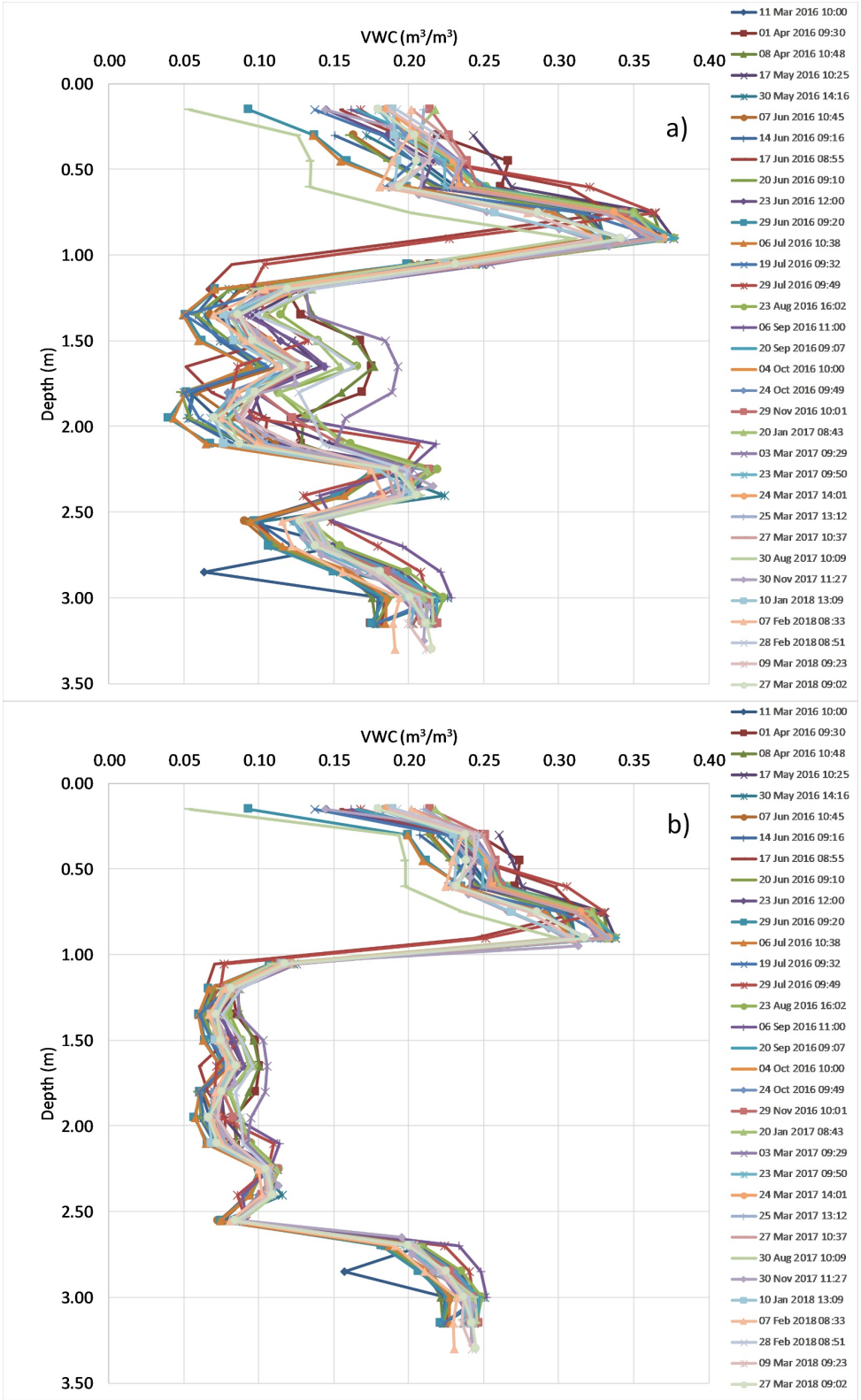

Figure H.6: Calculated VWC at AT3 based on equation for a) all or b) sorted core intervals.

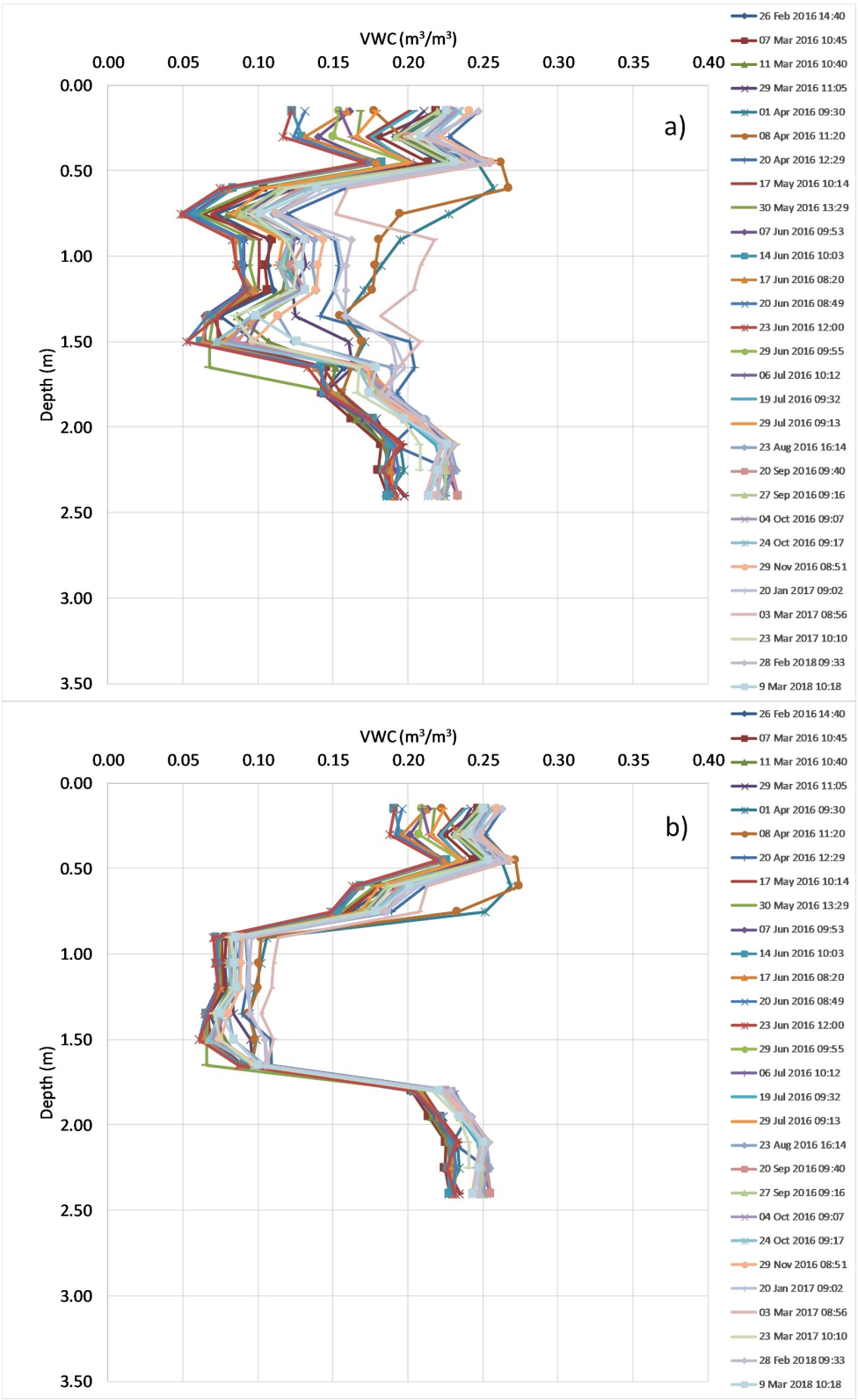


Figure H.7: Calculated VWC at AT4 based on equation for a) all or b) sorted core intervals.

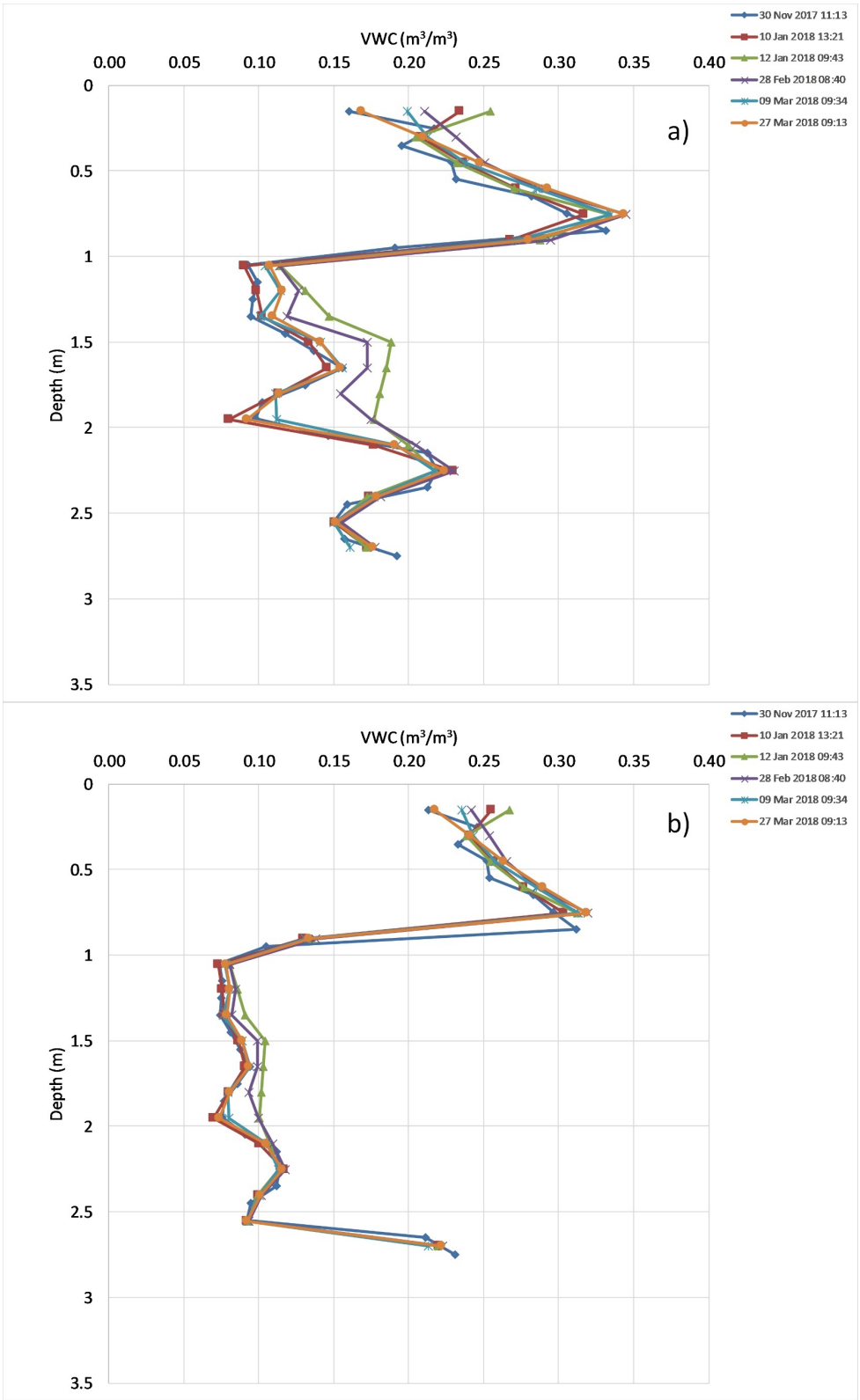


Figure H.8: Calculated VWC at AT5 based on equation for a) all or b) sorted core intervals.

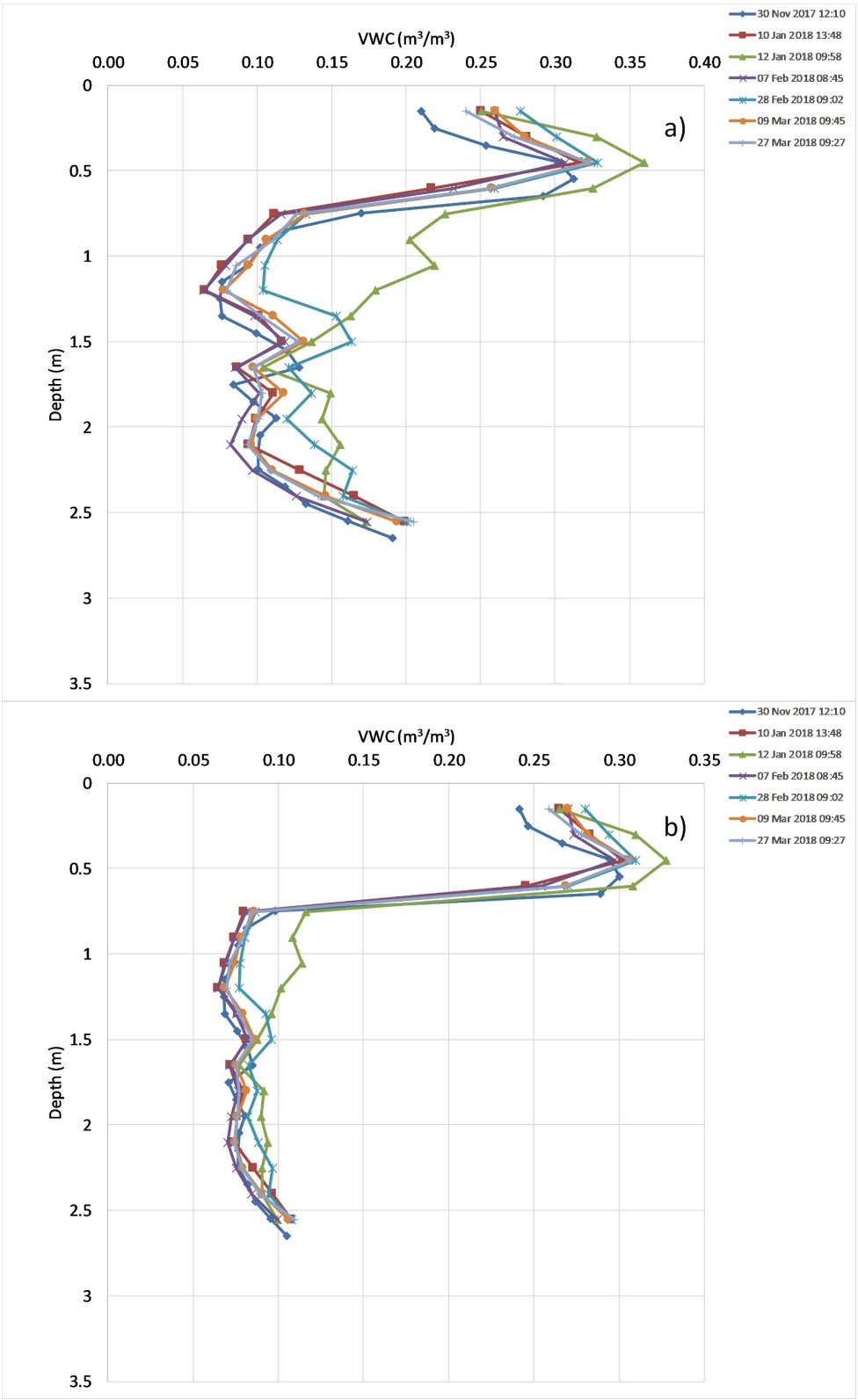


Figure H.9: Calculated VWC at AT6 based on equation for a) all or b) sorted core intervals.

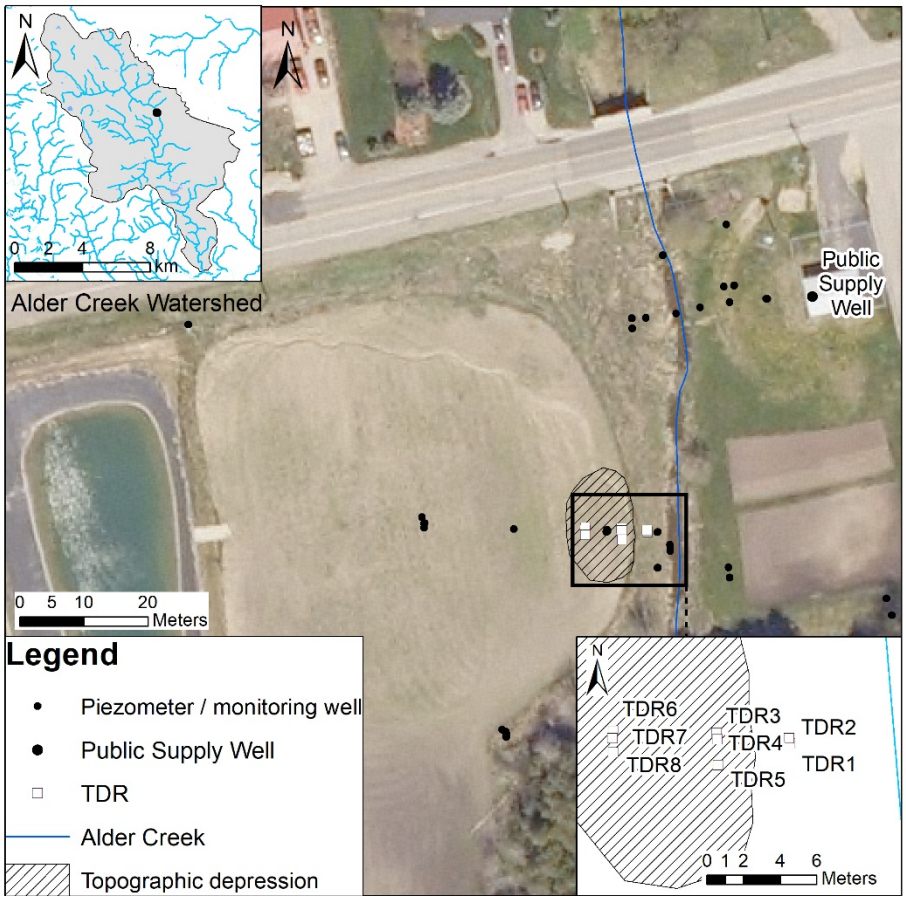


Figure H.10: Locations of TDR sensors at the Mannheim site (CH2MHILL and SSPA, 2003; DMTI, 2011; First Base Solutions, 2006; GRCA, 1998; Hillier, 2014; Wiebe et al., 2019). The base of the topographic depression is shown with hatching.

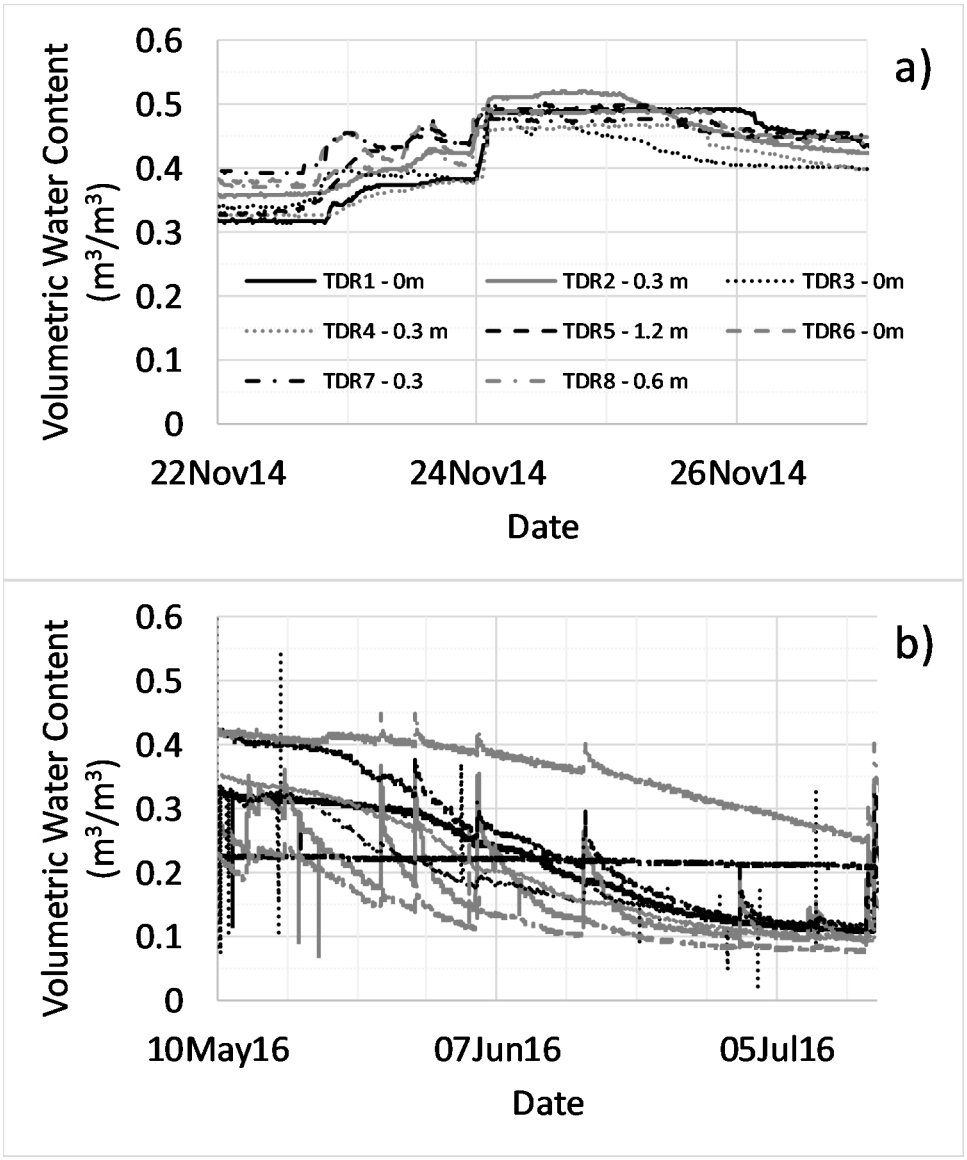


Figure H.11: TDR sensor measurements (Wiebe et al., 2019) under a) maximum, and b) minimum moisture conditions. The depths listed are for the top of each probe.

# Appendix I

# Event Catalogue

Table I.1. Event observations (Wiebe et al., 2019).

| Event # | Date | Amplitude of water level rise (m) | | | | | | Stream Max. Level (m asl)* | WS4 Rainfall (mm)† | Comments |
|---|---|---|---|---|---|---|---|---|---|---|
| | | Creek | CPP1 | CPP3 | CPP8 | CPP6 | DFR pond | | | |
| 1 | 24 Nov 2014 | 0.55 | 1.73 | 2.36 | #N/A | 0.5 | 0.15 | 336.05 | 65 | Some flow in floodplain. |
| 2 | 26 Dec 2014 | 0.22 | 0.24 | 0.32 | #N/A | 0.04 | #N/A | 335.59 | 21.6 | |
| 3 | 4 Jan 2015 | 0.4 | 0.73 | 0.86 | #N/A | 0.06 | 0.04 | 335.79 | 17.8 | |
| 4 | 11 Mar 2015 | 0.44 | 0.73 | 0.95 | #N/A | 0.12 | 0.06 | 336.06 | 4.6 | Possibly floodplain flow. Snowmelt. |
| 5 | 30 Mar 2015 | 0.09 | 0.17 | 0.27 | #N/A | 0.02 | #N/A | 335.51 | 5 | Snowmelt. |
| 6 | 31 Mar 2015 | 0.04 | 0.07 | 0.19 | #N/A | 0 | #N/A | 335.48 | 0.2 | Snowmelt. |
| 7 | 1 Apr 2015 | 0.04 | 0.06 | 0.14 | #N/A | 0.04 | #N/A | 335.48 | 0 | Snowmelt. |
| 8 | 3 Apr 2015 v1 | 0.16 | 0.47 | 0.73 | #N/A | 0.01 | #N/A | 335.61 | 0 | Snowmelt. |
| 9 | 3 Apr 2015 v2 | 0.03 | 0.13 | 0.22 | #N/A | 0 | #N/A | 335.57 | 3.6 | Snowmelt. |
| 10 | Aug 2016 | 0.36 | 1.22 | 1.7 | #N/A | 0.25 | 0.08 | 335.7 | 2.6 | WS4 rainfall negligible despite response. |
| 11 | Nov 2016 | 0.13 | 0.9 | 1.23 | 0.49 | 0 | 0.1 | 335.46 | 21.4 | |
| 12 | Dec 2016 | 0.22 | 0.54 | 1.18 | 0.45 | #N/A | 0.18 | 335.7 | 14 | |
| 13 | 4 Jan 2017 | 0.22 | 0.82 | 1.33 | 0.37 | 0.1 | 0.1 | 335.58 | 12.2 | Snowmelt? |
| 14 | 10 Jan 2017 | 0.64 | 1.31 | 1.53 | 1.1 | 0.27 | 0.16 | 336.03 | 52.6 | Floodplain flow likely. Creek level very high. Snowmelt. Rain: event a) 21.6 mm; event b) 31 mm. |
| 15 | 17 Jan 2017 | 0.12 | 0.32 | 0.68 | 0.12 | 0 | 0.12 | 335.45 | 12.2 | |
| 16 | Feb 2017 | 0.21 | 0.8 | 1.46 | 0.5 | 0.03 | 0.15 | 335.47 | 15.8 | |
| 17 | 25 Feb 2017 | 0.26 | 0.72 | 1.17 | 0.48 | 0.08 | 0.11 | 335.6 | 17.2 | Snowmelt. |
| 18 | 1 Mar 2017 | 0.49 | 0.94 | 1.13 | 0.62 | 0.21 | 0.16 | 335.87 | 21.2 | |

Table I.1. (Continued)

| Event # | Date | Amplitude of water level rise (m) | | | | | | Stream Max. Level (m asl)* | WS4 Rainfall (mm)† | Comments |
|---|---|---|---|---|---|---|---|---|---|---|
| | | Creek | CPP1 | CPP3 | CPP8 | CPP6 | DFR pond | | | |
| 19 | 7 Mar 2017 | 0.58 | 0.6 | 0.96 | 0.29 | 0.09 | 0.14 | 335.59 | 12.2 | |
| 20 | 27 Mar 2017 | 0.07 | 0.22 | 0.61 | 0.16 | 0 | 0.03 | 335.37 | 13.8 | |
| 21 | 31 Mar 2017 | 0.1 | 0.53 | 0.97 | 0.18 | 0.02 | 0.03 | 335.39 | 10.6 | |
| 22 | 4 Apr 2017 | 0.2 | 0.57 | 0.91 | 0.43 | 0.06 | 0.04 | 335.48 | 15.8 | |
| 23 | 6 Apr 2017 | 0.24 | 0.45 | 0.63 | 0.31 | 0.09 | 0.06 | 335.57 | 9.6 | Snowmelt. |
| 24 | 10 Apr 2017 | 0.03 | 0.07 | 0.17 | 0.05 | 0.07 | 0.02 | 335.34 | 5.4 | Snowmelt. |
| 25 | 11 Apr 2017 | 0.01 | 0.18 | 0.35 | 0.13 | 0 | 0.05 | 335.33 | 6.2 | |
| 26 | 20 Apr 2017 | 0.5 | 0.96 | 1.28 | 0.56 | 0.15 | 0.1 | 335.67 | 27 | |
| 27 | 30 Apr 2017 | 0.2 | 0.63 | 1.05 | 0.29 | 0.04 | 0.05 | 335.49 | 14.2 | |
| 28 | 4 May 2017 | 0.42 | 0.9 | 1.03 | 0.64 | 0.29 | 0.07 | 335.82 | 32.6 | |
| 29 | 16 Jul 2017 | 0.36 | 1.05 | 1.66 | 0.89 | 0.21 | 0.18 | 335.57 | 27.2 | |
| 30 | 5 Nov 2017 | 0.07 | 0.09 | 0.09 | 0.07 | 0 | 0 | 335.29 | 11.2 | |
| 31 | 18 Nov 2017 | 0.17 | 0.42 | 0.62 | 0.48 | 0.04 | 0 | 335.4 | 25.8 | |
| 33 | 11 Jan 2018 | 0.11 | 0.26 | 0.49 | 0.74 | 0.24 | 0.13 | 335.79 | 13.8 | |
| 34 | 22 Jan 2018 | 0.47 | 0.66 | 0.76 | 0.59 | 0.3 | 0.27 | 336.13 | 20.8 | Snowmelt. Possibly floodplain flow. Pictures before and after suggest ground may still have been frozen. |
| 35 | 15 Feb 2018 | 0.46 | 0.74 | 1.03 | 0.31 | 0.17 | 0.2 | 335.74 | 30.4 | Snowmelt. Small amount of overland flow. Creek slightly wider than bankfull width. |
| 36 | 4 Apr 2018 | 0.2 | 0.73 | 1.22 | 0.66 | 0.06 | 0.03 | 335.47 | 15.6 | |
| 37 | 15 Apr 2018 | 0.23 | 0.97 | 1.4 | 0.68 | 0.15 | 0.1 | 335.49 | 28.2 | |
| 38 | 20 Apr 2018 | 0.14 | 0.28 | 0.52 | 0.19 | 0.06 | 0.02 | 335.38 | 8.4 | |

* asl = above sea level.

† Rainfall over up to 4 antecedent days

# Appendix J

# Effective precipitation estimates for the Mannheim site

Effective precipitation estimates (Figure J.1, i.e., P – AET, where P is precipitation and AET is actual evapotranspiration) for the HydroGeoSphere (HGS; Aquanty, 2015a) Wedge2 model were developed from rainfall measurements at the Mannheim site (WS4; Wiebe et al., 2019), snowmelt estimates derived from the Roseville Environment Canada weather station (Government of Canada, 2019), and time-varying estimates of the ratio of actual evapotranspiration to precipitation (i.e., AET/P). Snowmelt estimates were derived manually based on the daily snowfall data and snowpack thickness data (Government of Canada, 2019) via the following process. The cumulative snowfall during a period between melt events (i.e., times when the snowpack thickness decreased and air temperatures were > 0°C) was calculated, and then a percentage of this total height was distributed daily during melt events based on the estimated severity of the melting. A ratio of 0.1 was assumed for calculation of the snow water equivalent from snowpack thickness (SWE = 0.1 × snowpack thickness). Warmer temperatures and greater daily reductions of snowpack were assumed to correspond to larger snowmelt values. While this is an approximation that assumes that frozen soil plays a negligible role in preventing infiltration, the impact of the exact timing of snowmelt infiltration on the Nov 2014 and Jul 2017 events is expected to be minimal because they occurred under unfrozen soil conditions. An uncertainty of a few days for melting amounts is not expected to significantly impact the analysis.

AET/P ratios were approximated based on a conceptual model that assumed some evaporation or sublimation in winter and a maximum ratio during the summer. The AET fraction of daily precipitation was approximated based on a base ratio ($AET_{daily}/P_{daily}$) of 0.15 between 26 Dec and 15 Jan of each year, and a maximum ratio of 0.9 between 25 Apr and 7 Sep of each year, with linear interpolation in between. The average annual AET/P ratio (0.64) was set to the value obtained from the Budyko curve (Appendix A; e.g., Gentine et al., 2012), where reference evapotranspiration ($ET_o$) estimates (ETo Calculator program; Raes, 2009) were based on 46 years of daily Roseville temperature data and an average wind speed estimate obtained from measurements at seven local weather stations over about 4 years (Appendix A; Wiebe et al., 2019), and average precipitation was calculated from 46 years of daily Roseville data, (AquaResource, 2008; Government of Canada, 2019; OMNR, 2007).

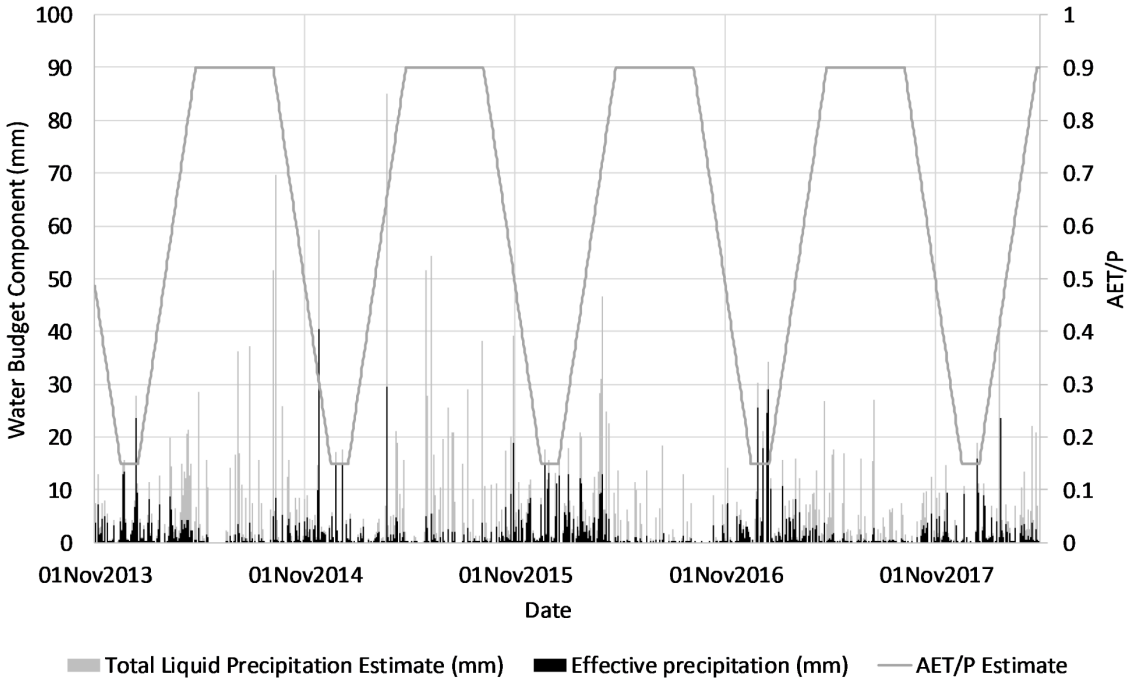


Figure J.1: Total and effective precipitation, along with estimated variation of the AET/P ratio (Appendix A; AquaResource, 2008; Gentine et al., 2012; Government of Canada, 2019; OMNR, 2007; Wiebe et al., 2019).

# Appendix K

# Single well hydraulic (slug) tests at the Mannheim site

Single well hydraulic testing was conducted at the Mannheim site on 1 Oct 2018 and 17 Oct 2018. The hydraulic conductivity (K) values derived from these slug tests complement earlier tests conducted by Missori (2015). This appendix contains a map of the piezometer locations (Figure K.1), a cross-section showing the slug test averages at different piezometers (Figure K.2), summaries of the results (overall – Table K.1; for individual piezometers – Table K.2; for CPP18 constant head tests – Table K.3), and graphs of the Hvorslev (1951) and Bouwer and Rice (1976) analyses (Figures K.3 to K.36). Recommendations by Butler (1998) regarding the $h/h_0$ intervals over which to match the line of best fit (0.15 to 0.25 for Hvorslev and 0.2 to 0.3 for Bouwer and Rice) were followed except where noted. All Hvorslev analyses (basic time lag, variable head, or constant head) were conducted for case G (Hvorslev, 1951). Bouwer and Rice analyses were conducted in Aquifer Test 7.0 (Waterloo Hydrogeologic, 2016).

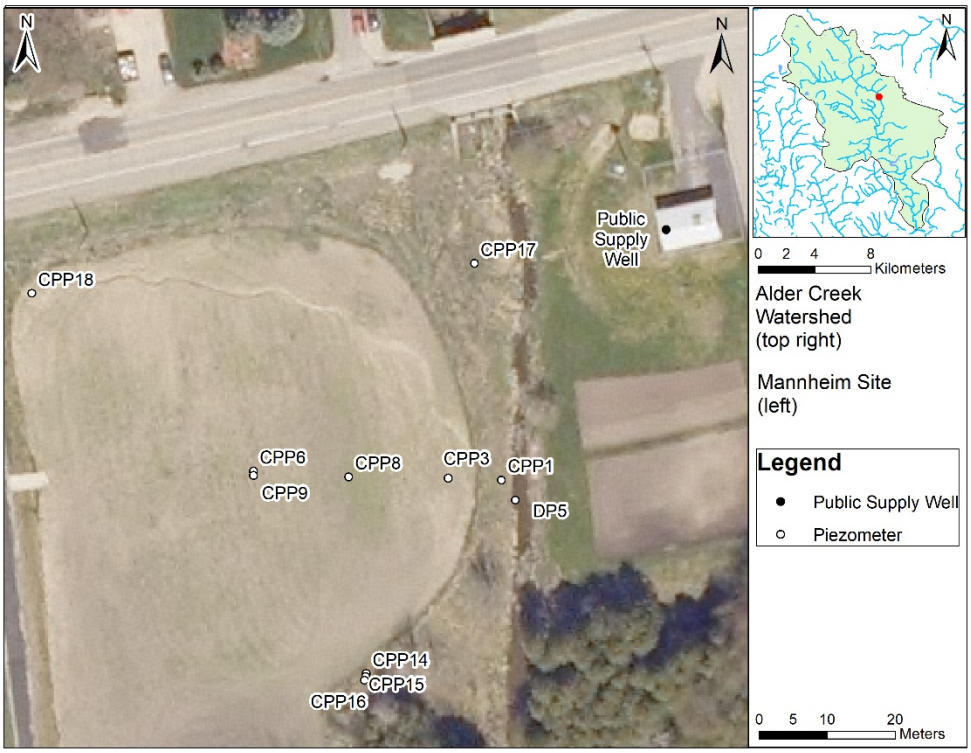


Figure K.1: Locations of wells at which single well hydraulic tests were performed in 2018 (DMTI, 2011; First Base Solutions, 2006; GRCA, 1998).

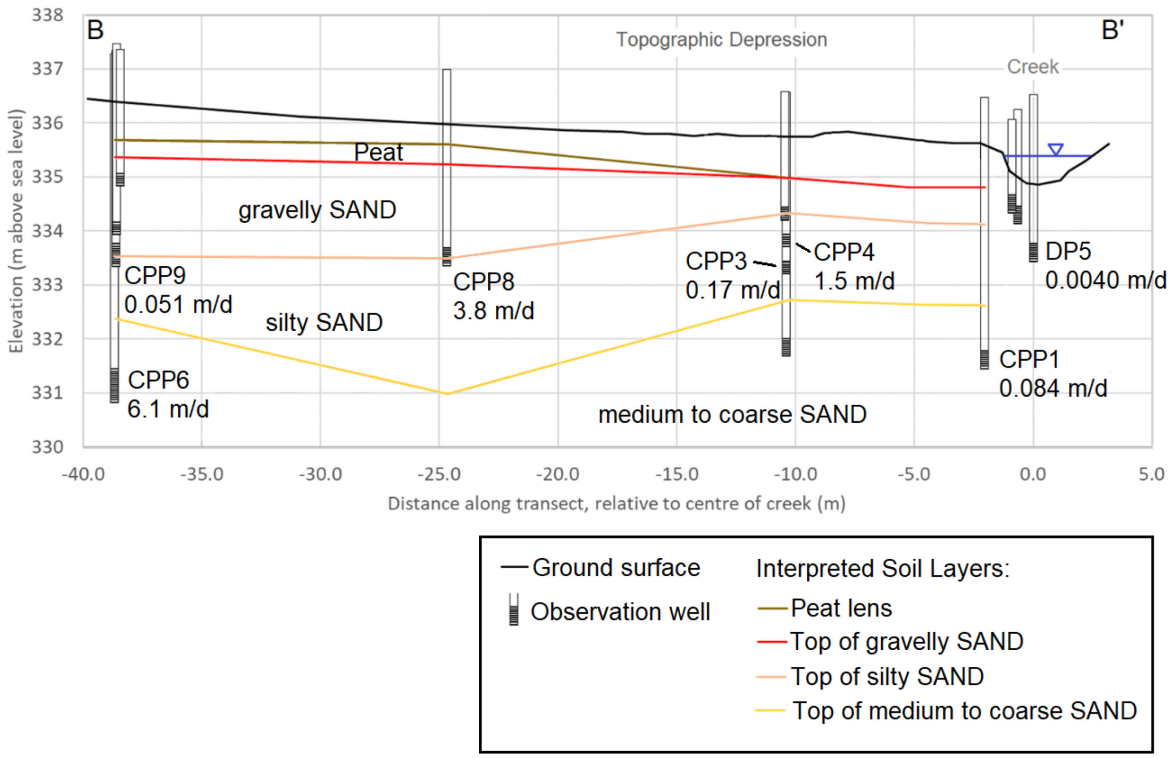


Figure K.2: Average slug test results along a cross-section perpendicular to the creek (Menkveld, 2019; Missori, 2015). The location of cross-section B-B' is shown on Figure 3.4 in plan view.

Table K.1. Summary of recommended hydraulic conductivity (arithmetic average) at the Mannheim site piezometers. The recommended values account for Missori (2015) data where noted.

| Piezometer | $K_{Hvorslev}$ (m/s) | No. of values considered in Hvorslev estimate | $K_{Bouwer\&Rice}$ (m/s) | No. of values considered in Bouwer and Rice estimate | Comments |
|---|---|---|---|---|---|
| CPP1 | 1.2E-06 | 7 | 9.7E-07 | 7 | Average includes four values (excludes two outliers) from Missori (2015) |
| CPP3 | 2.7E-06 | 2 | 2.0E-06 | 4 | Hvorslev average includes only the two higher results. |
| CPP4 | 2.4E-05 | 7 | 1.7E-05 | 7 | Average of the seven Missori (2015) values. |
| CPP6 | 7.3E-05 | 5 | 7.1E-05 | 5 | Average includes one value from Missori (2015). |
| CPP7 | 3.8E-06 | 9 | 3.6E-06 | 9 | Average of the nine Missori (2015) values. |
| CPP8 | 8.8E-05 | 2 | 4.4E-05 | 2 | |
| CPP9 | 9.7E-07 | 4 | 5.9E-07 | 4 | |
| CPP10 | 7.2E-05 | 1 | 5.6E-05 | 1 | Chose higher of the two Missori (2015) values; they differ by one order of magnitude. |
| CPP14 | 1.1E-07 | 2 | 1.0E-07 | 2 | |
| CPP15 | 2.1E-07 | 2 | 1.6E-07 | 2 | Two initial lower values were excluded |
| CPP16 | 2.2E-06 | 1 | 7.5E-07 | 1 | Second test excluded (one order of magnitude different) |
| CPP17 | 5.5E-07 | 2 | 3.0E-07 | 2 | |
| CPP18 | 9.7E-05 | 6 | 7.9E-05 | 4 | |
| DP5 | 6.1E-08 | 2 | 4.6E-08 | 2 | First value excluded (2 orders of magnitude lower). |

Table K.2. Summary of hydraulic conductivity (K) estimates at piezometers.

| Piezometer / Test No. | Method (FH = falling head; RH = rising head) | $K_{Hvorslev}$ (m/s) | $K_{Bouwer\&Rice}$ (m/s) | Comments (eqn = equation; H = head) |
|---|---|---|---|---|
| CPP1 / 1 | solid slug, FH | 1.2E-06 | 1.0E-06 | |
| CPP1 / 2 | solid slug, RH | 1.2E-06 | 9.9E-07 | |
| CPP1 / 3 | water addition, FH | 9.7E-07 | 8.1E-07 | |
| CPP3 / 1 * | solid slug, FH | 2.3E-06 | 2.4E-06 | |
| CPP3 / 2 * | solid slug, RH | 7.7E-07 | 1.3E-06 | |
| CPP3 / 3 | water addition, FH | 3.1E-06 | 3.1E-06 | |
| CPP3 / 4 | pump out - RH | 7.7E-07 | 1.2E-06 | |
| CPP6 / 1 * | solid slug, RH | 8.1E-05 | 6.9E-05 | |
| CPP6 / 2 * | solid slug, FH | 8.1E-05 | 6.7E-05 | |
| CPP6 / 3 * | solid slug, RH | 7.0E-05 | 7.1E-05 | |
| CPP6 / 4 * | solid slug, RH | 8.0E-05 | 7.1E-05 | |
| CPP8 / 1 * | solid slug, FH | 1.1E-04 | 5.5E-05 | |
| CPP8 / 2 * | solid slug, FH | 6.9E-05 | 3.3E-05 | |
| CPP9 / 1 * | water addition, FH | 3.8E-07 | 4.4E-07 | |
| CPP9 / 2 * | water addition, FH | 6.7E-07 | 7.6E-07 | |
| CPP9 / 3 * | pump out - RH | 9.1E-07† | 6.2E-07‡ | Hvorslev-Variable H. eqn. |
| CPP9 / 4 | pump out - RH | 9.5E-07 | 5.3E-07 | |
| CPP14 / 1 * | solid slug, FH | 8.3E-08† | 7.4E-08 | Development needed? |
| CPP14 / 2 | water addition, FH | 1.4E-07 | 1.3E-07 | |
| CPP15 / 1 | water addition, FH | 1.4E-08 | 1.4E-08 | |
| CPP15 / 2 | water addition, FH | 6.9E-08 | 5.5E-08‡ | |
| CPP15 / 3 | water addition, FH | 2.7E-07 | 2.1E-07‡ | |
| CPP15 / 4 | water addition, FH | 1.4E-07 | 1.2E-07‡ | |
| CPP16 / 1 * | water addition, FH | 2.2E-06† | 7.5E-07‡ | Hvorslev-Variable H. eqn. |
| CPP16 / 2 | water addition, FH | 2.9E-07† | 1.0E-07‡ | Hvorslev-Variable H. eqn. |
| CPP17 / 1 * | water addition, FH | 8.3E-07† | 3.5E-07‡ | |
| CPP17 / 2 | water addition, FH | 2.8E-07 | 2.0E-07 | |
| CPP18 / 1 * | solid slug, FH | 9.7E-05 | 8.3E-05 | |
| CPP18 / 2 * | solid slug, RH | 8.4E-05 | 8.9E-05 | |
| CPP18 / 3 * | solid slug, FH | 5.7E-05 | 5.8E-05 | |
| CPP18 / 4 * | solid slug, RH | 8.0E-05 | 8.7E-05 | |
| CPP18 / 5 | constant head pump out | 1.3E-04 | N/A | Hvorslev-Constant H. eqn. |
| CPP18 / 6 | constant head pump out | 1.3E-04 | N/A | Hvorslev-Constant H. eqn. |
| DP5 / 1 | water addition, FH | 5.9E-10 | N/A | Hvorslev-Variable H. eqn. |
| DP5 / 2 | water addition, FH | 6.1E-08† | 4.5E-08‡ | Hvorslev-Variable H. eqn. |
| DP5 / 3 | water addition, FH | 6.1E-08† | 4.7E-08‡ | Hvorslev-Variable H. eqn. |

* Performed on 1 Oct 2018. All other tests were performed on 17 Oct 2018.
† Data do not enter 0.15 to 0.25 fitting range recommended by Butler (1998) for the Hvorslev method.
‡ Data do not enter the 0.2 to 0.3 fitting range recommended by Butler (1998) for the Bouwer and Rice method.

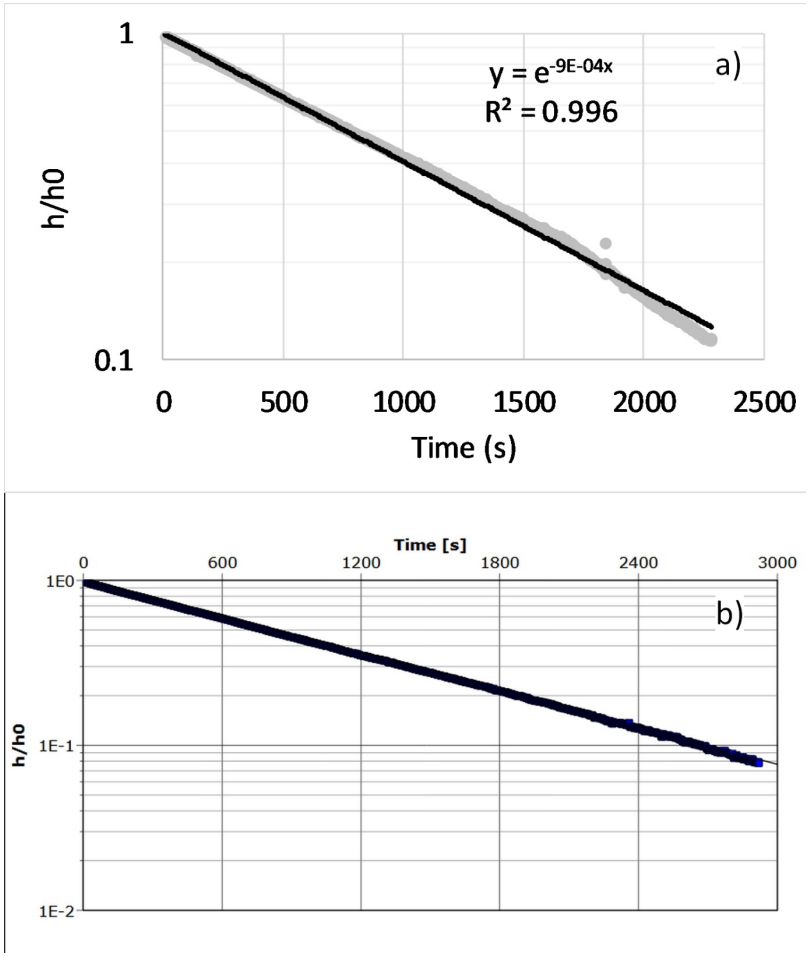


Figure K.3: a) Hvorslev and b) Bouwer and Rice plots for slug test CPP1 / 1.

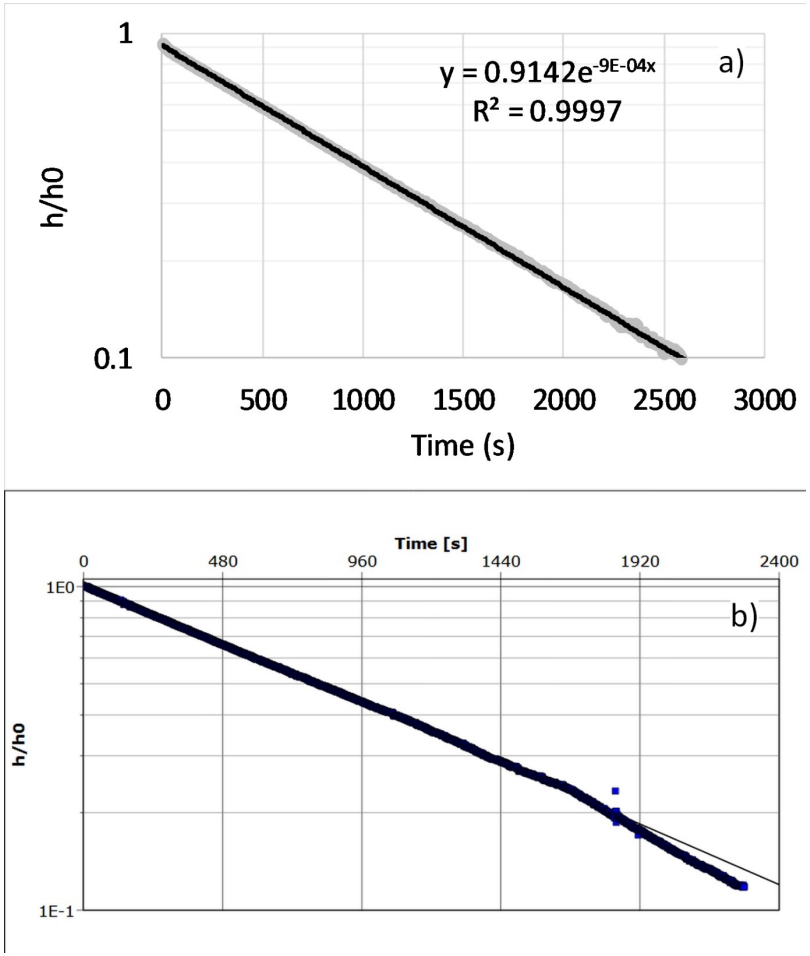


Figure K.4: a) Hvorslev and b) Bouwer and Rice plots for slug test CPP1 / 2.

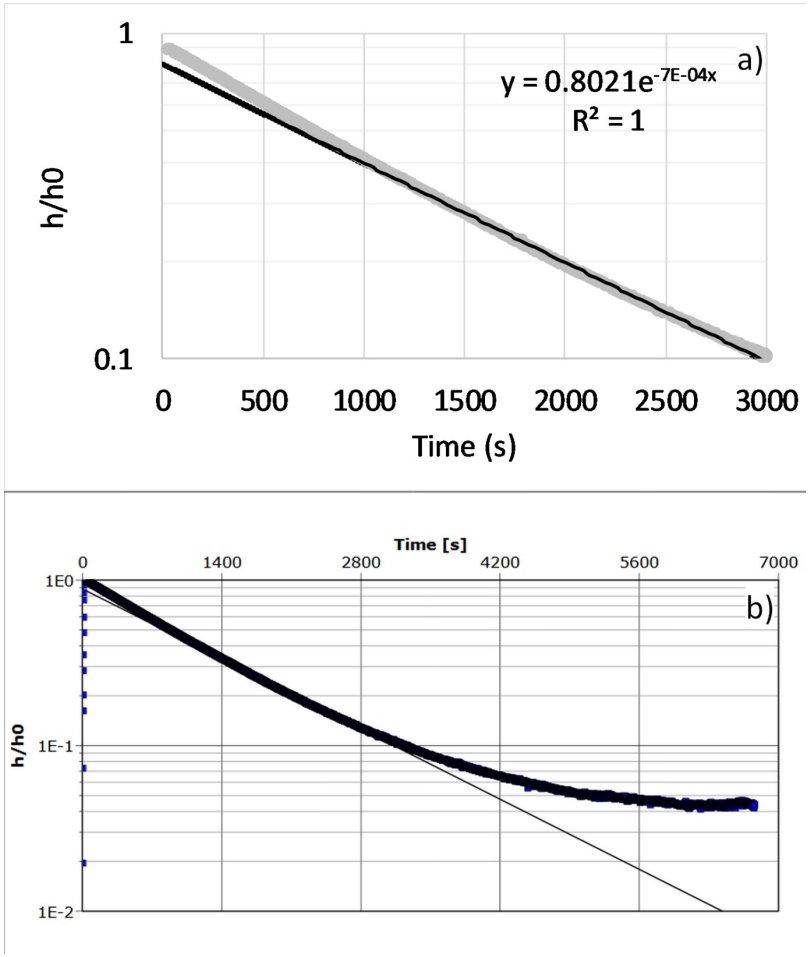


Figure K.5: a) Hvorslev and b) Bouwer and Rice plots for slug test CPP1 / 3.

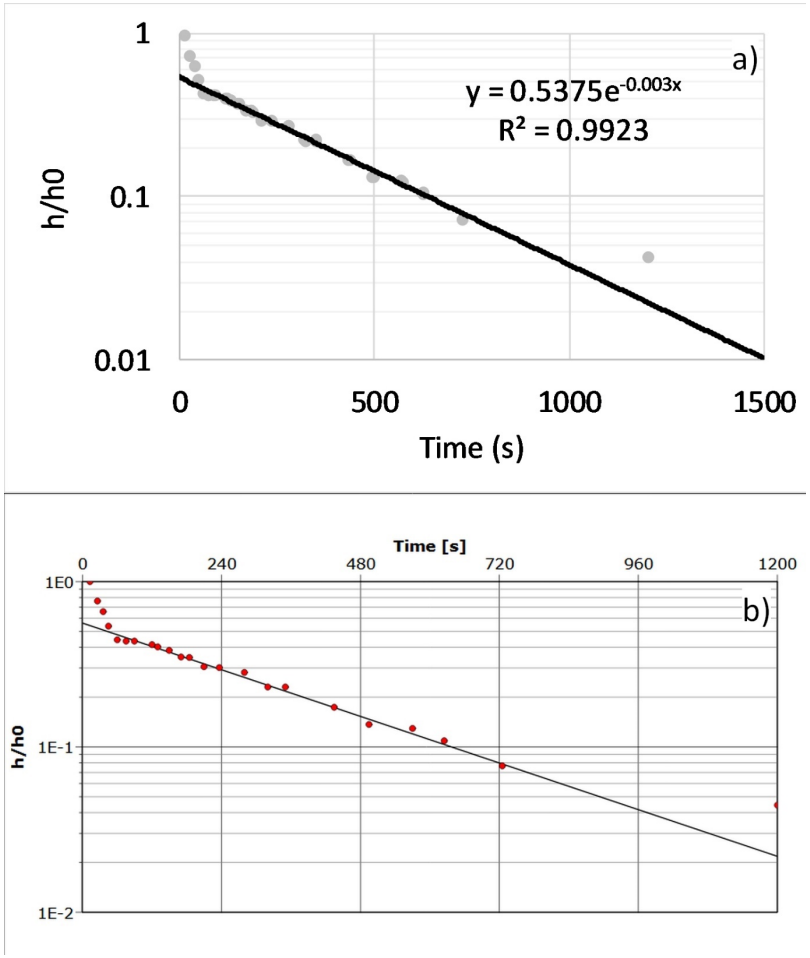


Figure K.6: a) Hvorslev and b) Bouwer and Rice plots for slug test CPP3 / 1.

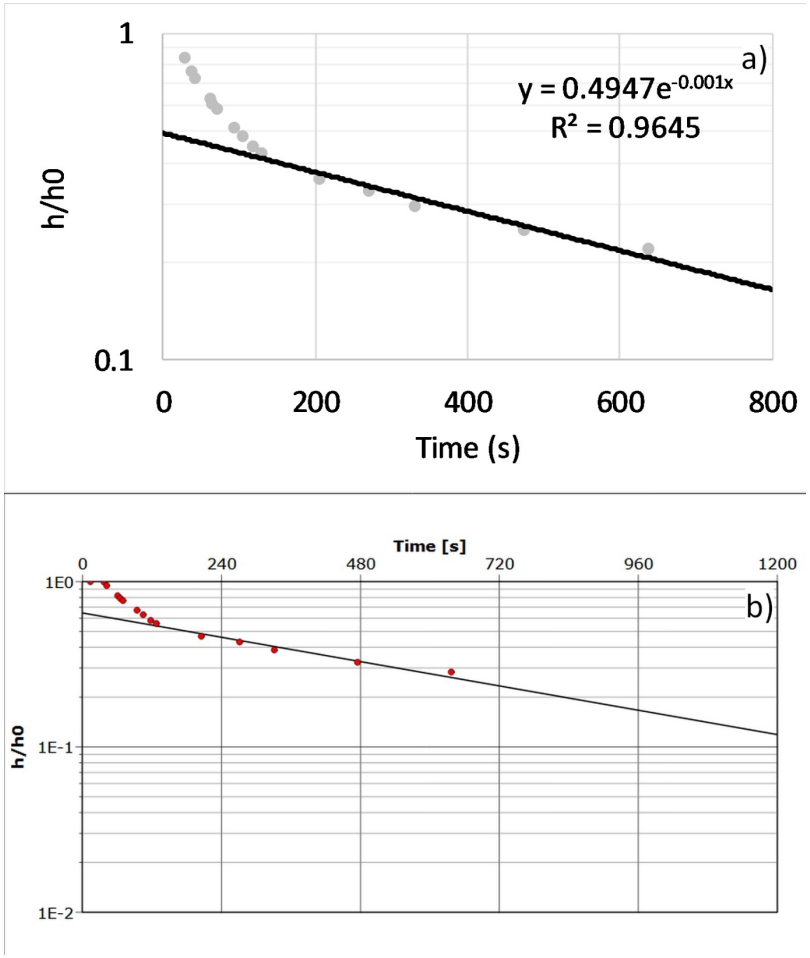


Figure K.7: a) Hvorslev and b) Bouwer and Rice plots for slug test CPP3 / 2.

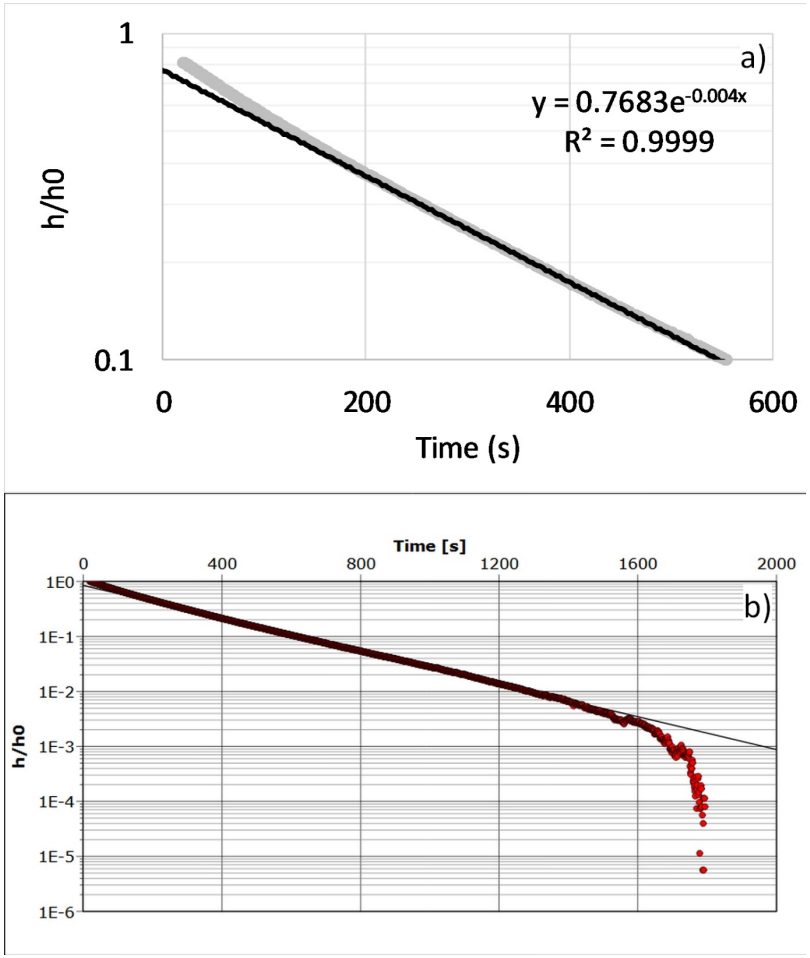


Figure K.8: a) Hvorslev and b) Bouwer and Rice plots for slug test CPP3 / 3.

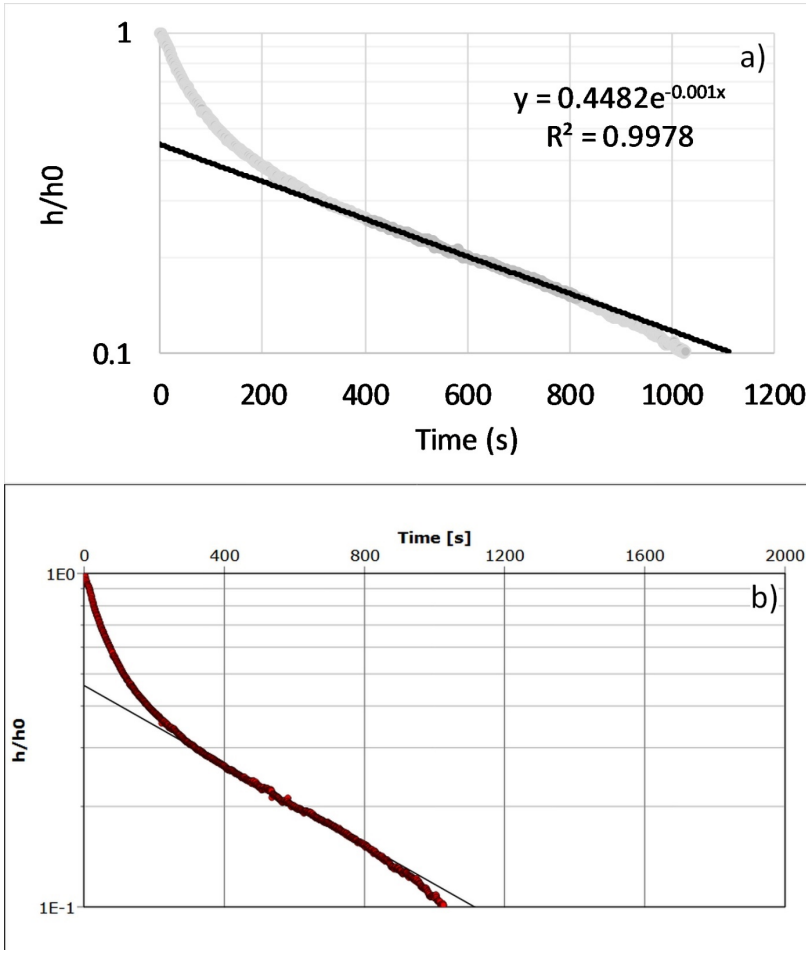


Figure K.9: a) Hvorslev and b) Bouwer and Rice plots for slug test CPP3 / 4.

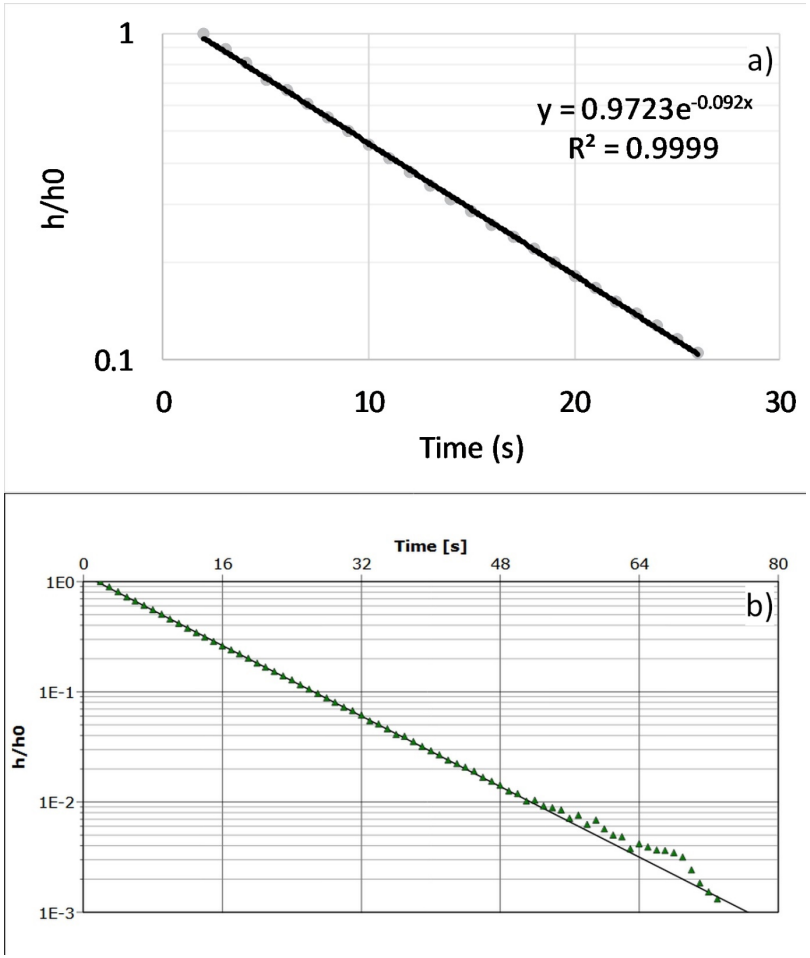


Figure K.10: a) Hvorslev and b) Bouwer and Rice plots for slug test CPP6 / 1.

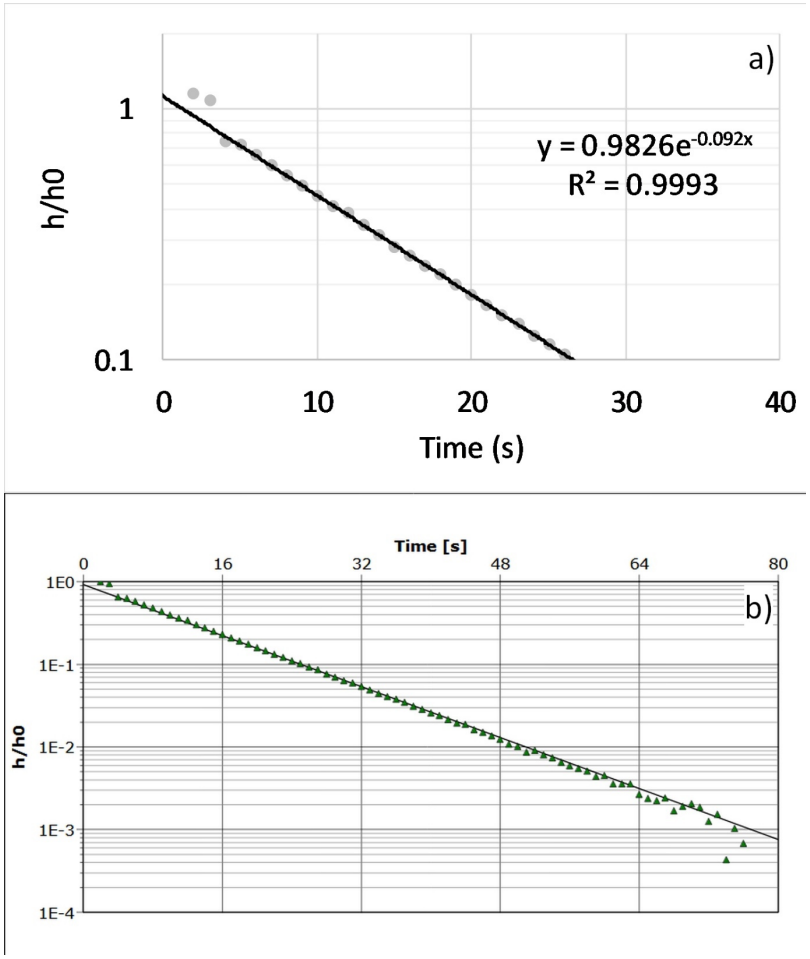


Figure K.11: a) Hvorslev and b) Bouwer and Rice plots for slug test CPP6 / 2.

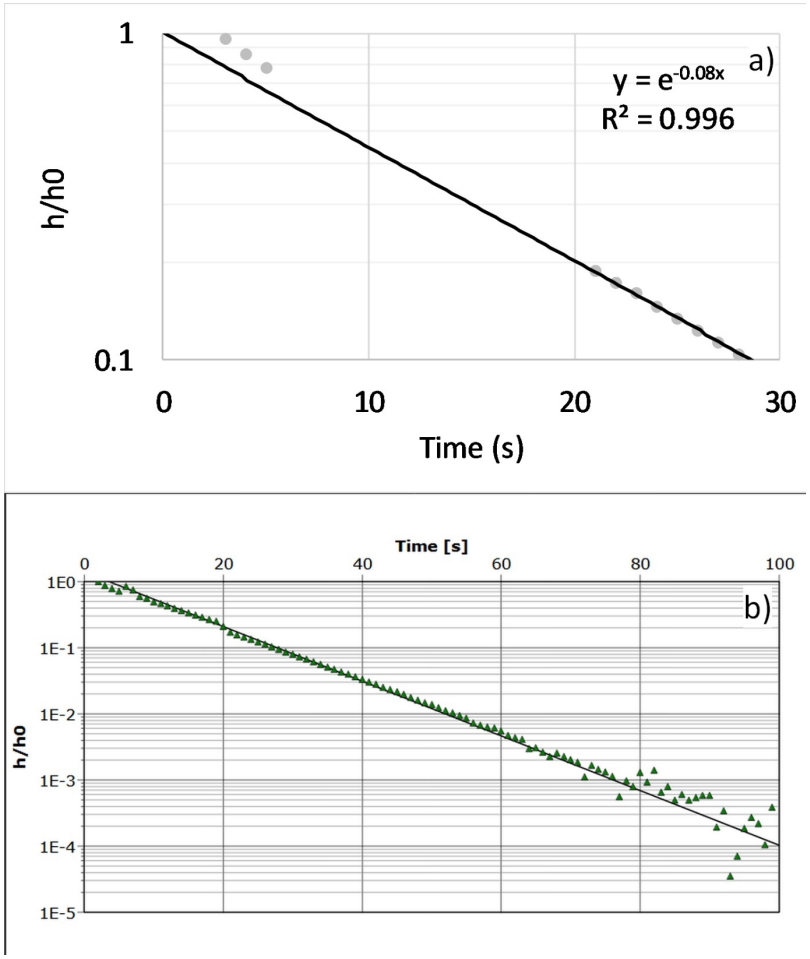


Figure K.12: a) Hvorslev and b) Bouwer and Rice plots for slug test CPP6 / 3. The logger cable moved temporarily when slug was removed.

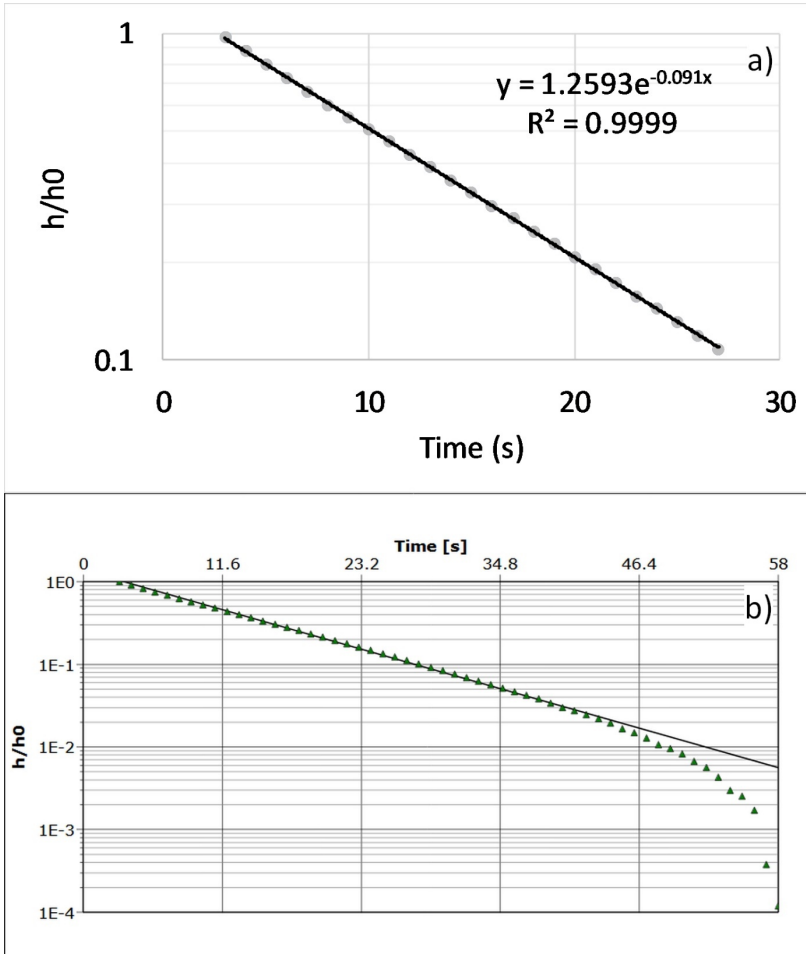


Figure K.13: a) Hvorslev and b) Bouwer and Rice plots for slug test CPP6 / 4.

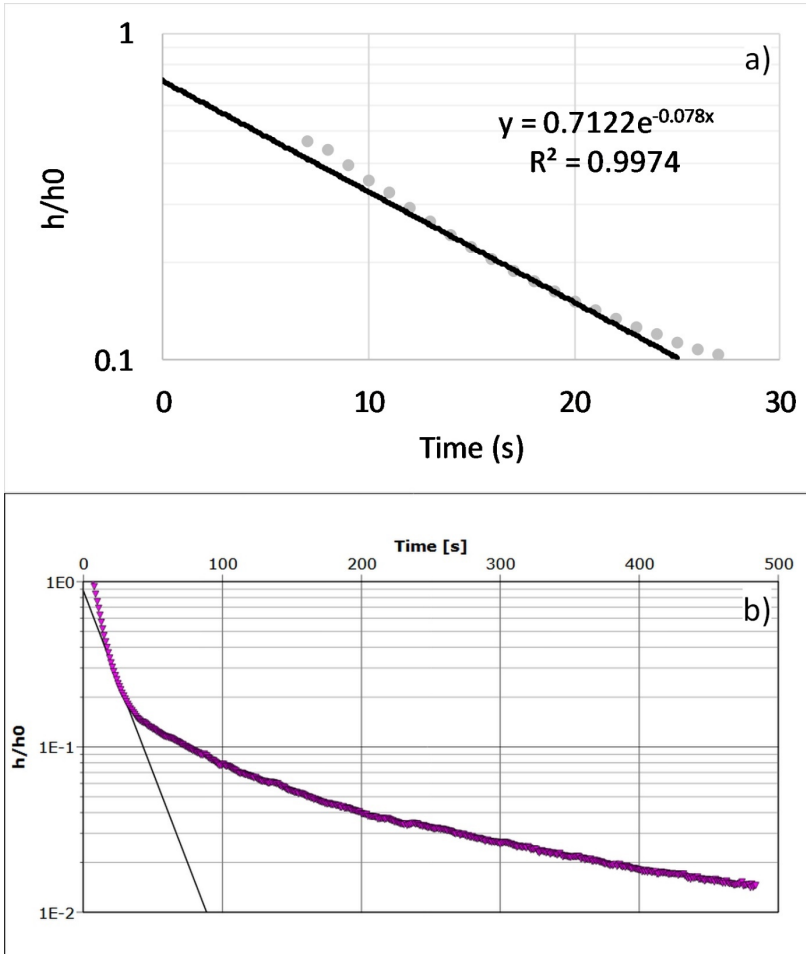


Figure K.14: a) Hvorslev and b) Bouwer and Rice plots for slug test CPP8 / 1.

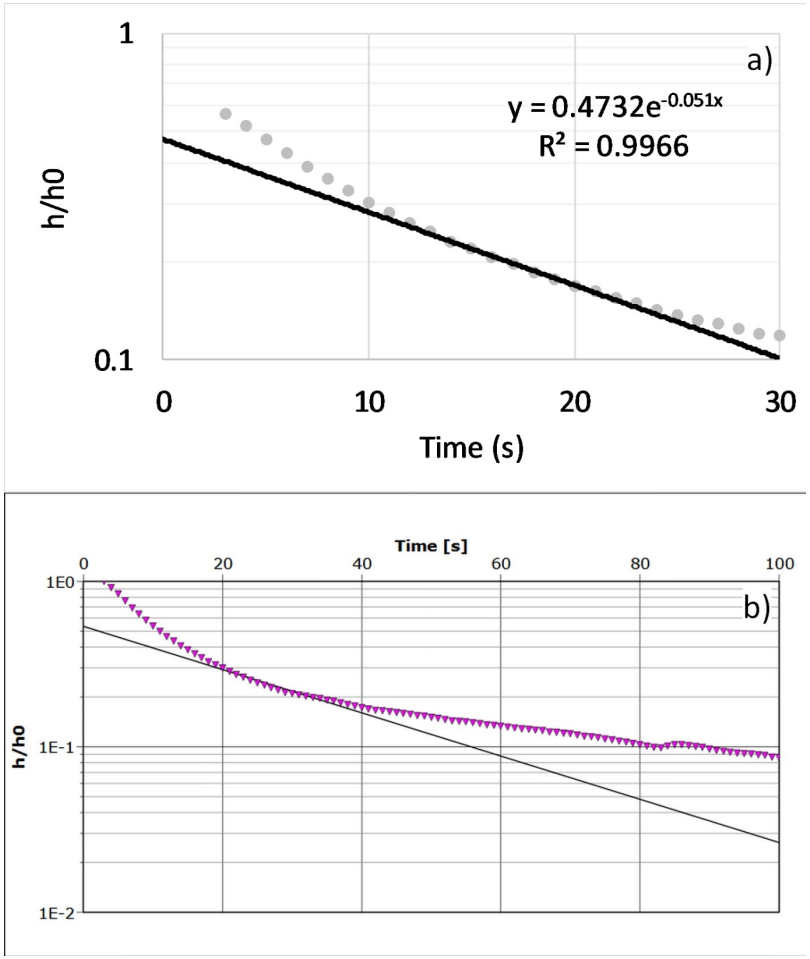


Figure K.15: a) Hvorslev and b) Bouwer and Rice plots for slug test CPP8 / 2.

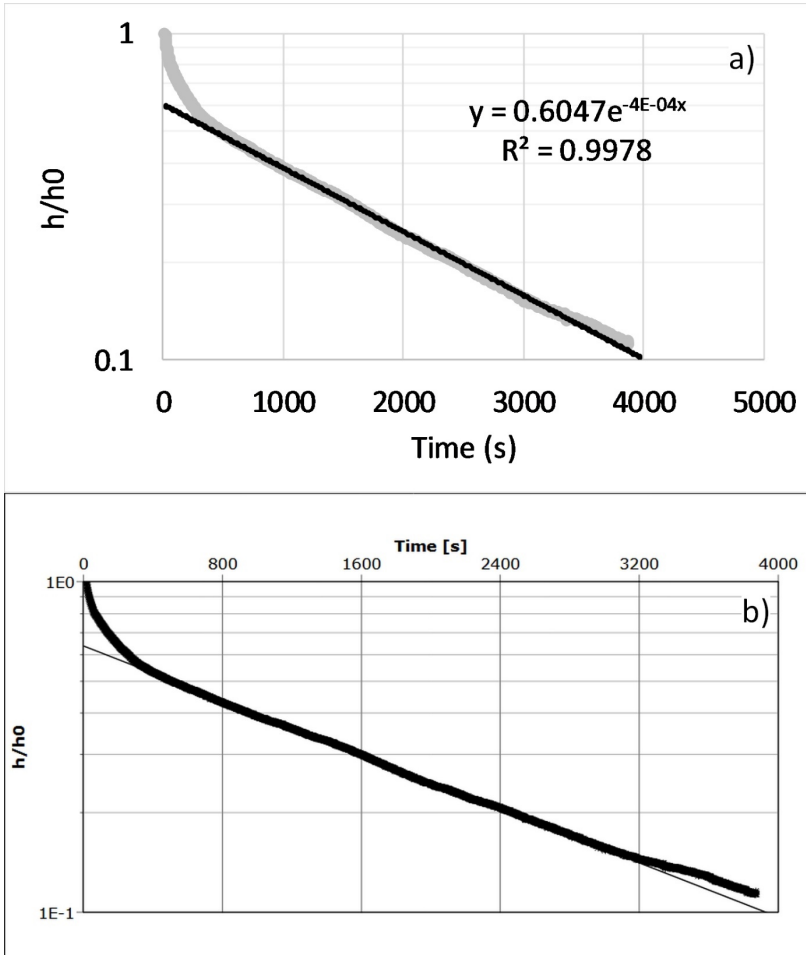


Figure K.16: a) Hvorslev and b) Bouwer and Rice plots for slug test CPP9 / 1.

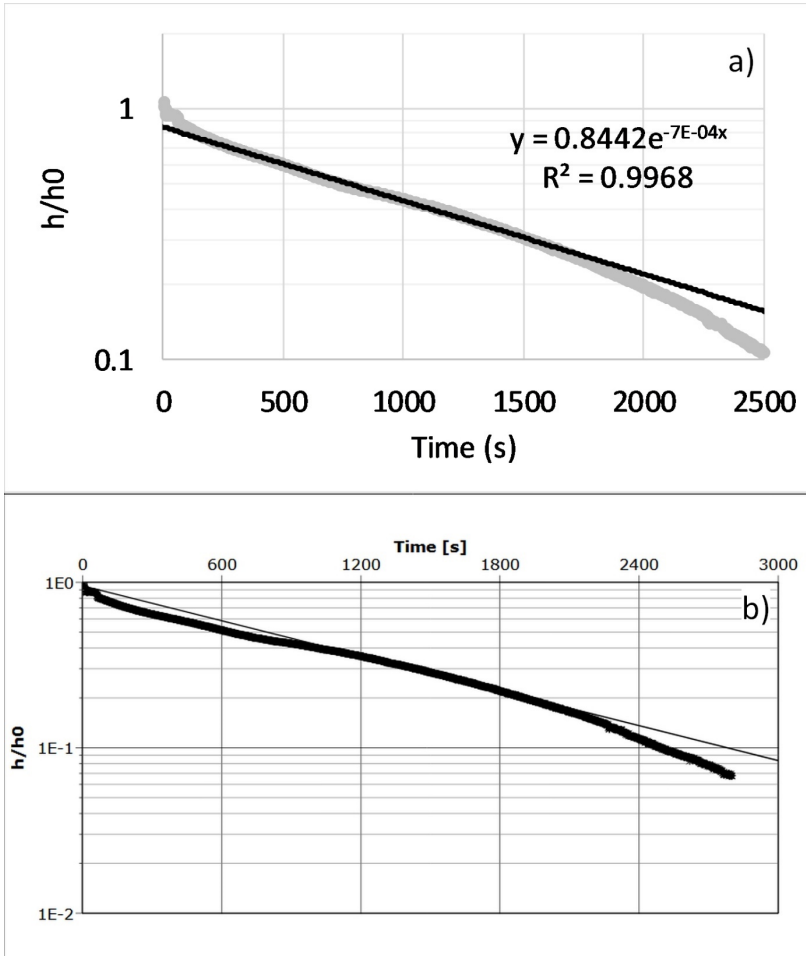


Figure K.17: a) Hvorslev and b) Bouwer and Rice plots for slug test CPP9 / 2.

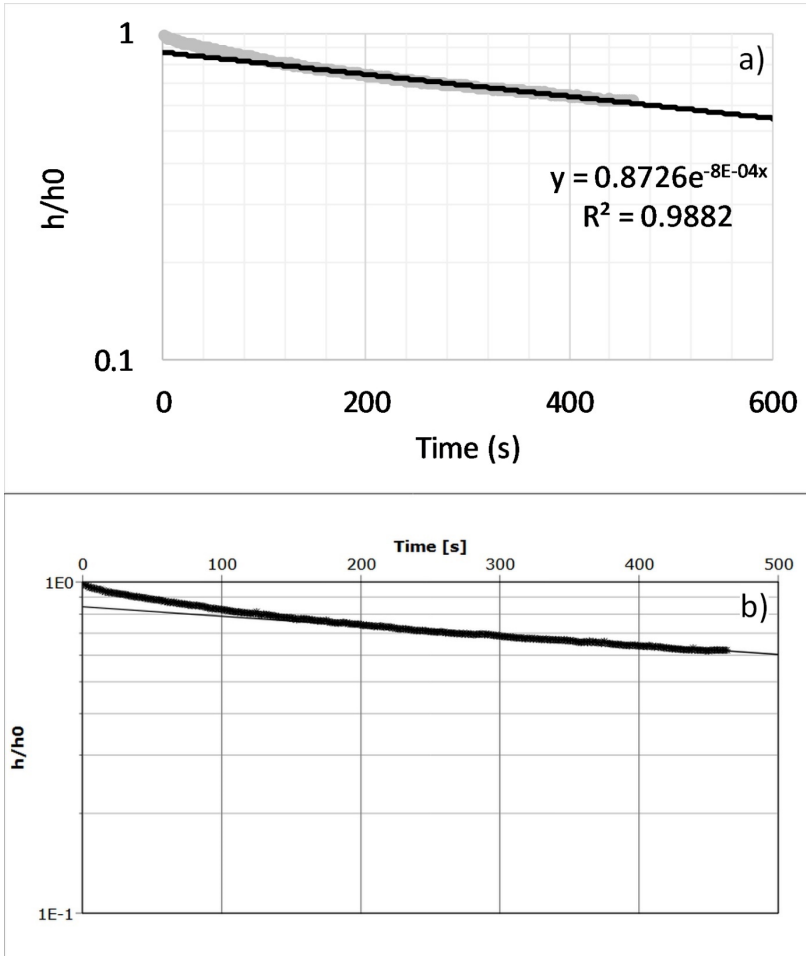


Figure K.18: a) Hvorslev and b) Bouwer and Rice plots for slug test CPP9 / 3.

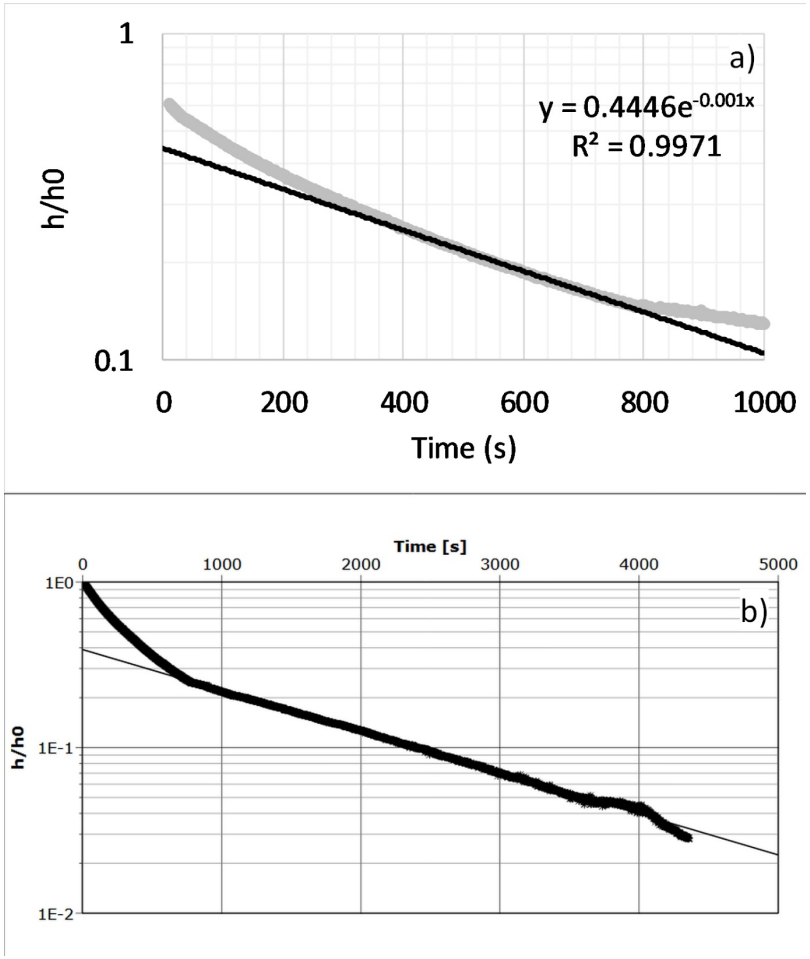


Figure K.19: a) Hvorslev and b) Bouwer and Rice plots for slug test CPP9 / 4.

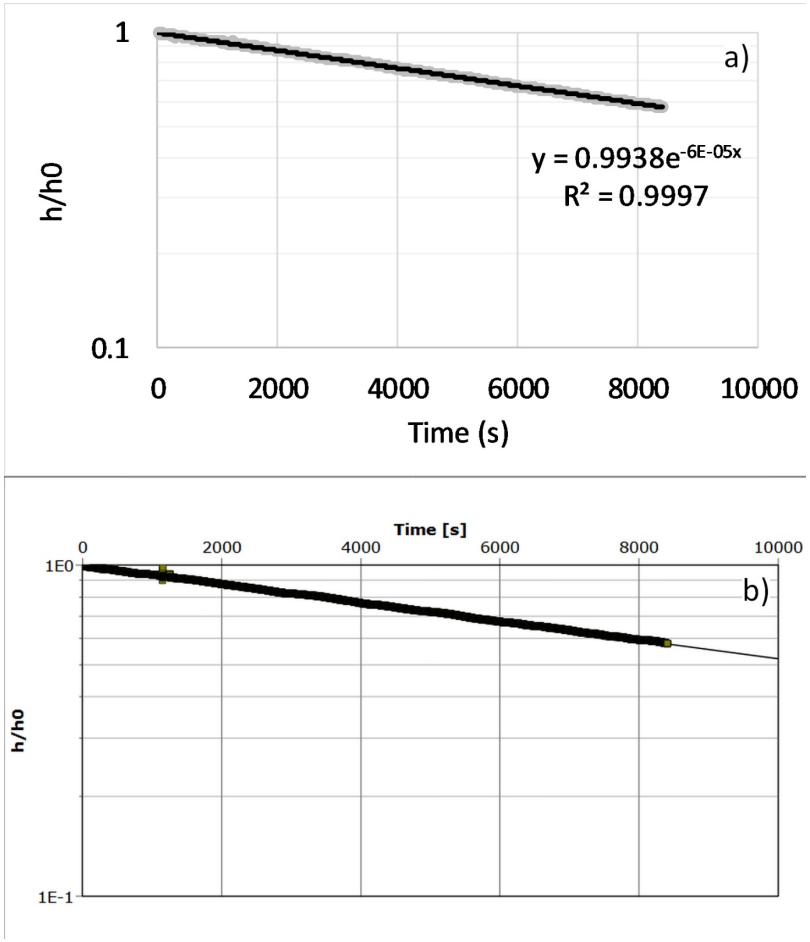


Figure K.20: a) Hvorslev and b) Bouwer and Rice plots for slug test CPP14 / 1.

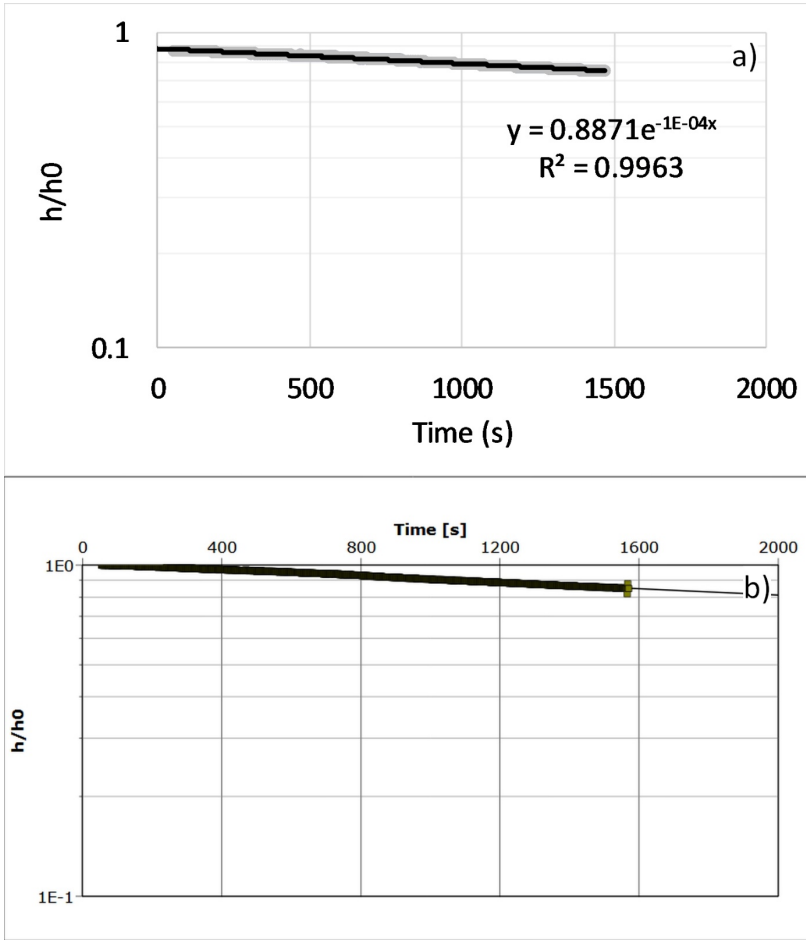


Figure K.21: a) Hvorslev and b) Bouwer and Rice plots for slug test CPP14 / 2.

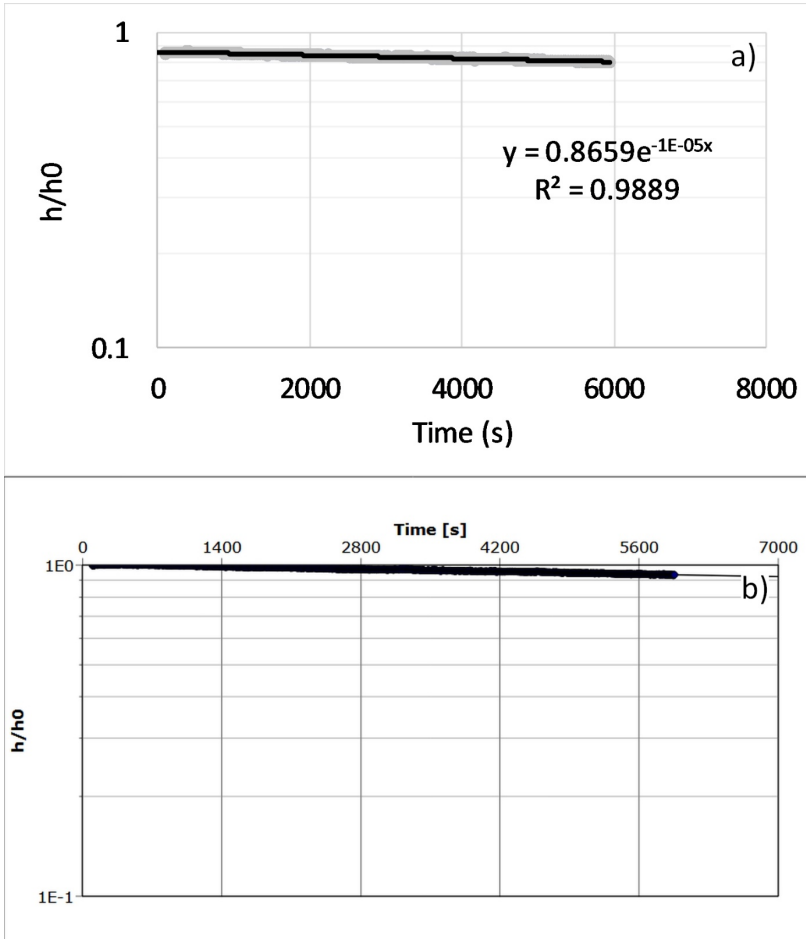


Figure K.22: a) Hvorslev and b) Bouwer and Rice plots for slug test CPP15 / 1.

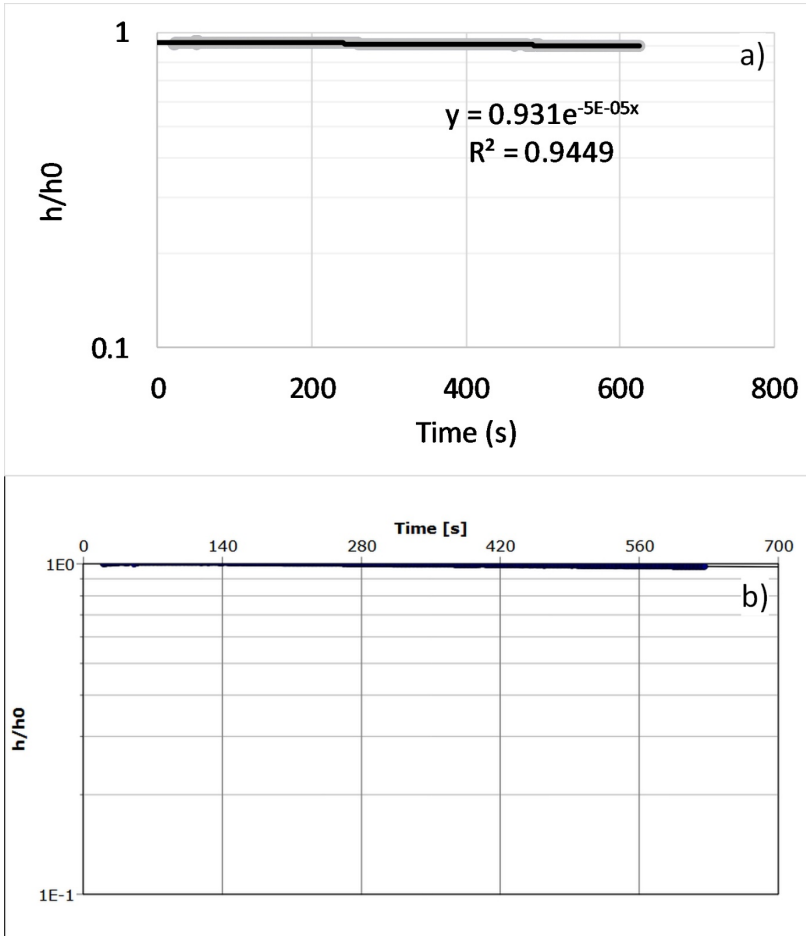


Figure K.23: a) Hvorslev and b) Bouwer and Rice plots for slug test CPP15 / 2.

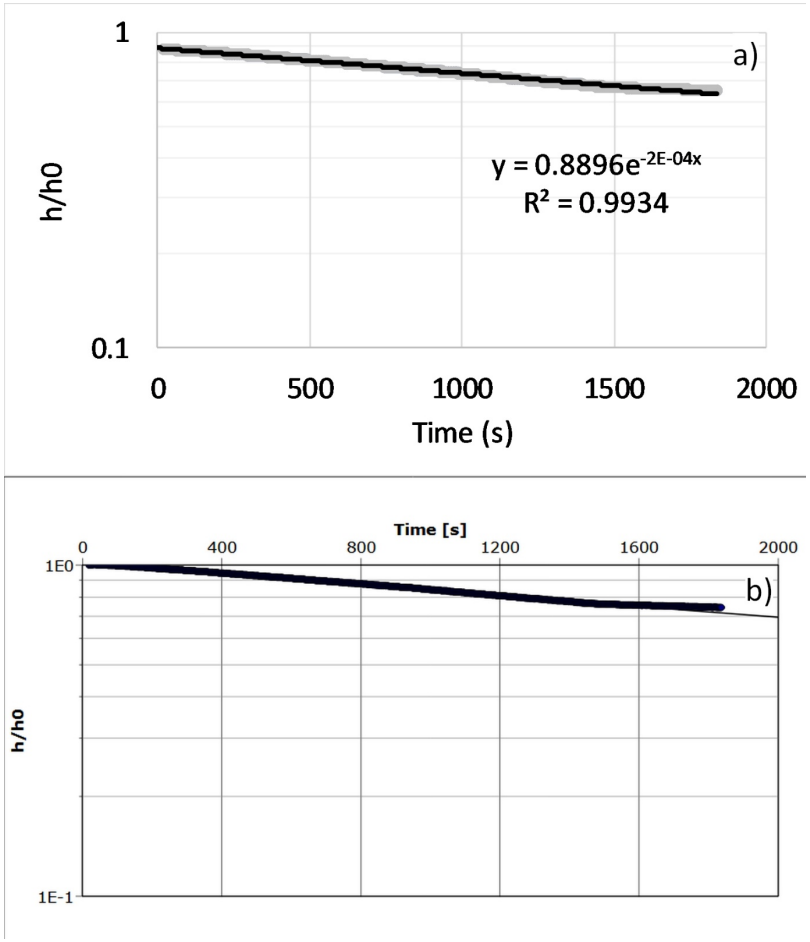


Figure K.24: a) Hvorslev and b) Bouwer and Rice plots for slug test CPP15 / 3.

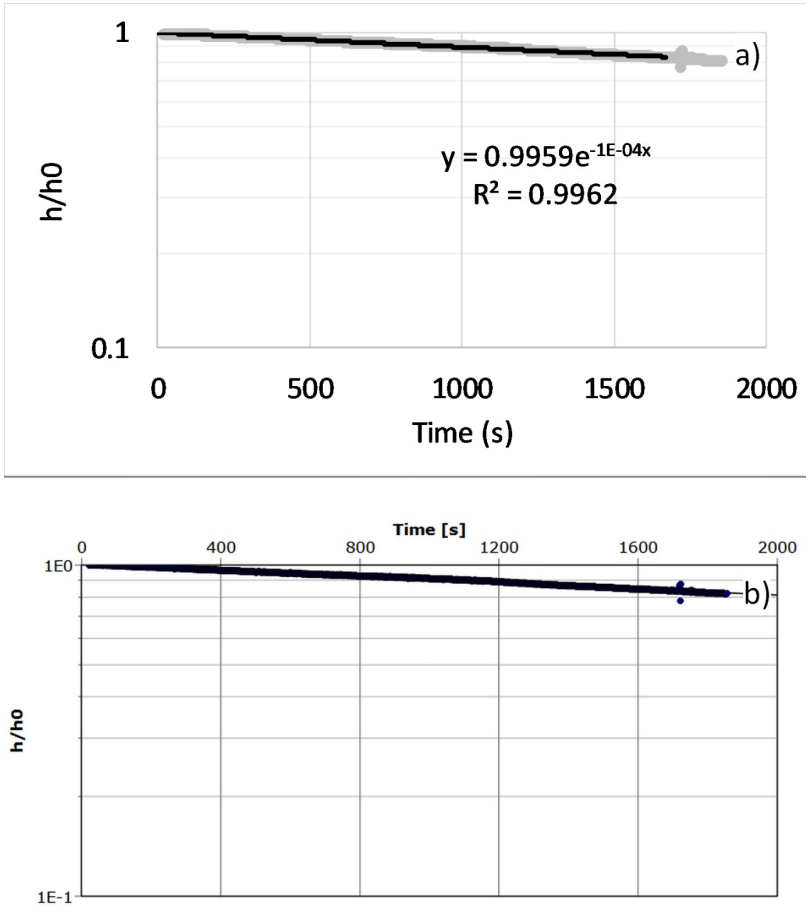


Figure K.25: a) Hvorslev and b) Bouwer and Rice plots for slug test CPP15 / 4.

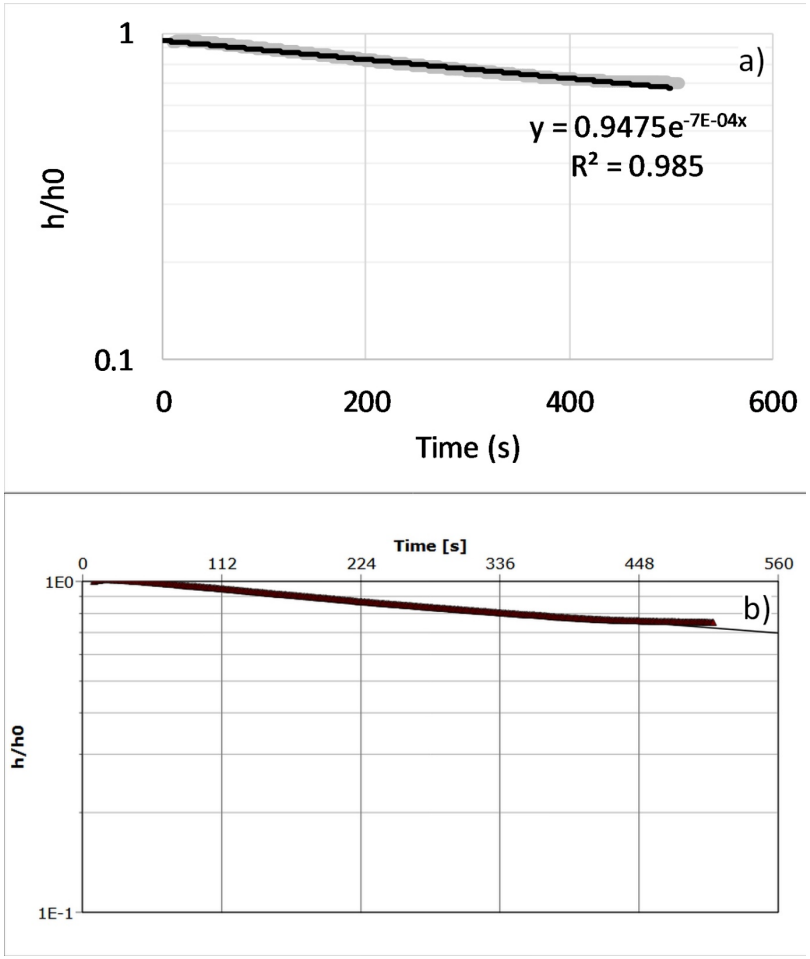


Figure K.26: a) Hvorslev and b) Bouwer and Rice plots for slug test CPP16 / 1.

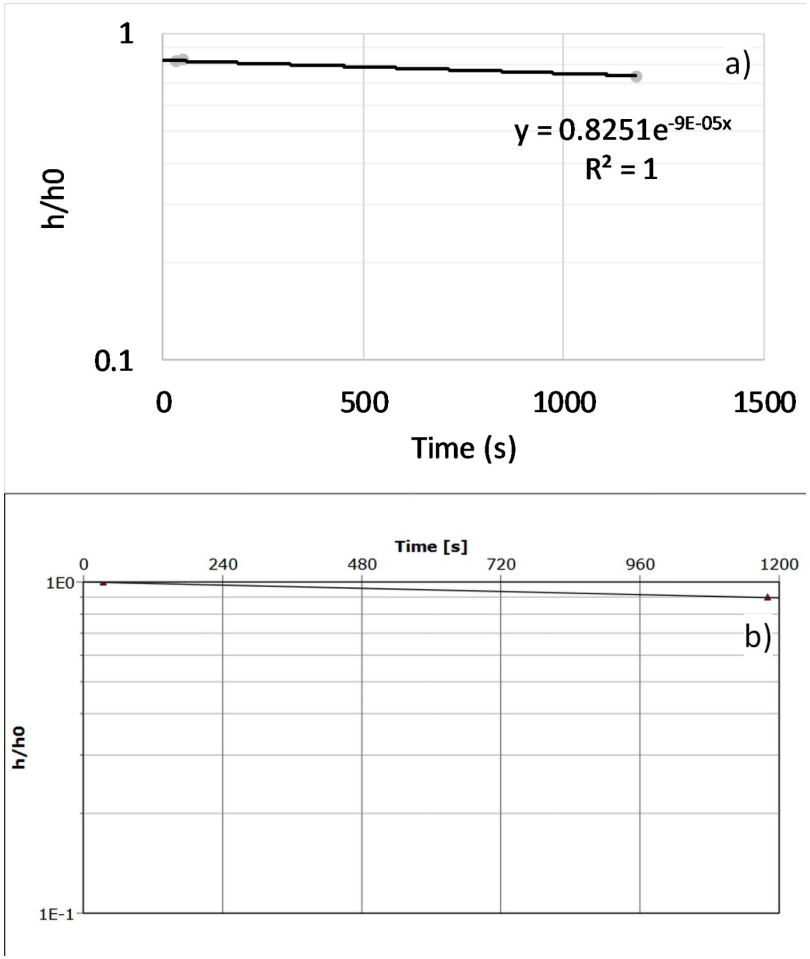


Figure K.27: a) Hvorslev and b) Bouwer and Rice plots for slug test CPP16 / 2.

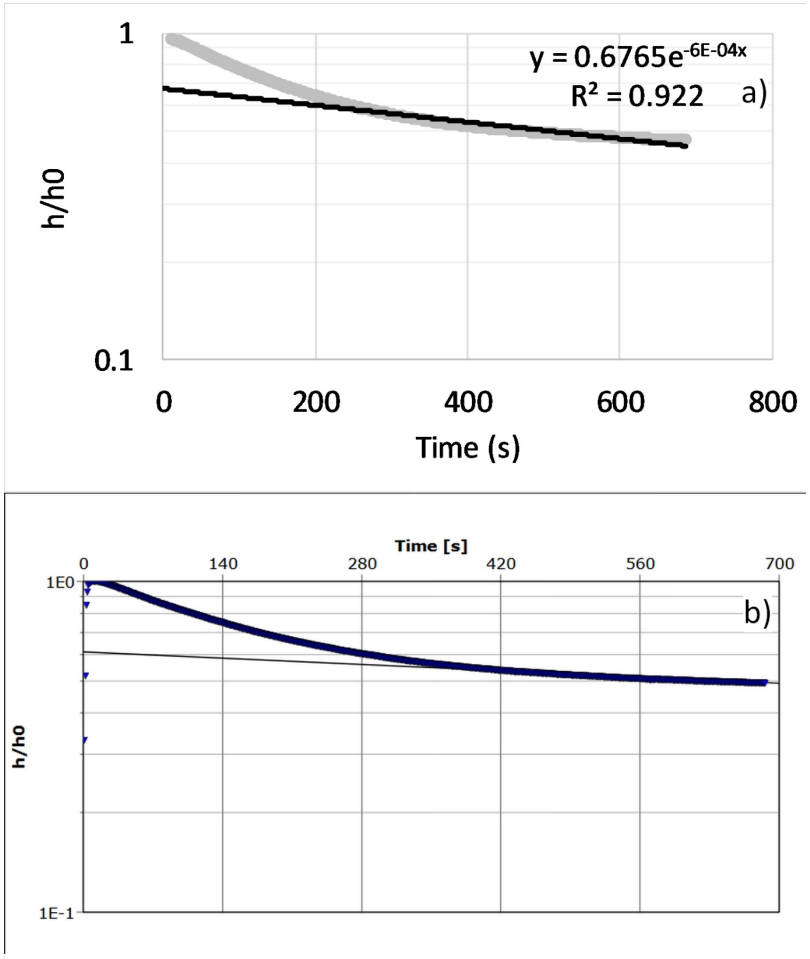


Figure K.28: a) Hvorslev and b) Bouwer and Rice plots for slug test CPP17 / 1.

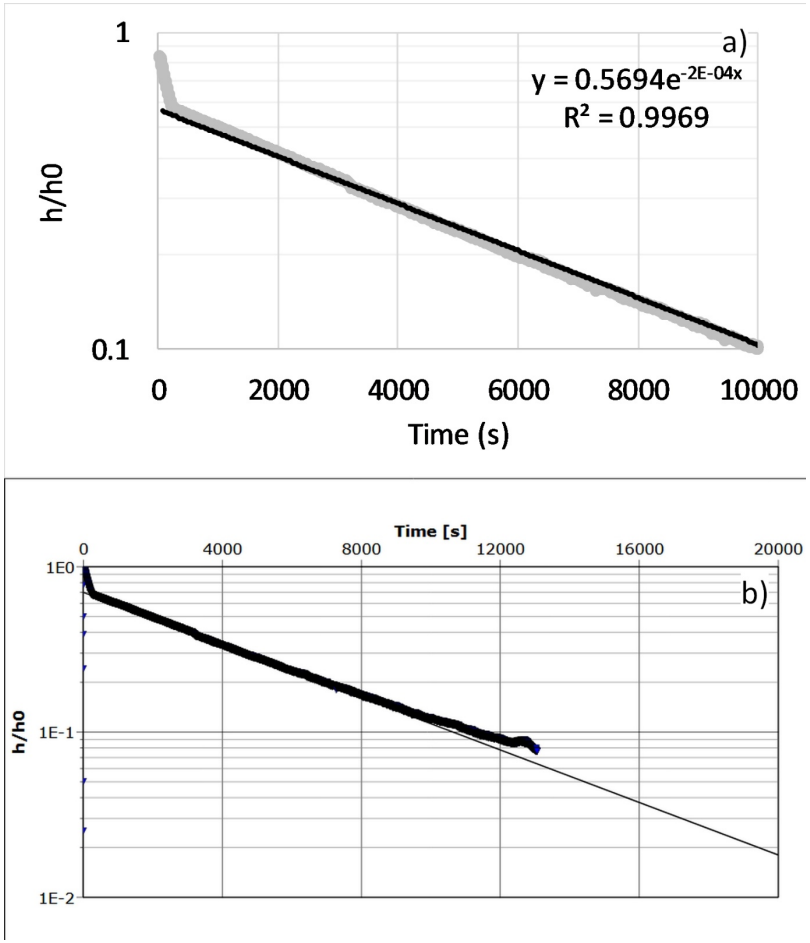


Figure K.29: a) Hvorslev and b) Bouwer and Rice plots for slug test CPP17 / 2.

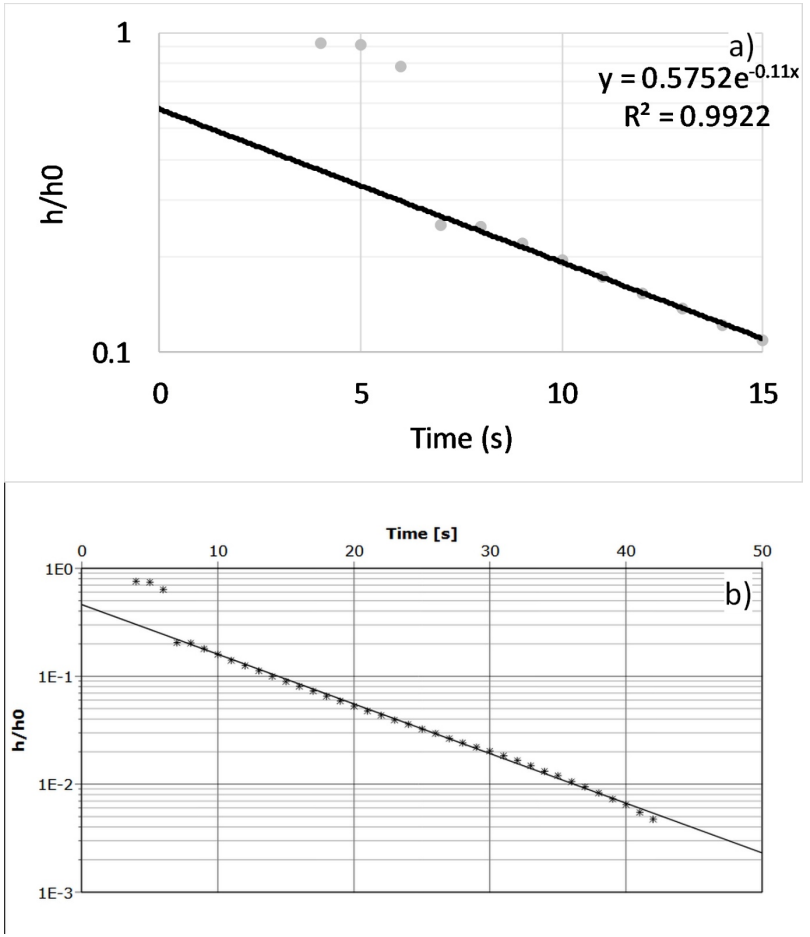


Figure K.30: a) Hvorslev and b) Bouwer and Rice plots for slug test CPP18 / 1.

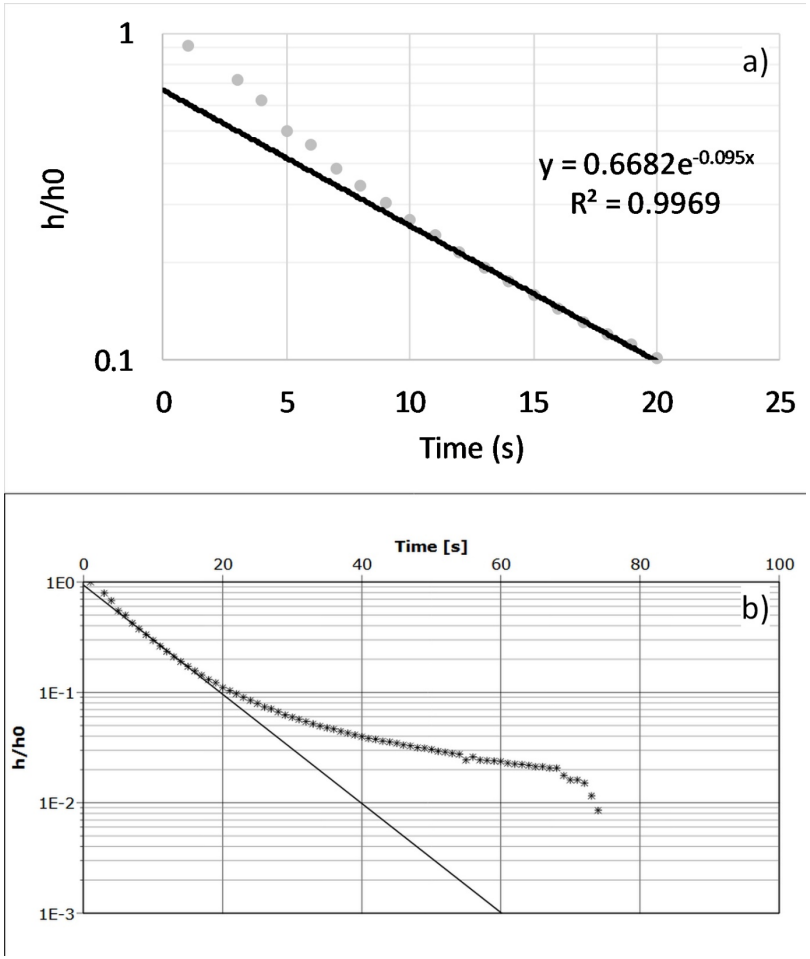


Figure K.31: a) Hvorslev and b) Bouwer and Rice plots for slug test CPP18 / 2.

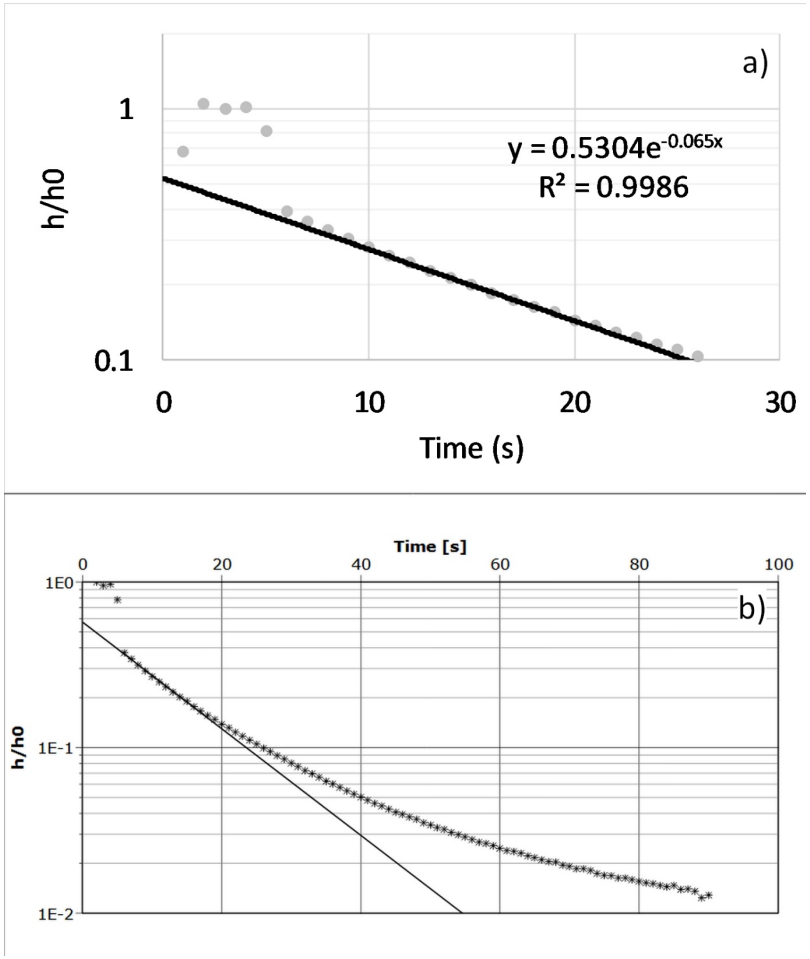


Figure K.32: a) Hvorslev and b) Bouwer and Rice plots for slug test CPP18 / 3.

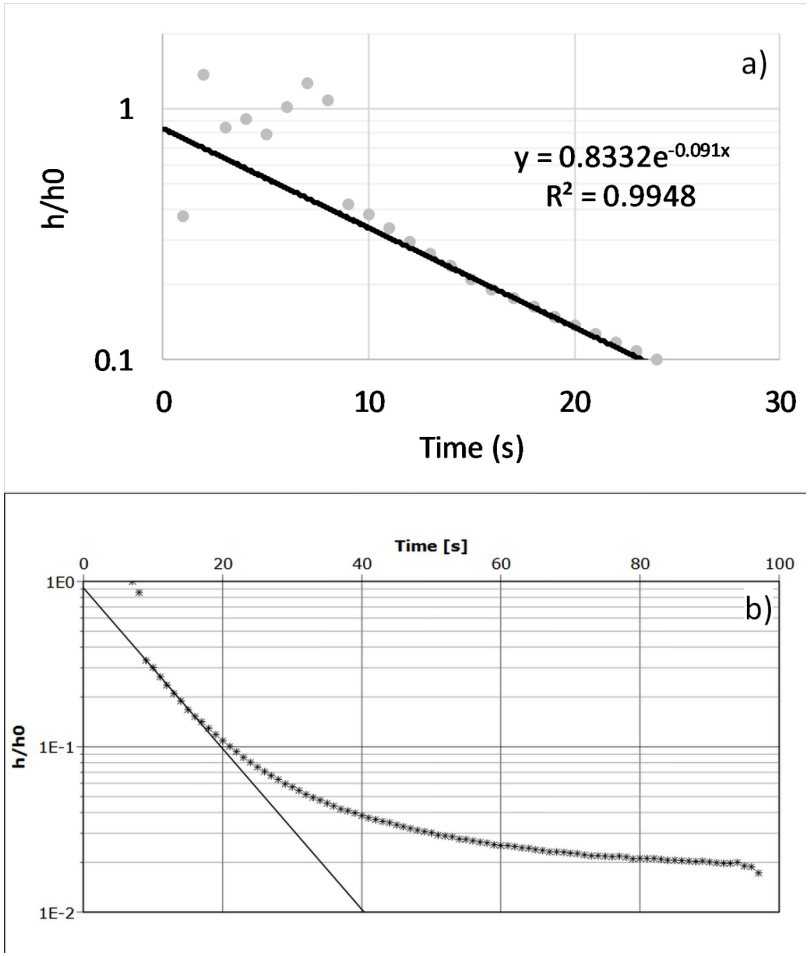


Figure K.33: a) Hvorslev and b) Bouwer and Rice plots for slug test CPP18 / 4.

Table K.3. Constant head tests at CPP18.

| **CPP18 Constant Head Pump-Out Test 1 (CPP18 / 5)** | |
|---|---|
| Type | Rising head |
| Well screen length (cm) | 30 |
| Well diameter (cm) | 2.6 |
| Hc (Difference between static and constant water level; cm) | 8.3 |
| Q (Flow rate; $cm^3/s$) | 6.589786 |
| K (cm/s) | 0.013 |
| K (m/s) | 0.00013 |

| **CPP18 Constant Head Pump-Out Test 2 (CPP18 / 6)** | |
|---|---|
| Type | Rising head |
| Well screen length (cm) | 30 |
| Well diameter (cm) | 2.6 |
| Hc (Difference between static and constant water level; cm) | 4.2 |
| Q (Flow rate; $cm^3/s$) | 3.32585 |
| K (cm/s) | 0.013 |
| K (m/s) | 0.00013 |

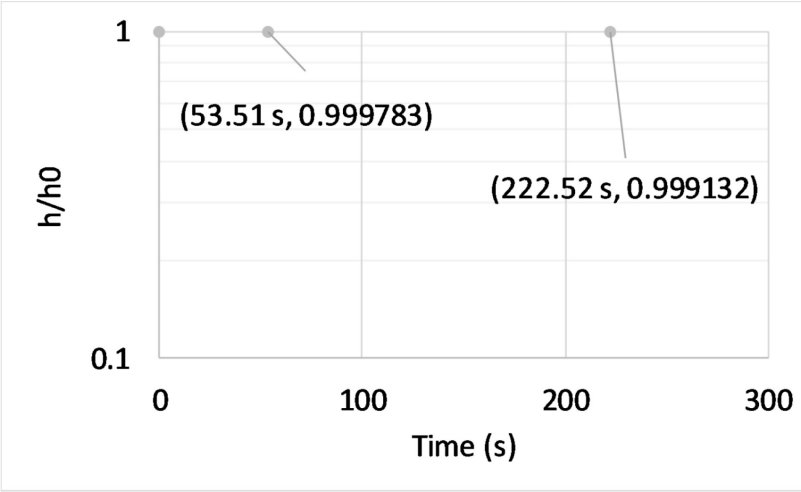


Figure K.34: Hvorslev plot for slug test DP5 / 1.

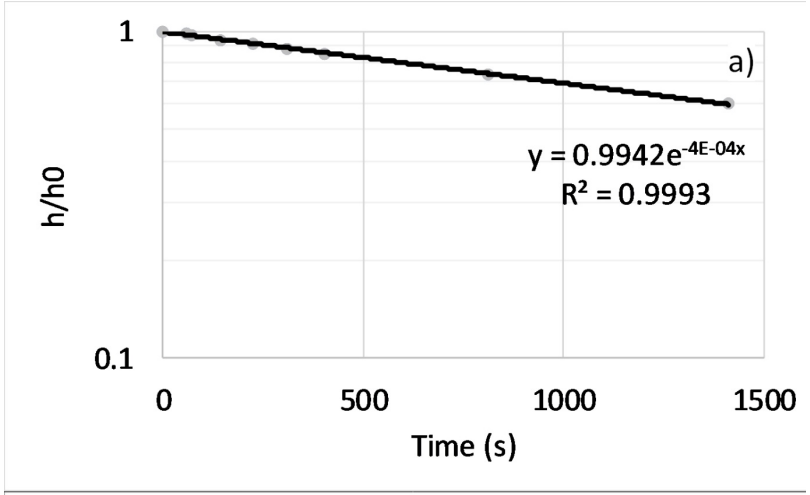


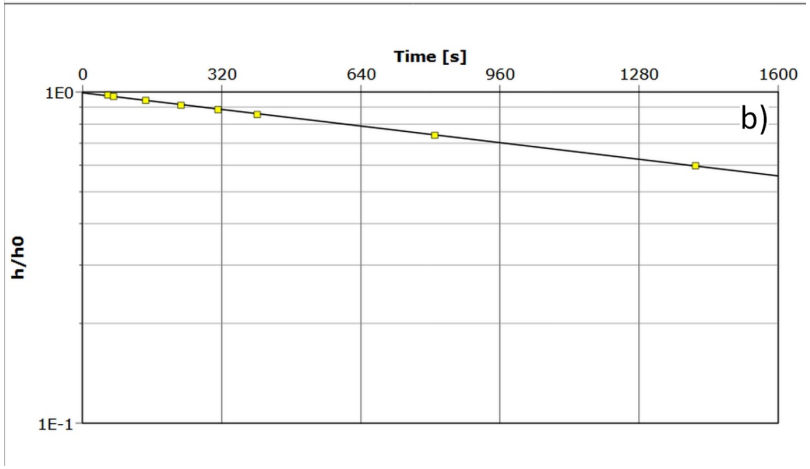


Figure K.35: a) Hvorslev and b) Bouwer and Rice plots for slug test DP5 / 2.

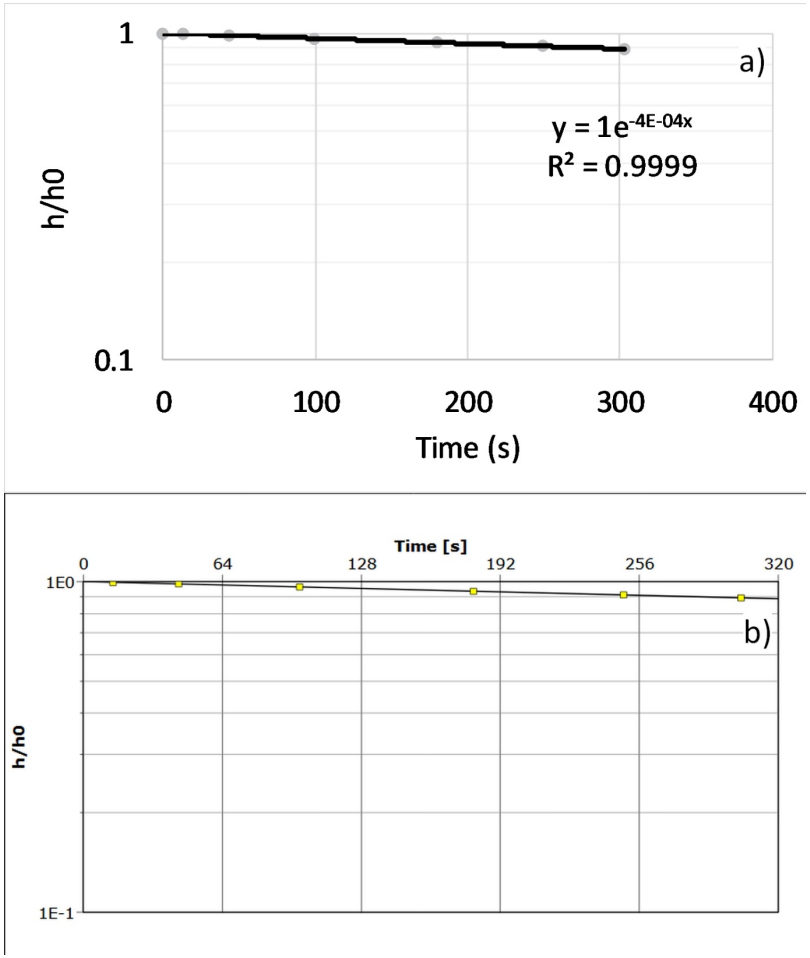


Figure K.36: a) Hvorslev and b) Bouwer and Rice plots for slug test DP / 3.

# Appendix L

## Calculation of theoretical steady state drawdown cone extent

The mathematical description of an ideal unconfined aquifer containing a pumping well with recharge entering the top of its drawdown cone may be developed based on the flow equation presented by Fetter (2001):

$$\frac{S}{T}\frac{\partial H}{\partial t} = \frac{\partial^2 H}{\partial r^2} + \frac{1}{r}\frac{\partial H}{\partial r} + \frac{w}{T}, \quad \text{L.1}$$

where $H$ is hydraulic head, $r$ is the radial distance from the pumping well, $T$ is transmissivity, $w$ is a source (> 0) or sink (< 0) term, $S$ is storativity, and $t$ is time. This corresponds to the basic conservation of mass equation,

$$Volumetric\ flow\ in - Volumetric\ flow\ out = Change\ in\ storage\ over\ time. \quad \text{L.2}$$

For steady state conditions, $\frac{\partial H}{\partial t} = 0$, and the equation becomes:

$$0 = \frac{\partial^2 H}{\partial r^2} + \frac{1}{r}\frac{\partial H}{\partial r} + \frac{w}{T}. \quad \text{L.3}$$

Replacing source/sink term $w$ with steady recharge rate, $q$, and multiplying all terms by $r$:

$$0 = r\frac{\partial^2 H}{\partial r^2} + \frac{\partial H}{\partial r} + \frac{rq}{T}. \quad \text{L.4}$$

Noting that $r\frac{\partial^2 H}{\partial r^2} + \frac{\partial H}{\partial r} = \frac{\partial}{\partial r}\left(r\frac{\partial H}{\partial r}\right)$ via the product rule,

$$0 = \frac{\partial}{\partial r}\left(r\frac{\partial H}{\partial r}\right) + \frac{rq}{T}. \quad \text{L.5}$$

Now, integrate both sides with respect to $\partial r$:

$$0 = \int \frac{\partial}{\partial r}\left(r\frac{\partial H}{\partial r}\right)\partial r + \int \frac{rq}{T}\partial r$$

$$0 = r\frac{\partial H}{\partial r} + \frac{r^2 q}{2T} + C_1, \quad \text{L.6}$$

where $C_1$ is a constant of integration. Multiplying all terms by $\frac{1}{r}$:

$$0 = \frac{\partial H}{\partial r} + \frac{rq}{2T} + \frac{C_1}{r} \quad \text{L.7}$$

Integrating all terms again with respect to $\partial r$, and then rearranging:

$$0 = \int \frac{\partial H}{\partial r}\partial r + \int \frac{rq}{2T}\partial r + \int \frac{C_1}{r}\partial r$$

$$0 = H + \frac{r^2 q}{4T} + C_1 \ln r + C_2$$

$$H = -\frac{r^2 q}{4T} - C_1 \ln r - C_2, \qquad \text{L.8}$$

where $C_2$ is a second constant of integration.

The two boundary conditions for the system are:

1) The hydraulic head at the outer edge of the drawdown cone is zero, and

2) The volumetric flow rate at a distance equal to the well radius is the pumping rate, $Q$.

Mathematically,

$$H(r) = 0 \text{ at } r = R, \qquad \text{L.9a}$$

where R is the radius of the outer edge of the drawdown cone, and

$$Q = [(2\pi rb)\cdot(q_d)]_{r=r_w} = \left[(2\pi rb)\cdot\left(-K\frac{\partial H}{\partial r}\right)\right]_{r=r_w} = \left[-2\pi rT\frac{\partial H}{\partial r}\right]_{r=r_w}, \qquad \text{L.9b}$$

where $b$ is the saturated aquifer thickness, $q_d$ is the Darcy flux, $K$ is the hydraulic conductivity of the aquifer, $T = Kb$, and $r_w$ is the radius of the well. This second boundary condition is the product of the surface area of a cylinder with radius $r_w$ and length $b$, and the Darcy flux across this surface.

Rearranging Equation L.7, multiplying both sides by $(-2\pi rT)$, substituting boundary condition (2) (Equation L.9b), evaluating for $r = r_w$, and solving for $C_1$:

$$\frac{\partial H}{\partial r} = -\frac{rq}{2T} - \frac{C_1}{r}, \qquad \text{L.10}$$

$$\left[(-2\pi rT)\frac{\partial H}{\partial r}\right]_{r=r_w} = \left[\left(-\frac{rq}{2T} - \frac{C_1}{r}\right)(-2\pi rT)\right]_{r=r_w},$$

$$Q = \pi r_w^2 q + 2\pi T C_1,$$

$$C_1 = \frac{Q - \pi r_w^2 q}{2\pi T} \qquad \text{L.11}$$

Applying boundary condition (1) to Equation L.8:

$$0 = -\frac{R^2 q}{4T} - C_1 \ln R - C_2. \qquad \text{L.12}$$

Substituting $C_1$ into Equation L.12 and solving for $C_2$:

$$0 = -\frac{R^2 q}{4T} - \frac{Q - \pi r_w^2 q}{2\pi T} \ln R - C_2, \text{ and}$$

$$C_2 = -\frac{R^2 q}{4T} - \frac{Q - \pi r_w^2 q}{2\pi T} \ln R \qquad \text{L.13}$$

Substituting $C_1$ and $C_2$ into Equation L.8 and rearranging provides the complete expression for the head $H$ at any radius $r$:

$$H = -\frac{r^2 q}{4T} - C_1 \ln r - C_2,$$

$$H = -\frac{r^2 q}{4T} - \frac{Q - \pi r_w^2 q}{2\pi T} \ln r - \left(-\frac{R^2 q}{4T} - \frac{Q - \pi r_w^2 q}{2\pi T} \ln R\right),$$

$$H = \frac{q}{4T}(R^2 - r^2) + \frac{Q - \pi r_w^2 q}{2\pi T} \ln \frac{R}{r} \qquad \text{L.14}$$

Now, starting with Equation L.10, find the radial extent of the drawdown cone at steady state by calculating the radius, $r_d$, at which $\frac{\partial H}{\partial r} = 0$:

$$\frac{\partial H}{\partial r} = -\frac{rq}{2T} - \frac{C_1}{r},$$

$$\left[\frac{\partial H}{\partial r}\right]_{r=r_d} = \left[-\frac{rq}{2T} - \frac{Q - \pi r_w^2 q}{2\pi r T}\right]_{r=r_d},$$

$$0 = -\frac{r_d q}{2T} - \frac{Q - \pi r_w^2 q}{2\pi r_d T}$$

$$(2T)(0) = \left(-\frac{r_d q}{2T} - \frac{Q - \pi r_w^2 q}{2\pi r_d T}\right)(2T)$$

$$0 = -r_d q - \frac{Q - \pi r_w^2 q}{\pi r_d}$$

$$r_d q = -\frac{Q - \pi r_w^2 q}{\pi r_d}$$

$${r_d}^2 = -\frac{Q - \pi r_w^2 q}{\pi q}$$

$$r_d = \sqrt{-\frac{Q - \pi r_w^2 q}{\pi q}} \qquad \text{L.15}$$

Substituting the average pumping rate for the public supply well (K22A) from 1991 to 2000 (CH2MHILL and SSPA, 2003), an average recharge rate for the Alder Creek watershed (M.H. Brouwers, pers. comm., 2017; Matrix and SSPA, 2014a), and an approximate well radius, and solving for the radial extent of the drawdown cone, $r_d$:

$Q = -3010.85\ m^3/d$

$q = 321\ mm/yr\ = 0.0008794\ m/d$

$r_w = 0.1\ m$

$$r_d = \sqrt{-\frac{Q-\pi r_w^2 q}{\pi q}},$$

$$r_d = \sqrt{-\frac{(-3010.85 m^3/d)-\pi(0.1m)^2(0.0008794 m/d)}{\pi \cdot 0.0008794 m/d}},$$

$$r_d = 1043.9\ m\ \approx 1040\ m.$$

Thus, the radial extent of the drawdown cone for an average historical pumping rate and a steady state system is approximately 1040 m.

# Appendix M
# Background information on the HGS modelling

Table M.1 provides details on the properties used during the modelling for Chapter 3. All HydroGeoSphere (HGS) models employed finite difference mode rather than finite element mode (Aquanty, 2019a). The area of the base of the topographic depression in the Wedge2 grid was 154 $m^2$ (actual: 156 $m^2$). The base of the depression and the creek were located at minimum distances of 41.2 m (same as actual) and 26.7 m (same as actual) from the pumping well, respectively.

The soil properties of the streambed were estimated by using a transient 1D column model in HGS (dimensions: 1 m by 1 m by 2.22 m). Average creek and CPP13 water levels were used during the spin-up period (approximately to steady state), and then vented transducer water level time series were used to specify heads during a transient simulation. The creek water level was applied as a transient head boundary condition at the top of the column and CPP13 water levels were applied at the bottom boundary. Hydraulic conductivity values were adjusted by trial and error to match modelled and manual water levels at the three drive-point piezometers installed under the streambed. Results generated unsaturated conditions between the base of the creek and the water table during certain times of the year, as observed in the field, though DP4 water levels were about 30 cm lower than observed (Figures M.1 and M.2). Temperatures could not be used to assist the matching process because of instrument failure.

The spin-up procedure for the Wedge1 model involved two stages in order to obtain a radial water level profile (Appendix L) with the following characteristics: a drawdown cone produced by pumping at the well, a peak in the water table at the outer extent of the drawdown cone, and then a decline in water level to the outer boundary fixed head boundary condition (Figure M.3). Constant recharge was applied to the top of the wedge model domain during each stage of the spin-up. First, no pumping was specified at the inner arc of the domain while a fixed head boundary condition was applied to the outer arc of the domain. Second, the well screen was specified over representative nodes of the inner arc, the pump was turned on with the effective pumping rate (i.e., pumping rate, Q, multiplied by ratio of the angle of the wedge to 360°) at one node at the bottom of the screen, and the outer arc boundary fixed head was again specified. This procedure was applied prior to matching the 2002 pumping test data and also to obtain long-term (60 year) vertical head profiles at nodes 183.6 m from the well for use as boundary conditions for the Wedge2 Model.

Topography in the Wedge2 Model was specified as follows. Elevations were simplified to be 335.9 m asl for all nodes except those near the creek and the base of the topographic depression. The creek channel was trapezoidal with the elevation of the interior streambed nodes at 335.10 m asl. The bank closer to the well (i.e., apex of the wedge) had an elevation of 335.90 m asl, and the bank farther from the well had an elevation of 335.70 m asl. The base of the topographic depression consisted of four boundary nodes with elevations of 335.90 m asl at radii of 41.2 m from the well for one arc and 52.9 m from the well for the other arc. The interior nodes within base of the topographic depression had elevations of 335.75 m asl. The elevations of nodes in between the edges of the creek and the base of the topographic depression varied linearly along a slope from 335.70 m asl at the creek bank to 335.90 at the edge of the base of the topographic depression.

The spin up procedure for the Wedge2 event simulations was slightly different from the procedure for Wedge1 and involved a fixed head boundary condition (H = 328 m) at the inner arc nodes at (x = 1.0 m, y = 0.0 m) and (x = 0.95 m, y = 0.32 m) in the first stage, and then pumping at the (x = 1.0 m, y = 0.0 m) node in the second stage. The vertical head profiles from a 60-year run of a modified version of the Wedge1 Model (where the clay lens and all laterally adjacent elements were split into two layers) were applied at the outer nodes of the wedge for all Wedge2 runs.

Figure M.4 shows matching of additional water level data during the Vadose Zone Model calibration. Early time rapid responses by CPP3, CPP4, and CPP5 were not captured by the simulation. Water levels at CPP3 and CPP4 were very similar to each other in the observed data (despite being installed in different boreholes 0.3 m apart, with bentonite pellets backfilled in the boreholes above the screens) but differed in the simulations. The complexity of the shallow soil layering (e.g., influential lower permeability silt layers necessary in the model to obtain a good match at CPP5) likely contributed to the discrepancy of the observed and simulated water levels. Lateral flows to CPP8 and CPP6 were not well represented by the model. This is not likely an issue due to the predominantly vertical flow beneath ponding in the base of the topographic depression.

Figure M.5 provides background information on the creek water levels and cumulative effective precipitation applied to the Wedge2 Model during simulations. Table M.2 lists the dispersivity values used for the soil layers in the Wedge2 model. Settings used in the HGS models are listed in Table M.3. Settings used in parameter estimation (via PEST; Doherty, 2015) are listed in Table M.4. Regularization was added to each PEST run via the ADDREG1 utility.

Table M.1. Model input parameters for simulations in Chapter 3.

| | | | Boundary Conditions | | | | | | | | |
|---|---|---|---|---|---|---|---|---|---|---|---|
| **Model** | **Sim. Type** | **Initial Head (m)** | **Lateral (m)** | **Outer Arc of Wedge (m)** | **Inner arc of Wedge (L/s)** | **DFR Pond sh (m)** | **Specified head duration (d)** | **Recharge Rate (m/d)** | **DFR Pond Recharge Rate (m/d)** | **Creek water level (m)** | **Total time (d)** |
| Vadose Zone*,† | st.st¶ spin-up | 332.0 | sh; 333.4 | N/A | N/A | N/A | N/A | 9.041E-4 | 1.533E-3 | sh; 335.4 | 3650 |
| | tran | from above | sh; 333.4 | N/A | N/A | 335.8 | 0.27 | obs. rain | obs. rain | sh; 335.4 | 4.0 |
| Wedge1 - pumping test‡ | st.st spin-up | 332.5 | no flow | sh; 329.26 | no flow | N/A | N/A | 0.0008 | N/A | N/A | 3650 |
| | tran | from above | no flow | sh; 329.26 | sf; 42 | N/A | N/A | 0.0008 | N/A | N/A | 39 |
| Wedge1 – spin-up‡ | st.st spin-up | from above | no flow | sh; 329.26 | sf; 42 | N/A | N/A | 0.0008 | N/A | N/A | 21900 |
| Wedge2 – N1§ | tran spin-up | from above | no flow | sh; profile from Wedge1 spin-up v1 | sf; 42 | N/A | N/A | ep | ep | ot†† | 360 |
| | tran | from above | | | | 335.85 | 1.00 | | ep** | | 205 |
| Wedge2 – J1§ | tran spin-up | from above | | | | N/A | N/A | | ep | | 395 |
| | tran | from above | | | | 335.8 | 0.48 | | ep** | | 205 |

* Shaded rows correspond to calibration simulations. † 100 m x 100 m x 23 to 26 m, where the base elevation of the model was 311.76 m asl, and the upper surface approximated ground surface topography. There were 49 layers with 692 nodes and 1302 elements per slice. Number of slices of nodes equals number of layers plus 1. ‡ Wedge1: 18.64° wedge; inner radius = 0.23 m; outer radius = 2400 m; ~24.14 m tall; 38 nodes per slice; 70 layers. § Wedge2: 18.64° wedge; inner radius = 1.0 m; outer radius = 183.6 m; ~24.14 m tall; 320 nodes per slice; 71 layers. ¶ Abbreviations: "st.st" = steady state; "tran" = transient; “from above” = from run described in row of table immediately above; "sh" = specified head; "sf" = specified flux; "ep" = effective precipitation time series; “ot” = observed transient head; “obs. rain” = observed rainfall at weather station WS4 (Wiebe et al., 2019). ** Effective precipitation was not applied to the base of the topographic depression while the specified head boundary condition was applied. †† Creek depth observed at field sensor (30 min interval) was used to calculate water level at the nodes representing the creek.

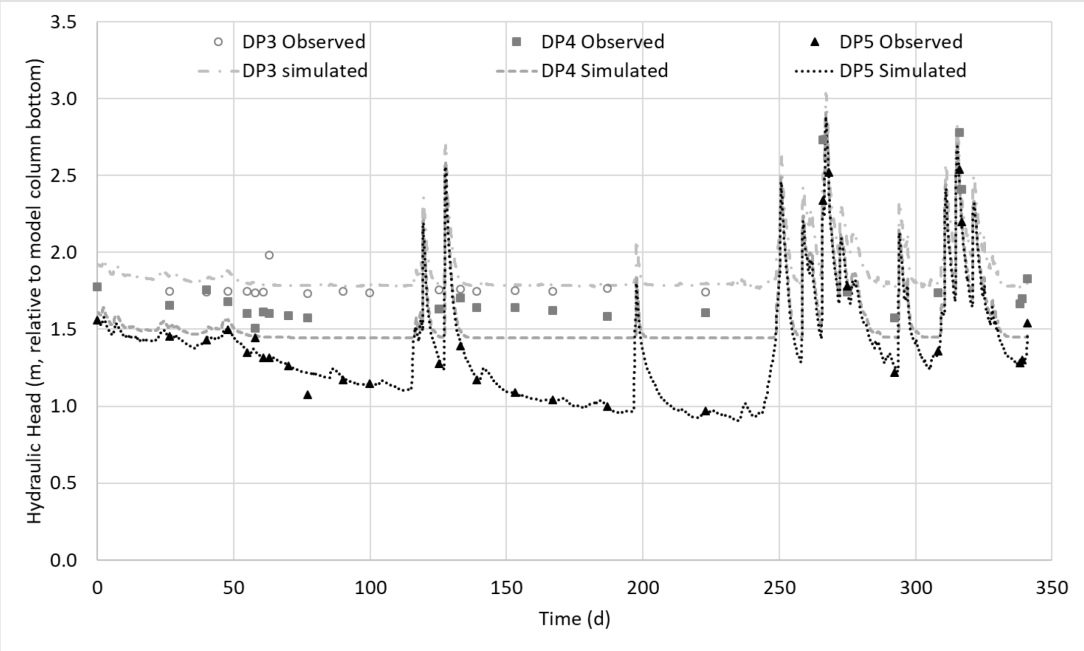


Figure M.1: Observed and simulated hydraulic head values versus time at drivepoints beneath creek for the Streambed Model.

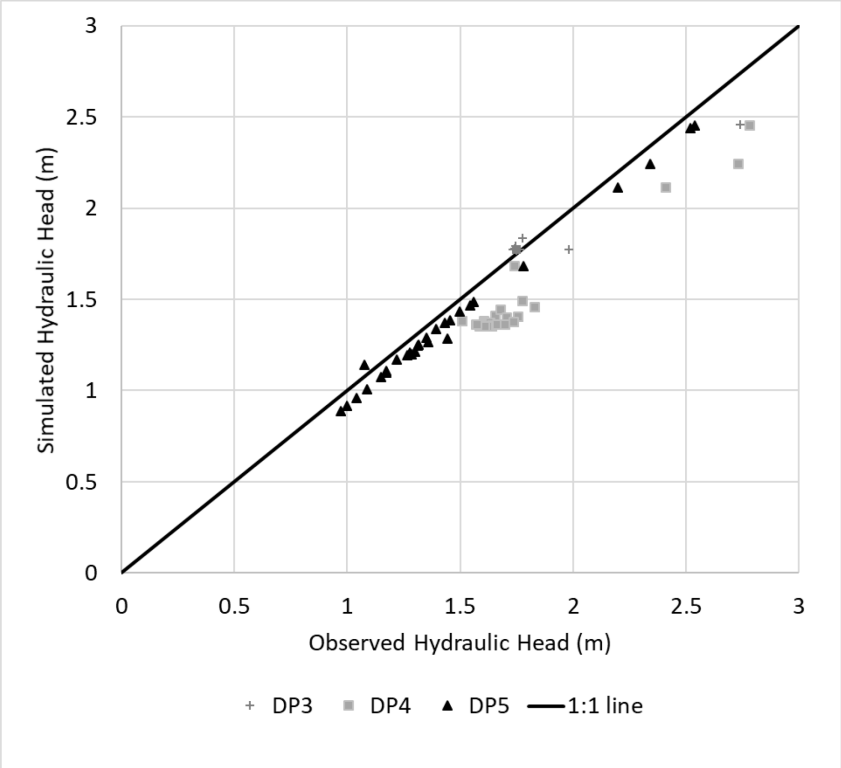


Figure M.2: Comparison of observed and simulated hydraulic head values at drivepoints beneath creek for the Streambed Model.

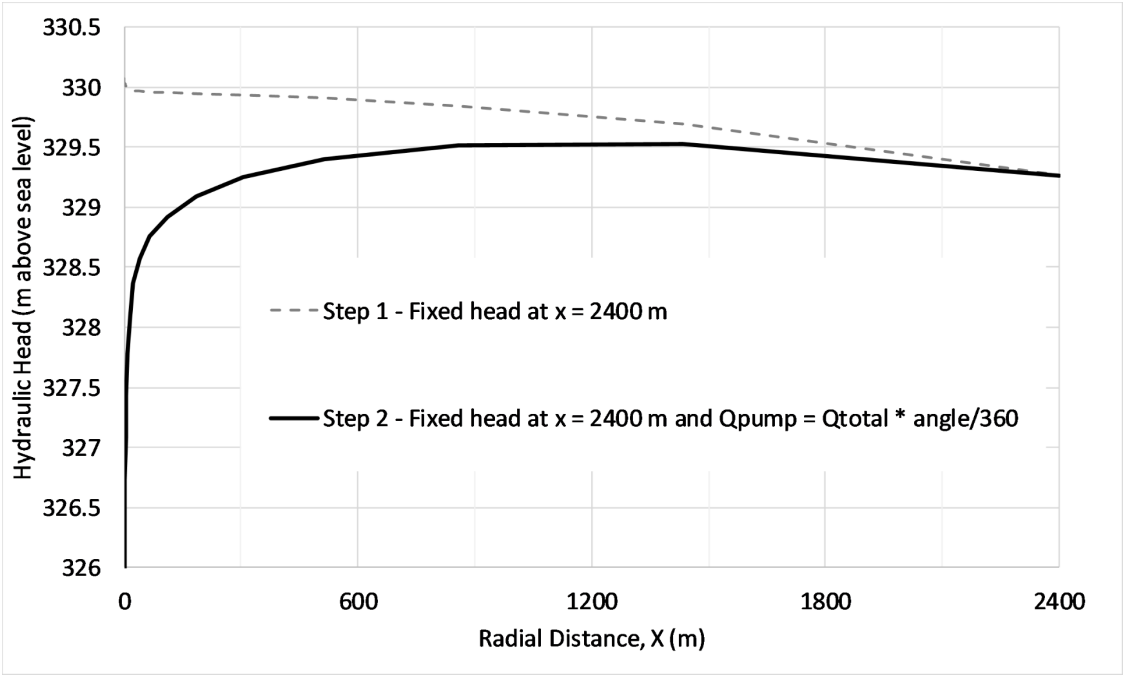


Figure M.3: X-axis profile of water table during spin-up process for Wedge1 model.

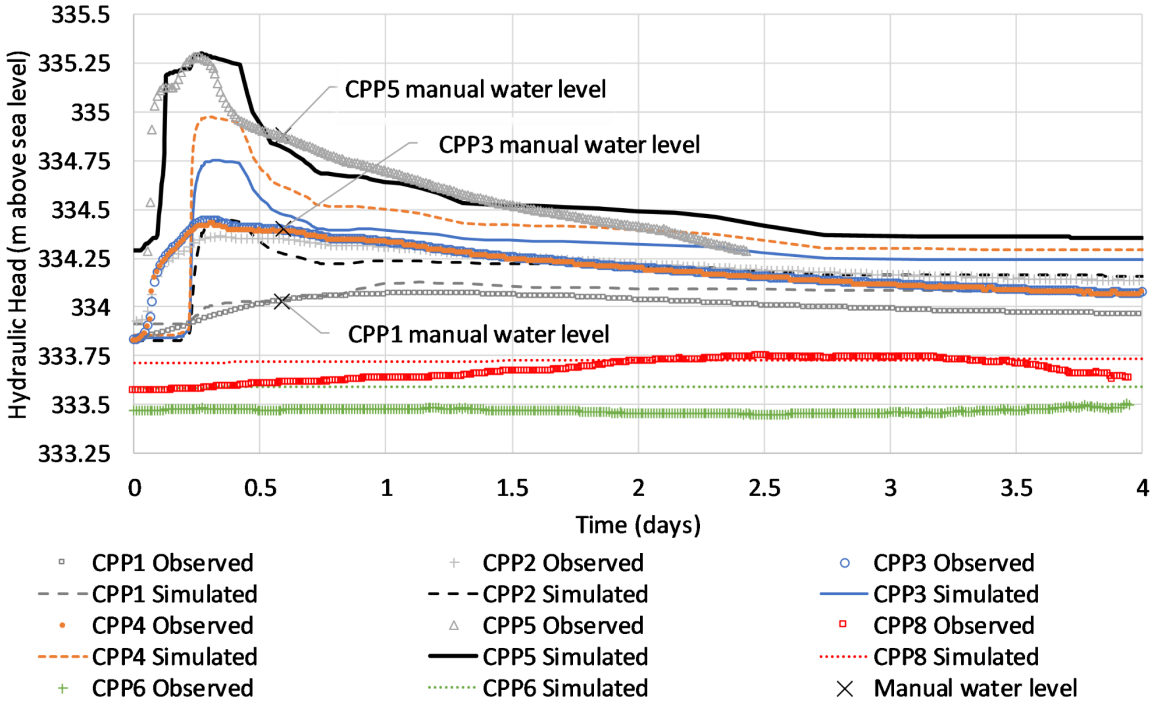


Figure M.4: Matching of observed and simulated (Vadose Zone Model) water levels at all wells, including additional wells not shown in Figure 3.7a. Observed water levels at CPP1, CPP2, and CPP5 between t = 0.0 days and t = 0.3 days were used for calibration via PEST.

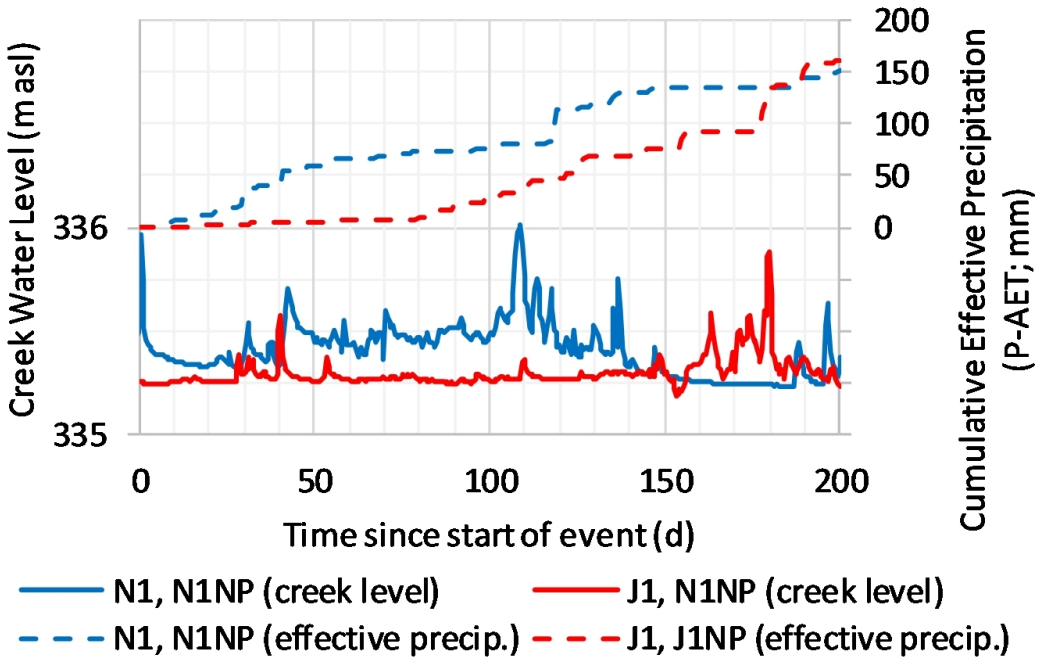


Figure M.5: Creek water levels and cumulative effective precipitation for the Wedge2 simulations.

Table M.2. Dispersivity values

| Soil Unit | Longitudinal dispersivity*, $\alpha_L$ (m) | Transverse dispersivity, $\alpha_T$ (m) | Vertical transverse dispersivity, $\alpha_{VT}$ (m) |
|---|---|---|---|
| Silty Topsoil | 0.15 | 0.015 | 0.0015 |
| Silt1 | 0.15 | 0.015 | 0.0015 |
| Gravelly Sand | 2.0 | 0.20 | 0.020 |
| Silt2 | 0.15 | 0.015 | 0.0015 |
| Silty Sand | 1.0 | 0.10 | 0.010 |
| Sand and Gravel | 5.0 | 0.50 | 0.050 |
| Silt3 | 0.15 | 0.015 | 0.0015 |
| Streambed | 0.15 | 0.015 | 0.0015 |
| Clay Lens | 0.15 | 0.015 | 0.0015 |

* Values for vadose zone layers were based on Rockhold et al. (2016); low permeability saturated zone layers were assigned similar values to lower permeability vadose zone layers

Table M.3. Options employed in the HydroGeoSphere models.

| Model | Option | Value |
|---|---|---|
| All models (Vadose Zone, Streambed, Wedge1, Wedge2) | Units | kilogram-metre-day |
| | transient flow | - |
| | unsaturated | - |
| | remove negative coefficients | - |
| | compute underrelaxation factor | - |
| | finite difference mode | - |
| | dual nodes for surface flow | - |
| | integrated finite difference for overland flow | - |
| | Maximum timestep multiplier | 1.5 |
| | Minimum timestep multiplier | 0.5 |
| | Flow solver convergence criteria | 1.0e-8 |
| | Newton maximum iterations (typical setting) | 15 |
| | Newton target iterations (typical setting) | 12 |
| | Jacobian epsilon | 1.0e-6 |
| | Newton absolute convergence criteria | 1.0e-3 |
| | Newton residual convergence criteria | 1.0e-3 |
| | Newton maximum update for head | 0.25 m |
| | Newton maximum update for depth | 1000 m |
| | Newton head change target | 1.1 m |
| | Saturation change target | 0.1 |
| | Water depth change target | 1000 m |
| Wedge2 | Maximum timestep | 0.03 days |
| | Minimum timestep | 1e-17 days |
| | Transport time weighting | 1.0 |
| | Tortuosity | 1.0 |
| | Control volume | - |
| | Upstream weighting of velocities (x-, y-, and z-direction) | 1.0 |
| | Flow maximum iterations | 2000 |
| | Transport solver convergence criteria | 1.0e-10 |
| | Transport solver maximum iterations | 2000 |
| | Surface domain longitudinal dispersivity | 1.0 m |
| | Surface domain transverse dispersivity | 0.1 m |
| | Surface-subsurface coupling dispersivity | 1.0 m |

Table M.4 Parameter Estimation Options used in PEST

| Model | Option | Value | Option | Value |
|---|---|---|---|---|
| Vadose Zone | **Control data** | | | |
| | RSTFLE | restart | RELPARMAX | 3.0 |
| | PESTMODE | regularization | FACPARMAX | 3.0 |
| | NPAR | 21 | FACORIG | 0.001 |
| | NOBS | 80 | | |
| | NPARGP | 3 | PHIREDSWH | 0.1 |
| | NPRIOR | 15 | | |
| | NOBSGP | 9 | NOPTMAX | 20 |
| | | | PHIREDSTP | 0.005 |
| | NTPLFLE | 3 | NPHISTP | 5 |
| | NINSFLE | 6 | NPHINORED | 4 |
| | PRECIS | Double | RELPARSTP | 0.005 |
| | DPOINT | point | NRELPAR | 4 |
| | NUMCOM | 1 | | |
| | JACFILE | 0 | ICOV | 1 |
| | MESSFILE | 0 | ICOR | 1 |
| | | | IEIG | 1 |
| | RLAMBDA1 | 10 | | |
| | RLAMFAC | -3 | | |
| | PHIRATSUF | 0.3 | | |
| | PHIREDLAM | 0.01 | | |
| | NUMLAM | 10 | | |
| | **singular value decomposition** | | | |
| | SVDMODE | 1 | | |
| | MAXSING | 10 | | |
| | EIGTHRESH | 5E-7 | | |
| | EIGWRITE | 0 | | |
| | **parameter groups** | | | |
| | PARGPNME | k | r | hbc |
| | INCTYP | relative | relative | relative |
| | DERINC | 0.001 | 0.001 | 0.001 |
| | DERINCLB | 0.0 | 0.0 | 0.0 |
| | FORCEN | switch | Switch | switch |
| | DERINCMUL | 2.0 | 2.0 | 2.0 |
| | DERMTHD | parabolic | Parabolic | parabolic |

Table M.4 (Continued)

| Model | Option | Value | Value | Value |
|---|---|---|---|---|
| Vadose Zone | **parameter data*** | | | |
| | PARNME | rdfr | rbkgd | houter |
| | PARTRANS | log | log | log |
| | PARCHGLIM | factor | factor | factor |
| | PARVAL1 | 1.018442826E-04 | 8.269428721E-04 | 333.398221159 |
| | PARLBND | 0.00001 | 0.0007397 | 330 |
| | PARUBND | 0.0032876 | 0.0009041 | 333.4 |
| | PARGP | r | r | hbc |
| | SCALE | 1.0 | 1.0 | 1.0 |
| | OFFSET | 0.0 | 0.0 | 0.0 |
| | DERCOM | 1 | 1 | 1 |
| | | | | |
| | PARNME | topsoilx | topsoily | topsoilz |
| | PARTRANS | log | tied | log |
| | PARCHGLIM | factor | factor | factor |
| | PARVAL1 | 3.073879919009 | 3.073879919009 | 8.4866338458103 |
| | PARLBND | 0.01 | 0.01 | 0.01 |
| | PARUBND | 10 | 10 | 10 |
| | PARGP | k | k | k |
| | SCALE | 1.0 | 1.0 | 1.0 |
| | OFFSET | 0.0 | 0.0 | 0.0 |
| | DERCOM | 1 | 1 | 1 |
| | | | | |
| | PARNME | ksilt1x | ksilt1y | ksilt1z |
| | PARTRANS | log | tied | log |
| | PARCHGLIM | factor | factor | factor |
| | PARVAL1 | 0.06768472699043 | 0.06768472699043 | 4.0E-2 |
| | PARLBND | 0.001 | 0.001 | 0.001 |
| | PARUBND | 1 | 1 | 1 |
| | PARGP | k | k | k |
| | SCALE | 1.0 | 1.0 | 1.0 |
| | OFFSET | 0.0 | 0.0 | 0.0 |
| | DERCOM | 1 | 1 | 1 |

Table M.4 (Continued)

| Model | Option | Value | Value | Value |
|---|---|---|---|---|
| Vadose Zone | PARNME | kgravsandx | kgravsandy | kgravsandz |
| | PARTRANS | log | tied | log |
| | PARCHGLIM | factor | factor | factor |
| | PARVAL1 | 39.54575034217531 | 39.54575034217531 | 12.89004780478210 |
| | PARLBND | 1 | 1 | 1 |
| | PARUBND | 100 | 100 | 70 |
| | PARGP | k | k | k |
| | SCALE | 1.0 | 1.0 | 1.0 |
| | OFFSET | 0.0 | 0.0 | 0.0 |
| | DERCOM | 1 | 1 | 1 |
| | | | | |
| | PARNME | ksilt2x | ksilt2y | ksilt2z |
| | PARTRANS | log | tied | log |
| | PARCHGLIM | factor | factor | factor |
| | PARVAL1 | 0.06611983524067 | 0.06611983524067 | 4.0E-2 |
| | PARLBND | 0.001 | 0.001 | 0.001 |
| | PARUBND | 1 | 1 | 1 |
| | PARGP | k | k | k |
| | SCALE | 1.0 | 1.0 | 1.0 |
| | OFFSET | 0.0 | 0.0 | 0.0 |
| | DERCOM | 1 | 1 | 1 |
| | | | | |
| | PARNME | ksiltsandx | ksiltsandy | ksiltsandz |
| | PARTRANS | log | tied | log |
| | PARCHGLIM | factor | factor | factor |
| | PARVAL1 | 0.33 | 0.33 | 0.12 |
| | PARLBND | 0.01 | 0.01 | 0.01 |
| | PARUBND | 5 | 5 | 5 |
| | PARGP | k | k | k |
| | SCALE | 1.0 | 1.0 | 1.0 |
| | OFFSET | 0.0 | 0.0 | 0.0 |
| | DERCOM | 1 | 1 | 1 |

Table M.4 (Continued)

| Model | Option | Value | Value | Value |
|---|---|---|---|---|
| Vadose Zone | PARNME | ksilt3x | ksilt3y | ksilt3z |
| | PARTRANS | log | tied | log |
| | PARCHGLIM | factor | factor | factor |
| | PARVAL1 | 0.0019 | 0.0019 | 0.001 |
| | PARLBND | 0.0001 | 0.0001 | 0.0001 |
| | PARUBND | 1 | 1 | 1 |
| | PARGP | k | k | k |
| | SCALE | 1.0 | 1.0 | 1.0 |
| | OFFSET | 0.0 | 0.0 | 0.0 |
| | DERCOM | 1 | 1 | 1 |

| Model | Option | Value | Option | Value |
|---|---|---|---|---|
| Wedge1[†] | **Control data** | | | |
| | NPAR | 21 | | |
| | NOBS | 80 | | |
| | NPARGP | 3 | | |
| | NPRIOR | 15 | | |
| | NOBSGP | 9 | NOPTMAX | 30 |
| | | | | |
| | NINSFLE | 6 | | |
| | **singular value decomposition** | | | |
| | MAXSING | 6 | | |
| | **Option** | **Value** | **Value** | **Value** |
| | **parameter data[‡]** | | | |
| | PARNME | ksgx | ksgy | ksgz |
| | PARTRANS | log | tied | log |
| | PARCHGLIM | factor | factor | factor |
| | PARVAL1 | 75 | 75 | 25 |
| | PARLBND | 50 | 50 | 1 |
| | PARUBND | 120 | 120 | 90 |
| | PARGP | k | k | k |
| | SCALE | 1.0 | 1.0 | 1.0 |
| | OFFSET | 0.0 | 0.0 | 0.0 |
| | DERCOM | 1 | 1 | 1 |

Table M.4 (Continued)

| Model | Option | Value | Value | Value |
|---|---|---|---|---|
| Wedge1† | PARNME | khsiltx | khsilty | khsiltz |
| | PARTRANS | log | tied | log |
| | PARCHGLIM | factor | factor | factor |
| | PARVAL1 | 2E-3 | 2E-3 | 3E-3 |
| | PARLBND | 1E-4 | 1E-4 | 1E-4 |
| | PARUBND | 100 | 100 | 100 |
| | PARGP | k | k | k |
| | SCALE | 1.0 | 1.0 | 1.0 |
| | OFFSET | 0.0 | 0.0 | 0.0 |
| | DERCOM | 1 | 1 | 1 |
| | | | | |
| | PARNME | kclayx | kclayy | kclayz |
| | PARTRANS | log | tied | log |
| | PARCHGLIM | factor | factor | factor |
| | PARVAL1 | 1E-3 | 1E-3 | 1E-3 |
| | PARLBND | 1E-4 | 1E-4 | 1E-4 |
| | PARUBND | 9E-3 | 9E-3 | 9E-3 |
| | PARGP | k | k | k |
| | SCALE | 1.0 | 1.0 | 1.0 |
| | OFFSET | 0.0 | 0.0 | 0.0 |
| | DERCOM | 1 | 1 | 1 |
| | | | | |
| | PARNME | houter | rech | |
| | PARTRANS | log | log | |
| | PARCHGLIM | factor | factor | |
| | PARVAL1 | 329.425 | 0.0008219 | |
| | PARLBND | 328.0 | 0.0008 | |
| | PARUBND | 330.0 | 0.00095 | |
| | PARGP | hbc | r | |
| | SCALE | 1.0 | 1.0 | |
| | OFFSET | 0.0 | 0.0 | |
| | DERCOM | 1 | 1 | |

* tied parameters: ktopsoily – ktopsoilx, ksilt1y – ksilt1x, kgravsandy – kgravsandx, ksilt2y –ksilt2x, ksiltsandy – ksiltsandx, and ksilt3y – ksilt3x

† Only parameters that were different from the Vadose Zone Model PEST file information above are listed.

‡ tied parameters: ksgy – ksgx, khsilty – khsiltx, and kclayy – kclayx

# Appendix N
# Rainfall and AET generation

This appendix provides background information on the stochastic generation of annual rainfall and actual evapotranspiration (AET) estimates. Probabilities (relative frequencies) of 1) the observed intervals between rainy days and 2) the observed rainfall amounts were calculated from the 46 years of daily rainfall data (Government of Canada, 2019) from the Roseville Environment Canada weather station. Figure N.1 shows the relative frequency distribution for the number of days with 0 mm rainfall that occurred in between days with rainfall > 0 mm. The mixing fraction and two scale parameters (Eqn. 4.5) for the time intervals between rainy days were $p$ = 0.116, $\beta_1$ = 0.554, and $\beta_2$ = 3.46. Figure N.2 shows the relative frequency distribution for non-zero rainfall amounts themselves. The mixing fraction and two scale parameters for non-zero rainfall amounts were $p$ = 0.503, $\beta_1$ = 2.09, and $\beta_2$ = 13.3. The observed data in these two graphs were fitted using the Levenberg-Marquardt algorithm (Gavin, 2009, 2019) in the scientific computation program GNU Octave (Eaton et al., 2011) to solve for the three parameters of a mixed exponential distribution equation (e.g., Li et al., 2013).

A large number (19,761) of stochastic, 46-year, daily rainfall time series were generated by drawing random variables from the best fit mixed exponential curves for the time intervals and rainfall amounts. The weighted average watershed precipitation was calculated annually based on the areas of the Thiessen polygons for three virtual stations (25.85 km$^2$ for the region corresponding to VS1, 45.61 km$^2$ for the region corresponding to VS2, and 6.597 km$^2$ for the region corresponding to VS3).

Figures N.3 to N.6 provide background information on the generation of AET estimates via AET/P ratios. Figure N.3 shows the locations of 45 US MOPEX (Duan et al., 2006) watersheds with $\overline{PET}/\bar{P}$ ratios within ± 0.05 of the ratio derived based on the Roseville weather station data (Government of Canada, 2019). Six US MOPEX watersheds with $\overline{PET}/\bar{P}$ ratios this range were removed from the analysis because they were considered to have too few years of data (< 40 years), and five additional MOPEX watersheds with ratios within this range were removed from the analysis because their data were not approximately normally distributed about the Budyko curve (leaving 45 watersheds after the removals). Figure N.4 shows the annual scatter of points about the Budyko curve for these 45 watersheds. In order to estimate the standard deviation describing the variation of the annual AET/P

ratios about the Budyko curve from the 45 watersheds, their annual PET/P ratios were binned (width = 0.1) and the standard deviation of the AET/P ratio was calculated for each bin. The maximum standard deviation was chosen. Figure N.5 shows an example of one realization's 46 annual points, which were generated based on: 1) annual PET/P ratios (i.e., $PET_{Roseville,yr}/P_{WS,yr}$, which is the ratio of the PET value calculated for the year to the interpolated total precipitation for the watershed for the year), 2) a mean value of AET/P from the Budyko curve equation (Gentine et al., 2012), 3) the derived maximum standard deviation from the 45 MOPEX watersheds, and 4) a random normal function within GNU Octave (Eaton et al., 2011). Figure N.6 shows all annual points over all realizations. All generated values are shown in Figure N.6, though only those AET estimates leading to recharge rates within the 95% confidence interval were used in the calculations.

Figure N.7 shows the corrected AETvz/P points for the case where there was no variation about the Budyko curve prior to AET correction to remove saturated zone AET. This figure is analogous to Figure 4.5b. Figure N.8 shows the frequency distributions of $AET_{VZ}$ for the cases of $AET_{tot}/P$ scatter and no scatter about the Budyko curve.

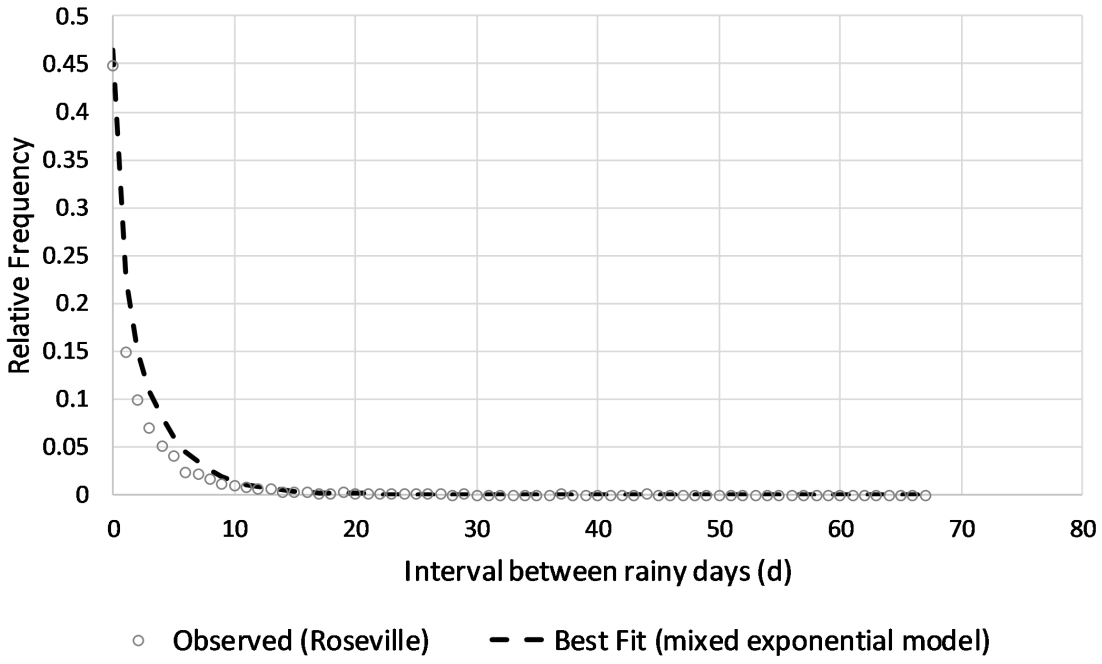


Figure N.1: Observed (Government of Canada, 2019) and fitted (Gavin, 2009, 2019) probability distributions of intervals between rainy days.

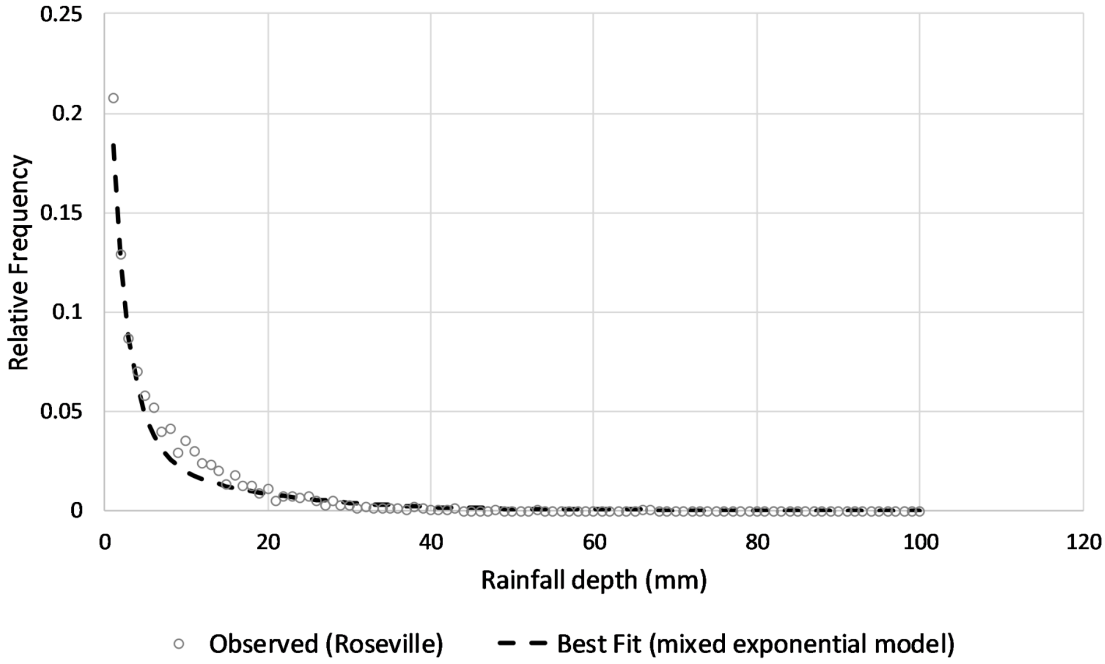


Figure N.2: Observed (Government of Canada, 2019) and fitted (Gavin, 2009, 2019) probability distributions of daily rainfall amounts.

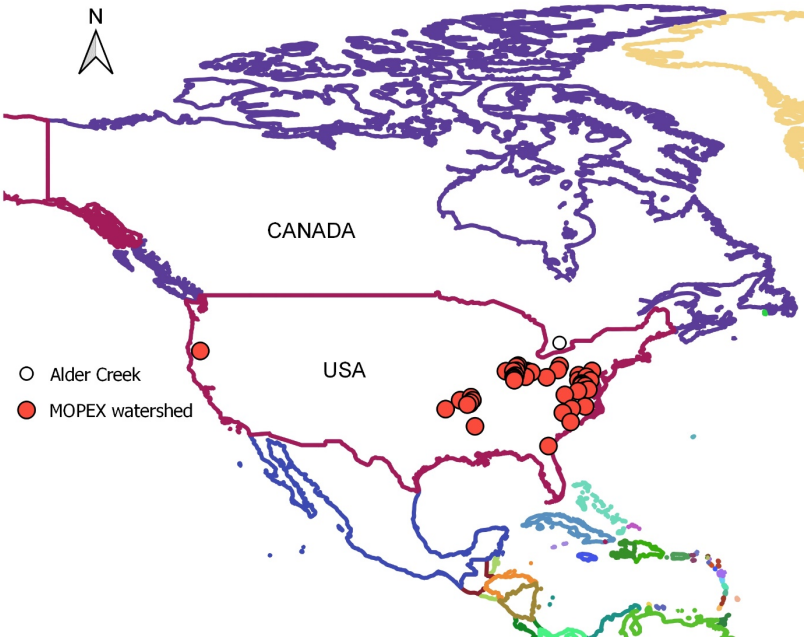


Figure N.3: Locations of the 45 selected US MOPEX (Duan et al., 2006) watersheds with $\overline{PET}/\bar{P}$ ratios within ± 0.05 of the ratio derived for Alder Creek (Sandvik, 2009).

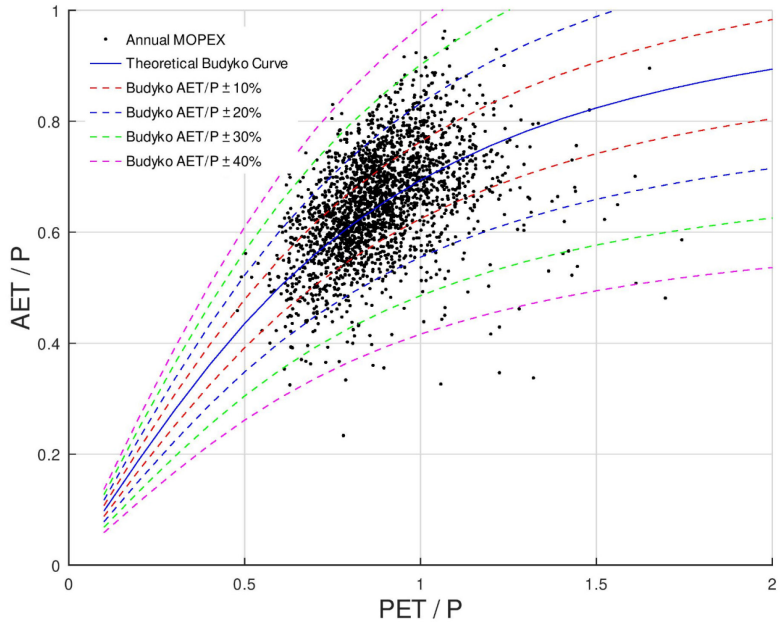


Figure N.4: Observed variation about the Budyko curve for 45 US MOPEX (Duan et al., 2006) watersheds.

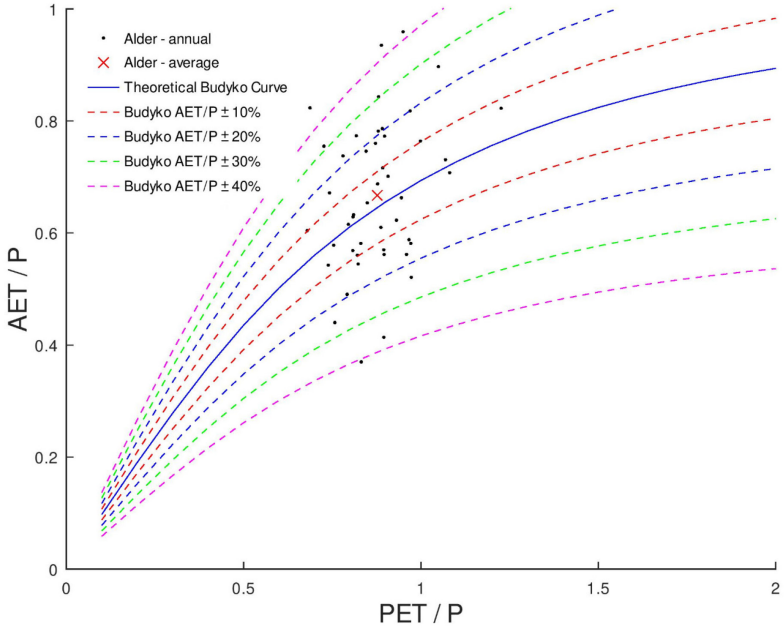


Figure N.5: Variation about the Budyko curve for one realization (46 annual points). Points shown were not corrected for the vadose zone correction factor.

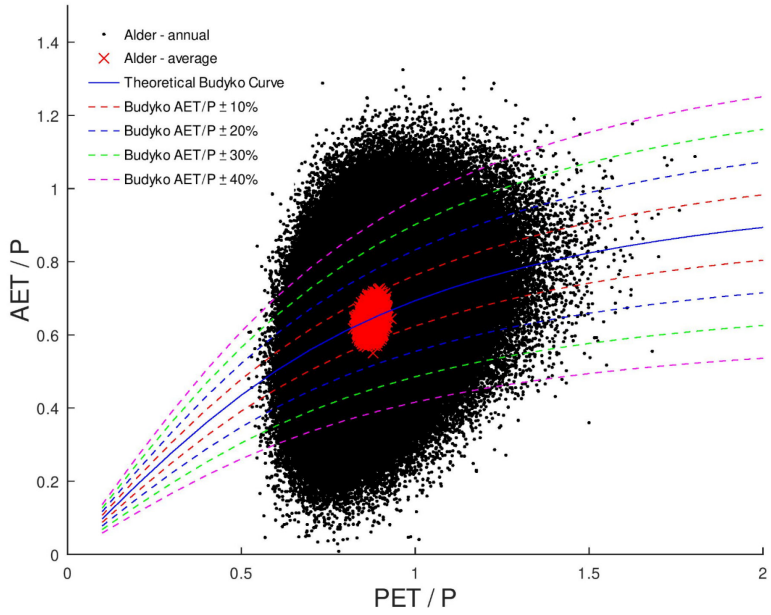


Figure N.6: Variation about the Budyko curve for all 16,778 realizations. Points shown were not corrected for the vadose zone correction factor.

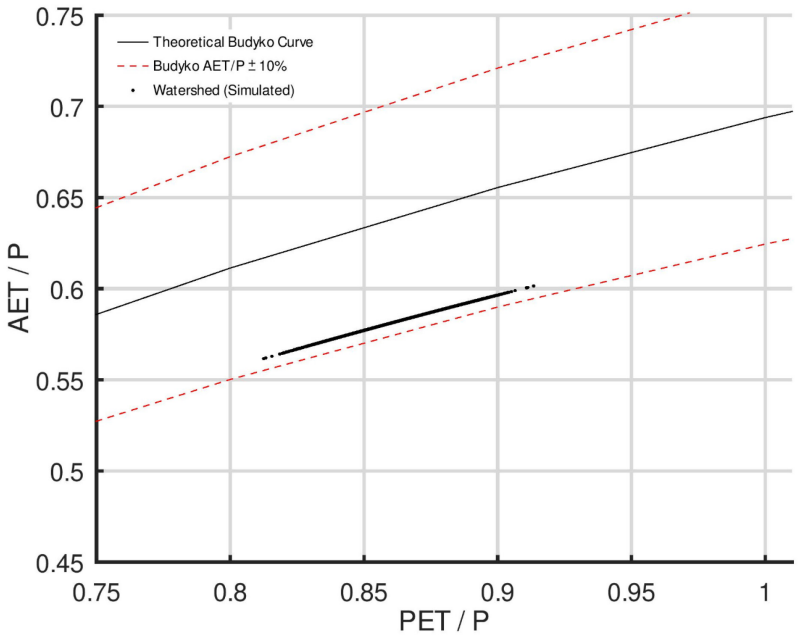


Figure N.7: $\overline{AET_{VZ}}/\overline{P_{WS}}$ ratios for the case of no scatter about the Budyko curve prior to the vadose zone correction. Points shown were corrected for saturated zone AET.

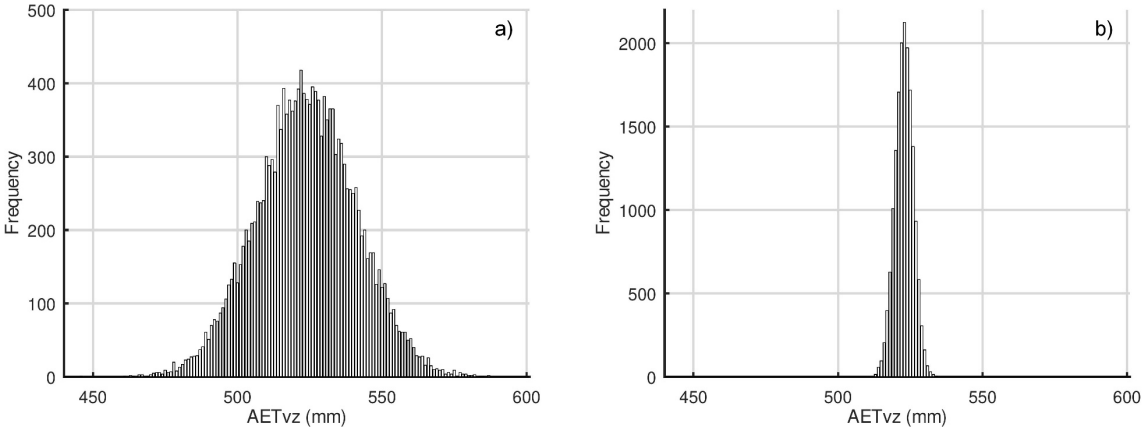


Figure N.8: Frequency distributions of $\overline{AET_{VZ}}$ results for the cases of a) scatter and b) no scatter about the Budyko curve prior to the vadose zone correction. Data shown were corrected for saturated zone AET.

# Appendix O

# Octave code for water budget calculations

This appendix is a file containing GNU Octave (Eaton et al., 2011) scripts used in the water budget calculations in Chapter 4.

The file name of this appendix is "AppendixO-Octave_WB_code_Alder.pdf".

If you accessed this thesis from a source other than the University of Waterloo, you may not have access to this file. You may access it by searching for this thesis on https://uwspace.uwaterloo.ca/.

# Appendix P

# Calculation of the vadose zone AET correction factor

The Budyko curve (Budyko, 1961; Gentine et al., 2012) allows the ratio of $\overline{AET_{Tot}}/\bar{P}$ (long-term average total actual evapotranspiration to long-term average precipitation) to be estimated based on an estimate of the aridity index for a watershed (i.e., the ratio of long-term average potential evapotranspiration to long-term average precipitation, $\overline{PET}/\bar{P}$). However, a vadose zone water budget requires an estimate for the ratio of long-term average vadose zone evapotranspiration to precipitation ($\overline{AET_{VZ}}/\bar{P}$) rather than $\overline{AET_{Tot}}/\bar{P}$. Thus, a correction factor equivalent to the ratio $\overline{AET_{VZ}}/\overline{AET_{Tot}}$ was necessary to correct the $\overline{AET_{Tot}}$ estimate from the Budyko curve. This appendix develops an estimate of the $\overline{AET_{VZ}}/\overline{AET_{Tot}}$ correction factor from analysis from the Alder Creek watershed. Figure P.1 shows areas within the watershed where the water table is expected to be high, i.e., at or near ground surface. These areas (mapped as bog, marsh, open water, and swamp) constitute about 7% of the total watershed area (OMNR, 2008; ROW, 2010).

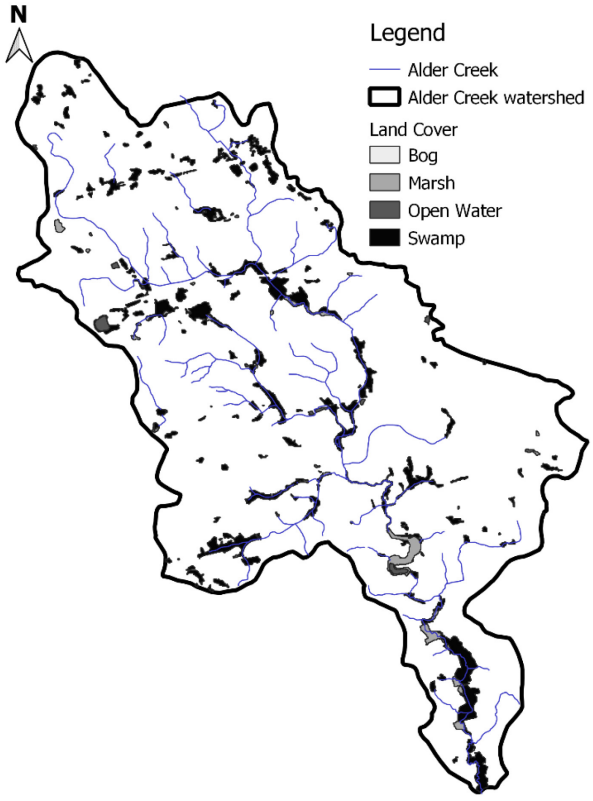


Figure P.1: Land cover areas within the Alder Creek watershed where the water table could be expected to be at or near ground surface (DMTI, 2011; GRCA, 1998; OMNR, 2008; ROW, 2010).

On an average annual basis, where quantities are stated per unit overall watershed area:

$$\overline{AET_{Tot}} = \overline{AET_{VZ}} + \overline{AET_{SZ}}, \quad \text{P.1}$$

where $\overline{AET_{Tot}}$ is the average total AET for the watershed $[m^3 \cdot m^{-2} yr^{-1}]$, $\overline{AET_{VZ}}$ is the contribution of AET from areas where the water table is not expected to be in the immediate vicinity of ground surface $[m^3 \cdot m^{-2} yr^{-1}]$, and $\overline{AET_{SZ}}$ is the contribution of AET from areas where the water table may be expected to be at or near ground surface $[m^3 \cdot m^{-2} yr^{-1}]$. *VZ* denotes "vadose zone" and *SZ* denotes "saturated zone". If the water table is at or very close to the ground surface, it is assumed here that AET occurs directly from the saturated zone. Let $A_1$ be the area corresponding to $\overline{AET_{VZ}}$ (water table not at or near ground surface) and let $A_2$ be the area corresponding to $\overline{AET_{SZ}}$ (where the water table is at or near ground surface; represented by areas mapped as bog, marsh, open water, or swamp). Let $A$ be the overall watershed area. Based on land cover mapping (OMNR, 2008; ROW, 2010):

$$A_1 = 0.93A \quad \text{P.2a}$$

$$A_2 = 0.07A \quad \text{P.2b}$$

Then:

$$\overline{AET_{VZ}} = \frac{\overline{V_{AETvz}}}{A} = \frac{\overline{h_{AETvz}} \times A_1}{A} = \frac{\overline{h_{AETvz}} \times 0.93A}{A} = (0.93)\overline{h_{AETvz}}, \text{ and} \quad \text{P.3a}$$

$$\overline{AET_{SZ}} = \frac{\overline{V_{AETsz}}}{A} = \frac{\overline{h_{AETsz}} \times A_2}{A} = \frac{\overline{h_{AETsz}} \times 0.07A}{A} = (0.07)\overline{h_{AETsz}}, \quad \text{P.3b}$$

where $\overline{V_{AETx}}$ is the volume of AET from component $x$ (*VZ* or *SZ*), and $\overline{h_{AETx}}$ is the rate in $mm \cdot yr^{-1}$ for component $x$ within the respective area ($A_1$ or $A_2$). Assuming that the AET rate in the area with a high water table ($A_2$) is not limited by water availability,

$$h_{AETsz} = \overline{PET}, \quad \text{P.4}$$

where $\overline{PET}$ is the average long-term potential evapotranspiration. $\overline{PET}$ was estimated to be 775 $mm \cdot yr^{-1}$ (Appendix A) based on Roseville temperature data (Government of Canada, 2019) and local wind speed data from the watershed (Wiebe et al., 2019) using the ETo Calculator program (Raes, 2009).

The ratio for which an estimate is desired is the $\overline{AET_{VZ}}/\overline{AET_{Tot}}$ correction factor. Dividing all terms of Equation P.1 by $\overline{AET_{Tot}}$ and re-arranging, the following is obtained:

$$\frac{\overline{AET_{Tot}}}{\overline{AET_{Tot}}} = \frac{\overline{AET_{VZ}}}{\overline{AET_{Tot}}} + \frac{\overline{AET_{SZ}}}{\overline{AET_{Tot}}},$$

$$\frac{\overline{AET_{VZ}}}{\overline{AET_{Tot}}} = 1 - \frac{\overline{AET_{SZ}}}{\overline{AET_{Tot}}}, \qquad \text{P.5}$$

The correction factor can now be estimated using an estimate of $\overline{AET_{Tot}}$ derived from the Budyko curve, the $\overline{PET}$ estimate noted above, and the long-term average annual precipitation at the Roseville weather station (907 mm; AquaResource, 2008; Government of Canada, 2019; OMNR, 2007):

$$\frac{\overline{AET_{VZ}}}{\overline{AET_{Tot}}} = 1 - \frac{\overline{AET_{SZ}}}{\overline{AET_{Tot}}}$$

$$\frac{\overline{AET_{VZ}}}{\overline{AET_{Tot}}} = 1 - \frac{0.07\overline{h_{AETsz}}}{\overline{AET_{Tot}}}$$

$$\frac{\overline{AET_{VZ}}}{\overline{AET_{Tot}}} = 1 - \frac{0.07 \times 775mm \cdot yr^{-1}}{577mm \cdot yr^{-1}}$$

$$\frac{\overline{AET_{VZ}}}{\overline{AET_{Tot}}} = 0.91$$

If reasonable relative uncertainty values are assigned to the $A_2$, $\overline{h_{AETsz}}$, and $\overline{AET_{Tot}}$ variables, the uncertainty of this $\overline{AET_{VZ}}/\overline{AET_{Tot}}$ ratio can be estimated. If the relative uncertainty of $A_2$ is ±20%, and the uncertainty of $\overline{h_{AETsz}}$ and $\overline{AET_{Tot}}$ are each ±10%, then:

$$\text{Let } x = \frac{0.07\overline{h_{AETsz}}}{\overline{AET_{Tot}}} = \frac{0.07 \times 775mm \cdot yr^{-1}}{577mm \cdot yr^{-1}} = 0.09$$

$$\delta x_{rel} = \pm\sqrt{\left(\delta A_{2_{rel}}\right)^2 + \left(\delta\overline{h_{AETsz}}_{rel}\right)^2 + \left(\delta\overline{AET_{Tot}}_{rel}\right)^2}$$

$$\delta x_{rel} = \pm\sqrt{0.2^2 + 0.1^2 + 0.1^2} = \pm 0.24$$

$$\delta\left(\frac{\overline{AET_{VZ}}}{\overline{AET_{Tot}}}\right)_{abs} = \delta x_{abs} = \pm(\delta x_{rel})(x) = \pm(0.24)(0.09) = \pm 0.02$$

$$\therefore \frac{\overline{AET_{VZ}}}{\overline{AET_{Tot}}} = 0.91 \pm 0.02$$

In the above, $\delta x_{rel}$ is the relative uncertainty for $x$, and $\delta x_{abs}$ is the absolute uncertainty for $x$. These calculations were based on common uncertainty equations (e.g., Taylor, 1997). The uncertainty of the assumption inherent in Equation P.4 (i.e., the degree to which $\overline{PET}$ is representative for regions with a high water table) is not specifically quantified here.

# Appendix Q

# Estimation of total streamflow for the Alder Creek watershed

An estimate for the total streamflow for the Alder Creek watershed may be derived from three water budget equations. The first is a vadose zone water budget, illustrated in Figure Q.1.

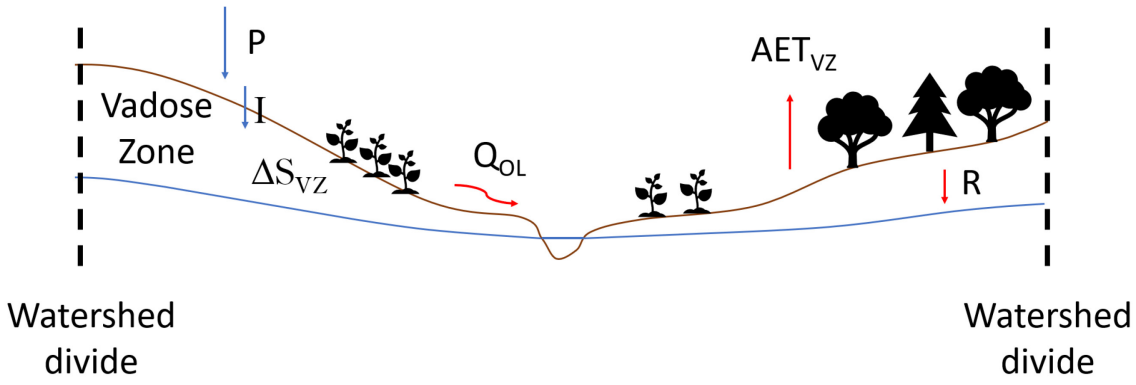


Figure Q.1: Components related to a vadose zone water budget.

Based on the general mass balance equation,

$$Change\ in\ storage\ over\ time = Volumetric\ flow\ in - Volumetric\ flow\ out \qquad \text{Q.1}$$

the vadose zone water budget may be described by (Eqn. Q.2):

$$\overline{\Delta S_{VZ}} = \bar{I} - \overline{AET_{VZ}} - \bar{R}, \qquad \text{Q.2}$$

where $\overline{\Delta S_{VZ}}$ is the change in storage of water in the vadose zone, $\bar{I}$ is infiltration, $\overline{AET_{VZ}}$ is actual evapotranspiration originating from the vadose zone, and $\bar{R}$ is recharge. Infiltration is the difference between precipitation ($\bar{P}$) and overland runoff ($\overline{Q_{OL}}$, which is the surface water fraction of streamflow):

$$\bar{I} = \bar{P} - \overline{Q_{OL}} \qquad \text{Q.3}$$

All components are stated in mm per year, and the overbars indicate long-term average values. Total streamflow for the watershed is equal to the sum of overland flow and groundwater baseflow, i.e.,

$$\overline{Q_{Tot}} = \overline{Q_{OL}} + \overline{Q_{BF}} \quad \text{Q.4}$$

This is the second water budget equation. Baseflow may be described by the baseflow index (BFI), or fraction of total streamflow that is composed of groundwater discharge:

$$\overline{BFI} = \overline{Q_{BF}}/\overline{Q_{Tot}}, \quad \text{Q.5}$$

Therefore,

$$\overline{Q_{OL}} = (1 - \overline{BFI})\overline{Q_{Tot}} \quad \text{Q.6}$$

Assuming that the storage change in the vadose zone is 0 mm over the long-term, inserting $\bar{I} = \bar{P} - \overline{Q_{OL}}$, and rearranging Eqn. Q.2:

$$(1 - \overline{BFI})\overline{Q_{Tot}} = \bar{P} - \overline{AET_{VZ}} - \bar{R} \quad \text{Q.7}$$

The third water budget equation is a budget for the saturated zone, illustrated by Figure Q.2.

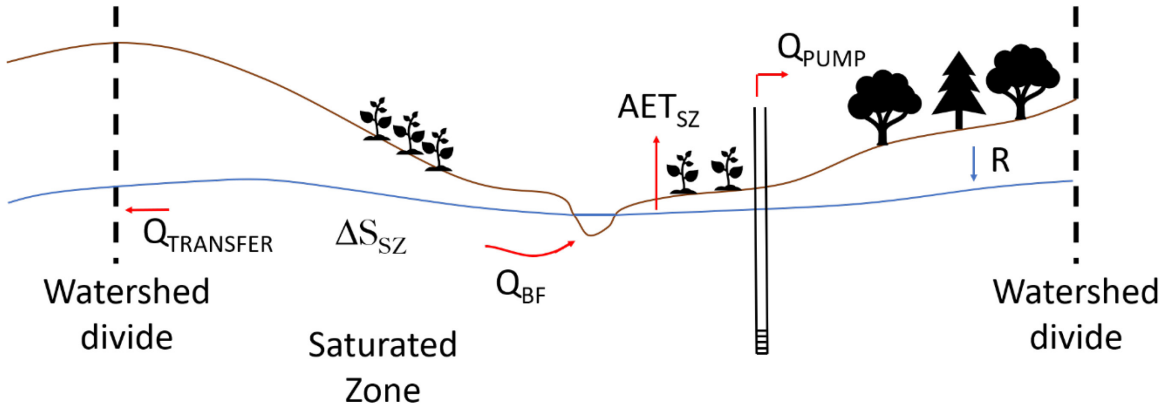


Figure Q.2: Components of a saturated zone water budget.

A mass balance equation leads to the following:

$$\overline{\Delta S_{SZ}} = \bar{R} - \overline{Q_{BF}} - \overline{Q_{PUMP}} - \overline{AET_{SZ}} - \overline{Q_{TRANSFER}}, \quad \text{Q.8}$$

where $\overline{\Delta S_{SZ}}$ is storage chanage, $\bar{R}$ is recharge, $\overline{Q_{BF}}$ is the baseflow component of total watershed streamflow, $\overline{AET_{SZ}}$ is actual evapotranspiration originating from the saturated zone, and $\overline{Q_{TRANSFER}}$ is ground water flow out of the watershed. Assuming that the storage change is 0 mm and the inter-basin groundwater flow is 0 mm over the long-term, the equation can be rearranged to solve for baseflow:

$$\overline{Q_{BF}} = \bar{R} - \overline{Q_{PUMP}} - \overline{AET_{SZ}}$$
$$(\overline{BFI})\overline{Q_{Tot}} = \bar{R} - \overline{Q_{PUMP}} - \overline{AET_{SZ}} \quad \text{Q.9}$$

Substituting the baseflow term from Eqn. Q.9 into Eqn. Q.7 and solving for $\overline{Q_{Tot}}$:

$$(1 - \overline{BFI})\overline{Q_{Tot}} = \bar{P} - \overline{AET_{VZ}} - \bar{R}$$
$$\overline{Q_{Tot}} - (\overline{BFI})\overline{Q_{Tot}} = \bar{P} - \overline{AET_{VZ}} - \bar{R}$$
$$\overline{Q_{Tot}} - (\bar{R} - \overline{Q_{PUMP}} - \overline{AET_{SZ}}) = \bar{P} - \overline{AET_{VZ}} - \bar{R}$$

Noting that $\overline{AET_{TOT}} = \overline{AET_{VZ}} + \overline{AET_{SZ}}$:

$$\overline{Q_{Tot}} = \bar{P} - \overline{AET_{TOT}} - \overline{Q_{PUMP}} \quad \text{Q.10}$$

Substituting estimates for long-term average precipitation (Government of Canada, 2019), $\overline{AET_{TOT}}$ from the Budyko curve (Budyko, 1961; Gentine et al., 2012; Raes, 2009; Wiebe et al., 2019), and average groundwater extraction per unit watershed area (Matrix and SSPA, 2014b):

$$\overline{Q_{Tot}} = \bar{P} - \overline{AET_{TOT}} - \overline{Q_{PUMP}}$$
$$\overline{Q_{Tot}} = 900\ mm - (0.64)(900\ mm) - \left(23{,}000\frac{m^3}{d}\right)\left(365\frac{d}{yr}\right)(1000\ mm/m)/(78{,}000{,}000\ m^2)$$
$$\overline{Q_{Tot}} = 216\ mm$$

Total streamflow appears to increase by a factor of 1.54 between the WSC gauge (140.5 mm; WSC, 2019) and the watershed outflow on average. The overall watershed area (78 km$^2$) is a factor of 1.65 times the gauged area (47.4 km$^2$).

If the hypothesis by CH2MHILL and SSPA (2003) that the lower reaches of Alder creek receive increased baseflow is correct, then the minimum baseflow index estimate (0.60) for the Upper Grand River watersheds from Neff et al. (2005) is reasonable. The baseflow index for the area above the New Dundee WSC gauge (WSC, 2019) within the Alder Creek watershed was calculated to be 0.56 using the PART hydrograph separation program (Barlow et al., 2015). Solving for recharge by rearranging Eqn. Q.7 and applying the vadose zone correction factor from Appendix P, and the minimum baseflow index from Neff et al. (2005):

$$\bar{R} = \bar{P} - \overline{AET_{VZ}} - (1 - \overline{BFI})\overline{Q_{Tot}}$$

$$\bar{R} = 900\,mm - (0.64)(0.91)(900\,mm) - (1 - 0.60)(216\,mm)$$

$$\bar{R} = 290\,mm$$

Thus, recharge is estimated to be slightly (~10%) less than the value estimated by Matrix and SSPA (2014a), which was 321 mm (M.H. Brouwers, pers. comm., 2017).